

3D Printed Microfluidic Devices for Particle and Cell Analysis



Sarah Margaret Hampson
Department of Chemistry

A Doctoral Thesis. Submitted in partial fulfilment of the
requirements for the award of the degree of Doctor of
Philosophy of Loughborough University.

2019

Contents

Table of Figures	viii
Table of Tables	xvii
Acknowledgements.....	xix
List of Abbreviations	xx
Abstract	1
Chapter 1 Introduction.....	2
1.1 Particle/cell analysis.....	2
1.1.1 Manual microscopy techniques.....	3
1.1.2 Static image analysis	3
1.1.3 Dynamic image analysis.....	4
1.1.4 Laser diffraction.....	6
1.1.5 Dynamic light scattering.....	7
1.1.6 Nanoparticle tracking analysis.....	8
1.1.7 Flow cytometry.....	9
1.1.8 Resistive Pulse Sensing.....	10
1.1.9 Summary.....	12
1.2 Particle/cell separation.....	14
1.3 Lab-on-a-chip devices.....	14
1.3.1 Microfluidics.....	15
1.4 Microfluidic partide/cell analysis.....	16
1.4.1 Imaging flow cytometry.....	17
1.4.2 Optical flow cytometry.....	17
1.4.3 Electroration.....	18
1.4.4 Static electrical impedance spectroscopy.....	18
1.4.5 Dynamic electrical impedance spectroscopy.....	19
1.4.6 Flow resistive pulse sensing.....	20
1.4.7 Summary.....	20
1.5 Microfluidic partide separation.....	21
1.5.1 Pinched flow fractionation.....	22
1.5.2 Inertial separation.....	23
1.5.3 Deterministic lateral displacement.....	23
1.5.4 Electrophoretic separation	24
1.5.5 Dielectrophoretic separation	24

1.5.6 Acoustophoretic separation.....	24
1.5.7 Magnetophoretic separation	25
1.5.8 Summary.....	27
1.6 Conventional microfluidic fabrication methods	28
1.6.1 Silicon and glass photolithography	28
1.6.2 Polymer fabrication.....	30
1.6.3 Elastomer soft-lithography	30
1.6.4 Summary and outlook.....	32
1.7 Additive manufacturing	33
1.7.1 Fused deposition modelling.....	33
1.7.2 Selective laser sintering and selective laser melting.....	34
1.7.3 Ultrasonic consolidation	34
1.7.4 Stereolithography	35
1.7.5 Binder jetting.....	35
1.7.6 Laminated object manufacturing	36
1.8 Additively-manufactured microfluidics	36
1.9 Comparison of lithographically-made and 3D printed microfluidics.	37
1.10 Comparison of optical and electrochemical particle analysis methods	40
1.11 Chapter summary.....	42
1.12 Thesis Hypothesis.....	42
1.13 Thesis Aims and Objectives	43
1.14 References.....	43
Chapter 2 Theory.....	61
2.1 Introduction.....	61
2.2 Microfluidics.....	61
2.2.1 Microfluidic flow behaviour	61
2.2.2 Particle transport in microfluidic flow.....	64
2.3 Additively manufactured microfluidics.....	64
2.3.1 Resolution.....	65
2.3.2 Staircase effect	65
2.3.3 Support structures	67
2.3.4 SLA overhangs	67
2.3.5 Build direction	68
2.3.6 Effects on laminar flow by microchannel errors	69
2.3.6.1 Dimensional errors	69
2.3.6.2 Surface roughness	69

2.4 Additive manufacturing by stereolithography	70
2.5 Optical flow cytometry	71
2.5.1 Hydrodynamic focusing	71
2.5.2 Optical detection	73
2.5.3 Microfluidic optical flow cytometry.....	73
2.6 Resistive pulse sensing.....	74
2.6.1 Pulse analysis.....	75
2.6.2 Ion current rectification.....	77
2.7 Magnetophoretic separation.....	78
2.8 References.....	79
Chapter 3 Microfluidic printing by stereolithography	84
3.1 Abstract.....	84
3.2 Introduction.....	85
3.3 Aims and Objectives.....	89
3.4 Materials and Methods.....	89
3.4.1 Materials.....	89
3.4.1.1 Chemicals and reagents	89
3.4.1.2 Beads.....	90
3.4.2 Methods.....	90
3.4.2.1 Drafting and stereolithography.....	90
3.4.2.2 Cover layer.....	90
3.4.2.3 Threads.....	91
3.4.3.4 Optical microscopy	91
3.4.3.5 Image analysis.....	91
3.4.3.6 Fluidic control	91
3.4.3.7 Focused dye stream sizing.....	92
3.4.3.8 Particle wafer absorption study.....	92
3.4.3.9 Particle channel adsorption study.....	92
3.4.3.10 Particle quantification by TRPS	93
3.4.3.11 Particle suspension flow in X-direction hydrodynamic junction.....	93
3.4.3.12 Statistical methods	93
3.5 Results & Discussion.....	93
3.5.1 Device design.....	93
3.5.2 Optical chip prototype.....	95
3.5.2.1 Build direction effects: channel quality	97
3.5.2.2 Build direction effects: dye testing.....	101

3.5.2.3 Build direction effects: minimum core stream size.....	102
3.5.3 Sensor grooves	104
3.5.4 Threads	107
3.5.5 Resistive pulse sensing chip	108
3.5.5.1 Pore resolution study.....	108
3.5.6 Particle fouling investigation.....	112
3.5.6.1 Cured Accura® 60 structure.....	112
3.5.6.2 Cured Accura® 60 wafer adsorption study.....	113
3.5.6.3 Fouling into Accura® 60 microfluidic channels	116
3.5.6.4 Particle adsorption onto support structures	117
3.6 Conclusions.....	118
3.7 References.....	119
Chapter 4 3D printed microfluidic lab-on-a-chip device with integrated optical detection for particle counting and analysis.....	125
4.1 Abstract	125
4.2 Introduction.....	126
4.3 Aims and Objectives	128
4.4 Materials and Methods.....	128
4.4.1 Materials	128
4.4.1.1 Chemicals and reagents	128
4.4.1.2 Beads.....	128
4.4.2 Methods.....	129
4.4.2.1 Device drafting.....	129
4.4.2.2 Stereolithography and post-print processing.....	129
4.4.2.3 Optical fibre embedding	129
4.4.2.4 Device sealing	130
4.4.2.5 Fluidic control	130
4.4.2.6 Microscopy and image processing	130
4.4.2.7 UV/visible spectroscopy.....	130
4.4.2.8 Dye analysis procedure	130
4.4.2.9 Particle analysis procedure.....	131
4.4.2.10 Signal processing.....	131
4.4.2.11 Genetic algorithm optimisation	131
4.4.2.12 Statistical Methods	133
4.5 Results and Discussion.....	133
4.5.1 Final flow cytometer design.....	133

4.5.2 Chip experimental parameters.....	135
4.5.3 Dye stream testing.....	135
4.5.3.1 Effects of inner/sheath flow ratio and total flow rate on core stream width.....	135
4.5.3.1 Effect of inner/sheath flow ratio on core stream stability.....	138
4.5.3.2 Effect of overall flow rate on core stream stability.....	139
4.5.3.3 Core stream absorbance comparison to theoretical values.....	140
4.5.4 Optimisation of particle flow cytometry by genetic algorithm.....	141
4.5.4.1 Genetic algorithm partide runs.....	144
4.5.5 Particle counting.....	151
4.5.6 Particle sizing.....	154
4.6 Conclusions.....	155
4.7 References.....	156
Chapter 5 Additive manufacture of a resistive pulse sensing microfluidic device.....	160
5.1 Abstract.....	160
5.2 Introduction.....	161
5.3 Aims and Objectives.....	163
5.4 Materials and Methods.....	163
5.4.1 Materials.....	163
5.4.1.1 Chemicals and reagents.....	163
5.4.1.2 Beads.....	164
5.4.1.3 Cells.....	164
5.4.2 Methods.....	164
5.4.2.1 Device drafting.....	164
5.4.2.2 Stereolithography and post-print processing.....	164
5.4.2.3 Electrode embedding.....	165
5.4.2.4 Device sealing.....	165
5.4.2.5 Fluidic control.....	165
5.4.2.6 Noise shielding and set-up.....	165
5.4.2.7 Data collection.....	165
5.4.2.8 Current-voltage response measurements.....	166
5.4.2.9 Particle runs.....	166
5.4.2.10 Cell runs.....	166
5.4.2.11 Photography and microscopy.....	166
5.4.2.12 FEM modelling.....	166
5.4.2.13 Statistical methods.....	167
5.5 Results & discussion.....	167

5.5.1 Chip concept.....	167
5.5.2 Device parameters.....	168
5.5.2.1 Pore channel dimensions.....	170
5.5.3 Current-voltage response.....	173
5.5.4 Predicted pulse magnitudes.....	181
5.5.5 Faraday cage shielding.....	182
5.5.6 Particle quantification.....	183
5.5.7 Particle throughput.....	184
5.5.8 Particle pulse shapes.....	185
5.5.9 Finite element method pulse simulation.....	188
5.5.10 Pore channel scanning electron microscopy imaging.....	190
5.5.11 20 and 30 μm bead mixture analysis.....	190
5.5.12 Analysis of 10 μm beads.....	192
5.5.13 Analysis of skeletal muscle cells.....	194
5.5 Conclusions:.....	195
5.6 References.....	196
Chapter 6 3D printed devices for particle magnetic separation.....	200
6.1 Abstract.....	200
6.2 Introduction.....	201
6.3 Aims and Objectives.....	203
6.4 Materials and Methods.....	204
6.4.1 Materials.....	204
6.4.1.1 Chemicals and reagents.....	204
6.4.1.2 Beads.....	204
6.4.2 Methods.....	204
6.4.2.1 Magnetic field measurements of small rod magnet.....	205
6.4.2.2 Device fabrication.....	205
6.4.2.3 Fluidic control.....	205
6.4.2.4 Flow rate measurements.....	206
6.4.2.5 Non-magnetic particle runs.....	206
6.4.2.6 Magnetic particle runs.....	206
6.4.2.7 Particle quantification by TRPS.....	206
6.4.2.8 Investigation of spiral separator mixing.....	207
6.4.2.9 Fluorescent particle visualisation.....	207
6.4.2.10 Microscopy, photography and video filming.....	207
6.5 Results and Discussion.....	207

6.5.1 Magnetic field measurements through air and Accura® 60	208
6.5.2 Y-junction magnetic separator device prototype.....	208
6.5.2.1 Fluid flow measurement	209
6.5.2.2 Magnetic partide testing	210
6.5.2.3 Non-magnetic particle testing	211
6.5.3 Integrated magnetic separator/resistive pulse sensing device: 1 st prototype	211
6.5.3.1 Flow testing	213
6.5.3.2 Particle separation testing.....	214
6.5.4 Integrated magnetic separator/resistive pulse sensing device: 2 nd prototype.....	216
6.5.5 Spiral magnetic separator devices	218
6.5.5.1 Fluid flow measurement	219
6.5.5.2 Investigation of fluid mixing across channel bridges.....	220
6.5.5.3 Fluorescent particle testing.....	220
6.5.5.4 Single-turn bridged magnetic separator device.....	221
6.5.6 Advanced spiral magnetic separator device	222
6.6 Conclusions.....	222
6.7 References.....	223
Chapter 7 Conclusions and Further work.....	226
7.1 Conclusions.....	226
7.2 Further work.....	228
7.2.1 Additively manufactured microfluidic fabrication.....	228
7.2.2 Optical partide analysis device.....	229
7.2.3 Resistive pulse sensing partide analysis device	230
7.2.4 Magnetic separator devices.....	230
7.2.5 Concluding remarks.....	230
7.3 References.....	231
Chapter 8 Attended Conferences.....	233
Chapter 9 Publications	234

Table of Figures

<i>Figure 1.1 Schematic illustrating static imaging analysis. Particles are dispersed over a surface, usually a microscope slide, which is moved under the field of view of a camera for image capture.</i>	<i>4</i>
<i>Figure 1.2 Showing dynamic imaging analysis. Particle flow is typically in a flow cell perpendicular to the optical path.</i>	<i>5</i>
<i>Figure 1.3 Schematic of typical laser diffraction configuration. Light from a red wavelength laser and/or a blue wavelength laser is passed through a particulate sample in a flow cell, and the angular variation in the resulting scattered light is measured by a series of photodiode detectors.</i>	<i>6</i>
<i>Figure 1.4 Schematic showing typical dynamic light scattering (DLS) set-up. A laser beam is passed through a particle suspension and intensity fluctuations monitored by photomultiplier tubes.</i>	<i>8</i>
<i>Figure 1.5 Schematic showing nanoparticle tracking analysis (NTA), covering scattering of laser light by a particle suspension within a flow cell, and subsequent magnification and detection.</i>	<i>9</i>
<i>Figure 1.6 Schematic showing optical flow cytometry (FC) processes: hydrodynamic focusing of sample flow into single-file by flanking sheath flows, followed by laser detection of individual particles.</i>	<i>10</i>
<i>Figure 1.7 Schematic showing resistive pulse sensing (RPS). A particle suspended in a conducting fluid translocates through a pore, causing a sudden drop in the measured background ionic current.</i>	<i>11</i>
<i>Figure 1.8 Sample analysis size ranges of common particle/cell analysis techniques.</i>	<i>12</i>
<i>Figure 1.9 Example configurations for two magnet system types for LOC magnetophoresis: a) external macroscale magnets: (i) simple flow chamber and (ii) advanced, sub-population sorting flow chamber, and b) internal magnets: controllable micro-electromagnet matrix. The external magnet systems utilise continuous separation whilst the internal magnet system involves magnetic trapping. Blue dots=non-magnetic particles, grey dots=magnetic particles.</i>	<i>26</i>
<i>Figure 1.10 Basic photolithographic fabrication process for a silicon or glass microfluidic chip, encompassing photomask drafting and etching, micropattern etch mask fabrication, device sealing and inlet/outlet drilling.</i>	<i>29</i>
<i>Figure 1.11 Basic soft lithography fabrication process for a PDMS microfluidic chip, encompassing photomask drafting and etching, micropattern master mould fabrication, PDMS casting and device sealing.</i>	<i>31</i>
<i>Figure 1.12 Fabrication of 3D printed microfluidic device, encompassing only device drafting and printing.</i>	<i>37</i>
<i>Figure 2.1 Illustration of dye tracer transport in a) turbulent flow as commonly seen in macroscale flow systems b) laminar flow as commonly seen in microfluidic flows and c) transitional flow.</i>	

Streamlines are designated by straight black lines parallel to the mean flow. The dye trace is represented by a red line. Eddies are represented by curved black arrows. 61

Figure 2.2 Illustrations of velocity flow profiles for a) turbulent flow and b) laminar flow³. Arrows represent the overall mean flow path..... 62

Figure 2.3 Illustration of the staircase effect occurring on a curved part surface in SLA. TL=layer height. The effect is greater at smaller part angles. 66

Figure 2.4 Illustration of the effects on different shapes of microchannels by AM: a) microchannel cross-sectional outlines and b) corresponding resultant AM structures, showing build layers. 66

Figure 2.5 Illustration of laser overcure occurring in microchannel cross-section: a) intended build of microchannel with build direction outlined, and b) subsequent printed channel with laser-overcure occurring on microchannel ceiling²⁹. 68

Figure 2.6 Illustration depicting the three possible build directions for an object 69

Figure 2.7 Illustration of two main configurations of SLA: a) free surface, or “bath” configuration and b) constrained surface, or “bat” configuration. Build platform movement during build is denoted by red arrow. 71

Figure 2.8 Schematic of flow cytometry hydrodynamic focusing process inside flow focusing chamber. 72

Figure 2.9 Typical two-dimensional hydrodynamic focusing junction as used in microfluidic systems. 74

Figure 2.10 Schematic of a continuous microfluidic RPS sensing junction, including sensing orifice and electrode pair for electric field generation. 75

Figure 2.11 Illustration of example current vs. time profile of ‘square’ particle blockade events as typically see in a cylindrical pore. Three key characteristics are highlighted: frequency, duration and magnitude..... 76

Figure 2.12 Linear current-voltage relationship as seen when no ICR is present. b) Non-linear current-voltage relationship, indicative of ICR⁷⁹. 78

Figure 3.1 Schematic of microfluidic device production, encompassing printing, rinsing, sensor embedding and sealing steps..... 95

Figure 3.2 Schematic illustrating hydrodynamic focusing and detection processes in the 3D printed optical device. 96

Figure 3.3 CAD file of optical chip prototype. 96

Figure 3.4 Illustration showing the build directions used in hydrodynamic junction prototype printing. Printing directions are given in blue. The different channels are labelled. 97

<i>Figure 3.5 Hydrodynamic focusing junction prototypes printed in the three build directions (top-to-bottom, X, Y and Z), and after thread tapping.....</i>	<i>98</i>
<i>Figure 3.6 Photographs of hydrodynamic focusing junctions built in the three build directions:.....</i>	<i>99</i>
<i>Figure 3.7 Dye solution flows in hydrodynamic focusing junctions (middle row) and Y-junctions (bottom row) printed in the three build directions (top row) a) Y-direction, b) X-direction and c) Z-direction.....</i>	<i>102</i>
<i>Figure 3.8 Plots of measured dyed core stream diameters created with different inner/sheath flow rate ratios for hydrodynamic focusing prototypes printed in the 3 different build directions at a 200 mbar inner flow. The smallest possible stable core stream diameters are indicated. Error bars denote standard deviation of five separate width measurements taken from one image.....</i>	<i>103</i>
<i>Figure 3.9 Illustration of a fibre/electrode groove cross-section on a printed part surface. The groove allows full fitting of a circular waveguide/wire whose edge is flush with the part surface, impossible with semi-circular grooves, but is susceptible to leaks on either side.</i>	<i>104</i>
<i>Figure 3.10 CAD files of 3D printed wafers made with surface a) straight and b) diagonal, 45° grooves.....</i>	<i>104</i>
<i>Figure 3.11 Deviation from nominal groove width as in STL file (grey) by straight (blue) and diagonal (red) grooves. Points denote mean width of sets of three groove repeats, with 15 measurements taken of each pore. Error bars denote the standard deviation of the mean pore widths in each set of three repeats.....</i>	<i>105</i>
<i>Figure 3.12 3D printed 1/16" threads printed a) horizontally and b) vertically, the former displaying laser overcure present on the thread 'ceiling'.</i>	<i>107</i>
<i>Figure 3.13 CAD file of RPS pore channel array. Pores had lengths of 500 μm, and square width and depth cross-sections of 110 μm, 100 μm, 90 μm, 80 μm, 70 μm, 60 μm, 50 μm and 40 μm. There were six repeats made of each pore dimension.</i>	<i>108</i>
<i>Figure 3.14 Photographs of RPS open pore channels, made by SLA in Accura® 60 in the Y-direction build, in HR mode, showing a range of nominal widths (rows, top-to-bottom): 110 μm, 100 μm, 90 μm, 80 μm, 70 μm, 60 μm, 50 μm, 40 μm.</i>	<i>109</i>
<i>Figure 3.15 Mean measured pore widths in printed pore array wafer, calculated from the mean widths of each pore in a set of six repeats, with 15 separate width measurements made on every pore repeat. Error bars denote the standard deviation of the mean pore widths in each set of six repeats.....</i>	<i>110</i>
<i>Figure 3.16 Mean measured width variation within pore channels in printed pore array wafer.....</i>	<i>111</i>
<i>Figure 3.17 Mean measured pore channel width ranges found in printed pore array wafer.</i>	<i>111</i>

Figure 3.18 Structures of charged polymers: a) PEI, positively-charged polymer and b) PAAMA, negatively-charged polymer.	114
Figure 3.19 Photograph of printed Accura® 60 wafer during particle adsorption study. Aliquots (250 µL) of different particle suspensions have been added to each wafer section to incubate.	115
Figure 3.20 Photographs of 1000 µm diameter, internal, X-direction channels in Accura® 60 for second particle fouling study. a) Set of 4 solo channels and b) bridged pair of channels.	117
Figure 3.21 Photograph of support structure artefact inside X-direction build flow cytometer device, showing adsorbed particles.	117
Figure 4.1 Flow chart illustrating the closed-loop optimisation of experimental conditions described in this chapter.	132
Figure 4.2 a) CAD design of final optical flow cytometer design, featuring juts to hold the device inside the Nikon Optiphot microscope system used. b) Photograph of printed optical flow cytometer device. Embedded optical fibres protrude out of the side of the device.	134
Figure 4.3 Focusing of a central stream of methylene blue (aq. solution) across a range of inner/sheath flow ratios and total flow rates. The grey boxes indicate pressures beyond the working range of the pump system.	137
Figure 4.4 Decrease in measured output light intensity at 665 nm with increase in inner/sheath flow ratio (due to the increasing width of the focused dye stream). Variance in core stream width due to different total overall flow rate also shown.	138
Figure 4.5 Shows a linear plot of the measured absorbance at 665 nm (aqueous methylene blue λ_{max}) for different thicknesses of dye core streams, with the sheath flow held steady under 200 mbar pressure. Plot and R2 value include a (0,0) value. b) Shows the corresponding λ_{max} absorbance signal over time for the different core stream thicknesses. Absorbance fluctuation increases with core stream width.	139
Figure 4.6 Scatter plot of mean measured dyed core stream width SD versus total overall flow rate, for different inner/sheath ratios.	140
Figure 4.7 Plot of core stream sizes gained from absorbance measurements and application of Beer–Lambert Law, for MB core streams over a range of inner/sheath flow ratios at 200 mbar sheath flow (red), in comparison to core stream sizes gained by image analysis of dye stream photographs (blue).	141
Figure 4.8 Diagram illustrating Pareto optimality. Point a dominates point c, as it is superior in both objectives. Additionally, point a is inferior to point b in terms of objective 1, but it is superior in terms of objective 2. In this situation neither point is superior. As neither point to inferior to any other point in the dataset, they are said to be non-dominated; they form the Pareto front.	143

Figure 4.9 Recorded pulse spectrum for run ‘H1’ in genetic algorithm (see Table 12), involving a 30 μm particle core stream (1.91×10^5 particles mL^{-1}) dyed with MB and analysed via a 105 μm core optical fibre. A very low baseline light intensity of approximately 39 counts was measured, which is significantly below the minimum 125 count threshold set. Particle pulses are obscured by the resultant signal-to-noise ratio.....145

Figure 4.10 Sample of recorded pulse spectrum for run ‘P1’ in genetic algorithm (see Table 4.3), involving a 1.35×10^5 particles mL^{-1} 30 μm particle core stream analysed via a 50 μm core optical fibre at 2.40 inner/sheath flow ratio and 304 mbar total pressure.146

Figure 4.11 Sample of recorded pulse spectrum for run ‘I1’ in genetic algorithm (see Table 4.3), involving a 1.97×10^5 particles mL^{-1} 30 μm particle core stream analysed via a 105 μm core optical fibre at 2.65 inner/sheath flow ratio and 303 mbar total pressure.146

Figure 4.12 Findings of GA optimisation of optical particle analysis experimental parameters. Plots a)–c) denote the same evaluated experimental parameters coloured by performance in terms of a) pulse magnitude variation, b) pulse periodicity variation (time between pulses) and b) mean pulse magnitude. d) Denotes the same points coloured by algorithm generation. e) Example pulse spectrum gained under non-optimised conditions (“I2”), versus f) that gained under optimum conditions “A2”. Plots a)-d) created by William Rowe (Loughborough University, Department of Chemistry).149

Figure 4.13 Recorded pulse spectrum for found optimum run ‘A2’ in genetic algorithm (see Table 4.4), involving a 8.06×10^3 particles mL^{-1} 30 μm particle core stream analysed via a 105 μm core optical fibre at 2.63 inner/sheath flow ratio and 207 mbar total pressure.150

Figure 4.14 Recorded pulse spectrum for run ‘H2’ in genetic algorithm (see Table 4.4), involving a 1.35×10^5 particles mL^{-1} 30 μm particle core stream analysed via a 105 μm core optical fibre. Sample suspension flow appears unstable, as indicated by large bursts of pulses.150

Figure 4.15 Plot of pulse count measured versus particle concentration by the printed optical chip, each count captured over 100 s at the deduced optimised conditions for 30 μm beads.....151

Figure 4.16 Examples of particle runs from the 30 μm bead count calibration graph: a) 1×10^3 particles mL^{-1} b) 1×10^4 particles mL^{-1} c) 5.5×10^4 particles mL^{-1} d) 1.0×10^5 particles mL^{-1} , all run under the found optimum conditions. a)–c) Fall in the calibration graph region. d) Falls in the graph plateau region.153

Figure 4.17 Recorded pulse spectra at found optimised conditions (‘A2’) for a) 30 μm beads (2.5×10^4 beads mL^{-1}) b) 10 μm beads (2.5×10^4 beads mL^{-1}) c) a 1:1 mixture of the two beads (each 1.25×10^4 beads mL^{-1}). The red line denotes the mean baseline light intensity, with the green lines denoting $3 \times \text{SD}$ of the noise from a blank run. d) Histogram showing percentage of pulses vs. signal intensity for

10 μm beads (2.5×10^4 beads mL^{-1}), 30 μm beads (2.5×10^4 beads mL^{-1}), and the 1:1 mixture (1.25×10^4 beads mL^{-1}).	154
Figure 5.1 Schematic illustrating a) particle translocation through the pore channel under microfluidic flow, and b) resulting pulses from different-sized particles.	167
Figure 5.2 Illustration of pore device channel cross-section. H_c (channel height), H_p (pore channel height), L_p (pore channel length), L_r (ramp length).	168
Figure 5.3 CAD files of the two device configurations used for the microfluidic RPS device, with features labelled: a) more compact design featuring horizontal threads, and b) larger design featuring vertical threads.	169
Figure 5.4 Photographs of two different pore device configurations, with embedded electrodes and cover layer. a) A larger chip design with vertical threads, and b) a more compact chip but with horizontal threads.	170
Figure 5.5 Dimensions of the three different pore channels investigated: two high aspect-ratio pore channels a) $H_p, W_p=100 \mu\text{m}$ and $L_p=500 \mu\text{m}$ and b) $H_p, W_p=80 \mu\text{m}$ and $L_p=500 \mu\text{m}$, and one lower aspect-ratio pore channel c) $H_p, W_p, L_p=100 \mu\text{m}$.	172
Figure 5.6 Photograph of the three pore sizes printed in Accura [®] 60: a) $H_p, W_p=100 \mu\text{m}$, $L_p=500 \mu\text{m}$, 3 separate device repeats (i)–(iii), b) $H_p, W_p, L_p=100 \mu\text{m}$, c) $H_p, W_p=80 \mu\text{m}$,	173
Figure 5.7 Effect of flow rate on I-V curves for pore channel $H_p, W_p=100 \mu\text{m}$, $L_p=500 \mu\text{m}$ at a) KCl (0.5 mM) and b) KCl (1.0 mM).	174
Figure 5.8 Effect of flow rate on I-V curves for pore channel $H_p, W_p, L_p=100 \mu\text{m}$ in KCl (0.5 mM)	175
Figure 5.9 Effect of electrolyte concentration on I-V curves of $H_p, W_p=100 \mu\text{m}$, $L_p=500 \mu\text{m}$ pore at 50 mbar. a) And b) are repeat runs.	176
Figure 5.10 Current-voltage responses for a printed $H_p, W_p=100 \mu\text{m}$, $L_p=500 \mu\text{m}$ pore channel, for a) a range of flow rates and KCl (0.25 mM), and b) for a range of KCl concentrations at 2 different flow rates (55 mbar and 75 mbar).	178
Figure 5.11 Current-voltage responses for a printed $H_p, W_p, L_p=100 \mu\text{m}$ pore channel, for a) a range of flow rates and KCl (0.25 mM), and b) for a range of KCl concentrations at 2 different flow rates (55 mbar and 75 mbar).	179
Figure 5.12 Current-voltage responses for a printed $H_p, W_p=80 \mu\text{m}$, $L_p=500 \mu\text{m}$ pore channel, for a) a range of flow rates and KCl (0.25 mM), and b) for a range of KCl concentrations at 2 different flow rates (55 mbar and 75 mbar).	180
Figure 5.13 Overlaid I-V curves for KCl (1.0 mM) in the $H_p, W_p=100 \mu\text{m}$, $L_p=500 \mu\text{m}$ pore for the two current amplifiers used: the eOne (Elements) and QSensing3 (Izon Science). The former saturates rapidly.	181

Figure 5.14 Photographs of the custom-made Faraday cage obtained by Nanopore Solutions that was used for RPS particle/cell studies. a) Shows the initial steel sheets (1 mm thickness) before welding and drilling of holes, and b) shows the finished Faraday cage (box and lid).182

Figure 5.15 Correlation curve of pulse frequency measured by the Hp, Wp=100 μm , Lp=500 μm printed RPS pore channel with increasing particle concentration for particle diameter=30 μm , 50 mbar and 75 mbar applied pressure. Points represent means of 3 repeat runs. Trendlines were forced through the origin (0,0). Error denote standard deviation of triplicate runs.183

Figure 5.16 Plots of measured particle rate (pulse frequency) over a range of flow rates for 30 μm bead suspensions (7.5×10^3 beads mL^{-1}), in different printed RPS pore devices:185

Figure 5.17 Gained pulse information from a Hp, Wp=100 μm , Lp=500 μm pore channel RPS chip, using 30 μm beads (7.5×10^3 particles mL^{-1}), KCl (0.25 mM), +5.64 V applied voltage at applied pressures: blue=45 mbar, orange=65 mbar, grey=85 mbar, yellow=105 mbar: a) pulse magnitude distribution, b) pulse duration, c) scatter plot of pulse duration versus magnitude, and d) example pulse shapes for the different flow rates.....186

Figure 5.18 Gained pulse information from a Hp, Wp, Lp=100 μm pore channel RPS chip, using 30 μm beads (7.5×10^3 particles mL^{-1}), KCl (0.25 mM), +5.64 V applied voltage at applied pressures: blue=45 mbar, orange=65 mbar, grey=85 mbar, yellow=105 mbar: a) pulse magnitude distribution, b) pulse duration, c) scatter plot of pulse duration versus magnitude, and d) example pulse shapes for the different flow rates.187

Figure 5.19 Examples of pulse shapes gained from a run of 30 μm beads (7.5×10^3 particles mL^{-1}) in a Hp, Wp=80 μm , Lp=500 μm pore, applied pressure: 35 mbar, KCl (0.25 mM), +5.64 V applied voltage.188

Figure 5.20 Predicted pulse shape generated by FEM by Peter Hauer, University of Wellington, School of Chemical and Physical Sciences, for a Hp, Wp=105 μm , Lp=545 μm pore channel, particle diameter=30 μm , voltage=+5.64 V, $\sigma=3.675$ mS/m (KCl, 0.5 mM). The vertical lines indicate the beginning of the ramp structures.....189

Figure 5.21 SEM images taken of 'pore copy 1', a Hp, Wp=100 μm , Lp=500 μm pore (accurate dimensions: Hp, Wp=105 μm , Lp=545 μm). a) Pore channel profile, b) view looking down pore channel, c) view of one of the ramps, d) view of other ramp.190

Figure 5.22 Results of analysis of 20 μm and 30 μm bead mixtures by a printed Hp, Wp=80 μm , Lp=100 μm RPS chip in KCl (0.25 mM), +4.5 V, 100 mbar (a–c), KCl (0.5 mM), +3.58 V, 100 mbar....191

Figure 5.23 Analysis of 10 μm beads via Hp, Wp=80 μm , Lp=500 μm pore channel, 300 mbar applied pressure, 3.0×10^4 beads mL^{-1} in PBS (5 mM), +4.24V applied voltage: a) Photograph of pore channel after run ended due to bead blockage, showing that channel was effectively blocked off by tape to be

~35 μm diameter. b) Frequency plot of measured pulse magnitudes centred around mean of 0.8 nA.
c) Section of recorded pulse spectrum. d) Examples of recorded pulses.....193

Figure 5.24 Gained size data measured by the printed RPS chip of a population of skeletal muscle cells (5×10^3 cells mL^{-1} , 75 mbar, KCl, 0.25 mM). Repeat runs are denoted as ‘cells 1’, ‘cells 2’ and ‘cells 3’. Blue histogram denotes 30 μm calibration bead run (5×10^3 bead m^{-1} , 75 mbar, KCl, 0.25 mM)...194

Figure 6.1 B-field measurements taken by a Hall Probe at increasing distances from a) the end and b) the side of a Neodymium rod magnet, in through air and through Accura® 60 polymer.....208

Figure 6.2 Linear magnetic separator device prototype, with Y-junction and magnet compartment. Writing denotes magnet distance from junction.209

Figure 6.3 Measured flow rates of each line of the Y-junction magnetic separator prototype at a range of applied pressures. Plots and R^2 values include a (0,0) point.209

Figure 6.4 Collected fluid outputs from the Y-junction linear magnetic chip prototype at 2 mm magnet distance, after a 1 μm particle suspension (1.1×10^8 particles mL^{-1} in PBS) was run through at 50 mbar. Left-to-right: collected magnetic line output, collected magnetic line output, collected non-magnetic line output, and a control suspension (5.0×10^7 particles mL^{-1} in PBS) for comparison.210

Figure 6.5 Magnetic particle fouling (indicated by the red arrow) onto the microchannel wall adjacent to the magnet housing, observed after magnetic particle testing.....211

Figure 6.6 Initial prototype of combined magnetic separation/RPS measurement chip. The gap between the RPS channels is to allow sealing of the inner electrode grooves with glue to ensure water tightness.212

Figure 6.7 Photographs of RPS pore channel pairs in a combined particle magnetic separation/RPS analysis chip, made by SLA in Accura® 60.212

Figure 6.8 Tuning of focused MB (1 mM, aq) streams in the Y-junction of the combined magnetic separation/RPS chip. a) 100 mbar applied across all 3 inlets, b) 30 mbar applied across all 3 inlets c) topmost sheath flow=35 mbar, other flows 30 mbar d) topmost flow=40 mbar, other flows 30 mbar.213

Figure 6.9 Stills from videos recorded of attempted magnetic particle separation in the combined magnetic separation RPS chip using a 6.9 kg pull magnet, at 30 mbar applied pressure to all three lines. a) Magnet distance=0 mm, b) Magnet distance=2 mm, c) Magnet distance=7 mm, d) Magnet distance=2 mm and dye (MB, 1 mM) used in the particle suspension. Particle suspension=30 μm magnetic particles (1.0×10^4 particles mL^{-1}) and 20 μm non-magnetic particles (1.0×10^4 particles mL^{-1}) in KCl (0.25 mM), TWEEN (0.5%) and MB (1 mM), aq. Under all conditions, the non-magnetic particles did not travel down the magnetic line. Time: (i)=1 s, (ii)=2 s, (iii)=3 s.215

Figure 6.10 Combined magnetic separation/RPS measurement chip concept: a) illustration of separation process (initial hydrodynamic focusing followed by magnetic actuation of magnetic particles into a separate output line) and b) chip CADfile, outlining various sections including single magnetic housing in a trough configuration.217

Figure 6.11 Second prototype of combined magnetic separation/RPS measurement chip. a) View of top of chip. b) View from side of chip, showing support structures present inside the chip magnet compartment.218

Figure 6.12 Photographs of three printed spiral magnetic separators printed via SLA in Accura® 60 polymer, each comprising of a central magnet cavity surrounded by two parallel, bridged microfluidic channels. Left to right: a) bridges: 6, pitch: 10.0 mm, shielding polymer thickness: 3.0 mm, and air gap: 1.0 mm, turns: 4, b) bridges: 12, pitch: 7.0 mm, shielding polymer thickness: 3.0 mm, turns: 7, c) bridges: 12, pitch: 5.0 mm, shielding polymer thickness: 2.0 mm, turns: 7.219

Figure 6.13 Top-down view of 4.5 mm pitch spiral separator, showing three channel bridges at different heights.219

Figure 6.14 Unequal flow rates observed in 10.0 mm pitch helical separator device at a range of applied pressure. Plots and R² values include an (0,0) point.220

Figure 6.15 Photograph of helical device (6 bridge, 10.0 mm pitch separator) under visualisation box after flush with fluorescent beads, showing deposited beads on the channel floors.221

Figure 6.16 Photographs of a single-turn, bridged magnetic separation device, printed via SLA in Accura® 60 polymer, bridges: 7, pitch: 4.5 mm, shielding polymer thickness: 3.0 mm, turns: 1. Three channel blockages are denoted by red arrows.221

Figure 6.17 Concept, bridged, double-spiralled magnetic separator device. The non-magnetic line (pink) consists of a gentle spiral that encircles the central magnet cavity, and is itself encircled by the magnetic line (blue), a much tighter spiral. The two are connected by a series of bridges (bright blue) that radiate outwards from the points of the magnetic line spiral closest to the magnet.222

Table of Tables

<i>Table 1.1 Comparison of particle analysis methods.</i>	13
<i>Table 1.2 Comparison of microfluidic particle analysis methods</i>	21
<i>Table 1.3 Comparison of microfluidic particle separation methods.</i>	27
<i>Table 1.4 Comparison of costs, timescales, skills and equipment required in lithographical and AM manufacture of microfluidic devices.</i>	39
<i>Table 1.5 Performance parameters of optical and electrochemical commercial and microfluidic particle/cell analysis methods</i>	41
<i>Table 3.1 Measured mean channel widths of focusing junctions in the three build directions, averaged over 3 device copies, 10 measurements taken of each channel.</i>	100
<i>Table 3.2 Measured mean variation within hydrodynamic focusing junction channels built in the 3 build directions (averaged over three device copies, 10 measurements taken of each channel): an indication of channel wall roughness</i>	101
<i>Table 3.3 Mean widths (stemming from sets of three groove repeats, with 15 separate measurements taken of each pore), difference from nominal values, and SD between grooves and within grooves of printed straight grooves.</i>	106
<i>Table 3.4 Mean widths (stemming from sets of three groove repeats, with 15 separate measurements taken of each pore), difference from nominal values, and SD between grooves and within grooves of printed diagonal grooves.</i>	106
<i>Table 3.5 Chemical components found in uncured 3D Systems Accura® 60 photopolymer resin</i>	113
<i>Table 3.6 Mean counted adsorbed beads of opposite charge on the varying uncoated and coated sections of an Accura® 60 wafer, averaged from five separate 40 x 40 µm sections</i>	115
<i>Table 4.1 Signal processing procedure for the two different sets of experiments for the optical particle counter chip.</i>	131
<i>Table 4.2 A summary of the three objectives used by the GA to rank experiment runs, listing how they were measured and the instruction of the GA for each.</i>	144
<i>Table 4.3 Particle runs generated by the GA, first generation, as carried out by William Rowe (Loughborough University, Department of Chemistry)</i>	147
<i>Table 4.4 Particle runs generated by the GA, second generation, as carried out by William Rowe (Loughborough University, Department of Chemistry)</i>	147
<i>Table 4.5 Particle runs generated by the GA, third generation, as carried out by William Rowe (Loughborough University, Department of Chemistry)</i>	148
<i>Table 4.6 Circular surface areas of three particle sizes (30 µm, 10 µm and 4 µm) and the percentage area they cover of two optical fibre areas (50 µm and 105 µm)</i>	155

Table 5.1 Percent pore volume occupation of 30 μm , 20 μm , 10 μm , 4 μm diameter particles for the three different pores used.182

Acknowledgements

The author would like to thank the following individuals for their help during this project: David Thompson for his support in the stereolithography processes used throughout this project, Christopher Webster for his aid in the magnetic separator development work, Rowan Rimmington for his assistance in cell preparation and analysis, and Thomas Monaghan, Matthew Harding and Andrew Capel for their guidance in the additive manufacturing and embedded sensor development.

List of Abbreviations

2PP	Two Photon Polymerisation
μTAS	Micro Total Analysis System
ABS	Acrylonitrile butadiene styrene
AC	Alternating Current
AM	Additive Manufacturing
AFM	Atomic Force Microscopy
AFP	Alpha-Fetoprotein
CAGR	Compound Annual Growth Rate
CAD	Computer-Aided Design
CCF	Central Composite Face-centred
CMY	Cyan Magenta Yellow
CMYK	Cyan Magenta Yellow Key
CTC	Circulating Tumour Cell
CSA	Cross-Sectional Area
CV	Coefficient of Variation
DAD	Diode Array Detector
DC	Direct Current
DIA	Dynamic Image Analysis
DLD	Deterministic Lateral Displacement
DLP	Digital Light Printing
DLS	Dynamic Light Scattering
DNA	Deoxyribonucleic acid
DPV	Differential Pulse Voltammetry
DoE	Design of Experiments
EEG	Electroencephalogram
<i>E. coli</i>	Escherichia Coli
EIS	Electrical Impedance Spectroscopy
ELISA	Enzyme-Linked Immunosorbent Assay
EMO	Evolutionary Multiobjective Optimisation
FACS	Fluorescence-Activated Cell Sorting
FBC	Full Blood Count
FBG	Fibre Bragg Grating

FC	Flow Cytometry
FDM	Fused Deposition Modelling
FEM	Finite Element Method
FIB	Focused Ion Beam
FSC	Forward Scatter Count
GA	Genetic Algorithm
GC	Gas Chromatography
HBV	Hepatitis B Virus
HIV	Human Immunodeficiency Virus
HF	Hydrofluoric Acid
HPLC	High Performance Liquid Chromatography
HR	High Resolution
ICR	Ion Current Rectification
IFC	Imaging Flow Cytometry
IMS	Immunomagnetic Separation
IPA	Isopropyl Alcohol
IPN	Interpenetrating Network
KCl	Potassium Chloride
LAPS	Light-Addressable Potentiometric Sensor
LED	Light Emitting Diode
LOC	Lab-On-a-Chip
LOM	Laminated Object Manufacturing
MEMS	Microelectromechanical System
MB	Methylene Blue
MspA	Mycobacterium smegmatis porin A
NA	Numerical Aperture
NO	Nitric Oxide
NTA	Nanoparticle Tracking Analysis
PAD	Paper Analytical Device
PAAMA	Poly(acrylic acid co-maleic-acid)
PC	Polycarbonate
PDMS	Polydimethylsiloxane
PEEK	Polyether Ether Ketone
PEI	Polyethylenimine

PESA-II	Pareto Envelope-based Selection Algorithm II
PFF	Pinched Flow Fractionation
PLA	Polylactic Acid
PPSU	Polyphenylsulfone
POC	Point-Of-Care
PRF	Primary Radiation Force
PS	Polystyrene
PMT	Photomultiplier Tube
QC	Quality Control
RDS	Road Deposited Samples
RPS	Resistive Pulse Sensing
ROT	Electrotation
RSM	Response Surface Methodology
SD	Standard Deviation
SEM	Scanning Electron Microscopy
SFF	Solid-Freeform
SIA	Static Image Analysis
SLA	Stereolithography
SLM	Selective Laser Melting
SLS	Selective Laser Sintering
SPR	Surface Plasmon Resonance
SSC	Side Scatter Count
ssDNA	Single-Stranded Deoxyribonucleic Acid
STL	Standard Triangle Language or Standard Tessellation Language
RP	Rapid Prototyping
TEM	Transmission Electron Microscopy
TRPS	Tunable Resistive Pulse Sensing
UC	Ultrasonic Consolidation
UV	Ultraviolet
VIS	Visible
VOC	Volatile Organic Compound
XPS	X-ray Photoelectron Spectroscopy

Abstract

Particle/cell analysis is crucial in many health, industrial and environmental monitoring processes. Its integration into miniaturised lab-on-a-chip systems enables a host of portable technologies. However, current lab-on-a-chip lithographical fabrication methods are costly, time-consuming and restrictive in design, impeding their widespread implementation. This has led to 3D printing being explored as an alternative in recent years, due to its ability to form devices in a single step, and its three-dimensional freedom.

The aim of this thesis was to develop low-cost, microfluidic lab-on-a-chip devices for single particle analysis by 3D printing, encompassing characterisation and separation. Two in-line detection methods were investigated: optical and electrochemical, and device performance aspects including sensitivity, throughput, reproducibility and linear dynamic range were compared. Additionally, a number of continuous magnetophoretic particle separation modules were also printed and assessed, as a means of sample preparation in these devices. Lastly, the nature of particle adsorption, a key issue in microfluidic devices, was explored in these printed devices.

Embedded sensors in the form of optical fibres and wire electrodes were integrated into the devices inside a printed housing. An open-channel, surface printing style was utilised to improve feature resolution. The optical device was based upon flow cytometry, being composed of a hydrodynamic focusing chamber and light sensing zone, and its analysis was optimised by a genetic algorithm covering a number of flow and sample parameters. The electrochemical device contained a constrictive pore channel for resistive pulse sensing and was used inside a custom-made Faraday cage.

The optical and electrochemical chips could resolve 10 and 30 μm , and 20 and 30 μm beads, respectively. The optical device suffered from relatively low pulse uniformity, but was not as susceptible to blockages, and did not require electrical noise shielding, as did the electrochemical device. In comparison, this pore sensing device was found to have superior resolving power, throughput and linear dynamic range, and was also able to resolve a population of skeletal muscle cells. In addition, some initial studies were carried out in printed magnetic separator prototypes, but these were cut short by the ending of the project. Finally, instead of particle adsorption occurring onto printed step structures within channels as we had originally hypothesised, it was found to mostly occur by entrapment into device inlets/outlets. It is believed that this work lays the foundation for further 3D printed microfluidic technologies for in-line particle/cell processing and analysis.

Chapter 1 Introduction

1.1 Particle/cell analysis

Analysis of microscopic bodies such as particles, cells and bacteria is crucial in an extremely wide array of fields. Particle size, along with particle size distribution, affects the product quality and performance of powders, suspensions, aerosols and emulsions in a great deal of industries. For example, particle characterisation is crucial in the formulation and manufacturing of a wide range of commercial products including cosmetics¹, pharmaceuticals¹, ceramics², cement³, abrasives⁴, paints⁵, inks⁶, coatings⁷, fertilisers⁸, soils⁹ and rubber products¹⁰. It is also used in the food and beverage industry for a great deal of products such as sugars and cocoa¹¹. In all of these applications, one or a number of different particle characteristics may be measured including particle size, size distribution, concentration, morphology and surface area. In addition to the analysis of manufactured particulate products, particle analysis is also used to detect unwanted, contaminant particles in products, for example in pharmaceuticals, where knowledge of the particulate burden is required in injectable products such as water for injection (WFI)¹².

In addition to industrial processes, particle analysis is critical in the development of nanotechnologies such as composite smart materials^{13,14}, and nanomaterials for energy applications including photovoltaics¹⁵ and batteries¹⁶. Furthermore, the predicted compound annual growth rate (CAGR) of 5.4% in the particle size analysis market has been mainly attributed to increasing research output involving nanoparticle applications in drug delivery and the medical device industry¹⁷.

A significant field related to single particle analysis is single cell analysis. Single cell counting and analysis are crucial tools in the medical and clinical fields, where they are used in disease diagnosis and monitoring, and health screening¹⁸. One key example is the Full Blood Count (FBC), the most common haematology test performed and consisting of counts of red blood cells, white blood cells, platelets and other parameters in order to assess general health and detect problems such as anaemia¹⁹.

Particle analysis is also used in environmental monitoring of air²⁰, water²¹, and solid samples such as road deposited sediments (RSDs)²², and includes monitoring of man-made particles emitted from processes such as vehicle combustion²³. Requirements for environmental particle analysis are forecast to grow due to increasing legislation and emerging issues, such as the rise in biodiesel usage²⁴, recent

microbead controversy²⁵ and concern over particulate release from widespread coal combustion in China²⁶. In addition, as the use of nanomaterials increases, such as in the medical field, it is predicted that their monitoring in the environment will become more significant²⁷.

Evidently, particle/cell analysis is critical in a wide range of both current and upcoming fields, from quality testing of a vast variety of products, to use in nanotechnology development, and in health and environmental applications. What follows is a review of common particle analysis techniques.

1.1.1 Manual microscopy techniques

Particles can be sized from images recorded by scanning electron microscopy (SEM), transmission electron microscopy (TEM), and atomic force microscopy (AFM). These techniques offer accurate particle sizing down to the nanoscale: 500 μm –10 nm for SEM²⁸, 5 μm –1 nm²⁸ for TEM and 8 μm –1 nm for AFM²⁹. They also give clear morphology information³⁰, which includes three-dimensional information in the case of AFM. However, sample preparation for electron microscopy is laborious³⁰: TEM requires a complicated and highly time-consuming process³¹, whilst SEM requires that nonconductive particles are coated, for example with platinum or palladium, destroying the sample in the process³². Another downside is that TEM and SEM analysis must be carried out under vacuum²⁸. In addition, AFM has an extremely limited single scan image size and a very low scanning speed³³. Furthermore, particle image sizing requires much time and labour, unless automated image analysis software is used³⁴. Thus, in order to examine sufficient numbers of particles to obtain statistically valid quantitative data, and with the rise in computing power, manual microscopy for particle analysis has now been largely superseded by automated image analysis³⁵.

1.1.2 Static image analysis

Static image analysis (SIA) is an automated technique for analysing particles, involving the acquisition of images whilst the particulate sample is kept stationary on an optical surface. The technique can characterise thousands of individual particles and analyse a dozen size and shape parameters within minutes³⁶. First, particles are dispersed as a dry powder onto an optically-clear surface—typically a microscope slide (Figure 1.1)³⁵. This slide is translated in the X-Y plane below a digital camera, which captures an image of the field of view. Following this, a grey-scale thresholding process is used to carry out image segmentation, isolating the particles from the background and forming a binary image of each particle³⁷. These images are then analysed by digital image processing to give morphological

and grey-scale measurements for each particle. From these individual particle measurements, image population statistics are generated, or algorithms are applied to filter and sort the particles into type categories according to size and shape.

Standard optical microscope systems can be adapted to carry out SIA³⁷ and so the technique is relatively low-cost, with the exception of motorised stages. Sample movement can be performed under computer control in order to reduce manual labour and speed up the process, but it is still relatively time-consuming³⁸.

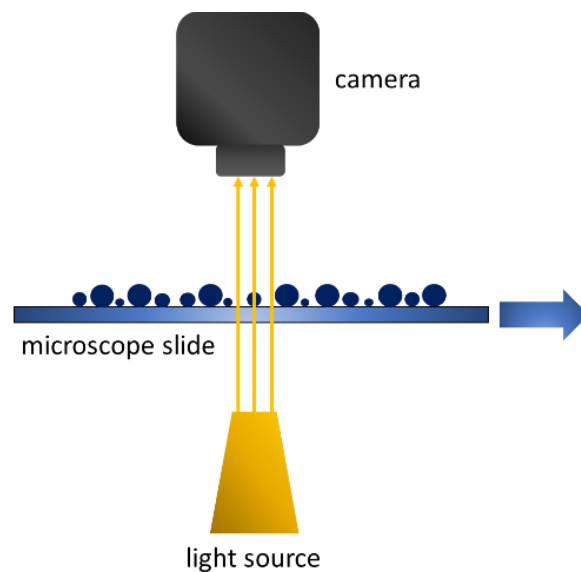


Figure 1.1 Schematic illustrating static imaging analysis. Particles are dispersed over a surface, usually a microscope slide, which is moved under the field of view of a camera for image capture.

Static image analysis is used to measure dry particles in the 1 mm–500 nm range³⁹. However, it is relatively limited in sample size, being unable to handle larger amounts of data³⁵. Additionally, its sample preparation method causes a bias when analysing irregular-shaped particles, which have a preferred orientation when laid on a horizontal surface⁴⁰.

1.1.3 Dynamic image analysis

To overcome the sampling rate limitations of SIA, an alternative technique was created where the image acquisition process was significantly accelerated, allowing much larger sampling on the scale of 80 particles s⁻¹⁴⁰ to 1200 particles s⁻¹⁴¹. This was achieved by the dynamic movement of the sample through the camera field of view during the imaging process: in dynamic imaging analysis (DIA)

particles flow past a camera in suspension (Figure 1.2) within a flow cell, allowing for larger sample imaging throughput. High speed flash illumination is used in conjunction with a synchronised camera to reduce particle motion blur. The data analysis steps in DIA are similar to that of SIA, and the technique can analyse particles sized from approximately 2.5 mm–20 μm ⁴¹.

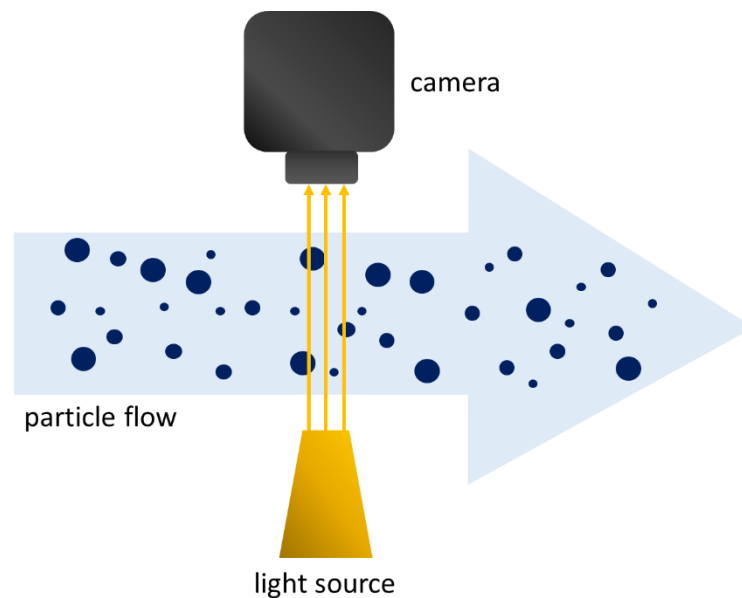


Figure 1.2 Showing dynamic imaging analysis. Particle flow is typically in a flow cell perpendicular to the optical path.

In addition to the increased sampling rate, DIA does not have the bias that exists in SIA when analysing irregular particles, as the particles are imaged in-flow in random orientations^{35,40}. However, DIA has worse depth of field issues than microscope-based SIA, in which a sample is covered with a coverslip on a slide, limiting the particle-containing plane relative to the optical axis and meaning that more particles will be correctly focused at high magnifications. In contrast, in order for the particles to be kept in focus in DIA, the flow cell depth must be restricted^{42,43}. Thus, at high magnifications, where the depth of field is low, the flow cell must be significantly narrowed⁴³ and so a sample must typically be filtered to prevent system clogging. This causes further challenges for highly heterogeneous samples, as sample fractionation into smaller size range components and running under different magnification and flow cell conditions is needed. Lastly, DIA image resolution is lower than that of SIA due to the faster image capture period⁴⁰.

1.1.4 Laser diffraction

Laser-based particle analysis methods offer greater sensitivity than particle profile imaging techniques such as SIA and DIA, as their resolution is not restricted by the diffraction limit, e.g. 250 nm for 488 nm light⁴⁴. Rather than carrying out direct particle diameter measurement from a minimum number of recorded pixels, these techniques involve measuring scattered laser light from a particle, and use this to calculate particle diameter. One example, laser diffraction (LD) (Figure 1.3), can size particles from approximately 8 mm–10 nm⁴⁵. It determines particle size from diffracted light intensity and its scattering angle³⁰, working on the principle that large particles have greater scattering intensity and smaller scattering angles than smaller particles. Instruments measure this intensity and angle, and apply an algorithm utilising Mie Scattering Theory, a theory predicting light scattering behaviour⁴⁶, to transform the scattered light data into a particle size distribution, which is reported as a volume equivalent sphere diameter: the diameter of a sphere having the same volume as the particle⁴⁷.

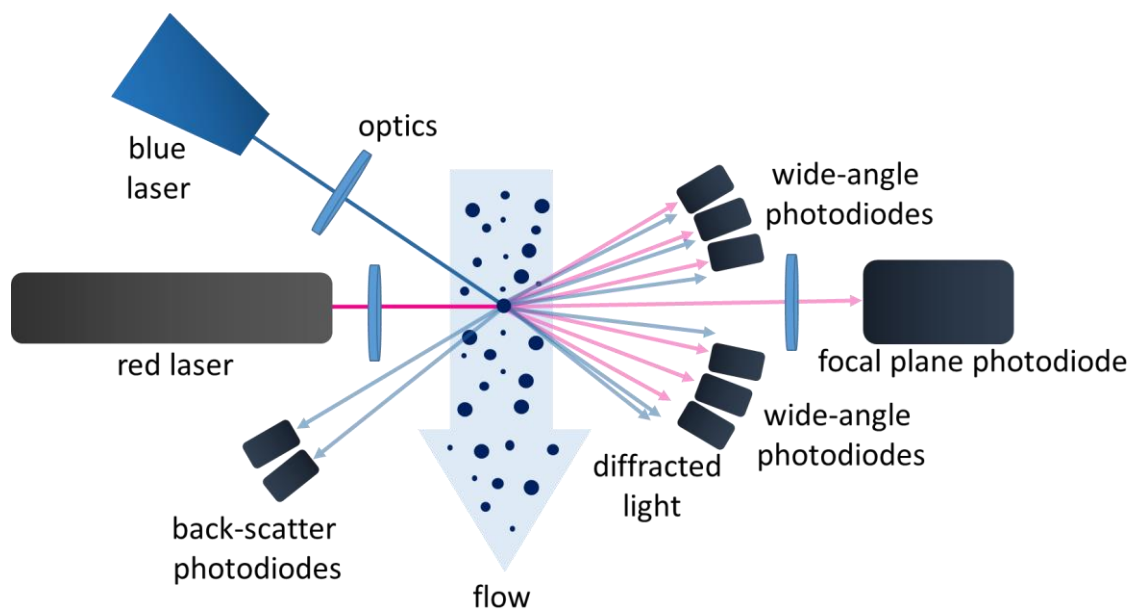


Figure 1.3 Schematic of typical laser diffraction configuration. Light from a red wavelength laser and/or a blue wavelength laser is passed through a particulate sample in a flow cell, and the angular variation in the resulting scattered light is measured by a series of photodiode detectors.

The general components of a laser diffraction system are illustrated in Figure 1.3. Probing of a particle suspension inside a flow cell is typically carried out using a red wavelength laser for larger particle sizes, or a lower wavelength, blue laser for smaller, submicron particles. Optics such as lenses and filters are utilised for light focusing and noise filtering. Laser diffraction has become the most popular

method for particle analysis due to its other advantages as well as its high sensitivity⁴⁸: it has a wide dynamic range relative to other particle analysis methods⁴⁸, and is also fast^{48,49}, and has good reproducibility^{48,49}. It also does not require calibration as it is an absolute measurement technique⁵⁰. In contrast, a critical disadvantage of laser diffraction is that it is an ensemble measurement method, where individual particles are not sized directly⁴⁸—instead, an average particle diameter is gained. This causes low resolution, with laser diffraction being poor at resolving multimodal populations⁵¹. Additionally, knowledge of sample optical properties is required for Mie theory to be utilised⁵², and the technique cannot measure particle shape or morphology information⁴⁰, which causes inaccuracy when sizing non-spherical samples. Laser diffraction also requires very low concentrations (<1% volume) in order to prevent multi-scattering, and so dilution is often required³⁰.

1.1.5 Dynamic light scattering

A laser-based particle analysis technique with an even greater sensitivity is dynamic light scattering (DLS) (Figure 1.4). This technique is able to size particles from approximately 1 μm –5 nm⁵³, and determines particle size by measuring particle motion: it measures the Brownian motion intensity of particles in suspension, via illumination with laser light followed by detection of intensity fluctuations over time in the resulting scattered light⁵⁴. Larger particles have slower Brownian motion than smaller particles. DLS measures the diffusion coefficient and interprets particle motion as free diffusion, translating this to particle size. DLS does not directly measure particle diameter—instead, it calculates particle hydrodynamic diameter, defined as the diameter of a hypothetical hard, spherical particle with the same diffusion behaviour as the particle being measured⁵⁵. A basic DLS set-up is shown in Figure 1.4. The particle suspension would typically be held inside a cuvette, and analysis would be carried out by 2 detectors: a right-angled photomultiplier tube (PMT) or a backscatter PMT for more concentrated samples.

Despite its excellent sensitivity, DLS has a number of issues. Firstly, like laser diffraction, it is an ensemble technique⁵¹, and thus is incapable of resolving individual populations within a polydisperse particle mixture unless the size difference is significant⁵⁶: ~ 30 nm at best⁵⁷. Furthermore, the presence of a small number of aggregates or large particles will skew the estimated mean diameter to an over-estimated value and can mask populations of small particles^{56,57}. Additionally, as the calculated hydrodynamic diameter includes the hydration layer around a particle, this value is often larger than the particle diameter gained from electron microscopy techniques³⁰.

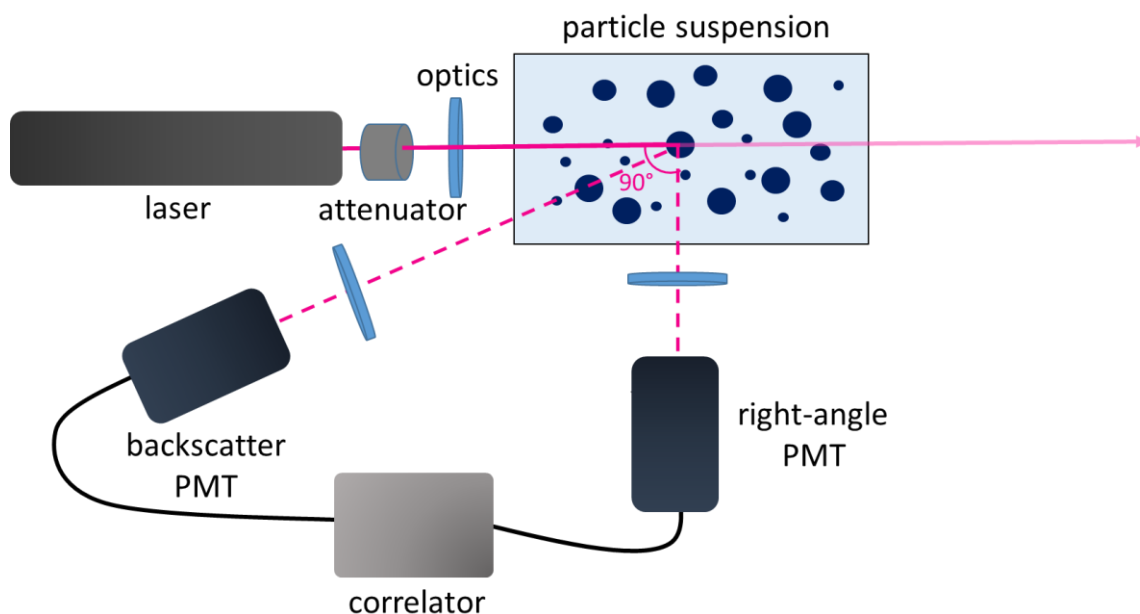


Figure 1.4 Schematic showing typical dynamic light scattering (DLS) set-up. A laser beam is passed through a particle suspension and intensity fluctuations monitored by photomultiplier tubes.

1.1.6 Nanoparticle tracking analysis

Another particle sizing method measuring particle Brownian motion is nanoparticle tracking analysis (NTA). NTA measures particle size by the simultaneous video tracking of large numbers of individual particles⁴⁸. Positions of particles within a 3D volume as projected onto a 2D image are recorded and processed, and particle movement from Brownian motion related to particle sphere equivalent hydrodynamic diameter via the Stokes–Einstein equation⁵⁸. Unlike laser diffraction and DLS, NTA measures particles individually: at known time intervals, a series of images is recorded and all spots in each image are analysed⁵⁸. Spots in the vicinity of spot coordinates on subsequent images can be attributed to the same particles, and thus, individual particles can be tracked⁴⁸, giving real-time particle visualisation, sizing and counting⁵⁸. A typical set-up for NTA is shown in Figure 1.5. A viewing cell in the form of a metallised optical element is illuminated by a laser beam. At its surface, nanoparticles in suspension can be directly visualised in real time, and produce a scatter pattern of spots, which is magnified by a microscope objective lens and recorded by a camera. NTA can measure particles between 1 µm–10 nm in diameter⁵⁸. However, despite determining particle size on a particle-by-particle basis, NTA has great difficulty in resolving a bimodal mixture⁵⁶. Also, NTA requires a limited concentration range that is relatively concentrated⁵⁸.

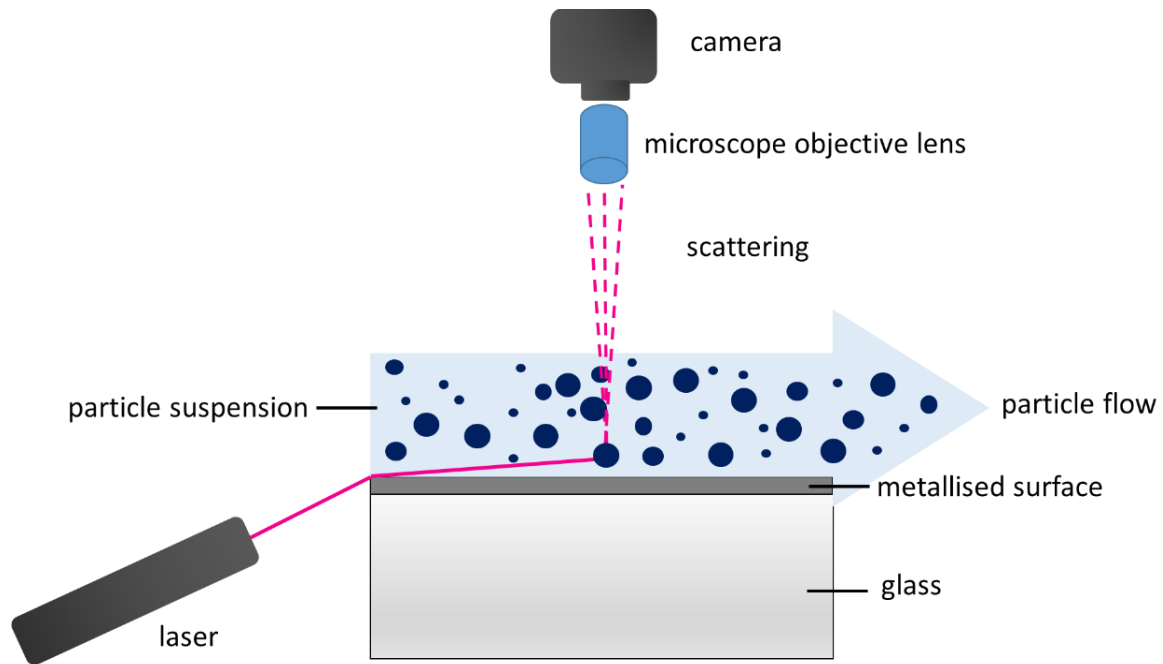


Figure 1.5 Schematic showing nanoparticle tracking analysis (NTA), covering scattering of laser light by a particle suspension within a flow cell, and subsequent magnification and detection.

1.1.7 Flow cytometry

Flow cytometry (FC) particle analysis primarily consists of two key steps: particle alignment via hydrodynamic flow focusing, followed by sample analysis by a detection system involving a laser for optical measurement⁵⁹ (Figure 1.6), or electrodes for impedance measurement⁵⁹. Because the sample is focused into single-file, analysis is performed on a particle-by-particle basis as the sample passes through the laser beam or electrode junction. Optical and impedance flow cytometry measure particle size by light scattering or obscuration, and volume, respectively. Traditional cytometer designs involve generation of a sheathed sample flow by situating of a glass capillary inside a larger one⁵⁹. Flanking sheath flows are typically buffer solution⁵⁹. Optical flow cytometry can detect particles/cells from 40 μm ⁶⁰–300 nm⁶¹ in diameter, and can analyse up to 10,000 particles/cells per second as well as collect multiparameter data⁶⁰, being able to analyse by both lightscattering or fluorescence⁶⁰. It is also effective at identifying small populations⁶², and can differentiate samples by optical properties such as refractive index (although the signal analysis can be complicated)⁶³.

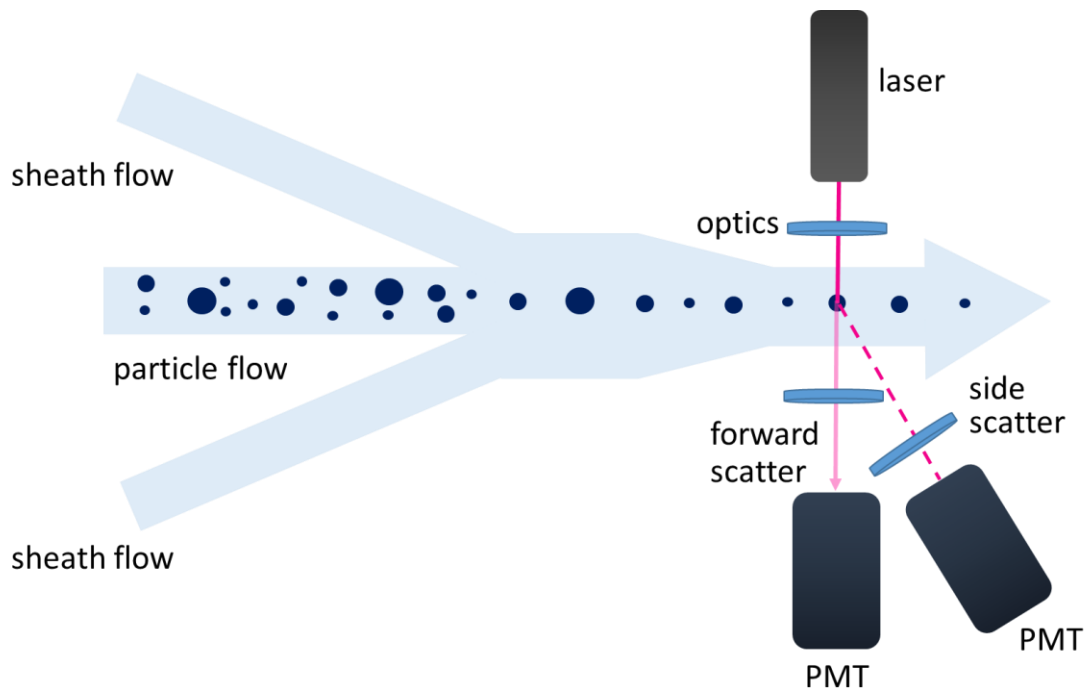


Figure 1.6 Schematic showing optical flow cytometry (FC) processes: hydrodynamic focusing of sample flow into single-file by flanking sheath flows, followed by laser detection of individual particles.

However, the technique requires calibration with size standards⁵⁹ and its apparatus is expensive relative to other particle analysis methods⁶⁴. In comparison, commercial impedance flow cytometers can only size particles between 70 μm –5 μm ⁶⁵. Flow cytometers often involve an incorporated separation technique: for instance, fluorescence-activated cell sorting (FACS) sorts cells into discrete sets based on their measured scattering or fluorescence properties⁵⁹.

1.1.8 Resistive Pulse Sensing

Resistive pulse sensing (RPS), a branch of Coulter counting, was originally developed in the 1950s for high throughput counting and sizing of blood cells⁶⁶. The technique involves measurement of an electrical resistance increase caused by passage of a particle through a narrow aperture nanopore containing a conducting fluid (Figure 1.7). Particle size is determined from the electrical current pulse resulting from the conductive fluid displacement under an electric field due to particle pore translocation.

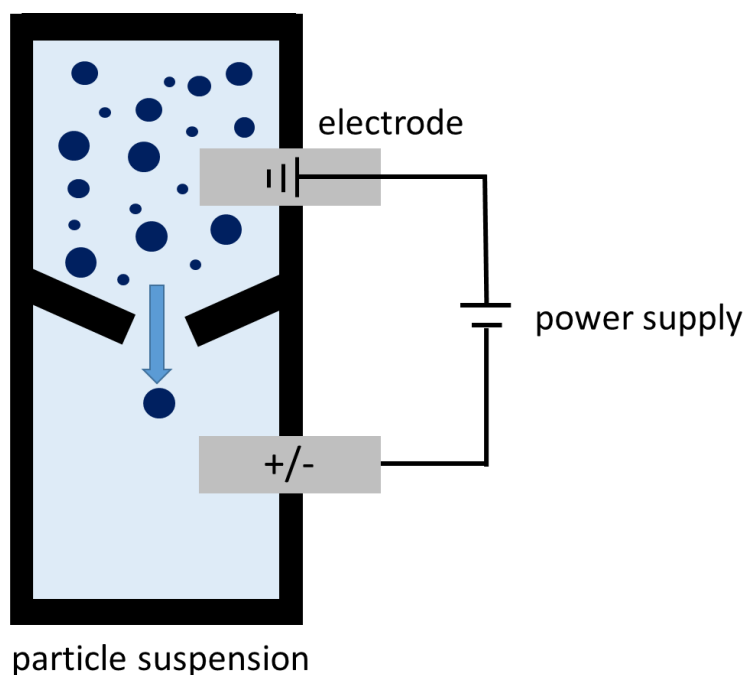


Figure 1.7 Schematic showing resistive pulse sensing (RPS). A particle suspended in a conducting fluid translocates through a pore, causing a sudden drop in the measured background ionic current.

The typical size range analysable by RPS by commercial instruments is approximately 300 μm ⁶⁷–50 nm⁶⁸. A relatively new subset technique, tuneable resistive pulse sensing, TRPS, can detect down to 40 nm⁶⁹, and offers far superior multimodal resolution to DLS and NTA⁵⁶. A micron-sized pore is produced by the mechanical puncturing of an elastic membrane⁷⁰. Improved resolution and sensitivity are achieved by tuning of the pore diameter⁷¹ via the radial stretching of its membrane. RPS systems can also achieve single molecule detection⁷², such as of proteins⁷³, and for DNA sequencing⁷⁴. As well as size, RPS can also be used to measure other particle properties such as charge in the form of ζ -potential^{75–77}. However, an intrinsic disadvantage of pore-based particle sizing techniques is blockages of the pore channel by particles too large to translocate through, or by aggregates consisting of particles attracted to the pore surface⁵⁶. This tendency limits the measurable size range and hinders analysis of highly polydisperse samples, as well as increasing analysis time through regular apparatus disassembly and cleaning. Other issues are that smaller particles will not be detected if the electrolyte volume displaced by them is not sufficient to create an RPS event signal greater than the background noise, and the low throughput of the technique, typically, 1000 particles min⁻¹⁷⁸.

1.1.9 Summary

A comparison of the different main particle/cell analysis techniques, including their respective advantages and disadvantages, is given in Table 1.1, and their respective sample size ranges given in Figure 1.8. Note that the latter shows ranges for commercial instruments, and excludes values for reported experimental systems.

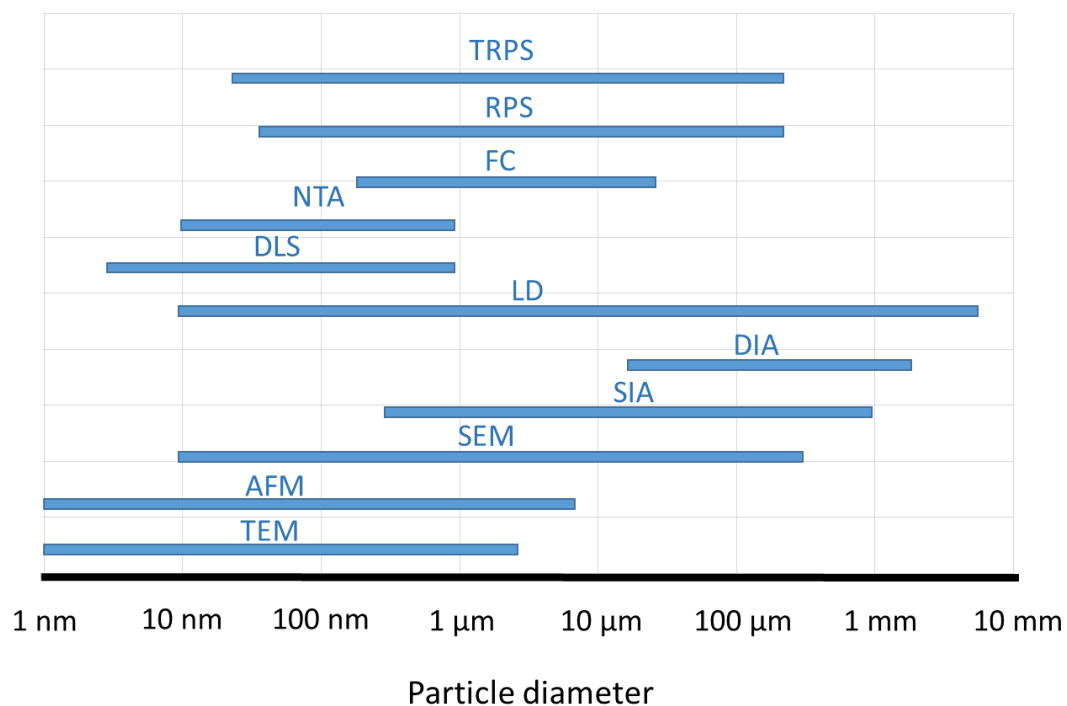


Figure 1.8 Sample analysis size ranges of common particle/cell analysis techniques.

Ensemble particle analysis techniques such as DLS, where the entire sample is analysed simultaneously to give a combined signal, often give only an average particle diameter value, and resolution of particles of similar size is poor. In contrast, discrete particle sizing techniques such as FC and RPS, analyse particles individually, and distributions are formed by placement of counts into 'size bins'.

Table 1.1 Comparison of particle analysis methods.

Technique	Discrete/ensemble	Type	Advantages	Disadvantages
SEM/TEM	Discrete	Imaging	<ul style="list-style-type: none"> • Able to produce physicochemical images. • Gives clear morphology characterisation. 	<ul style="list-style-type: none"> • Manual technique. High level of labour and time required. • Human error/subjectivity involved in particle measurement. <ul style="list-style-type: none"> • High instrument cost. • Sample may not be representative of population. <ul style="list-style-type: none"> • Require a vacuum
AFM	Discrete	Imaging	<ul style="list-style-type: none"> • Gives clear morphology characterisation. 	<ul style="list-style-type: none"> • Limited scan size and low scanning speed.
SIA	Discrete	Imaging	<ul style="list-style-type: none"> • Standard microscopy systems can be adapted • Produces sample images. 	<ul style="list-style-type: none"> • Sample throughput and morphology characterisation inferior to DIA.
DIA	Discrete	Imaging	<ul style="list-style-type: none"> • Sample throughput very high. • Produces sample images. • Gives clear morphology characterisation. 	<ul style="list-style-type: none"> • Sample filtering and fractionation is sometimes required.
DLS	Ensemble	Laser	<ul style="list-style-type: none"> • Extremely high sensitivity: can measure down to 5 nm⁵³. 	<ul style="list-style-type: none"> • Does not measure particle size directly. <ul style="list-style-type: none"> • Extremely low resolution. • Only suitable for submicron particles.
LD	Ensemble	Laser	<ul style="list-style-type: none"> • Wide linear dynamic range. <ul style="list-style-type: none"> • High reproducibility. <ul style="list-style-type: none"> • High speed. • Does not require calibration. 	<ul style="list-style-type: none"> • Does not measure particle size directly. • Needs low concentrations so dilution is often required. • When analysing small particles, knowledge of optical properties is required. • Does not give any morphology information.
NTA	Discrete	Laser	<ul style="list-style-type: none"> • Multiple particle parameters are measurable. 	<ul style="list-style-type: none"> • Poor resolution. • Limited concentration range.
FC	Discrete	Laser/ Electro-chemical	<ul style="list-style-type: none"> • Extremely high throughput. • Multiple particle parameters are measurable. • Effective at identifying small populations. 	<ul style="list-style-type: none"> • Requires size standards for calibration. • Equipment is relatively expensive.
RPS	Discrete	Electro-chemical	<ul style="list-style-type: none"> • Very high resolution. • Can measure other particle properties such as ζ-potential. 	<ul style="list-style-type: none"> • Prone to blockages. • Relatively low throughput.

1.2 Particle/cell separation

Particle or cell separation, i.e. the sorting of particles/cells into discrete populations based on their physical properties, is an important process in areas ranging from chemical and biological analyses⁷⁹ such as bead assays, diagnostics and disease monitoring⁷⁹, industrial applications including chemical and food processing, environmental assessment, and stem cell and cancer research⁷⁹.

Healthcare in particular is a key application area, with certain diseases altering cell physical properties (for example, cancerous epithelial cells are larger in size compared to healthy cells⁸⁰), making cell separation a powerful tool diagnostic tool. The separation and concentration of rare cells such as circulating tumour cells (CTCs) or fetal cells from blood is an initial sample preparation step in disease prognosis and diagnosis⁸¹. It is important in biomedical research: for instance, rare cell study can offer insight into specific targeted treatments for personalised medicine development⁸², and stem cell isolation is important for regenerative medicine research⁸³. Biochemical sample mixture separation is conventionally performed via batch processes such as filtration or centrifugation, but alternative, continuous separation techniques such as those carried out in lab-on-a-chip (LOC) systems are rising in popularity (see Chapter 1.5).

1.3 Lab-on-a-chip devices

Lab-on-a-chip is a multidisciplinary field of miniaturised technologies that encompasses electrical, mechanical and chemical engineering, analytical chemistry, and biochemistry⁸⁴. Miniaturisation in science and technology has been growing for decades, with a key step being the dawn of microelectronics in the late 1950s⁸⁵. Following the beginning of the micromanufacturing boom in the mid-1960s to early 1970s came the development of microsensors via bulk and surface micromachining of silicon⁸⁶. In this period, these new microfabrication methods were used to fabricate microelectromechanical systems (MEMS). These innovations were closely followed by groundbreaking developments in two very different areas: gas chromatography (GC) and inkjet printing: a micromachined silicon gas chromatograph was presented by Terry in the late 1970s^{87,88}, and in the same period, silicon inkjet printing nozzle arrays were produced by Bassous via anisotropic etching⁸⁹. These devices demonstrated for the first time that minute liquid volumes could be manipulated in microchannels.

The small sensing devices developed in the 1970s, and the subsequent research on the handling of small fluid volumes in microchannels, led to the concept of micro total analysis system (μ TAS) devices being proposed by Manz in 1990⁹⁰. Manz described analytical microchip devices incorporating sample pre-treatment, separation and detection into a single device. Hence, these “total analysis systems” would integrate separation techniques that could perform multi-component monitoring within a single device, and be able to carry out handling, analysis and detection of samples, as well as have stringent control over mass transport and measurements. At that time, sensors had poor selectivity and lifetime, and these new μ TAS systems were envisioned as a new revolution for chemical sensing. Thus, the original intention for this miniaturisation was not to improve portability by shrinking of device size but rather for boosting of analytical performance. However, scientists also recognised the benefits of the reduced consumption of reagents or mobile phase that came with smaller device size⁹¹.

Over the next few years came a number of papers describing μ TAS devices created for biomedical applications, such as deoxyribonucleic acid (DNA) analysis⁹² or bedside monitoring of patient blood pH, pO₂ and pCO₂⁹³. This latter example, along with others such as novel aerospace applications⁹⁴ described devices intended for use in hospitals or out in the field as opposed to in a conventional laboratory. The idea of these devices being small, easily portable laboratories⁹⁵ led to the coining of the term ‘lab-on-a-chip’ for them in the mid-1990s^{95–97}, along with the term ‘microfluidics’ to describe the channels of microlitre to picolitre fluid volumes often found within them⁹⁸.

1.3.1 Microfluidics

Microfluidic technology is one format of LOC devices⁸⁴. Microfluidics can be defined as systems in which fluid behaviour differs from conventional flow theory due to the small length scale of the system⁹⁹. When confined inside microscale channels, fluidic behaviour significantly differs from that of macroscale fluids, the most significant being the presence of laminar fluid flow, where fluid layers travel in parallel without eddies or turbulence, as characterised by low Reynolds numbers. This unique laminar flow behaviour, together with the continuous flow enabling high throughput, in-line processing such as detection and separation¹⁰⁰, leads to microfluidics being used as the driving force behind many lab-on-a-chip devices. The seminal paper of the field is that of Whitesides⁸⁴, in which he describes its history, advantages, typical components, and a vast range of current and projected bioanalysis and chemical synthesis applications predicted in commercial, health and environmental public monitoring and research areas. The field of microfluidics has rapidly increased in the last decade,

with the number of papers totalling approximately 10,000 in 2009¹⁰¹, now being over 40,000 today and more than 4,000 published annually¹⁰².

1.4 Microfluidic particle/cell analysis

By utilising the unique, precisely routable laminar flow found in microfluidics, high-throughput manipulation and accurate and sensitive individual detection of particles and cells is possible, all on a miniaturised scale¹⁰³. Microfluidic lab-on-a-chip devices enable reduced sample volumes, meaning that reagent costs and analysis times are minimised¹⁰⁴. As a result, when applied in health applications for the analysis of whole blood or other whole bodily fluid, microfluidics decrease invasiveness to patients¹⁰⁵. Additionally, massive parallelisation of these systems is made possible by the reduced device size in conjunction with the low fabrication cost, offering the possibility of high throughput analysis^{106,107}.

Assimilation of particle/cell analysis techniques into miniaturised, portable platforms affords a great variety of valuable tools for applications outside of the laboratory setting, including environmental monitoring tools such as: personal monitoring such as microfluidic airborne particulate measurements¹⁰⁸ for industrial workers or homes in areas of high air pollution¹⁰⁹. Field analysis applications such as on-site foreign microalgae identification in ship ballast water¹¹⁰, legionella in cooling water towers¹¹¹, and pollen viability analysis in seed and fruit industries (with dead pollen cells being smaller in size)¹¹² have all been demonstrated.

Particle characterisation is another application area of microfluidic particle analysis, for example in the form of quality control in the synthesis of particles for drug delivery, where size and morphology are crucial^{113,114}. The continuous flow used in microfluidic systems is complimentary to continuous manufacture over batch methods, and allows the production of more uniform particles¹¹⁵. Microfluidics has been suggested as an upcoming characterisation method in future pharmaceutical manufacturing¹¹⁶, and in biological processing¹¹⁷. Synthesis and in-line analysis can be integrated on-chip as has been achieved with nitrobenzene droplets¹¹⁸ and could lead to a fully integrated synthesis and quality control system. Another group has demonstrated in-line DLS coupled to the microfluidic synthesis of drug core-shell particles¹¹⁵.

The vast majority of particle/cell analysis microfluidic devices however have been focused on biological applications, with a particular focus on inexpensive POC devices for use in resource-poor settings, with

a number of reviews published on this subject over the last 7 years^{119–124}. Microfluidic particle/cell detection devices could answer the call for low-cost, easily-accessible health diagnostics technologies for the developing world, and match the World Health Organisation criteria for such devices, chiefly, affordable, sensitive and specific, user-friendly, rapid on-site use, largely equipment-free, and deliverable to end-users¹²⁵. Microfluidic whole blood counters could replace the requirement for bench-top haematology analysers in disease diagnosis. Microfluidic systems for POC use usually carry out analysis via cell detection analysis¹²¹ or particle detection in the form of bead assays¹²⁶.

Here we review common analysis techniques used in particle/cell sensing LOC devices. Some are adapted from macroscale techniques such as flow cytometry, whilst others are almost exclusively found in LOC systems.

1.4.1 Imaging flow cytometry

Imaging flow cytometry (IFC) systems are similar to the DIA technique and have two elements: an imaging system that acquires single-particle images at a high speed, and an image-processing element to analyse the acquired microscopic single-particle images¹²⁷. The image-processing element involves image segmentation as in DIA, as well as a tracking function to prevent re-counting of the same particle¹²⁷.

Label-free extremely high throughput of 100,000 particle s^{-1} are possible but require use of an expensive ultra-high-speed camera set-up¹²⁸. Lower-cost, lower-speed equipment cannot reliably characterise particle populations¹²⁹, and may require fluorescence labelling to increase sensitivity¹³⁰.

1.4.2 Optical flow cytometry

The first microfluidic flow cytometer was that of Sobeck in 1993¹³¹, and utilised integrated silicon waveguides in a forward scatter count (FSC) configuration. However, it was only used to analyse liquids and not particulate samples. Since then, a large number of optical microflow cytometers were developed that have been covered by a number of reviews^{132–137}. Devices have been created that can analyse FSC¹³⁸ or both FSC and side scatter count (SSC)¹³⁹ without labelling, as well as ones that can analyse beads by light obscuration¹⁴⁰. In the FSC configuration, light scattered in the direction of the laser is detected and indicates particle/cell size, whilst in the SSC configuration, light scattered at 90° to the laser direction is detected and infers cell granularity and density¹⁴¹. In the obscuration

configuration, instead of particle sizing being achieved by measuring a light signal increase, it is done by measuring drops in baseline light intensity caused by the physical blocking of a light path by a particle. Like benchtop commercial flow cytometers, microfluidic flow cytometers can differentiate samples by optical properties¹⁴². Devices also have high throughputs, ranging from 30 to 350 particles/cells s⁻¹¹³².

Fibre optic detection systems are low-cost and easily integrated into chips¹⁴³ but can give poor device replicability¹¹⁰ and can require precise alignment processes. A solution to these issues is fully integrated slab waveguides, such as those used in microfluidic cytometers by Watts, et al.^{144–146} and others^{147–149}. However, these do not have the option to be switched out or tuned, in which case a whole new device must be fabricated.

1.4.3 Electrorotation

Electrorotation (ROT) characterises particles/cells by their dielectric properties¹⁵⁰. The sample is placed into a medium with a different electric polarisability to its own, and an electric field generated by quadrupole electrodes. Particles/cells will rotate when subjected to a rotating electric field whilst within a medium with a non-uniform electric field¹⁵⁰. ROT monitors the rotational speed of the particles/cells as a function of the rotational electric field frequency, and applies Maxwell's Mixture Theory to gain dielectric property information¹⁵⁰. ROT does not require labelling as it studies intrinsic electrical properties of particles/cells¹⁵⁰. However, it is only suitable for studying extremely limited numbers of cells, as a single cell analysis can take as long as 30 minutes¹⁵⁰ and is not continuous, with a cell being held and rotated in the same spot inside the microfluidic device during characterisation¹⁵¹.

1.4.4 Static electrical impedance spectroscopy

Static electrical impedance spectroscopy (EIS) is another dielectric technique^{150,152}. Particles/cells are captured in a trapping zone which has an AC current applied across it. There are many different trapping systems used, including negative pressure traps¹⁵² and hydrodynamic traps¹⁵³. Usually, two different values are measured: the impedance magnitude (the ratio of the applied voltage amplitude to the measured current amplitude) and the phase (the phase shift by which the current lags behind the voltage)¹⁵⁴. The frequency of the applied electric field dictates the information gained: at frequencies ~100 kHz to ~1 MHz, particle/cell size and volume is measured¹⁵⁴, whilst at frequencies >1 MHz cell membrane information is obtained¹⁵⁴. Thus, EIS is a label-free technique for multi-

parameter analysis of large numbers of particles/cells^{150,154}. It is carried out in continuous flow, allowing continuous monitoring over time and so enabling studies of cell life cycles¹⁵⁴, including intracellular processes such as nucleation¹⁵⁴. Cells are cultured onto embedded electrode surfaces in a microfluidic device, and measured impedance increases with cell growth and decreases with cell death¹⁵⁵. However, comparison of quantitative impedance data across different cell types is challenging due to the signal dependence on cell adhesion, which is affected by morphological and chemical cell surface properties and the specific cell line. Thus, for reliable results to be obtained, only impedance values for cells of the same type can be compared¹⁵⁵. In addition, time is consumed carrying out sample trapping and release processes¹⁵⁰.

1.4.5 Dynamic electrical impedance spectroscopy

EIS can also be carried out dynamically, where the sample is analysed as it flows past a set of two or more electrodes^{150,155–157}. This version is for individual particle/cell counting and size and dielectric property measurement. The electrodes have an AC voltage applied to generate an electrode field, and as a particle/cell travels between them they bring about a change in the current flowing between the electrodes. This current change is measured and analysed to give information on particle/cell size and dielectric properties. In addition, impedance data can be collected at multiple frequencies, with different frequency bands corresponding to different intracellular components¹⁵⁶. Chip configuration can involve two^{158,159} or three^{160,161} coplanar, adjacent electrodes. However, due to electric field non-uniformity across the microfluidic channel, error is caused in the measured volume of off-centre particles¹⁵⁵. To rectify this, configurations of two^{162,163}, three¹⁶⁴ or more¹⁶⁴ parallel electrode pairs can be used, with certain pairs acting as references. However, thin channel dimensions are required to shorten the electrode distances¹⁵⁵, increasing the risk of clogging and lowering throughput. Alternatively, particles/cells can be hydrodynamically focused with a nonconductive sheath fluid to effectively narrow the sensing region^{157,165–169}, but this still involves issues measurement error with inaccuracies in the calculated core stream cross-sectional profile¹⁶⁸, and greater system intricacy covering convoluted electronics¹⁶⁷ and a large number of fluidic inputs¹⁶⁹.

Due to its dynamic nature, the technique is higher throughput than static EIS and can measure ~ 1000 cells s^{-1} ¹⁴⁷. Thus, unlike ROT and static EIS it can analyse a sufficiently large number of cells to obtain statistically meaningful data on a population within a relatively short amount of time¹⁵⁰. Also, unlike static EIS, information from single cells is gained from pulses corresponding to individual cells, with their amplitudes relative to the cell volume¹⁵⁵.

1.4.6 Flow resistive pulse sensing

RPS is an offshoot of dynamic EIS, involving a narrowed sensing orifice placed in between the electrodes that an AC or DC electric field is applied across^{170,171}. This orifice is significantly smaller than the microfluidic channel, and on each passing of a particle through it, a resistive pulse is generated, which is processed by an amplification circuit and a data acquisition device¹⁷² to give particle count and size information¹⁷⁰. The constricted pore channel dimensions give it a highly uniform electric field, leading to greater analytical precision than EIS¹⁷³. By tuning of the pore orifice dimensions and shape, high sensitivity and resolution can be achieved¹⁷⁰. However, sensitivity is inversely proportional to throughput as smaller pores are more susceptible to clogging at high sample concentrations¹⁷¹ and have a reduced flow rate¹⁷¹. In addition, as for other microfluidic electrochemical techniques, ionic concentration is critical but cannot be changed on-the-fly¹⁷⁴, and the electrodes have a limited shelf-life¹⁷⁴. An overview of the field of microfluidic and nanofluidic RPS is given by Song¹⁷⁰. Such devices have been developed with single-figure nm resolution, such as that of Peng, et al. which used embedded 2–10 nm diameter carbon nanotubes to detect ~1 nm single-stranded DNA (ssDNA)¹⁷⁵, and that of Harms, et al. that used milled glass nanochannels to distinguish between 32 and 35 nm diameter Hepatitis B virus (HBV) capsids¹⁷⁶.

1.4.7 Summary

Table 1.2 summarises various optical and electrochemical methods for particle/cell analysis in microfluidic systems. All of the methods can operate without sample labelling, although to achieve greater sensitivity in the optical methods, fluorescent labelling is sometimes used.

Optical methods are versatile techniques in that they encompass absorbance, fluorescence and chemiluminescence detection, thus allowing a great range of cell analysis bioassays to be carried out for POC applications¹⁷⁴. ROT, EIS and electrical impedance flow cytometry are able to analyse intracellular components, and RPS can analyse charge properties of a sample.

Table 1.2 Comparison of microfluidic particle analysis methods

Method	Analysis	Aspects analysed	Advantages	Disadvantages
IFC	Optical	<ul style="list-style-type: none"> • Size 	<ul style="list-style-type: none"> • Extremely high throughputs. 	<ul style="list-style-type: none"> • Extremely expensive equipment. • Lower-cost kit may require sample fluorescent labelling.
Optical flow cytometry	Optical	<ul style="list-style-type: none"> • Size • Optical properties 	<ul style="list-style-type: none"> • High throughput. • Relatively low-cost. 	<ul style="list-style-type: none"> • Detection system alignment and reproducibility an issue.
ROT	Dielectric	<ul style="list-style-type: none"> • Dielectric properties 	<ul style="list-style-type: none"> • Probes intrinsic cell electrical properties. 	<ul style="list-style-type: none"> • Extremely low throughput. • Sample is not in continuous flow. • Slow analysis process.
Static EIS	Dielectric	<ul style="list-style-type: none"> • Dielectric properties 	<ul style="list-style-type: none"> • Can carry out cell culture studies. <ul style="list-style-type: none"> • Can study intracellular components. 	<ul style="list-style-type: none"> • Ensemble analysis. • Data can only be compared for cells of the same type. • Trapping and release processes are slow. • Low throughput.
Dynamic EIS	Impedance	<ul style="list-style-type: none"> • Size • Intracellular processes 	<ul style="list-style-type: none"> • High throughput. <ul style="list-style-type: none"> • Can study intracellular components. 	<ul style="list-style-type: none"> • Signal can vary with particle transport mode unless intricate electrode array and electronics system used. <ul style="list-style-type: none"> • Very narrow channel dimensions may have to be used, leading to clogging risk and lower throughput.
RPS	Impedance	<ul style="list-style-type: none"> • Size • Charge properties 	<ul style="list-style-type: none"> • High sensitivity. <ul style="list-style-type: none"> • Very high resolution. 	<ul style="list-style-type: none"> • Prone to clogging. • Can be low throughput. <ul style="list-style-type: none"> • Electrode shelf-life. • Electrolyte concentration not changeable on-the-fly.

1.5 Microfluidic particle separation

Similar to microfluidic particle analysis, microfluidic particle separation takes advantage of microscale flow phenomena to achieve precise and high-throughput sorting. Mixture separation can be carried out by trapping, or performed continuously. Continuous separation in-flow with continuous injection and collection as well as real-time monitoring is possible, making microfluidic sorting ideal for

integration with upstream and downstream applications¹⁷⁷ including detection¹⁷⁸. Microfluidic separation is an important tool in LOC devices as a preconcentration step before analysis¹⁷⁸. A large body of research involves the separation and trapping of biological material from red blood cells¹⁷⁹ to rare cells^{180–182} such as stem cells¹⁸³ and CTCs^{184–188}. Other examples include the separation of bacteria from whole blood for sepsis diagnosis¹⁸⁹ and microorganism capture for water quality analysis¹⁹⁰. In addition, portable, rapid, early-monitoring devices for foodborne pathogenic bacteria can prevent food poisoning outbreaks and save lives¹⁹¹, as on-site detection of foodborne pathogens is far more rapid than conventional culturing techniques, e.g. 30 minutes versus 48–72 hours¹⁹². Microfluidic devices have been used to capture pathogens from various food products for analysis and/or quantification: chips have been made for the capture and detection of *E. coli* in milk^{192,193} and spinach¹⁹² samples. These often use trapping, either via antibody surface modification of chips^{194,195}, or other methods including pore membrane entrapment¹⁹⁶, and quantification is carried out on the captured pathogens. However, trapping separation devices tend to be single-use¹⁷⁸.

Physical separation methods do not require labelling and instead exploit differences in one of a number of particle properties including size, morphology, mass, density, and charge. Trapping methods involve the capture of sample components of a certain characteristic¹⁹⁷, whilst continuous separations are achieved via the deflection of sample components of a certain characteristic away from the main direction of flow, to a specific outlet for collection¹⁹⁸. Due to the predominantly laminar nature of microfluidic flow regimes, microchannel design and control of hydrodynamic flow can be utilised to guide particles or cells into specific flow stream lines for their separation¹⁷⁷. This deflection can be achieved by strategic positioning of obstacles in conjunction with laminar flow profiles (passive methods), or by use of an externally applied or internally induced force field (active methods)¹⁷⁷. The former uses the interaction between flow phenomena and channel structure with particles^{199–202}, whilst the latter method can involve acoustic^{203,204}, electric²⁰⁵, magnetic²⁰⁶ or other elements. Active methods require integration with additional equipment to provide the external field, but have higher separation performance than passive methods²⁰⁵. Passive methods however can require a very precise chip configuration optimised for a specific particle size of interest²⁰⁷. The different methods for particle/cell microfluidic separation are covered by various reviews^{177,198,205,208,209}.

1.5.1 Pinched flow fractionation

Pinched flow fractionation (PFF), a passive technique, is one of the simplest microfluidic separation methods. It uses a pinched (narrowed) microchannel segment to separate particles by size via laminar

flow, chiefly, its parabolic velocity profile, by addition of an extra buffer flow²⁰². In PFF, the particle mixture flow and buffer flow meet at the pinched segment, pushing the particle flow against the channel wall. Following this, on flowing out into a broadened region, particles of different sizes will follow different streamlines and so be separated.

The technique has a relatively very simple device configuration²⁰², but the pinched section must be of similar size to the particles/cells of interest, causing potential issues with fabrication and blocking²⁰⁷, and it has a limited separation distance²⁰⁷.

1.5.2 Inertial separation

Another passive separation method is inertial separation, which uses inertial fluid force¹⁹⁹. A wide range of different channel morphologies exist including straight¹⁹⁹, spiral^{210,211} and serpentine²¹². In straight microchannels, shear inertial lift and wall lift forces act in opposite directions on a particle (either pushing it to the wall or countering this force, respectively), creating an equilibrium force that focuses the particle position in the channel. In spiral microchannels, centrifugal forces are induced on particles to cause them to migrate outwards, and secondary flows called Dean flows also move particles in a vortex motion, separating out smaller particles whilst not affecting larger ones, which remain by the channel walls^{193,213}.

Inertial separation has a relatively simple device configuration²¹⁴ and offers high throughput, continuous sorting²¹⁴. However, the parallelisation of spiral or curved microchannels is difficult on the same substrate²¹⁴.

1.5.3 Deterministic lateral displacement

A third passive separation method is deterministic lateral displacement (DLD), which uses an array of uniform pillars to separate particles or cells based on size, spreading out sample components orthogonally to the flow direction^{200,201}. This technique offers particularly high resolution, being able to easily separate nanoscale components^{200,201}, and separation is rapid¹⁷⁷. However, highly precise device fabrication is required²⁰⁰.

1.5.4 Electrophoretic separation

Electrophoretic separation is a common technique in biochemistry for separating proteins and DNA molecules, but is also used as an active microfluidic separation method. It involves application of a homogenous (uniform) electric field to a flow of charged particles or cells to bring about migration according to electrokinetics^{215,216}. This migration is called the electrophoretic effect, or electrophoresis. Charged particles or cells separate according to electrophoretic mobility, which is affected by factors such as ζ -potential. In a microfluidic device the electric field can be supplied by internal electrodes in contact with flowing buffer²¹⁵, or by external electrodes²¹⁷.

Instrumentation is simple²⁰⁵ and the manipulation of electrokinetic factors allows a great degree of control²⁰⁵. The drawbacks of this technique are that the electrode configuration can be complicated¹⁷⁷, and it suffers from a low throughput²⁰⁵.

1.5.5 Dielectrophoretic separation

A related separation method is dielectrophoresis, which uses a heterogenous (non-uniform) electric field to separate particles or cells based on their dielectric properties^{218,219}. Because these properties depend on both particle composition and structure, it can separate by a greater number of particle properties than electrophoresis, allowing highly selective analysis^{218,219}. On subsection of a particle to a heterogeneous electric field, charges are induced and the particle becomes polarised along the electric field direction.

The advantages of this technique are that it offers high selectivity due to separation being based on numerous properties^{218,219}, and no sample labelling is required²²⁰. However, like electrophoretic separation, it suffers from low throughput²²⁰.

1.5.6 Acoustophoretic separation

Acoustophoretic separation is another active method, involving the induction of lateral displacement by acoustic standing waves. Acoustic forces can be generated from ultrasonic waves, and the axial acoustic primary radiation force (PRF) used to migrate particles. This can be done by flowing a particle/cell mixture over an acoustic transducer to split it into separate constituent flows^{203,204}. A standing sound wave is generated over the microchannel cross-section, orthogonal to the flow

direction. Usually, the wave is tuned so that the node is centred in the channel with 2 anti-nodes located at the edges, and particles/cells will migrate either towards the node or anti-node¹⁷⁷.

Acoustophoretic separation is gentle to cells and does not affect cell viability²²¹, and no physical contact is required between ultrasonic transducer and flow as a standing wave can be generated inside a microchannel by external equipment¹⁷⁷. However, it cannot separate nanoparticles smaller than $\sim 0.5 \mu\text{m}$ as acoustic force is proportional to the particle radius cube^{177,222}.

1.5.7 Magnetophoretic separation

As well as acoustic forces, magnetic forces can also be used to carry out microfluidic separations: magnetophoresis separates particles/cells by magnetic susceptibility²⁰⁶. In this separation method, not only can magnetic particles/cells be separated from others of different magnetic susceptibility and size, but also from non-magnetic material. This ability can be utilised to separate sample mixtures into sub-populations of differing magnetisation²²³. A magnetic field is used to bring about the separation and is provided by a magnet or magnet system, which does not need to be in contact with the fluid flow²²⁴. Generally, there are three main magnetophoretic configurations used within microfluidic devices: macro-sized external magnets, an internal microscale magnet system (often micro-electromagnets in the form of either single or multi-layered conducting wire matrices²²⁵ or spirals²²⁶), or more complicated hybrid systems utilising both internal and external magnets²²⁴. Examples of magnet systems are illustrated in Figure 1.9: external macroscale magnets are a relatively simple way of continuous separation of magnetic from nonmagnetic particle separation (Figure 1.9 a (i)), or of separation of magnetic particle subpopulations (Figure 1.9 a (ii)). Figure 1.9 b illustrates an example of an internal magnet system for magnetic particle trapping²²⁵. Microfluidic devices for particle/cell magnetic separation can operate via the trapping and detection of a sample population^{197,226,227}, but continuous magnetophoretic methods with the possibility for in-line detection also exist and include the three seminal papers by Pamme, et al. featuring a large separation chamber for particle sorting from particle aggregates²²⁸, particle population sorting²⁰⁷ and the sorting of two types of magnetically labelled cells as well as magnetic cells from non-magnetic cells²²³. Continuous magnetophoretic separation of cells has been of particular interest in recent years²²⁹ as the technique is gentle to cells¹⁸². However, magnetic labelling is usually required of non-magnetic samples unless the cells of interest have naturally high iron content²³⁰.

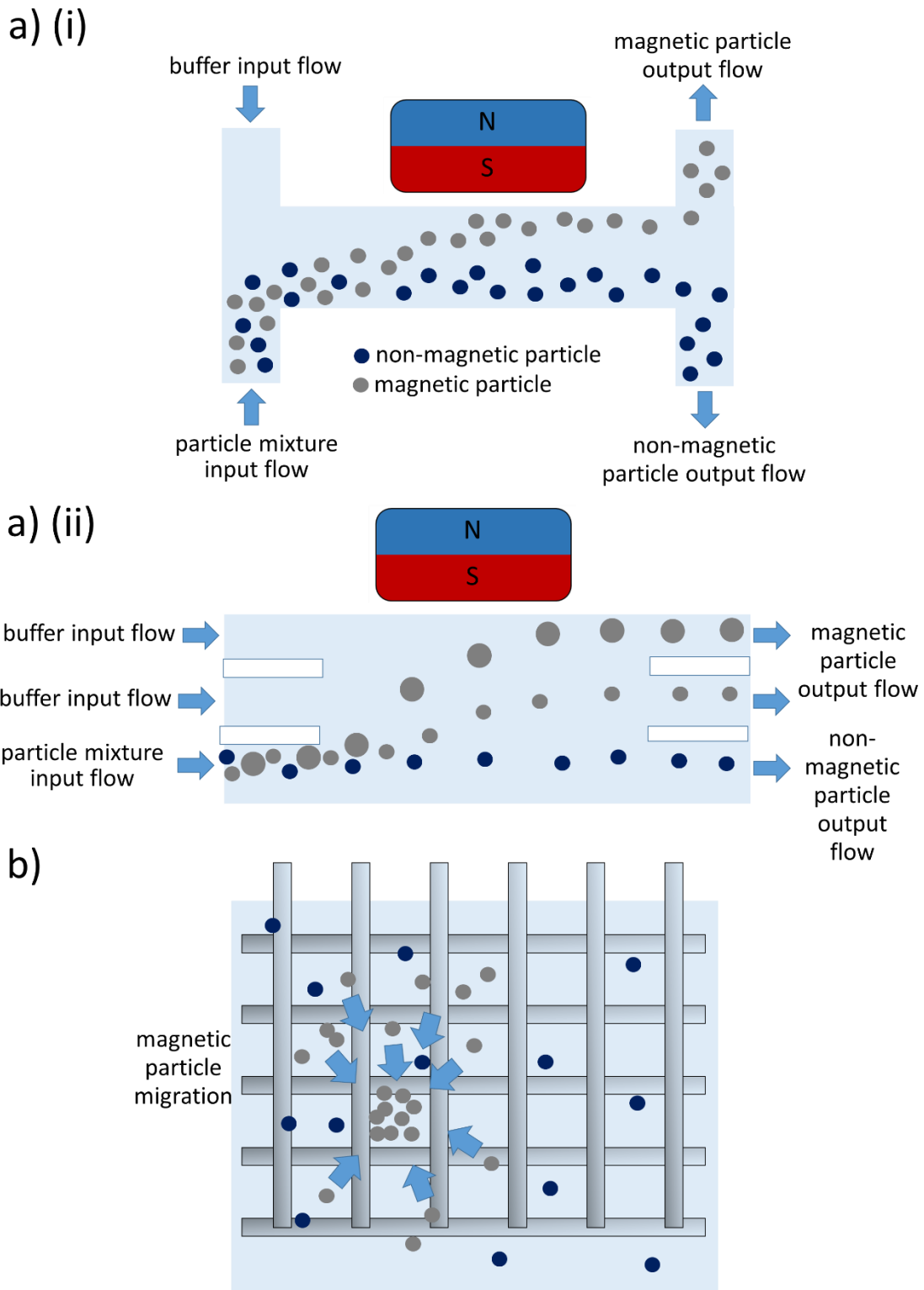


Figure 1.9 Example configurations for two magnet system types for LOC magnetophoresis: a) external macroscale magnets: (i) simple flow chamber and (ii) advanced, sub-population sorting flow chamber, and b) internal magnets: controllable micro-electromagnet matrix. The external magnet systems utilise continuous separation whilst the internal magnet system involves magnetic trapping. Blue dots=non-magnetic particles, grey dots=magnetic particles.

1.5.8 Summary

A summary of the various common microfluidic separation methods for particles and cells, along with their advantages and disadvantages, is given in Table 1.3. Other separation methods, such as size-exclusion filtration²³¹, are also used and are covered in the reviews given earlier.

Table 1.3 Comparison of microfluidic particle separation methods.

Method	Passive/active	Separation factors	Advantages	Disadvantages
PFF	Passive	<ul style="list-style-type: none"> • Size 	<ul style="list-style-type: none"> • Very simple device configuration. 	<ul style="list-style-type: none"> • Requires pinched section to be similar size to particles/cells. • Has limited separation distance.
Inertial focusing	Passive	<ul style="list-style-type: none"> • Size • Shape • Deformability 	<ul style="list-style-type: none"> • Simple device configuration. • High throughput. 	<ul style="list-style-type: none"> • Parallelisation of spiral or curved microchannels is difficult.
DLD	Passive	<ul style="list-style-type: none"> • Size 	<ul style="list-style-type: none"> • Very high resolution—can easily separate nanoscale components. • Fast separation. 	<ul style="list-style-type: none"> • Highly precise device structure required.
Electrophoresis	Active	<ul style="list-style-type: none"> • Electrophoretic mobility 	<ul style="list-style-type: none"> • Equipment is simple. • Manipulation of electrokinetic factors allows more control. 	<ul style="list-style-type: none"> • Electrode configuration can be challenging. • Low throughput.
Dielectrophoresis	Active	<ul style="list-style-type: none"> • Dielectric properties (polarisability, etc.) 	<ul style="list-style-type: none"> • Highly selective due to separation being based on numerous properties. • No labelling required. 	<ul style="list-style-type: none"> • Low throughput.
Acoustophoresis	Active	<ul style="list-style-type: none"> • Size 	<ul style="list-style-type: none"> • Gentle to cells—does not affect cell viability. • No physical contact required between ultrasonic transducer and flow. 	<ul style="list-style-type: none"> • Cannot separate small nanoparticles.
Magnetophoresis	Active	<ul style="list-style-type: none"> • Magnetic susceptibility • Size 	<ul style="list-style-type: none"> • Gentle to cells. • No physical contact required between magnet and flow. 	<ul style="list-style-type: none"> • Magnetic labelling is usually required of non-magnetic samples unless cell has naturally high iron content.

Several papers exist that demonstrate integrated separation and detection in the same microfluidic device, including electrophoretic separation and RPS detection of particles and microalgae²³². There also exist a handful of magnetic separation papers of this vein: magnetic capture and electrochemical detection of CTCs²³³, continuous magnetic separation of CTCs with impedance spectroscopy detection²³⁴ and magnetic separation and RPS sensing of endothelial cells²³⁵.

1.6 Conventional microfluidic fabrication methods

1.6.1 Silicon and glass photolithography

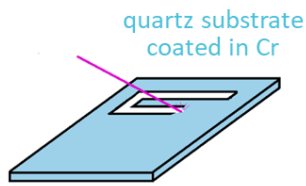
Stemming from its origins in semiconductor microelectronics, the original method of microfluidic fabrication was silicon processing. However, silicon as a microfluidic substrate has the downside of being relatively costly as well as optically opaque to certain UV/VIS wavelengths, limiting its use in optofluidic devices and so leading to glass being used as an alternative in this area²³⁶. The microfluidic fabrication process for both silicon and glass comprises substrate cleaning, followed by photolithography, and wet/dry etching and/or metal deposition steps to form the microfluidic channels²³⁷⁻²⁴⁰. During photolithography, the substrate undergoes application of a thin photoresist layer followed by UV exposure. This exposure is used to transfer a micropattern from a transparency mask to the photoresist layer, which is then either coated with a metallic thin-film or developed to create a mask for etching if subtractive features are desired²³⁹. Following microchannel formation and removal of the photoresist, the channels are sealed by bonding to a flat substrate (typically a glass or silicon wafer) by fusion, anodic or adhesive bonding²⁴⁰. Finally, inlets and outlets are drilled²⁴⁰. This basic photolithographic process of microfluidic fabrication is illustrated in Figure 1.10.

Due to their organic solvent resistance, high thermoconductivity, and stable electroosmotic mobility, the utilisation of silicon and glass for microfluidics has endured in certain applications such as microfluidics devices for organic synthesis^{241,242}. However, they also have downsides: their brittleness and lack of gas permeability prevents their use in cell culture devices and applications requiring flexibility²⁴¹. They also require highly trained staff and cleanroom facilities, as well as the use of corrosive chemicals such as hydrofluoric acid (HF), and there are many steps involved, leading to chip production being very time-consuming and expensive²⁴¹, mostly due to the cleanroom expenses and mask fabrication process²⁴³.

1) Photomask fabrication



a) Draft CAD file



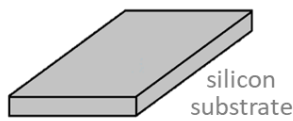
b) Laser etching



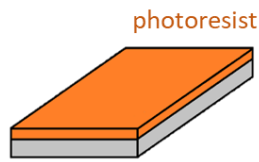
Photomask

2) Micropattern fabrication and 3) Device sealing

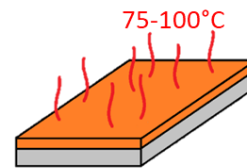
- (I) NH_4OH , H_2O_2 (aq) at 80°C
- (II) HF (aq)
- (III) HCl , H_2O_2 (aq) at 80°C



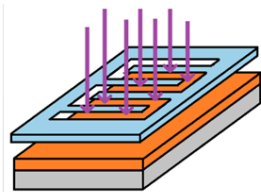
a) Substrate cleaning



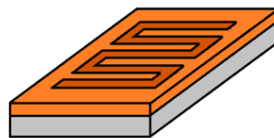
b) Spin-coat photoresist



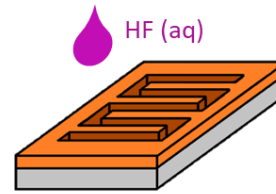
c) Bake



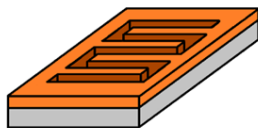
d) UV exposure



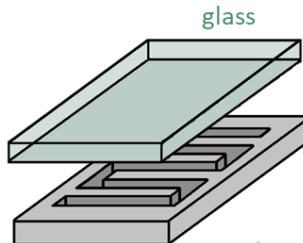
e) Removal of developed photoresist



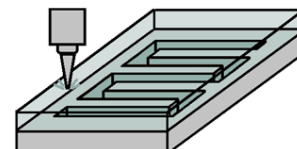
f) Etching



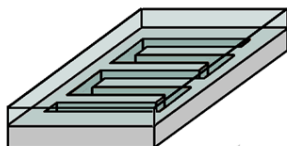
g) Photoresist removal



h) Device sealing



i) Inlet/outlet drilling



Microfluidic device

Figure 1.10 Basic photolithographic fabrication process for a silicon or glass microfluidic chip, encompassing photomask drafting and etching, micropattern etch mask fabrication, device sealing and inlet/outlet drilling.

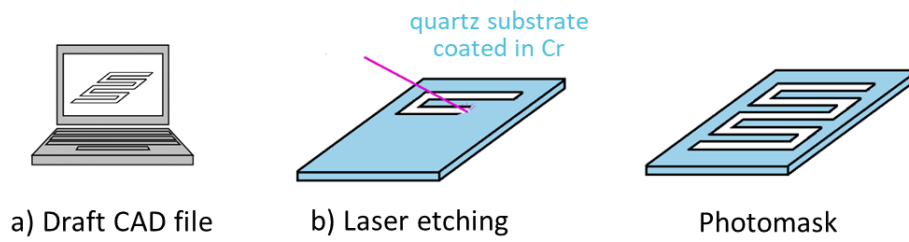
1.6.2 Polymer fabrication

The disadvantages of silicon and glass photolithography motivated a search for easier-to-use, more widely-applicable materials that culminated in the rise of polymers in the mid to late 1990s, which then went on to be the most popular material for microfluidic fabrication^{239,242,244}. These polymers are optically transparent and easily replicated²³⁹, and have simpler, cheaper microfluidic chip production methods: they do not require cleanrooms²⁴¹, microchannels are made via moulding or embossing instead of chemical etching²³⁹, and devices are sealed thermally or with adhesives instead of chemically bonded²⁴⁴. Polymers can be classified into three types: thermoset, thermoplastic, and elastomeric²⁴¹. Thermoset polymers cannot be reshaped post-curing due to their cross-linked structure. This family includes SU-8, which was previously used as a negative photoresist but was later adapted for microchannel fabrication²⁴⁵. In contrast, thermoplastics can be reshaped multiple times after curing, which is beneficial during their moulding and bonding process²⁴¹. This group includes polymethylmethacrylate (PMMA), polycarbonate (PC) and polystyrene (PS).

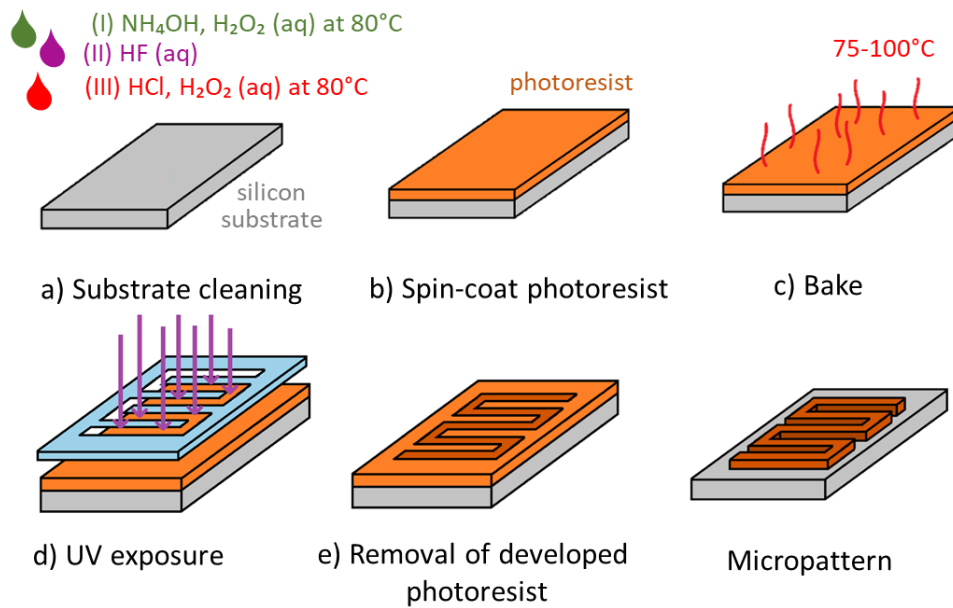
1.6.3 Elastomer soft-lithography

Elastomers contain reversibly-stretchable cross-linkages, and hence their use to produce microfluidics is dubbed 'soft-lithography'. By far the most commonly-used of this type is (polydimethylsiloxane) PDMS^{84,241,242}. The soft-lithography process for PDMS involves master mould creation followed by the formation of PDMS replicas from it²⁴⁶. A wide range of methods have been used for master mould creation, from 3D printing²⁴⁷ to laser ablation of spin-coated PDMS itself²⁴⁸, but it is commonly done via photolithography²⁴⁶. In this method, which was outlined by Duffy in 1998²⁴⁹, the microchannel system is drafted on a CAD program and a commercial printer used to produce a photomask made from this file. Then, this photomask is used on a photoresist layer placed on a silicon wafer to form the master mould. Once a master mould is made, the PDMS base and curing agent are mixed together into a liquid pre-polymer and poured over the mould^{246,250}. After curing, the mixture cross-links into an elastomeric solid, which is peeled off and sealed onto a flat substrate^{246,250}. Typically, PDMS devices are sealed with a glass or silicon wafer via a plasma oxidising process, or with a PDMS wafer via an adhesive process²⁴¹. The basic soft lithography fabrication process for PDMS microfluidic chips is shown in Figure 1.11, and has initial similarities to the silicon/glass microfluidic photolithography process in its creation of a photomask and micropattern. The popularity of PDMS is attributed to its ease of fabrication and relatively low production cost^{246,250}, and unique properties such as high elasticity²⁴¹.

1) Photomask fabrication



2) Micropattern fabrication



3) PDMS casting and 4) Device sealing

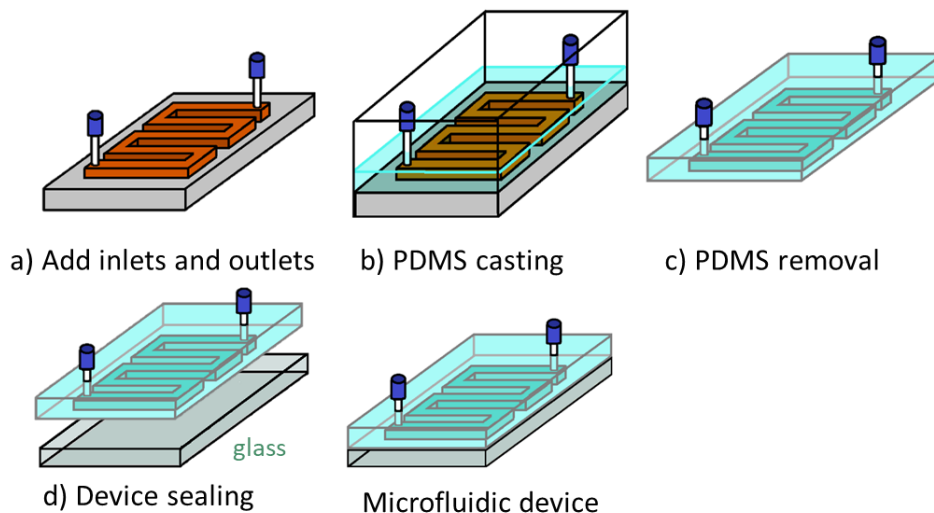


Figure 1.11 Basic soft lithography fabrication process for a PDMS microfluidic chip, encompassing photomask drafting and etching, micropattern master mould fabrication, PDMS casting and device sealing.

1.6.4 Summary and outlook

The original fabrication method of microfluidic LOC devices, silicon and glass photolithography, has largely been superseded by polymer moulding methods. Of these, by far the most popular is the use of PDMS. However, despite the advantages of PDMS fabrication and the aforementioned significant degree of ongoing research in the LOC field, interfacing of microfluidic LOCs from conceptual stages to real-world applications remains at a primitive stage, with very limited widespread device implementation²⁵¹. Commercialisation of LOCs from fundamental, proof-of-concept research to mass-manufactured products remains a slow and difficult process, with the vast majority of LOCs being restricted to use only in academic or specialist laboratory settings^{252,253}. Today, the only universally-ubiquitous LOC devices in the home (aside from inkjet printer cartridges) are the home pregnancy test and blood glucose-test²⁵², both simple membrane-based tests whose straightforward, robust science behind them has long been well-known and whose LOC development began in earnest in the 1970s^{254,255}. Beyond these success stories, membrane-based HIV diagnosis kits are growing in use in developing countries²⁵⁶, and a number of LOC devices have achieved moderate commercial success, the first of which was the battery-powered, electrochemical, silicon-based iStat system²⁵⁷ for measurement of various elements in blood including electrolytes and glucose. Volpatti, et al. list various commercial POC LOC devices either in development (at time of writing in 2015) or newly released, some still in development after 10–15 years, and with average funding needed to reach FDA approval being \$39 million²⁵².

The average cost of one soft-lithography-made microfluidic device has been estimated to be \$215 (not including the cleanroom fees required if using photolithography to produce the master mould)²⁵⁸. Furthermore, the time involved in the manual moulding process of PDMS is unsuited for commercialisation and is difficult to automate, as well as being incompatible for scaling-up to mass manufacturing of LOC devices²⁵³. In addition, there are also ongoing design and application limits: PDMS has major drawbacks in that its hydrophobicity leads to it being difficult to wet²⁵¹, as well as having a weakness to strong organic solvents, in whose presence it undergoes swelling and deformation²⁵⁹. Its material drawbacks coupled with its long fabrication procedure have been identified as a major set-back in the development of successful, commercialised LOC devices^{243,260}.

Due to these ongoing issues, alternatives to PDMS fabrication for microfluidics have been investigated. They include paper-based systems²⁶¹, which fall under the field of paper analytical devices (PADs), micromilling²⁶² and injection moulding²⁶³.

1.7 Additive manufacturing

Additive manufacturing (AM), commonly known as '3D printing', is also known in a number of industries as rapid prototyping (RP), or solid-freeform (SFF). It is a family of processes in which a digital model is used as the basis for layers of material to be successively layered under computer control, to form a three-dimensional object. Its invention is credited to Charles Hull²⁶⁴, who developed it originally as a method for rapid furniture prototype production. In the early 1980s Hull was employed by a company that produced UV-cured plastic coatings for furniture. A frustration with the lengthy time of one to two months required for plastic prototyping of new product designs motivated Hull to experiment with using UV light to selectively harden layers in a vat of photopolymer, eventually leading to his obtaining of a patent for stereolithography in 1986²⁶⁴. The process went on to be commercialised by Hull on founding of the company 3D Systems, and since then the size of the 3D printing industry was recently estimated by the 2017 Wohlers report to be over \$6 billion²⁶⁵.

Additive manufacturing has found application in an enormous range of areas. As a method of prototyping it is used in the automotive and aerospace industries to produce car and aeroplane part prototypes as well as finished parts²⁶⁶. Outside this, AM has found use in the food industry²⁶⁷ and in fashion²⁶⁸, as well as in architecture as a tool for creating structural models²⁶⁹, and has proven to be an extremely versatile tool for both fine artists and amateur craftsmen²⁷⁰. A significant area of AM research is medical applications such as prosthetics²⁷¹ and anatomical models for surgery planning²⁷² but tremendous promise has also been shown in the chemical sciences in areas as diverse as energy²⁷³, pharmaceuticals²⁷⁴ and advanced materials²⁷⁵.

'3D printing' is an umbrella term that encompasses a number of different additive processes, all based on additive construction carried out on an XYZ platform.

1.7.1 Fused deposition modelling

The fused deposition modelling (FDM) process was originally patented in 1992 by Stratasys²⁷⁶, but now FDM printers are produced by a number of companies that includes (but is not limited to) Hewlett Packard, Makerbot and UP, following expiration of the original patents. This, along with the rise of the RepRap self-replicating FDM printer and its open-source availability²⁷⁷, have helped fuel the popularity of the technique, with there now being more FDM printers than any other AM printer type in the world²⁷⁸. Coils of thermoplastic are fed into a heated head, where they melt. Following this, the

semimolten polymer is extruded onto an XYZ platform²⁷⁹ in layers. Typical thermoplastics used for FDM include ABS (acrylonitrile butadiene styrene), PLA (polylactic acid), polycarbonates and PPSU (polyphenylsulfone). Support structures are required for overhanging features to prevent parts distorting or falling over during the build process. These structures are printed simultaneously with the object in the same material and are removed after the build. In FDM, support structures are provided in the form of either support material from a separate deposition head, or a support made from the build material, which is then snapped off from the finished object post-printing.

The popularity of this 3D printing type stems from its aforementioned availability and low printer costs²⁸⁰, as well as its relative ease of use compared to other AM types. FDM can also print in more than one material, by pausing and changing the print material²⁸¹. However, it has very poor resolution unless using the most superior commercial models²⁷⁸. In addition, due to the circular shape of FDM extrusion nozzles, internal and external corners and edges have a rounded shape²⁷⁸.

1.7.2 Selective laser sintering and selective laser melting

The selective laser sintering (SLS) and selective laser melting (SLM) techniques use a high-powered laser to heat powdered material and bring about its binding together into a solid object²⁸². In SLS, a laser heats up powder beyond its glass transition temperature to bring about particle bonding and fusion, sintering the material together²⁸². In contrast, the laser in SLM is used to completely melt the powder²⁸². SLS can print in metals, nylon, ceramics and polycarbonates, but SLM can only print metals²⁸². However, the metal parts it produces are of higher quality than those made by SLS, as due to the complete melting and reforming of the powder, the resulting objects are highly dense, thus giving them superior strength and dimensional accuracy. Both SLS and SLM do not require support structures and have minimal post-processing involved²⁸². However, the energy required for the sintering or melting processes is high: over 300–500 times more than those used in photopolymerisation processes such as SLA²⁸². In addition, objects printed by these techniques have relatively rough surface finishes stemming from the large powder particle sizes used²⁸².

1.7.3 Ultrasonic consolidation

Like SLM, ultrasonic consolidation (UC) is primarily used to build metal objects. It was developed by White²⁸³ as a way to form objects from aluminium sheets, and later commercialised by her as the Solidica Formation™ rapid prototyping machine. Ultrasonic waves are used to bind sheets of metal foil

together. Thus, the technique involves far less heat relative to SLS and SLM and melting does not occur. Due to this gentler method of binding, embedding of delicate components is possible^{284,285}, and dimensional errors stemming from shrinkage and distortion in finished parts is less than those found in SLS and SLM metal parts²⁸⁵. However, UC is particularly sensitive to machine-to-machine variation²⁸⁵, and from defects at layer interfaces²⁸⁵.

1.7.4 Stereolithography

Stereolithography (SLA) is the original form of 3D printing and operates via curing or cross-linkage of a light-sensitive photopolymeric material by laser. The speed of this production method was faster than the model-making technologies of the time, thus, stereolithography (and later, 3D printing in general) soon became known as rapid prototyping. The original 1984 patent²⁶⁴ describes a bath of liquid photopolymeric emulsion in which a platform descends one layer at a time. Initially, the platform is positioned just below the polymeric resin surface. A UV laser is directed across this emulsion surface in the outline of the first layer of the object being produced. This initiates cross-linkage of the photopolymer, bringing about curing and hardening of this first layer into a solid. On completion of this first layer, the platform is lowered and the laser swept across to form the second layer. This process is repeated for subsequent layers until the entire object has been formed, after which the platform is raised up out of the bath and the finished object removed for cleaning. Support structures may be required during the build. Commercial SLA photocurable resins typically contain a monomer (typically an epoxy, vinyl ether or acrylate²⁸⁶) and often a comonomer, cross-linker and photoinitiator. The technique can produce very complex objects with a smooth surface finish²⁸⁷, but the main advantage of SLA is its higher resolution relative to other AM processes²⁵⁸. The related process of two-photon polymerisation²⁸⁸ (2PP) offers even better resolution but slower printing speeds.

1.7.5 Binder jetting

The binder jetting technique was created in the early 1990s at MIT²⁸⁹. It involves two parallel reservoirs of a plaster-based composite powder material. One reservoir acts as the build bed, and has a base that drops down one layer at a time as the build is carried out. The other is filled with fresh powder and acts as the feed bed, rising up to donate new powder as the build bed drops. Successive layers of powder material are bonded together by a binder inserted by an inkjet-style print head²⁹⁰. A separate support material is not required for this process as the object is supported by the surrounding powder in the bed. This powder can be reclaimed and used in a subsequent build. An extra advantage is that

this process can print in colour (this is achieved by replacing a single monochrome inkjet head with a four or five colour head printing either CMY or CMYK-coloured binders in addition to clear binder²⁹⁰).

1.7.6 Laminated object manufacturing

The laminated object manufacturing (LOM) process involves the building of objects from sheets of materials such as paper, plastic or metal²⁹¹ by fusing (or lamination) of them together by heat and pressure²⁹². The first LOM production machine was released in 1991 by US company Helix Inc.²⁹³ and involved gluing and laser cutting of a paper roll as it was unrolled. Firstly, a disposable base is produced consisting of a number of layers of material laminated to a retracted platform. Lamination is carried out with a heated roller, as each material sheet has a thermally active adhesive coating on the bottom side. As well as causing bonding by heating, the roller provides pressure to provide good contact between layers. A CO₂ laser is used to cut a cross-section in each layer, as well as to cut excess material in a cross-hatch pattern in order to support subsequent layers²⁹². The cross-section is freed from the material roll by cutting of a large rectangular outline, and the platform migrates down and the feed material advanced. This process repeats until the final layer is added. Lastly, the cross-hatched columns of excess material are removed. LOM with paper offers an extremely affordable form of 3D printing²⁹². However, LOM is limited only to materials that can be drawn into sheets and are suitable for use with adhesive²⁸¹.

1.8 Additively-manufactured microfluidics

In 2011 it was suggested that 3D printing could be a possible alternative to conventional soft-lithography microfluidic fabrication methods²⁶⁰. Waldbaur, et al. argued that AM could simplify the fabrication process by forming devices in a single step (Figure 1.12), thus nullifying the need for master mould production and replica moulding stages²⁶⁰. As a result, concept-to-chip prototyping and development time is shortened, and labour, time and costs are minimised. Since then, along with the recent advancements in commercial printers to reach levels of detail of a few hundred microns²⁹⁴, a number of other advantages of AM in microfluidic production have been recognised that have led to 3D printing being touted as having the power to completely revolutionise LOC device fabrication^{258,260,281,295-298}. In contrast to conventional microfluidic production where devices are built up of bonded layers, AM offers the ability to print an entire chip as one body²⁶⁰. This gives both three-dimensional design freedom, such as the spiral microfluidic separator device printed by Lee, et al.¹⁹³ and microencapsulation chip by Olvera-Trejo, et al.²⁹⁹, as well as prevents bonding and leakage issues.

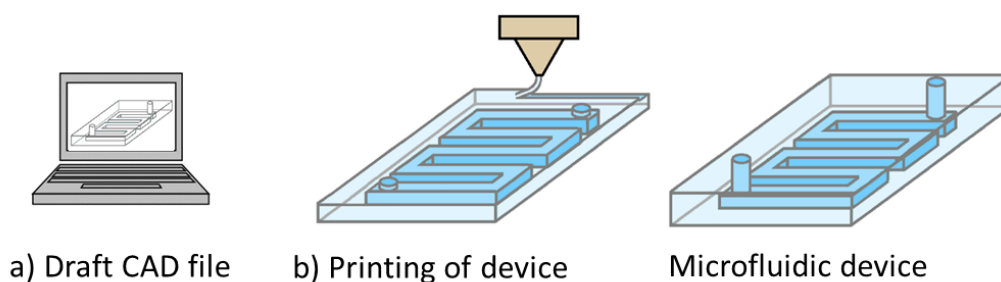


Figure 1.12 Fabrication of 3D printed microfluidic device, encompassing only device drafting and printing.

In addition, recently a number of major AM companies have showcased continuous, automated 3D printing systems for low-cost, rapid mass production: the Stratasys Demonstrator FDM system³⁰⁰, and the Form Cell and Figure 4 SLA systems offered by Formlabs³⁰¹ and 3D Systems³⁰⁰, respectively, with 24-hour remote monitoring and error detection, or greatly accelerated printing. Furthermore, as 3D printing improves as a technology with ongoing resolution advancement in commercial 3D printers and further capabilities constantly being developed, more microfluidic or optical elements are being additively manufactured such as valves²⁹⁷ and optical components³⁰². 3DP has been described as an enabling technology in microscale technologies³⁰³ that includes microfluidics³⁰⁴.

An early application of 3D printed microfluidic systems, and one that has enduring popularity, is that of synthesis. Early 3D printed microfluidic organic synthesis flow reactors were produced by the Cronin group^{305–307}, followed by others such as those of Capel, et al^{308,309}. The emerging field of 3D printed microfluidics with integrated sensing is presently dominated by devices employing electrochemical detection methods, usually in the form of integrated fittings enclosing embedded electrodes^{310–313}, or similar set-ups^{314–316}. Other printed sensors include an integrated chemoresistive gas sensor for the detection of volatile organic compounds (VOCs)³¹⁷, a light-addressable potentiometric sensor (LAPS)³¹⁸, and integrated optofluidic detection carried out by embedded optical fibres^{319,320}. At the time of writing of this thesis, no such printed microfluidic systems have been reported for particle or cell analysis, with all reported systems analysing liquid or gas analytes.

1.9 Comparison of lithographically-made and 3D printed microfluidics.

It has been postulated that microfluidic fabrication by 3D printing is significantly faster and cheaper than that of lithographic methods²⁶⁰. However, only one dedicated investigation into the associated costs and timescales of additive manufacturing of microfluidics versus those made by lithographic

methods exists: excluding cleanroom and EBL/laser-writing costs, Au et al.²⁵⁸ estimated the labour and materials costs of forming one single-layer PDMS microfluidic device via soft-lithography to be \$215, comprising: \$160 daily wage of a research assistant, \$10 silicon wafer, \$30 photomask, \$5 PDMS (50 g) and \$10 SU-8 and developer. This estimate splits costs as being 75% labour, 25% materials. Au et al. argued that these labour costs would be significantly reduced if the device fabrication time was shortened. The authors also predicted that fabrication costs would typically double for multilayer devices, assuming fabrication lasting two days, due to the need for additional master moulds, which they estimated would increase costs and production times in a roughly linear manner. In comparison, using AM, the total cost for production of the same chip was estimated to be only \$31. This encompassed 1.5 hours wage of a technician for printer set-up and device post-finishing (\$30), and \$1 resin. In comparison, the resin for the printed devices in this thesis cost between £3.50 and £12 (4–14.50 USD), but the labour costs would be similar. In terms of the start-up costs involved in microfluidic production, cleanrooms (required for master mould photolithography) typically cost between \$180–\$3500 per square feet³²¹⁻³²³ depending on class and facilities, with total costs being approx. \$160,000 for a small (200 ft²) compounding cleanroom³²³ to \$720,000 for a larger, 4000 ft² medical device cleanroom³²³. Furthermore, an EBL set-up often costs over 1 million USD³²⁴. In contrast, 3D printers do not require specialist laboratories, and the professional-grade SLA printer used in this project cost approximately £150,000 (180,000 USD), whilst high-end printers of other AM types cost even less, such as \$10,000 professional-grade FDM printers³²⁵. It must also be noted that third party fabrication services exist for both additively-manufactured parts and photolithographic photomasks; cost is dependent upon material, part size and minimum feature dimensions, but a photomask made by EBL typically has a 4-day turnaround³²⁶, whilst SLA services can fabricate same-day³²⁷.

Regarding fabrication timescales of the two methods, PDMS device formation (comprising photomask photolithography, substrate cleaning, spin-coating, baking, UV exposure, photoresist removal, PDMS mixing and curing and device sealing) takes a minimum of approximately 9.5 hours for a ~10 µm thick device when using a 4 hr, 60°C oven-controlled PDMS setting step, to 30.5 hours and upwards for a ~100 µm thick device and room temperature PDMS setting³²⁸⁻³³⁰. These times have been taken from protocols where a step requires a set period, such as baking, etching, UV exposure, etc. and do not include any manual handling steps such as PDMS device removal from the mould, or PDMS pouring. These times also assume an EBL/laser-writing step of 3 hrs^{331,332}, when this can exceed 24 hrs per 1 cm²³³³. In comparison, the devices in this project took 3.5-6 hrs to print, which was followed by 4 mins UV exposure and a final 1-2 hr rinsing step, the majority of which the chip was left soaking in a solvent

bath, and did not need staff present. Only approximately 2.5-3.5 hrs of manual labour was required throughout: set-up of the print run, part removal, and rinsing.

In terms of the skills and equipment training required in microfluidic fabrication, lithographic methods require use of drawing software to draft the photomask, EBL/laser-writing, vacuum chamber, spin-coater, contact aligner (for multilayer chips), UV exposure oven, and plasma treatment, as well as requiring cleanroom training and safe use and disposal of piranha solution for substrate and tool cleaning³²⁹, and use of a blade to remove the PDMS chip from its mould. In contrast, AM methods only require use of CAD and STL software, 3D printing, and minor post-printing work such as support structure removal, or in the case of this project: UV exposure and safe use and disposal of methanol.

These costs, timescales, skills and equipment are summarised in Table 1.4. As mentioned earlier, the costs and times reported for lithographically-made microfluidics assume a 3 hr EBL/laser writing run and a single layer device, with multilayer PDMS chips requiring additional contact alignment by a trained engineer.

Table 1.4 Comparison of costs, timescales, skills and equipment required in lithographical and AM manufacture of microfluidic devices.

Microfluidic fabrication	Lithography	3D printing
Estimated total time	10-31 hrs for single-layer chip ³²⁸⁻³³⁰	Approximately 5 hrs
Estimated cost (labour and materials)	\$215 for single-layer chip (excl. cleanroom fees) ²⁵⁸	\$31 ²⁵⁸
Required staff skills/knowledge and equipment	<ul style="list-style-type: none"> • Drawing software • EBL/laser-writing • Cleanroom training • Piranha solution use and disposal <ul style="list-style-type: none"> • Vacuum chamber • Spin-coating • Contact aligner (multilayer chips) <ul style="list-style-type: none"> • UV exposure oven • Plasma treatment <ul style="list-style-type: none"> • Blade 	<ul style="list-style-type: none"> • CAD and STL software <ul style="list-style-type: none"> • 3D printing • UV exposure oven • Use of methanol solvent / removal of support structures /etc.
Facilities and start-up costs	<ul style="list-style-type: none"> • Cleanroom: \$160,000+³²³ • EBL: >\$1 million³²⁴ 	Approx. \$10-150k ³²⁵

1.10 Comparison of optical and electrochemical particle analysis methods

A number of performance parameters for optical and electrochemical particle /cell analysis techniques in commercial benchtop systems as well as reported microfluidic platforms are covered in Table 1.5, as according to the available surveyed literature. Of these, the laser-based techniques DLS, LD and NTA have the highest sensitivities, being able to detect down to 5-10 nm particles^{45,53,58}. However, the former two techniques are unable to differentiate individual beads/cells, instead carrying out ensemble analysis. LD has the widest detectable size range of 8 nm–10 μm ⁴⁵. In comparison, the static microfluidic techniques SEIS and ROT have very narrow reported ranges of only 15 μm ³³⁴⁻³³⁸. However, the studies surveyed were relatively limited in number and only investigated cells of this range, and thus these minimum and maximum values should not be taken as absolute values of what is possible. Additionally, ROT systems also involve a restricted cell diameter range for stable rotation via induced torque force within microchannels³³⁹. It should also be noted that the reported particle diameter ranges given in the table for RPS and TRPS would be split across several separate pore diameters; they would not be achievable with one single pore width due to blockage susceptibility and signal noise. Of the above techniques, microfluidic IFC systems have the highest throughputs, with chips reported able to detect 50,000³⁴⁰–100,000 cells s^{-1} ^{128,340} by use of wide field of view, high speed cameras^{128,340}. LD has the next highest possible throughput, albeit in the form of an ensemble, averaged diameter. In contrast, RPS has the lowest throughput due to its pore constriction; a paper reporting a 1300 s^{-1} throughput of 100 nm beads via a microfluidic RPS chip incorporating a nanofilter and fluidic resistor divider exists³⁴¹, but typically, maximum flow rates of 2-3 s^{-1} are reported^{342,343}. However, despite its high throughput, IFC has a relatively poor LDR due to depth of field issues when particles are nonuniformly distributed through the microchannel¹²⁷. FC has the widest LDR, due to its hydrodynamic focusing narrowing particles into a thin stream eliminating this issue⁵⁹. In comparison, RPS has the narrowest LDR, again due to pore constriction.

Table 1.5 Performance parameters of optical and electrochemical commercial and microfluidic particle/cell analysis methods.

Detection System type	Optical											Electrochemical					
	Commercial						Microfluidic					Commercial					
	SIA	DIA	DLS	LD	NTA	FC	IFC	OFC	RPS	TRPS	ROT	SEIS	DEIS	RPS			
Technique	Discrete	Discrete	Ensemble	Ensemble	Discrete	Discrete	Discrete	Discrete	Discrete	Discrete	Discrete	Discrete	Discrete	Discrete			
Analysis	Discrete	Discrete	Ensemble	Ensemble	Discrete	Discrete	Discrete	Discrete	Discrete	Discrete	Discrete	Discrete	Discrete	Discrete			
Min. particle diameter	500 nm ³⁹	20 µm ⁴¹	5 nm ⁵³	10 nm ⁴⁵	10 nm ⁵⁸	300 nm ⁶¹	250 nm ¹²⁹	1 µm ^{344,345}	50 nm ⁶⁸	40 nm ⁶⁹	5 µm ^{334,335}	10 µm ^{336,337}	500 nm ¹⁶⁰	30 nm ¹⁷⁶			
Max. particle diameter	1 mm ³⁹	2.5 mm ⁴¹	1 µm ⁵³	8 mm ⁴⁵	1 µm ⁵⁸	40 µm ⁶⁰	20 µm ^{127,128}	30 µm ³⁴⁶	300 µm ⁶⁷	300 µm ⁶⁷	20 µm ³³⁴	25 µm ³³⁸	100 µm ¹¹²	50 µm ³⁴⁷			
Max. particle throughput	Not in flow	1200 s ^{-1,41}	Not in flow	20,000 s ^{-1,348}	1500 s ^{-1,349}	10,000 s ^{-1,60}	100,000 s ^{-1,128,340}	350 s ^{-1,132}	250 s ^{-1,350}	20 s ^{-1,78}	Not in flow	Not in flow	1200 s ^{-1,141}	1300 s ^{-1,341} but typically 2-3 s ^{-1,342,343}			
LDR (cells/particles ml⁻¹)	Not typically used to measure conc.	Not typically used to measure conc.	Cannot measure conc.	Cannot measure conc.	1X10 ⁶ –1X10 ^{9,351}	1X10 ³ –1X10 ^{7,352}	1x10 ² –3x10 ^{3,353}	2.5x10 ⁴ –1.0x10 ^{6,354}	5x10 ⁴ –1x10 ^{7,355}	5x10 ⁴ –5x10 ⁶ for 2 µm–11 µm beads, to 1x10 ⁹ –1x10 ¹¹ for 40–255 nm beads ³⁵⁶	Cannot measure conc.	Not typically used to measure conc.	1x10 ⁴ –1x10 ^{9,158}	5X10 ⁶ –5X10 ^{7,343}			

1.11 Chapter summary

Particle/cell analysis and separation are used in a great many areas, from manufacturing in various industries, to health applications such as disease diagnosis. Its use is also increasing in fields such as environmental monitoring.

These techniques have been integrated into microfluidic lab-on-a-chip to facilitate a huge host of advanced technologies including many for use outside of the laboratory in in-field applications. Among many other uses, these devices could fulfil the need for affordable, portable POC biomedical analysers for resource-poor settings. Microfluidics involves microscale flow phenomena with unique characteristics that can be employed to enable fast and accurate continuous analysis and/or separation of particles and cells on a convenient, miniaturised scale.

However, the current, conventional soft-lithography and photolithographical methods of microfluidic fabrication are time-consuming, expensive and cause restriction in design freedom. These pitfalls are impeding the widespread implementation and commercialisation of lab-on-a-chip devices as a whole.

Over the last 7 years 3D printing has been investigated as an alternative to these conventional fabrication methods. AM has a number of advantages over traditional microfluidic fabrication, including the ability to build devices in one step (which shortens the device development stages as well as decreases costs) and three-dimensional design freedom.

So far, 3D printed microfluidics for organic synthesis and liquid/gas sensing have already been demonstrated. This work focuses on the development of 3D printed microfluidic devices for particle/cell analysis.

1.12 Thesis Hypothesis

The hypothesis of this thesis is that 3D printing can be used to fabricate microfluidic lab-on-a-chip devices for the in-line, continuous optical/electrochemical analysis of particles or cells, as an alternative to conventional lithographic methods.

1.13 Thesis Aims and Objectives

This project aims to develop 3D printed microfluidic LOC devices for continuous single-particle/cell analysis. It is intended that the research findings will contribute to emerging research exploring additive manufacturing as an alternative to conventional microfluidic fabrication methods, specifically, in the hitherto uncovered area of particle/cell analysis, which has wide application. In addition, this project also aimed to develop printed continuous magnetic separation modules as a means of sample preparation for these aforementioned LOC systems.

These above aims raise the following core project objectives:

- Evaluate and compare printed chips with two different types of low-cost, label-free, embedded detection systems: optical and electrochemical, in terms of numerous performance aspects: sensitivity, resolving power, throughput, linearity and ease of use.
- Develop printed continuous magnetic separators and assess them in terms of their separation efficiency.
- Investigate the nature of particle adsorption in these 3D printed devices, if any.

1.14 References

- 1 C. Washington, *Particle Size Analysis In Pharmaceuticals And Other Industries: Theory and Practice*, Ellis Horwood Limited, Chichester, UK, 1992.
- 2 B. Lee and S. Komarneni, Eds., *Chemical Processing of Ceramics*, Taylor & Francis Group, Boca Raton, FL, USA, 2nd edn., 2005.
- 3 E. C. Muly, N. Frock, Harold and D. Grammes, *IEEE Trans. Ind. Appl.*, 1979, **1A–15**, 323–330.
- 4 D. V. De Pellegrin, N. D. Corbin, G. Baldoni and A. A. Torrance, *Tribol. Int.*, 2009, **42**, 160–168.
- 5 G. Buxbaum, in *Industrial Inorganic Pigments*, ed. G. Buxbaum, Wiley, NY, USA, 2nd edn., 1998, pp. 1–42.
- 6 J. Mendel, D. Bugner and A. D. Bermel, *J. Nanoparticle Res.*, 1999, **1**, 421–424.
- 7 T. Provder, *Prog. Org. Coatings*, 1997, **32**, 143–153.
- 8 G. Hoffmeister, S. C. Watkins and J. Silverberg, *J. Agric. Food Chem.*, 1964, **12**, 64–69.
- 9 P. Fisher, C. Aumann, K. Chia, N. O’Halloran and S. Chandra, *PLoS One*, 2017, **12**, 1–20.
- 10 A. A. Rashid and S. R. Yahya, in *Natural Rubber Materials: Volume 2: Composites and Nanocomposites*, The Royal Society of Chemistry, Cambridge, UK, 2014, pp. 550–573.
- 11 J. Dodds, in *Handbook of Food Powders: Processes and Properties*, eds. B. R. Bhandari, N.

- Bansal, M. Zhang and P. Schuck, Woodhead Publishing, Cambridge, UK, 2013, pp. 309–338.
- 12 British Pharmacopoeia Commission, *British Pharmacopoeia 2005*, The Stationary Office, London, 2005.
- 13 H. S. Jung, S. H. Kwon, H. J. Choi, J. H. Jung and Y. G. Kim, *Compos. Struct.*, 2016, **136**, 106–112.
- 14 M. Benelmekki, in *Designing Hybrid Nanoparticles*, Morgan & Claypool Publishers, San Rafael, CA, USA, 2015, pp. 1–14.
- 15 F. J. M. Colberts, M. M. Wienk and R. A. J. Janssen, *ACS Appl. Mater. Interfaces*, 2017, **9**, 13380–13389.
- 16 L. Zhang, J. Mu, Z. Wang, G. Li, Y. Zhang and Y. He, *J. Alloys Compd.*, 2016, **671**, 60–65.
- 17 Markets and Markets Research Private Ltd., AST 3899: Nanoparticle Analysis Market by Technology (DLS, NTA, XRD, SMPS, CPC, NSAM), Analysis Type (Size, Zeta Potential, Weight, Flow properties), End-user (Pharmaceutical & Biopharmaceutical Companies, Academic Research Institutions)—Global Forecast to 2020 [online], 2015. [Accessed 07/12/2017]. Available from: <https://www.marketsandmarkets.com/Market-Reports/nanoparticle-analysis-market-89508030.html>.
- 18 U. Walter and J. Buer, in *Single Cell Analysis: Technologies and Applications*, ed. D. Anselmetti, Wiley-VCH Verlag GmbH, Weinheim, Germany, 2009, pp. 175–250.
- 19 J. Carton, R. Daly and P. Ramani, *Pathology as a Clinical Discipline*, Oxford University Press Inc., New York, USA, 2007.
- 20 M. Elmes and M. Gasparon, *J. Environ. Manage.*, 2017, **202**, 137–150.
- 21 M. Filella, in *Environmental Colloids and Particles: Behaviour, Separation and Characterisation*, eds. K. J. Wilkinson and J. R. Lead, John Wiley & Sons, Ltd., Chichester, UK, 2007, pp. 18–94.
- 22 P. Loganathan, S. Vigneswaran and J. Kandasamy, *Crit. Rev. Environ. Sci. Technol.*, 2013, **3389**, 1315–1348.
- 23 J. Merkisz and J. Pielecha, in *Nanoparticle Emissions in Combustion Engines*, eds. J. Merkisz and J. Pielecha, Springer International Publishing, Cham, Switzerland, 2015, pp. 27–46.
- 24 Y. Wang, H. Liu and C. F. Lee, *Renew. Sustain. Energy Rev.*, 2016, **64**, 569–581.
- 25 D. Sedlak, *Environ. Sci. Technol.*, 2017, **51**, 7747–7748.
- 26 R. B. Finkelman and L. Tian, *Int. Geol. Rev.*, 2017, **60**, 1–11.
- 27 G. E. Batley, J. K. Kirby and M. J. Mclaughlin, *Acc. Chem. Res.*, 2013, **46**, 854–862.
- 28 H. G. Merkus, in *Particle Size Measurements: Fundamentals, Practice, Quality*, Springer Science+Business Media, LLC, Dordrecht, Netherlands, 2009, pp. 195–217.

- 29 N. Kumar and S. Kumbhat, in *Essentials in Nanoscience and Nanotechnology*, eds. N. Kumar and S. Kumbhat, John Wiley & Sons Inc., Hoboken, NJ, USA, 2016, p. 106.
- 30 F. Babick, in *Suspensions of Colloidal Particles and Aggregates*, Springer International Publishing, Cham, Switzerland, 2016, pp. 7–74.
- 31 G.-Y. A. Tan, L. Ge, C. Pan, T. S. Ng and W. Jing-Yuan, in *Recent Advances in Biotechnology Volume 2*, ed. M. Koller, Bentham, Sharjah, UAE, 2016, pp. 3039–310.
- 32 P. Echlin, *Handbook of Sample Preparation for Scanning Electron Microscopy and X-Ray Microanalysis*, NY, USA, Cambridge, UK, 2009.
- 33 V. Bučinskas, A. Dzedzickis, N. Šešok, E. Šutinys and I. Iljin, in *Dynamical Systems: Theoretical and Experimental Analysis*, ed. J. Awrejcewicz, Springer International Publishing, Cham, Switzerland, 2016, p. 40.
- 34 N. Feltin, S. Ducourtieux and A. Delvallée, in *Metrology and Standardization for Nanotechnology: Protocols and Industrial Innovations*, eds. E. Mansfield, D. L. Kaiser, D. Fujita and M. Van de Voorde, Wiley-VCH Verlag GmbH, Weinheim, Germany, 2017, p. 207.
- 35 B. J. Ennis, W. Witt, R. Weinekötter, D. Sphar, E. Gommeran, R. H. Snow, T. Allen, G. J. Raymus and J. D. Litster, in *Perry's Chemical Engineer's Handbook*, eds. D. W. Green and R. H. Perry, McGraw-Hill Education, New York City, NY, USA, 8th edn., 2008, pp. 13–14.
- 36 Malvern Panalytical, Morphologi[®] G3 User Manual [online], 2018 [Accessed 27/10/2018]. Available from: <https://www.malvernpanalytical.com/en/learn/knowledge-center/user-manuals/MAN0410EN>.
- 37 A. F. Rawle, in *Pharmaceutical Suspensions From Formulation Development to Manufacturing*, eds. A. K. Kulshreshtha, O. N. Singh and G. M. Wall, Springer, New York City, NY, USA, 2010, pp. 177–230.
- 38 International Organization for Standardization, ISO 13322-1 Particle size analysis—Image analysis methods—Part 1: Static image analysis, [online], 2014 [Accessed 14/11/2017]. Available from: <https://www.iso.org/standard/51257.html>.
- 39 S. H. Ramadugu, V. K. Puli and Y. V. Pathak, in *Handbook of Nutraceuticals Volume II: Scale-up, Processing and Automation*, ed. Y. V. Pathak, Taylor & Francis Group, Boca Raton, FL, USA, 2011, p. 180.
- 40 R. Sidwell, in *Multiparticulate Drug Delivery: Formulation, Processing and Manufacturing*, ed. A. R. Rajabi-Siahboomi, Springer Science+Business Media, LLC, NY, USA, 2017, p. 16.
- 41 T. Allen, in *Powder Sampling and Particle Size Determination*, Elsevier B.V., Amsterdam, Netherlands, 2003, pp. 142–207.
- 42 G. Rabinski and D. Thomas, *Water Sci. Technol.*, 2004, **50**, 19–26.

- 43 American Society for Testing and Materials International, *Designation: E3060-16: Standard Guide for Subvisible Particle Measurement in Biopharmaceutical Manufacturing Using Dynamic (Flow) Imaging Microscopy*, West Conshohocken, PA, US, 2016.
- 44 D. Keller, N. Olivier, T. Pengo and G. Ball, in *Standard and Super-Resolution Bioimaging Data Analysis: A Primer*, eds. A. Wheeler and R. Henriques, John Wiley & Sons, Ltd., Chichester, UK, 2018, pp. 201–202.
- 45 S. W. Andrews, D. M. Nover, J. E. Reuter and S. G. Schladow, *Water Resour. Res.*, 2011, **47**, 1–12.
- 46 T. Wriedt, in *The Mie Theory: Basics and Applications*, eds. W. Hergert and T. Wriedt, Springer-Verlag Berlin Heidelberg, Berlin, Germany, 2012, pp. 53–71.
- 47 M. Rhodes, in *Introduction to Particle Technology*, John Wiley & Sons, Ltd., Hoboken, NJ, USA, 2nd edn., 2008, pp. 1–28.
- 48 X. Renliang, *Particuology*, 2015, **18**, 11–21.
- 49 Z. Ma, H. G. Merkus, J. G. A. E. de Smet, C. Heffels and B. Scarlett, *Powder Technol.*, 2000, **111**, 66–78.
- 50 R. Xu, in *Particle Characterization: Light Scattering Methods*, Kluwer Academic Publishers, NY, USA, 2002, pp. 111–181.
- 51 E. Olson, *Pharm. Technol.*, 2018, **42**, 28–33.
- 52 H. G. Merkus, in *Particle Size Measurements: Fundamentals, Practice, Quality*, Springer Science+Business Media, LLC, Dordrecht, Netherlands, 2009, pp. 259–285.
- 53 H. G. Merkus, in *Particle Size Measurements: Fundamentals, Practice, Quality*, Springer Science+Business Media, LLC, Dordrecht, Netherlands, 2009, pp. 299–317.
- 54 R. Tantra, K. N. Robinson and J. C. Jarman, in *Nanomaterial Characterization: An Introduction*, ed. R. Tantra, John Wiley & Sons Inc., Hoboken, NJ, USA, 2016, pp. 137–139.
- 55 C. Demetzos, in *Pharmaceutical Nanotechnology: Fundamentals and Practical Applications*, ed. C. Demetzos, Springer Science+Business Media, LLC, Singapore, 2016, p. 56.
- 56 W. Anderson, D. Kozak, V. A. Coleman, Å. K. Jämting and M. Trau, *J. Colloid Interface Sci.*, 2013, **405**, 322–330.
- 57 X. Bi, S. Lee, J. F. Ranville, P. Sattigeri, A. Spanias, P. Herckes and P. Westerhoff, *J. Anal. At. Spectrom.*, 2014, **29**, 1630–1639.
- 58 M. Wright, in *Nanoparticles in Biology and Medicine. Methods in Molecular Biology (Methods and Protocols)*, ed. M. Soloviev, Humana Press, Totowa, NJ, USA, 2012.
- 59 H. M. Shapiro, *Practical Flow Cytometry*, John Wiley & Sons Inc., Hoboken, NJ, 4th Ed., 2003.
- 60 B. H. Estridge and A. P. Reynolds, *Basic Clinical Laboratory Techniques*, Cengage Learning,

- Delmar, Canada, 6th edn., 2012.
- 61 E. Van Der Pol, A. G. Hoekstra, A. Sturk, C. Otto, T. G. Van Leeuwen and R. Nieuwland, *J. Thromb. Haemost.*, 2010, **8**, 2596–2607.
- 62 D. F. Alvarez, K. Helm, J. DeGregori, M. Roederer and S. Majka, *Am. J. Physiol. Lung Cell. Mol. Physiol.*, 2010, **298**, 127–130.
- 63 M. Venkatapathi, B. Rajwa, K. Ragheb, P. P. Banada, T. Lary, J. P. Robinson and E. D. Hirleman, *Appl. Opt.*, 2008, **47**, 678–686.
- 64 A. Givan, *Flow Cytometry—First Principles*, John Wiley & Sons Inc., New York, 2nd Ed., 2001.
- 65 Alpha Z32 For Impedance Flow Cytometry [online], 2018 [Accessed 01/11/2018]. Available from: <https://www.amphasys.com/impedance-flow-cytometry>.
- 66 W. H. Coulter, Means for Counting Particles Suspended in a Fluid, United States, Patent number: 2656508A, 20/10/1953.
- 67 Izon Science Ltd., qMicro [online], 2018 [Accessed 02/10/2018]. Available from: <https://izon.com/qmicro/>.
- 68 D. Bartczak and H. Goenaga-Infante, in *Nanomaterial Characterisation: An Introduction*, ed. R. Tantra, John Wiley & Sons, Inc., Hoboken, NJ, USA, 2016, p. 68.
- 69 M. Sivakumaran and M. Platt, *Nanomed. (London)*, 2016, **11**, 2197–2214.
- 70 S. J. Sowerby, M. F. Broom and G. B. Petersen, *Sensors Actuators B Chem.*, 2007, **123**, 325–330.
- 71 G. S. Roberts, D. Kozak, W. Anderson, M. F. Broom, R. Vogel and M. Trau, *Small*, 2010, **6**, 2653–2658.
- 72 H. Bayley, and C. R. Martin, *Chem. Rev.*, 2000, **100**, 2575–2594.
- 73 A. Han, G. Schürmann, G. Mondin, R. A. Bitterli, N. G. Hegelbach, N. F. de Rooij, and U. Staufer, *Appl. Phys. Lett.*, 2006, **88**, 093901.
- 74 C. C. Harrell, Y. Choi, L. P. Horne L. A. Baker, Z. S. Siwy and C. R. Martin, *Langmuir*, 2006, **22**, 10837–10843
- 75 E. L. C. J. Blundell, R. Vogel and M. Platt, *Langmuir*, 2016, **32**, 1082–1090.
- 76 E. L. C. J. Blundell, M. J. Healey, E. Holton, M. Sivakumaran, S. Manstana and M. Platt, *Anal. Bioanal. Chem.*, 2016, **408**, 5757–5768.
- 77 E. Weatherall and G. R. Wilmott, *Analyst*, 2015, **140**, 3318–3334.
- 78 E. L. C. J. Blundell, L. J. Mayne, E. R. Billinge and M. Platt, *Anal. Methods*, 2015, **7**, 7055–7066
- 79 M. B. Dainiak, A. Kumar, I. Y. Galaev and B. Mattiasson, in *Cell Separation: Fundamentals, Analytical and Preparative Methods*, eds. A. Kumar, I. Y. Galaev and B. Mattiasson, Springer-Verlag Berlin Heidelberg, Berlin, Germany, 2007, pp. 1–18.

- 80 S. Suresh, *Acta Mater.*, 2007, **55**, 3989–4014.
- 81 E. Racila, D. Euhus, A. J. Weiss, C. Rao, J. McConnell, W. M. M. Terstappen, Leon and J. W. Uhr, *Proc. Natl. Acad. Sci. USA*, 1998, **95**, 4589–4594.
- 82 S. J. Cohen, C. J. A. Punt, N. Iannotti, B. H. Saidman, K. D. Sabbath, N. Y. Gabrail, J. Picus, M. Morse, E. Mitchell, M. C. Miller, G. V Doyle, H. Tissing, L. W. M. M. Terstappen and N. J. Meropol, *J. Clin. Oncol.*, 2008, **26**, 3213–3221.
- 83 M. Reinhardt, A. Bader and S. Giri, *Expert Rev. Med. Devices*, 2015, **12**, 353–364.
- 84 G. M. Whitesides, *Nature*, 2006, **442**, 368–373.
- 85 E. Keonjian, *Microelectronics: Theory, Design and Fabrication*, McGraw Hill, New York City, NY, USA, 1963.
- 86 B. Frazier, C. Friedrich and R. Warrington, *IEEE Trans. Ind. Electron.*, 1995, **42**, 1460–1465.
- 87 S. C. Terry, PhD thesis, Stanford University, 1975.
- 88 S. C. Terry, J. H. Jerman and J. B. Angell, *IEEE Trans. Electron Devices*, 1979, **26**, 1880–1886.
- 89 E. Bassous, H. H. Taub and L. Kuhn, *Appl. Phys. Lett.*, 1977, **31**, 135–137.
- 90 A. Manz, N. Graber and H. M. Widmer, *Sensors Actuators B Chem.*, 1990, **B1**, 244–248.
- 91 D. R. Reyes, D. Iossifidis, P.-A. Auroux and A. Manz, *Anal. Chem.*, 2002, **74**, 2623–2636.
- 92 C. S. Effenhauser, A. Manz and H. M. Widmer, *Anal. Chem.*, 1995, **67**, 2284–2287.
- 93 W. Gumbrecht, D. Peters, W. Schelter, W. Erhardt, J. Henke, J. Steil and U. Sykora, *Sensors Actuators B Chem.*, 1994, **19**, 704–708.
- 94 I. Walther, B. H. van der Schoot, S. Jeanneret, P. Arquint, N. F. de Rooij, V. Gass, B. Bechler, G. Lorenzi and A. Cogoli, *J. Biotechnol.*, 1994, **38**, 21–32.
- 95 C. S. Effenhauser and A. Manz, *Am. Lab.*, 1994, **26**, 15–16.
- 96 G. Urban, G. Jobst, P. Svasek, M. Varahram, I. Moser and E. Aschauer, in *Micro Total Analysis Systems: Proceedings of the μ TAS '94 Workshop*, eds. A. Van den Berg and P. Bergveld, Kluwer Academic Publishers, Enschede, The Netherlands, 1994.
- 97 T. Studt, Expanding beyond silicon IC technologies, *R&D*, June, 1996.
- 98 P. Gravesen, J. Branebjerg and O. Jensen, *J. Micromech. Microeng.*, 1993, **3**, 168–182.
- 99 N.-T. Nguyen and S. T. Wereley, in *Fundamentals and Applications of Microfluidics*, Artech House, Norwood, MA, USA, 2nd edn., 2006, pp. 1–2.
- 100 W. Yang and A. T. Woolley, *J. Lab. Autom.*, 2010, **15**, 198–209.
- 101 D. Mark, S. Haeberle, G. Roth, F. von Stetten and R. Zengerle, *Lab Chip*, 2010, **39**, 1153–1182.
- 102 Institute for Scientific Information (ISI), Web of Science, search term “microfluidic” [online], 2017 [Accessed 22/10/2017]. Available from: <http://wok.mimas.ac.uk/>.
- 103 T. A. Duncombe, A. M. Tentori and A. E. Herr, *Nat. Rev.*, 2015, **16**, 554–567.

- 104 J. J. Agresti, E. Antipov, A. R. Abate, K. Ahn, A. C. Rowat, J.-C. Baret, M. Marquez, A. M. Klibanov, A. D. Griffiths and D. A. Weitz, *Proc. Natl. Acad. Sci.*, 2010, **107**, 4004–4009.
- 105 E. Sollier and D. Carlo, in *Microfluidic Technologies for Human Health*, eds. U. Demirci, A. Khademhosseini, R. Langer and J. Blander, World Scientific Publishing Co. Pte. Ltd., Singapore, 2012, pp. 311–340.
- 106 E. Brouzes, M. Medkova, N. Savenelli, D. Marran, M. Twardowski, J. B. Hutchison, J. M. Rothberg, D. R. Link, N. Perrimon and M. L. Samuels, *Proc. Natl. Acad. Sci.*, 2009, **106**, 14195–14200.
- 107 N. Déneraud, J. Becker, R. Delgado-Gonzalo, P. Damay, A. S. Rajkumar, M. Unser, D. Shore, F. Naef and S. J. Maerkl, *Proc. Natl. Acad. Sci.*, 2013, **110**, 15842–15847.
- 108 I. Paprotny, F. Doering, P. A. Solomon and M. Richard, *Sensors Actuators A Phys.*, 2013, **201**, 506–516.
- 109 K. A. Koehler and T. Peters, *Curr. Environ. Health Rep.*, 2015, **2**, 399–411.
- 110 J. Wang, J. Zhao, Y. Wang, W. Wang, Y. Gao, R. Xu and W. Zhao, *Micromachines*, 2016, **7**, 1–17.
- 111 N. Yamaguchi, Y. Tokunaga, S. Goto, Y. Fujii, F. Banno and A. Edagawa, *Nat. Sci. Reports*, 2017, **7**, 1–8.
- 112 I. Heidmann and M. Di Berardino, in *Plant Germline Development. Methods in Molecular Biology Volume 1669*, ed. A. Schmidt, Humana Press, NY, USA, 2017.
- 113 D. Liu, H. Zhang, F. Fontana, J. T. Hirvonena and H. A. Santos, *Lab Chip*, 2017, **17**, 1856–1883.
- 114 Q. Xu, M. Hashimoto, T. T. Dang, T. Hoare, D. S. Kohane, G. M. Whitesides, R. Langer and D. G. Anderson, *Small*, 2009, **5**, 1575–1581.
- 115 R. Donno, A. Gennari, E. Lallana, J. M. Rios, D. La Rosa, K. Treacher, K. Hill, M. Ashford and N. Tirelli, *Int. J. Pharm.*, 2017, **534**, 97–107.
- 116 J. Rantanen and J. Khinast, *J. Pharm. Sci.*, 2015, **104**, 3612–3638.
- 117 M. Karle, S. K. Vahist, R. Zengerle and F. von Stetten, *Anal. Chim. Acta*, 2016, **929**, 1–22.
- 118 C. Kunstmann-Olsen, M. M. Hanczyc, J. Hoyland, S. Rasmussen and H.-G. Rubahn, *Sensors Actuators B. Chem.*, 2016, **229**, 7–13.
- 119 W. Su, X. Gao, L. Jiang and J. Qin, *J. Chromatogr. A*, 2015, **1377**, 13–26.
- 120 S. T. Sanjay, G. Fu, M. Dou, F. Xu, R. Liu, H. Qi and X. Li, *Analyst*, 2015, **140**, 7062–7081.
- 121 W. Jung, J. Han, J. Choi and C. H. Ahn, *Microelectron. Eng.*, 2015, **132**, 46–57.
- 122 M. Junkin and S. Tay, *Lab Chip*, 2014, **14**, 1246–1260.
- 123 A. M. Foudeh, T. F. Didar, T. Veres and M. Tabrizian, *Lab Chip*, 2012, **12**, 3249–3266.
- 124 W. G. Lee, Y.-G. Kim, B. G. Chung, U. Demirci and A. Khademhosseini, *Adv. Drug Deliv. Rev.*,

- 2010, **62**, 449–457.
- 125 A. M. Urdea, L. A. Penny, S. S. Olmsted, M. Y. Giovanni, P. Kaspar, A. Shepherd, P. Wilson, C. A. Dahl, S. Buchsbaum, G. Moeller and D. C. H. Burgess, *Nature*, 2006, **422**, 412–418.
- 126 T. Konry, S. S. Bale, A. Bhushan, K. Shen, E. Seker, B. Polyak and M. Yarmush, *Mikrochim Acta.*, 2012, **176**, 251–269.
- 127 Y. J. Heo, D. Lee, J. Kang, K. Lee and W. K. Chung, *Sci. Rep.*, 2017, **7**, 1–9
- 128 K. Goda, A. Ayazi, D. R. Gossett, J. Sadasivam, C. K. Lonappan and E. Sollier, *Proc. Natl. Acad. Sci.*, 2012, **109**, 11630–11635.
- 129 C. Haiden, T. Wopelka, M. Jech, D. Puchberger-Enengl, E. Weber, F. Keplinger and M. J. Vellekoop, *Procedia Eng.*, 2012, **47**, 680–683.
- 130 H. Zhu, S. Mavandadi, A. F. Coskun, O. Yaglidere and A. Ozcan, *Anal. Chem.*, 2011, **83**, 6641–6647.
- 131 D. Sobek, A. M. Young, M. L. Gray and S. D. Senturia, in *Micro Electro Mechanical Systems, MEMS '93, Proceedings—An Investigation of Micro Structures, Sensors, Actuators, Machines, and Systems*, IEEE, New York, 1993, pp. 219–224.
- 132 Y. Zhang, B. R. Watts, T. Guo, Z. Zhang, C. Xu and Q. Fang, *Micromachines*, 2016, **6**, 1–21.
- 133 M. E. Piyasena and S. W. Graves, *Lab Chip*, 2014, **14**, 1044–1059.
- 134 M. I. Lapsley, L. Wang and T. J. Huang, *Biomark. Med.*, 2013, **7**, 75–78.
- 135 M. Frankowski, J. Theisen, A. Kummrow, P. Simon, N. Bock and M. Schmidt, *Sensors*, 2013, **13**, 4674–4693.
- 136 S. H. Cho, J. M. Godin, C.-H. Chen, W. Qiao, H. Lee and Y.-H. Lo, *Biomicrofluidics*, 2010, **4**, 1–23.
- 137 D. A. Ateya, J. S. Erickson, P. B. Howell, L. R. Hilliard, J. P. Golden and F. S. Ligler, *Anal. Bioanal. Chem.*, 2008, **391**, 1485–1498.
- 138 G.-B. Lee, C.-H. Lin and G.-L. Chang, *Sensors Actuators A Phys.*, 2003, **103**, 165–170.
- 139 N. Pamme, R. Koyama and A. Manz, *Lab Chip*, 2003, **3**, 187–192.
- 140 D. M. Betters, *J. Adv. Pract. Oncol.*, 2015, **6**, 435–440.
- 141 M. Rosenauer, W. Buchegger, I. Finoulst, P. Verhaert and M. Vellekoop, *Microfluid. Nanofluidics*, 2011, **10**, 761–771.
- 142 S. Kostner and M. J. Vellekoop, *Sensors Actuators B Chem.*, 2008, **132**, 512–517.
- 143 J. Wu and M. Gu, *J. Biomed. Opt.*, 2011, **16**, 1–12.
- 144 B. R. Watts, Z. Zhang, C. Xu, X. Cao and M. Lin, *Biomed. Opt. Express*, 2012, **3**, 2784–2793.
- 145 B. R. Watts, Z. Zhang, C. Q. Xu, X. Cao and M. Lin, *Electrophoresis*, 2012, **33**, 3236–3244.
- 146 B. R. Watts, T. Kowpak, Z. Zhang, C. Xu and S. Zhu, *Biomed. Opt. Express*, 2010, **1**, 848–860.

- 147 D. Spencer, G. Elliott and H. Morgan, *Lab Chip*, 2014, **14**, 3064–3073.
- 148 K. T. Kotz, A. C. Petrofsky, R. Haghgooie, R. Granier, M. Toner and R. G. Tompkins, *Technol. (Singap. World Sci.)*, 2013, **1**, 27–36.
- 149 J. Godin and Y. Lo, *Biomed. Opt. Express*, 2010, **1**, 1472–1479.
- 150 M. A. Mansor and M. R. Ahmad, *Int. J. Mol. Sci*, 2015, **16**, 12686–12712.
- 151 C. I. Trainito, O. Français and B. Le Pioufle, *Electrophoresis*, 2015, **36**, 1115–1122.
- 152 A. Han and A. B. Frazier, *Lab Chip*, 2006, **1**, 1412–1414.
- 153 T. Wenlai, T. Dezhi, N. I. Zhonghua, X. Nan and Y. I. Hong, *Sci. China Technol. Sci.*, 2017, 1–9.
- 154 Z. Zhu, O. Frey, N. Haandbaek, F. Franke, F. Rudolf and A. Hierlemann, *Nat. Sci. Reports*, 2015, **5**, 1–14.
- 155 M. Carminati, in *Progress Reports on Impedance Spectroscopy: Measurements, Modeling and Application*, ed. O. Kanoun, De Gruyter Oldenbourg, Berlin, Germany, 2017, pp. 119–130.
- 156 K. C. Cheung, M. D. Berardino, G. Schade-Kampmann, M. Hebeisen, A. Pierzchalski, J. Bocsi, A. Mittag and A. Tárnok, *Cytom. Part A*, 2010, **77A**, 648–666.
- 157 T. Sun and H. Morgan, *Microfluid. Nanofluidics*, 2010, **8**, 423–443.
- 158 M. A. Mansor, M. Takeuchi, M. Nakajima, Y. Hasegawa and M. R. Ahmad, *Appl. Sci.*, 2017, **7**, 1-10.
- 159 M.-H. Wang and W.-H. Chang, *Biomed. Res. Int.*, 2015, **2015**, 871603 pages 1–9.
- 160 C. H. Clausen, G. E. Skands, C. V. Bertelsen and W. E. Svendsen, *Micromachines*, 2015, **6**, 110–120.
- 161 J. Kirkegaard, C. H. Clausen, R. Rodriguez-Trujillo and W. E. Svendsen, *Biosensors*, 2014, **4**, 257–272.
- 162 K. Cheung, S. Gawad and P. Renaud, *Cytom. Part A*, 2005, **65A**, 124–132.
- 163 D. Holmes, D. Pettigrew, C. H. Reccius, J. D. Gwyer, C. Van Berkel, J. Holloway, D. E. Davies and H. Morgan, *Lab Chip*, 2009, **9**, 2881–2889.
- 164 D. Spencer, F. Caselli, P. Bisegna and H. Morgan, *Lab Chip*, 2016, **16**, 2467–2473.
- 165 M. Frankowski, P. Simon, N. Bock, A. El-Hasni, U. Schnakenberg and J. Neukammer, *Eng. Life Sci.*, 2015, **15**, 286–296.
- 166 J. Chen, C. Xue, Y. Zhao, D. Chen, M.-H. Wu and J. Wang, *Int. J. Mol. Sci.*, 2015, **16**, 9804–9830.
- 167 M. Evander, A. J. Ricco, J. Morser, G. T. A. Kovacs, L. L. K. Leung and L. Giovangrandi, *Lab Chip*, 2013, **13**, 722–729.
- 168 C. Bernabini, D. Holmes and H. Morgan, *Lab Chip*, 2011, **11**, 407–412.
- 169 R. Rodriguez-Trujillo, O. Castillo-Fernandez, M. Garrido, M. Arundell, A. Valencia and G. Gomila, *Biosens. Bioelectron.*, 2008, **24**, 290–296.

- 170 Y. Song, J. Zhang and D. Li, *Micromachines*, 2017, **8**, 1–19.
- 171 M. Carminati, *J. Sensors*, 2017, **2017**, 1–15.
- 172 J. Sun, Y. Kang, E. M. Boczek and X. Jiang, *Electroanalysis*, 2013, **25**, 1023–1028.
- 173 O. A. Saleh and L. L. Sohn, in *Nano and Microsensors for Chemical and Biological Terrorism Surveillance*, ed. B.-H. Tok, Jeffrey, Royal Society of Chemistry, Cambridge, UK, 2008, pp. 60–81.
- 174 N. M. M. Pires, T. Dong, U. Hanke and N. Hoivik, *Sensors*, 2014, **14**, 15458–15479.
- 175 R. Peng, X. S. Tang and D. Li, *Small*, 2018, **14**, 1–11.
- 176 Z. D. Harms, D. G. Haywood, A. R. Kneller, L. Selzer, A. Zlotnick and S. C. Jacobson, *Anal. Chem.*, 2015, **87**, 699–705.
- 177 N. Pamme, *Lab Chip*, 2007, **7**, 1644–1659.
- 178 L. Armbrecht and P. S. Dittrich, *Anal. Chem.*, 2017, **89**, 2–21.
- 179 A. J. Mach and D. Di Carlo, *Biotechnol. Bioeng.*, 2010, **107**, 302–311.
- 180 M. Antfolk and T. Laurell, *Anal. Chim. Acta*, 2017, **965**, 9–35.
- 181 D. Pappas, *Analyst*, 2016, **141**, 525–535.
- 182 Y. Chen, P. Li, P.-H. Huang, Y. Xie, J. D. Mai, L. Wang, N.-T. Nguyen and T. J. Huang, *Lab Chip*, 2014, **14**, 626–645.
- 183 A. Menachery, N. Kumawat and M. Qasaimeh, *Trends Anal. Chem.*, 2017, **89**, 1–12.
- 184 J. M. Jackson, M. A. Witek, J. W. Kamande and S. A. Soper, *Chem. Soc. Rev.*, 2017, **46**, 4245–4280.
- 185 A. Khamenehfar and P. C. H. Li, *Curr. Pharm. Biotechnol.*, 2016, **17**, 810–821.
- 186 J. H. Myung and S. Hong, *Lab Chip*, 2015, **15**, 4500–4511.
- 187 P. P. Madhuprasad, T. Kumeria, D. Losic and M. Kurkuri, *RSC Adv.*, 2015, **5**, 89745–89762.
- 188 K. Hyun and H. Jung, *Lab Chip*, 2014, **14**, 45–56.
- 189 M. A. Faridi, H. Ramachandraiah, I. Banerjee, S. Ardabili, S. Zelenin and A. Russom, *J. Nanobiotechnology*, 2017, **15**, 1–9.
- 190 D. Carugo, T. Octon, W. Messaoudi, A. L. Fisher, M. Carboni, N. R. Harris and P. Glynn-Jones, *Lab Chip*, 2014, **14**, 3830–3842.
- 191 M. Y. Wu, M. Hsu, S. Chen, D. Hwang, T. Yen and C. Cheng, *Trends Biotechnol.*, 2017, **35**, 288–300.
- 192 S. Q. Wang, F. Inci, T. Chaunzwa, A. Ramanujam, A. Vasudevan, S. Subramanian, A. C. F. Ip, B. Sridharan, U. A. Gurkan and U. Demirci, *Int. J. Nanomedicine*, 2012, **7**, 2591–2600.
- 193 W. Lee, D. Kwon, W. Choi, G. Y. Jung and S. Jeon, *Sci. Rep.*, 2015, **5**, 1–6.
- 194 Y. Jiang, S. Zou and X. Cao, *Anal. Methods*, 2016, **8**, 6668–6681.

- 195 X. Weng and S. Neethirajan, *Trends Food Sci. Technol.*, 2017, **65**, 10–22.
- 196 F. Tian, J. Lyu, J. Shi, F. Tan and M. Yang, *Sensors Actuators B. Chem.*, 2016, **225**, 312–318.
- 197 J. Nilsson, M. Evander, B. Hammarström and T. Laurell, *Anal. Chim. Acta*, 2009, **649**, 141–157.
- 198 A. Lenshof and T. Laurell, *Chem. Soc. Rev.*, 2010, **39**, 1203–1217.
- 199 N. Nivedita and I. Papautsky, in *Circulating Tumour Cells: Isolation and Analysis*, ed. Z. H. Fan, John Wiley & Sons Inc., Hoboken, NJ, USA, 2016, pp. 127–146.
- 200 B. H. Wunsch, J. T. Smith, S. M. Gifford, C. Wang, M. Brink, R. L. Bruce, R. H. Austin, G. Stolovitzky and Y. Astier, *Nat. Nanotechnol.*, 2016, **11**, 936–940.
- 201 L. R. Huang, E. C. Cox, R. H. Austin and J. C. Sturm, *Science*, 2004, **304**, 987–991.
- 202 M. Yamada, M. Nakashima and M. Seki, *Anal. Chem.*, 2004, **76**, 5465–5471.
- 203 A. Lenshof, C. Magnusson and T. Laurell, *Lab Chip*, 2012, **12**, 1210–1223.
- 204 F. Petersson, L. Aberg, A.-M. Swärd-Nilsson and T. Laurell, *Anal. Chem.*, 2007, **79**, 5117–5123.
- 205 T. Salafi, K. K. Zeming and Y. Zhang, *Lab Chip*, 2017, **17**, 11–33.
- 206 N. Pamme, J. C. T. Eijkel and A. Manz, *J. Magn. Magn. Mater.*, 2006, **307**, 237–244.
- 207 R. Zhou and C. Wang, *J. Micromechanics Microengineering*, 2015, **25**, 1–10.
- 208 P. Sajeesh and A. K. Sen, *Microfluid. Nanofluidics*, 2014, **17**, 1–52.
- 209 A. A. S. Bhagat, H. Bow, H. W. Hou, S. J. Tan, J. Han and C. T. Lim, *Med. Biol. Eng. Comput.*, 2010, **48**, 999–1014.
- 210 A. A. S. Bhagat, S. S. Kuntaegowdanahalli and I. Papautsky, *Lab Chip*, 2008, **8**, 1906–1914.
- 211 M. E. Warkiani, B. L. Khoo, L. Wu, A. K. P. Tay, A. A. S. Bhagat, J. Han and C. T. Lim, *Nat. Protoc.*, 2016, **11**, 134–148.
- 212 J. Zhang, S. Yan, R. Sluyter, W. Li, G. Alici and N.-T. Nguyen, *Sci. Rep.*, 2014, **4**, 1–9.
- 213 W. Al-Faqheri, T. H. G. Thio, M. A. Qasaimeh, A. Dietzel, M. Madou and A. Al-Halhouli, *Microfluid. Nanofluidics*, 2017, **21**, 1–23.
- 214 D. Di Carlo, *Lab Chip*, 2009, **9**, 3038–3046.
- 215 D. Wu, J. Qin and B. Lin, *J. Chromatogr. A*, 2008, **1184**, 542–559.
- 216 S. M. Kenyon, M. M. Meighan and M. A. Hayes, *Electrophoresis*, 2011, **32**, 482–493.
- 217 H. Jeon, Y. Kim and G. Lim, *Sci. Rep.*, 2016, **6**, 1–9.
- 218 P. R. C. Gascoyne and J. Vykoukal, *Electrophoresis*, 2002, **23**, 1973–1983.
- 219 M. Li, W. H. Li, J. Zhang and W. Wen, *J. Phys. D Appl. Phys.*, 2014, **47**, 1–32.
- 220 S. Yan, J. Zhang, M. Li, G. Alici, H. Du, R. Sluyter and W. Li, *Sci. Rep.*, 2014, **4**, 1–8.
- 221 P. Li, Z. Mao, Z. Peng, L. Zhou, Y. Chen, P.-H. Huang, C. I. Truica, J. J. Drabick, W. S. El-Deiry, M. Dao, S. Suresh and T. J. Huang, *Proc. Natl. Acad. Sci.*, 2015, **112**, 4970–4975.
- 222 N. Ota, Y. Yalikun, T. Suzuki, S. W. Lee, Y. Hosokawa, K. Goda and Y. Tanaka, *R. Soc. Open*

- Sci.*, 2019, **6**, 1-14.
- 223 N. Pamme and C. Wilhelm, *Lab Chip*, 2006, **6**, 974–980.
- 224 Q. Cao, X. Han and L. Li, *Lab Chip*, 2014, **14**, 2762–2777.
- 225 C. S. Lee, H. Lee and R. M. Westervelt, *Appl. Phys. Lett.*, 2001, **79**, 3308–3310.
- 226 Q. Ramadan, V. Samper, D. P. Poenar and C. Yu, *Biosens. Bioelectron.*, 2006, **21**, 1693–1702.
- 227 X. Sun, Z. Feng, S. Zhi, C. Lei, D. Zhang and Y. Zhou, *Sci. Rep.*, 2017, **7**, 1–8.
- 228 N. Pamme and A. Manz, *Anal. Chem.*, 2004, **76**, 7250–7256.
- 229 M. Hejazian, W. Li and N.-T. Nguyen, *Lab Chip*, 2014, **15**, 959–970.
- 230 C. W. Shields IV, C. D. Reyes and G. P. López, *Lab Chip*, 2015, **15**, 1230–1249.
- 231 S. M. McFaul, B. K. Lin and H. Ma, *Lab Chip*, 2012, **12**, 2369–2376.
- 232 Y. Song, R. Peng, J. Wang, X. Pan, Y. Sun and D. Li, *Electrophoresis*, 2013, **34**, 684–690.
- 233 T. S. Safaei, R. M. Mohamadi, E. H. Sargent and S. O. Kelley, *ACS Appl. Mater. Interfaces*, 2015, **7**, 14165–14169.
- 234 J. Kim, H. Cho, S. Han and K. Han, *Anal. Chem.*, 2016, **88**, 4857–4863.
- 235 F. Liu, K. Pawan, G. Zhang and J. Zhe, *Anal. Chem.*, 2016, **88**, 711–717.
- 236 A. Daridon, V. Fascio, J. Lichtenberg, R. Wütrich, H. Langen, E. Verpoorte and N. de Rooij, *Fresenius J Anal Chem*, 2001, **371**, 261–269.
- 237 A. Manz, D. J. Harrison, E. M. J. Verpoorte, J. C. Fettinger, A. Paulus, H. Lüdi and H. M. Widmer, *J. Chromatogr.*, 1992, **593**, 253–258.
- 238 P. Pal and K. Sato, *J. Micromechanics Microengineering*, 2009, **19**, 1–11.
- 239 K. F. Lei, in *Microfluidics in Detection Science*, eds. F. H. Labeed and H. O. Fatoyinbo, RSC, Cambridge, UK, 2014, pp. 1–28.
- 240 C. Iliescu, H. Taylor, M. Avram, J. Miao and S. Franssila, *Biomicrofluidics*, 2012, **6**, 1–16.
- 241 K. Ren, J. Zhou and H. Wu, *Acc. Chem. Res.*, 2013, **46**, 2396–2406.
- 242 S. K. Y. Tang and G. M. Whitesides, in *Optofluidics: Fundamentals, Devices, and Applications*, eds. Y. Fainman, D. Psaltis and C. Yang, McGraw-Hill Companies, Inc., NY, USA, 2010, pp. 7–32.
- 243 S. Richter, N.-T. Nguyen and A. Wego, in *Microfluidics and BioMEMS Applications*, ed. F. E. Tay, Springer Science+Business Media, LLC, Dordrecht, Netherlands, 2002, pp. 186–187.
- 244 H. Becker and L. E. Locascio, *Talanta*, 2002, **56**, 267–287.
- 245 R. J. Jackman, T. M. Floyd, R. Ghodssi, M. A. Schmidt and K. F. Jensen, *J. Micromechanics Microengineering*, 2001, **11**, 263–269.
- 246 J. C. McDonald and G. M. Whitesides, *Acc. Chem. Res.*, 2002, **35**, 491–499.
- 247 K. Kamei, Y. Mashimo, Y. Koyama, C. Fockenber, M. Nakashima, M. Nakajima, J. Li and Y. Chen, *Biomed. Microdevices*, 2015, **17**, 1–8.

- 248 Z. Isiksacan, M. T. Guler, B. Aydogdu, I. Bilican and C. Elbuken, *J. Micromech. Microeng.*, 2016, **26**, 1–13.
- 249 D. C. Duffy, J. C. McDonald, O. J. A. Schueller and G. M. Whitesides, *Anal. Chem.*, 1998, **70**, 4974–4984.
- 250 J. C. McDonald, D. C. Duffy, J. R. Anderson and D. T. Chiu, *Electrophoresis*, 2000, **21**, 27–40.
- 251 C. T. Culbertson, T. G. Mickleburgh, S. A. Stewart-James, K. A. Sellens and M. Pressnall, *Anal. Chem.*, 2014, **86**, 95–118.
- 252 L. R. Volpatti and A. K. Yetisen, *Trends Biotechnol.*, 2014, **32**, 347–350.
- 253 M. I. Mohammed, S. Haswell and I. Gibson, *Procedia Technol.*, 2015, **20**, 54–59.
- 254 M. L. Givner and G. Schilling, Pregnancy test device, United States, Patent number: US4033723A, 05/07/1977.
- 255 A. H. Clemens, Reflectance meter, United States, Patent number: US3604815A, 14/09/1971.
- 256 G. Wu and M. H. Zaman, *Bull. World Heal. Organ.*, 2012, **90**, 914–920.
- 257 F. White, Method and device for collecting, transporting and delivering micro samples of blood, United States, Patent number: US4393882A, 19/07/1983.
- 258 A. K. Au, W. Lee and A. Folch, *Lab Chip*, 2014, **14**, 1294–1301.
- 259 J. P. Rolland, R. M. Van Dam, D. a. Schorzman, S. R. Quake and J. M. DeSimone, *J. Am. Chem. Soc.*, 2004, **126**, 2322–2323.
- 260 A. Waldbaur, H. Rapp, K. Länge and B. E. Rapp, *Anal. Methods*, 2011, **3**, 2681–2716.
- 261 A. W. Martinez, S. T. Phillips, G. M. Whitesides and E. Carrilho, *Anal. Chem.*, 2010, **82**, 3–10.
- 262 D. J. Guckenberger, T. E. DeGroot, A. M. D. Wan, D. J. Beebe and E. W. K. Young, *Lab Chip*, 2015, **15**, 2364–2378.
- 263 U. M. Attia, S. Marson and J. R. Alcock, *Microfluid. Nanofluidics*, 2009, **7**, 1–28.
- 264 C. W. Hull, Apparatus for production of three-dimensional objects by stereolithography, United States, Patent number: 4575330A, 11/03/1986.
- 265 T. Wohlers, *Wohlers Report 2017: 3D Printing and Additive Manufacturing State of the Industry Annual Worldwide Progress Report*, Wohlers Association Inc., Fort Collins, CO, USA, 2017.
- 266 C. Barnatt, *3D Printing: The Next Industrial Revolution*, CreateSpace, Charleston, SC, 2013.
- 267 Z. Liu, M. Zhang, B. Bhandari and Y. Wang, *Trends Food Sci. Technol.*, 2017, **69**, 83–94.
- 268 Y. L. Yap and W. Y. Yeong, *Virtual Phys. Prototyp.*, 2014, **9**, 195–201.
- 269 P. Kocovic, in *3D Printing and Its Impact on the Production of Fully Functional Components: Emerging Research and Opportunities*, IGI Global, Hershey, PA, USA, 2017, p. 86.
- 270 S. Hoskins, *3D Printing for Artists, Designers and Makers*, Bloomsbury Publishing Plc, London,

- UK, 2013.
- 271 J. M. Zuniga, A. M. Carson, J. M. Peck, T. Kalina, R. M. Srivastava and K. Peck, *Prosthet. Orthot. Int.*, 2017, **41**, 205–209.
- 272 C. L. Ventola, *Pharm. Ther.*, 2014, **39**, 704–711.
- 273 K. Sun, T. Wei, B. Y. Ahn, J. Y. Seo, S. J. Dillon and J. A. Lewis, *Adv. Mater.*, 2013, **25**, 4539–4543.
- 274 S. A. Khaled, J. C. Burley, M. R. Alexander, J. Yang and C. J. Roberts, *Int. J. Pharm.*, 2015, **494**, 643–650.
- 275 D. T. Nguyen, C. Meyers, T. D. Yee, N. A. Dudukovic, J. F. Destino, C. Zhu, E. B. Duoss, T. F. Baumann, T. Suratwala, J. E. Smay and R. Dylla-Spears, *Adv. Mater.*, 2017, **29**, 1–5.
- 276 5121329, 1992.
- 277 R. Jones, P. Haufe, E. Sells, P. Iravani, V. Olliver, C. Palmer and A. Bowyer, *Robotica*, 2011, **29**, 177–191.
- 278 I. Gibson, D. Rosen and B. Stucker, in *Additive Manufacturing Technologies: 3D Printing, Rapid Prototyping, and Direct Digital Manufacturing*, Springer, NY, USA, 2nd edn., 2015, pp. 147–174.
- 279 T. Grimm, *User's Guide to Rapid Prototyping*, Society of Manufacturing Engineers, Dearborn, Michigan, US, 2004.
- 280 T. Wohlers, *Wohlers Report 2016: 3D Printing and Additive Manufacturing State of the Industry*, Wohlers Association Inc., Fort Collins, CO, USA, 2016.
- 281 B. C. Gross, J. L. Erkal, S. Y. Lockwood, C. Chen and D. M. Spence, *Anal. Chem.*, 2014, **86**, 3240–3253.
- 282 C. K. Chua and K. F. Leong, *3D Printing and Additive Manufacturing: Principles and Applications*, World Scientific Publishing Co. Pte. Ltd., Singapore, 5th edn., 2017.
- 283 D. R. White, *Adv. Mater. Process*, 2003, **161**, 64–65.
- 284 C. Y. Kong, R. C. Soar and P. M. Dickens, *Compos. Struct.*, 2004, **66**, 421–427.
- 285 G. D. J. Ram, Y. Yang and B. E. Stucker, *J. Manuf. Syst.*, 2006, **25**, 221–238.
- 286 F. W. Liou, *Rapid Prototyping and Engineering Applications: A Toolbox for Prototype Development*, CRC Press, Boca Raton, FL, USA, 2007.
- 287 D. Prasad, *Int. J. Adv. Ind. Eng.*, 2015, **3**, 115–119.
- 288 R. Liska, M. Schuster, R. Inführ, C. Turecek, C. Fritscher, B. Seidl, V. Schmidt, L. Kuna, A. Haase, F. Varga, H. Lichtenegger and J. Stampfl, *J. Coatings Technol. Res.*, 2007, **4**, 505–510.
- 289 E. M. Sachs, J. S. Haggerty, M. J. Cima and P. A. Williams, Three-dimensional printing techniques, United States, Patent number 5204055A, 20/04/1993.

- 290 R. Bogue, *Assem. Autom.*, 2014, **33**, 307–311.
- 291 A. Rosochowski and A. Matuszak, *J. Mater. Process. Technol.*, 2000, **106**, 191–198.
- 292 J. Park, M. J. Tari and H. T. Hahn, *Rapid Prototyp. J.*, 2000, **6**, 36–49.
- 293 M. Feygin, Apparatus and method for forming an integral object from laminations, United States, Patent number: 4752352A, 21/06/1998.
- 294 I. Gibson, in *Handbook of Manufacturing Engineering and Technology*, ed. A. Nee, Springer Verlag, London, 2013, pp. 2551–2552.
- 295 A. Lee, *Lab Chip*, 2013, **13**, 1660–1661.
- 296 P. Tseng, C. Murray, D. Kim and D. Di Carlo, *Lab Chip*, 2014, **14**, 1491–1495.
- 297 A. K. Au, N. Bhattacharjee, L. F. Horowitz, T. C. Chang and A. Folch, *Lab Chip*, 2015, **15**, 1934–1941.
- 298 P. F. O’Neill, A. Ben Azouz, M. Vázquez, J. Liu, S. Marczak, Z. Slouka, H. C. Chang, D. Diamond and D. Brabazon, *Biomicrofluidics*, 2014, **8**, 1–24.
- 299 D. Olvera-Trejo and L. F. Velásquez-garcía, *Lab Chip*, 2016, **16**, 4121–4132.
- 300 J. Kerns, 3D Printing Dives into Mass Production [online], 2017 [Accessed 25/08/17]. Available from: <https://www.machinedesign.com/3d-printing/3d-printing-dives-mass-production>.
- 301 N. Walker, Formlabs to help make 3D printing more accessible for SMEs [online], 2017 [Accessed 01/11/2017]. Available from: <http://www.manufacturingglobal.com/lean-manufacturing/formlabs-help-make-3d-printing-more-accessible-smes>.
- 302 G. Comina, A. Suska and D. Filippini, in *Proceedings Volume 10061 Microfluidics, BioMEMS, and Medical Microsystems XV*, San Francisco, US, 2017, vol. 100610E.
- 303 J. K. Hohmann, M. Renner, E. H. Waller and G. von Freymann, *Adv. Opt. Mater.*, 2015, **3**, 1488–1507.
- 304 M. J. Beauchamp, G. P. Nordin and A. T. Woolley, *Anal. Bioanal. Chem.*, 2017, **409**, 4311–4319.
- 305 V. Dragone, V. Sans, M. H. Rosnes, P. J. Kitson and L. Cronin, *Beilstein J. Org. Chem.*, 2013, **9**, 951–959.
- 306 P. J. Kitson, M. H. Rosnes, V. Sans, V. Dragone and L. Cronin, *Lab Chip*, 2012, **12**, 3267–3271.
- 307 P. J. Kitson, M. D. Symes, V. Dragone and L. Cronin, *Chem. Sci.*, 2013, **4**, 3099–3103.
- 308 G. W. Bishop, J. E. Satterwhite-Warden, I. Bist, E. Chen and J. F. Rusling, *ACS Sens.*, 2016, **1**, 197–202.
- 309 G. W. Bishop, J. E. Satterwhite, S. Bhakta, K. Kadimisetty, K. M. Gillette, E. Chen and J. F. Rusling, *Anal. Chem.*, 2015, **87**, 5437–5443.
- 310 J. L. Erkal, A. Selimovic, B. C. Gross, S. Y. Lockwood, E. L. Walton, S. McNamara, R. S. Martin

- and D. M. Spence, *Lab Chip*, 2014, **14**, 2023–2032.
- 311 M. E. Snowden, P. H. King, J. A. Covington, J. V Macpherson and P. R. Unwin, *Anal. Chem.*, 2010, **82**, 3124–3131.
- 312 A. J. Capel, A. Wright, M. J. Harding, G. W. Weaver, Y. Li, R. A. Harris, S. Edmondson, R. D. Goodridge and S. D. R. Christie, *Beilstein J. Org. Chem.*, 2017, **13**, 111–119.
- 313 A. J. Capel, S. Edmondson, S. D. R. Christie, R. D. Goodridge, R. J. Bibb and M. Thurstans, *Lab Chip*, 2013, **13**, 4583–90
- 314 G. Gaal, M. Mendes, T. P. De Almeida, M. H. O. Piazzetta, Â. L. Gobbi, A. Riul Jr and V. Rodrigues, *Sens. Actuators B Chem.*, 2017, **242**, 35–40.
- 315 S. A. N. Gowers, V. F. Curto, C. A. Seneci, C. Wang, S. Anastasova, P. Vadgama, G.-Z. Yang and M. G. Boutelle, *Anal. Chem.*, 2015, **87**, 7763–7770.
- 316 L. Krejcova, L. Nejdil, M. A. M. Rodrigo, M. Zurek, M. Matousek, D. Hynek, O. Zitka, P. Kopel, V. Adam and R. Kizek, *Biosens. Bioelectron.*, 2014, **54**, 421–427.
- 317 M. Paknahad, J. S. Bachhal, A. Ahmadi and M. Hoorfar, *Sens. Actuators B Chem.*, 2017, **241**, 55–64.
- 318 S. Takenaga, B. Schneider, E. Erbay, M. Biselli, T. Schnitzler, M. J. Schöning and T. Wagner, *Phys. Status Solidi Appl. Mater. Sci.*, 2015, **212**, 1347–1352.
- 319 T. Monaghan, M. J. Harding, R. A. Harris, R. J. Friel and S. D. R. Christie, *Lab Chip*, 2016, **16**, 3362–3373.
- 320 R. Walczak and K. Adamski, *J. Micromech. Microeng.*, 2015, **25**, 1–13.
- 321 R. Lawes, in *MEMS Cost Analysis: From Laboratory to Industry*, CRC Press, Boca Raton, FL, USA, 2013, pp. 147–148.
- 322 R. W. Welker, R. Nagarajan and C. E. Newberg, in *Contamination and ESD Control in High-Technology Manufacturing*, John Wiley & Sons Inc., Hoboken, NJ, USA, 2006, pp. 158-194.
- 323 Mecart Cleanrooms, Costing a Cleanroom Per Square Foot [online], 2018 [Accessed 20/08/19]. Available from: https://www.cleanroomtechnology.com/news/article_page/Costing_a_cleanroom_per_square_foot/139470.
- 324 Elsevier B.V., Electron Beam Lithography [online], 2019 [Accessed 19/08/19]. Available from: <https://www.sciencedirect.com/topics/engineering/electron-beam-lithography>.
- 325 D. Pranzo, P. Larizza, D. Filippini and G. Percoco, *Micromachines*, 2018, **9**, 1-27.
- 326 Compugraphics, FAQs: How Long Will It Take to Get My Mask? [online], 2017 [Accessed 19/08/19]. Available from: <https://www.compugraphics-photomasks.com/education-centre/faqs/?fbclid=IwAR3thMOztJ3mRexg0B1h412mQtsTQi7oIQk37BAw6DRe7BJFr3avJXTs2bc>.

- 327 Digits2Widgets, SLA Resin Fastest Production Time [online], 2018 (Accessed 19/08/19). Available from: <https://www.digits2widgets.com/sla-resin-3d-printing/>.
- 328 M.A. Lake, C. E. Narciso, K. R. Cowdrick, T. J. Storey, S. Zhang, J. J. Zartman, and D. J. Hoelzle, 'Microfluidic device design, fabrication, and testing protocols', *ProtocolExchange* [online], Preprint, 2015 [Accessed 19/08/2019]. Available from: <https://protocolexchange.researchsquare.com/article/nprot-4049/v1>.
- 329 J. Friend and L. Yeo, *Biomicrofluidics*, 2010, **4**, 1-5.
- 330 P. Mukherjee, F. Nebuloni, H. Gao, J. Zhou and I. Papautsky, *Micromachines*, 2019, **10**, 1-11.
- 331 R. Robbins, Photomask Making (Document Number: SP-07-001) [online], 2007 [Accessed 19/09/19]. Available from: <https://personal.utdallas.edu/~rar011300/LithographyProcess/PhotomaskMaking.pdf>.
- 332 Elsevier B.V., Electron Beam Lithography [online], 2019 [Accessed 19/08/19]. Available from: <https://www.sciencedirect.com/topics/materials-science/electron-optical-lithography>.
- 333 K. Li, J. Li, C. Reardon, C. S. Schuster, Y. Wang, G. J. Triggs, N. Damnik, J. Muenchenberger, X. Wang, E. R. Martins and T. F. Krauss, *Sci. Rep.*, 2016, **6**, 1-10.
- 334 Y. Wu, Y. Ren, Y. Tao, L. Hou and H. Jiang, *Anal. Chem.*, 2016, **88**, 11791-11798.
- 335 L.-H. Chau, W. Liang, F. Wing, K. Cheung, W. K. Liu, W. J. Li, S.-C. Chen and G.-B. Lee, *PLoS ONE*, 2013, **8**, 1-8.
- 336 S. C. Bürgel, Z. Zhu, N. Haandbæk, O. Frey, and A. Hierlemann, in Proceedings of the 25th IEEE International Conference on Micro Electro Mechanical Systems (MEMS), IEEE, Paris, 2012, pp. 1033-1036.
- 337 P. Ertl and R. Heer, *Elektrotech. Inftech.*, 2009, **126**, 47-50.
- 338 M.-H. Wang, M.-F. Kao, and L.-S. Jang, *Rev. Sci. Instrum.*, 2011, **82**, 1-11.
- 339 L. Huang, L. Tu, X. Zeng, L. Mi, X. Li, and W. Wang, *Micromachines*, 2016, **7**, 1-13.
- 340 A. S. Rane, J. Rutkauskaitė, A. deMello and S. Stavrakis, *Chem*, 2017, **3**, 588–602.
- 341 J.-L. Fraikin, T. Teesalu, C. M. McKenney, E. Ruoslahti and A. N. Cleland, *Nat. Nanotechnol.*, 2011, **6**, 308–313.
- 342 Y. Song, J. Yang, X. Pan and D. Li, *Electrophoresis*, 2015, **36**, 495–501.
- 343 Y. Song, H. Zhang, C. H. Chon, S. Chen, X. Pan and D. Li, *Anal. Chim. Acta*, 2010, **681**, 82–86.
- 344 B.R. Watts, Z. Zhang, C. Q. Xu, X. Cao and M. Lin, *Electrophoresis*, 2013, **35**, 271–281.
- 345 C. Mu, F. Zhang, Z. Zhang, M. Lin and X. Cao, *Sens. Actuators B Chem.*, 2011, **151**, 402–409.
- 346 D. Barat, D. Spencer, G. Benazzi, M. C. Mowlem and H. Morgan, *Lab Chip*, 2012, **12**, 118-126.
- 347 Y. Song, J. Wang, J. Yang, Y. Wu, N. Li, N. Gong, X. Pan, Y. Sun and D. Li, *Instrum. Sci. Technol.*, 2012, **40**, 305-315.

- 348 Malvern Panalytical Ltd., Insittec® Process [online], 2007 [Accessed 25/07/2019]. Available from: <http://pdf.directindustry.com/pdf/malvern-panalytical/on-line-particle-characterization-overview-brochure/14669-149948.html>.
- 349 M. J. H. Gerritzen, D. E. Martens, R. H. Wijffels and M. Stork, *J. Extracell. Vesicles.*, 2017, **6**, 1-9.
- 350 Beckman Coulter Inc., The Coulter Principle [online], 2019 [Accessed 25/07/2019]. Available from: <https://www.mybeckman.uk/resources/fundamentals/history-of-flow-cytometry/the-coulter-principle>.
- 351 Malvern Panalytical Ltd., NanoSight NTA Concentration Measurement Upgrade [online], 2015 [Accessed 25/07/2019]. Available from: <https://cdn.technologynetworks.com/TN/Resources/PDF/AN150430NTAConcMeasUpgrade.pdf>.
- 352 H. Yang, J. Daly and T. R. Tiersch, *Cytom. A.*, 2016, **89**, 350-356.
- 353 B. Kim, D. Kang and S. Choi, *Sensors*, 2019, **19**, 1-12.
- 354 G. Tianyi, PhD thesis, McMaster University, 2016.
- 355 Beckman Coulter Inc., Vi-CELLXR Cell Viability Analyzer Reference Manual [online], 2011 [Accessed 22/07/2019]. Available from: <https://www.usf.edu/research-innovation/rf/usf-connect/documents/vi-cell-xr-beckman-coulter.pdf>.
- 356 Izon Science Ltd., qNano User Manual [online], 2018 [Accessed 24/07/2019]. Available from: <https://sydney.edu.au/medicine/bosch/facilities/molecular-biology/nanoparticle-analysis/qNano%20Users%20Manual.pdf>.

Chapter 2 Theory

2.1 Introduction

As discussed in Chapter One, the aim of the work described in this thesis is to develop additively manufactured microfluidic devices for particle/cell analysis. This chapter gives an overview of the general theory key to this aim. Additional detailed theory is included in each chapter where relevant.

2.2 Microfluidics

2.2.1 Microfluidic flow behaviour

The behaviour of fluid flows found inside macroscale systems (Figure 2.1 a) significantly deviates from that of microscale fluid flows (Figure 2.1 b), due to a drastically different ratio of two groups of fluidic forces to each other, coupled with a far higher surface-to-volume ratio.

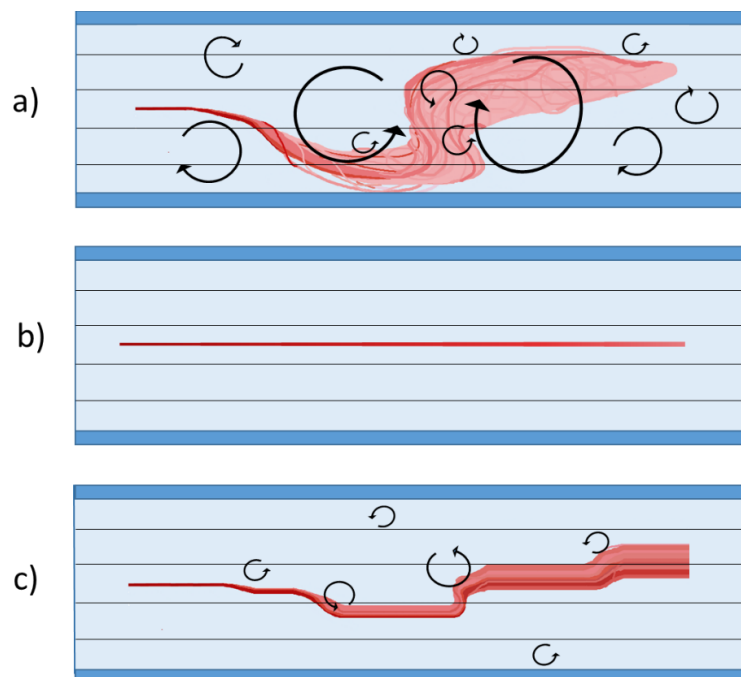


Figure 2.1 Illustration of dye tracer transport in a) turbulent flow as commonly seen in macroscale flow systems b) laminar flow as commonly seen in microfluidic flows and c) transitional flow. Streamlines are designated by straight black lines parallel to the mean flow. The dye trace is represented by a red line. Eddies are represented by curved black arrows.

Typical macroscale flows, such as fluids traversing pipes with centimetre scale diameters, can be described as being turbulent flow¹. Turbulent fluid motion features velocity fluctuations over time and in all three dimensions, caused by the presence of small and large disturbances in the form of eddies, sweeps and spontaneously occurring instabilities or irregular flows². In turbulent flow, molecular diffusion is insignificant compared to large-scale turbulent diffusion (also called eddy diffusion). A dye injected into a turbulent flow will immediately be mixed by the disorderly fluid particles and will rapidly disperse (Figure 2.1 a)—it will be carried along the path of general mean flow but will also be carried laterally across streamlines by large eddies, as well as being spread out (diffused) by smaller-scale stirring caused by smaller eddies.

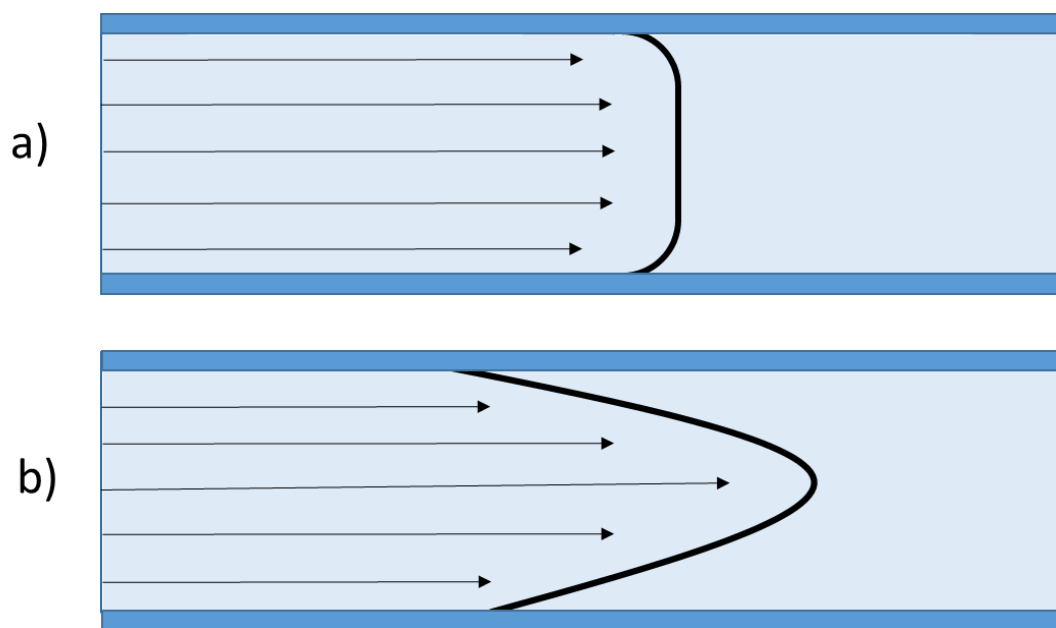


Figure 2.2 Illustrations of velocity flow profiles for a) turbulent flow and b) laminar flow³. Arrows represent the overall mean flow path.

The velocity flow profile for turbulent flow is flat³ (Figure 2.2 a)—namely, fluid flows at the same rate across the channel cross-section (with the exception of fluid flow adjacent to the channel wall, which is slightly slower). The velocity flow profile in turbulent flow is affected by channel roughness, with a rougher wall giving a less uniform flow velocity profile.

In contrast, microscale flow can take on much different behaviour, where fluid flow is extremely ordered. This is called laminar flow, as fluid flow travels in layers (lamina). Unlike turbulent flow, flow is smooth, steady and undisturbed—there is no macroscopic interchange of fluid particles between different layers, and dissimilar liquids can flow alongside one another for long distances without

significant mixing^{3,4}. In general, flow in microsystems is always laminar⁵. Dye molecules injected into a laminar flow will follow the streamlines exactly and have a neat, linear trace (Figure 2.1 b). Mixing with neighbouring fluid does not occur except by molecular diffusion, and so dye dispersion is very slow in comparison with turbulent flow. The velocity flow profile at any one section of a laminar flow is parabolic³ (Figure 2.2 b), with the velocity taken to be essentially 0 at the wall, and increasing with distance away from the wall until reaching the maximum velocity in the centre of the channel (for symmetrical channels).

These two contrasting fluid flow behaviours were outlined by Osborne Reynolds, who formally distinguished them by a dimensionless parameter known as Reynolds number, Re (Equation 2.1). Reynolds numbers states that a flow regime depends on three physical parameters: the flow field length of scale (e.g. the channel diameter), L , a velocity scale (e.g. the spatial average of the fluid velocity), V , and the kinematic viscosity, μ ⁶. The velocity scale is dictated by two parameters: v , the average fluid velocity, and ρ , the fluid density.

$$Re = \frac{\text{inertial forces}}{\text{viscous forces}} = \frac{VL}{\mu} = \frac{\rho vL}{\mu} \quad (2.1)$$

The flow field length and velocity scale make up the inertial forces, which can be thought of as the force due to the fluid momentum. Viscous forces arise from friction occurring between fluid layers. High Re values indicate the presence of flow disturbances, and typically, fluid flows with $Re > 4000$ are classified as turbulent flows. In turbulent flow, viscous forces are insignificant relative to the dominant inertial forces. Inertial forces are significant in macroscale flow, and so fluid flow at this scale features eddies and vortices. Laminar flow occurs at $Re < 2300$, but in systems with extremely smooth, vibration-free channel walls, values far higher have been reported⁶. In laminar flow, inertial effects are insignificant and viscous forces now dominate. Viscous forces dampen turbulent disturbances such as eddies. These viscous forces are frictional shear forces that arise from the relative motion of different fluid layers in a flowing liquid. Fluid flows with $2300 < Re < 4000$ are known as transitional flows. The upper and lower critical Reynolds numbers for this are affected by the degree of turbulent disturbances present, as well as channel surface roughness⁷. This type of flow can either be laminar or turbulent—in transitional flows, there are distinct regions of turbulent and laminar flow throughout a channel that fluctuate over time (Figure 2.1 c)⁸.

2.2.2 Particle transport in microfluidic flow

Particles suspended in a turbulent flow system will be channelled by the mean flow, but will also be dispersed across streamlines by turbulent eddies, etc. Thus, particle movement in turbulent flow is challenging to predict due to the presence of fine and large structures of turbulence present in addition to the large-scale motion of the dispersed phase^{9,10}. In contrast, similar for dye tracer transport, particle/cell transport in microfluidic flows is highly definable¹¹, predictable¹² and controllable¹³, allowing the creation of a great variety of microfluidic LOC devices for precise particle/cell handling and analysis as covered in Chapter 1. If no external forces are present, advection of neutrally buoyant particles in a laminar flow will be dominated by viscous forces, and the particles will follow fluid streamlines, at the velocity of the fluid¹³.

However, particles travelling in laminar flow will still experience numerous forces acting on them that can affect their position and advection. For example, they experience shear stresses that cause particle rotation: spherical particles rotate in a stable manner whilst non-spherical particles have chaotic or quasi-periodic rotation¹⁴. In addition, particles will also experience a number of forces involving lift, buoyancy, weight and drag that affect their height in the microchannel, and these forces greatly depend on particle density, size and fluid velocity¹⁵. Particles with a density equal to that of the fluid will not have a vertical velocity component and will remain at the same height, but denser particles will gradually sediment under gravity¹⁶. Interchange of particles across fluid streamlines can occur at high fluid velocities if inertial lift forces are introduced into the system, and this effect can be fine-tuned to allow precise particle manipulation—for example, curved channel geometries can be used to transport particles down precise paths¹³. Also, particles will undergo diffusion during advection, and the diffusion magnitude is a function of their size. Diffusion is only significant enough to move particles off streamline paths if particles are extremely small (in which case their location becomes stochastic)¹⁶.

2.3 Additively manufactured microfluidics

3D printing on the microscale has a number of unique challenges involved due to its intrinsic nature as an additive layering process. In AM, three-dimensional geometries are produced in a stepwise procedure via two-dimensional manufacturing stages. This additive fabrication process has a number of interrelated elements such as layer height, resolution, and dimensional accuracy.

2.3.1 Resolution

AM build resolution, the minimum possible detail dimension, is a critical factor in the quality of printed microfluidic devices. A key aspect of this resolution is layer thickness, which determines geometric resolution as well as surface qualities¹⁷, and is partly dictated by printer capabilities such as the smallest possible step actuatable by the system motor. Resolution-limiting factors across SLA and FDM are covered by Bhattacharjee¹⁸. In FDM, layer thickness is limited by the filament size extrudable by the nozzle diameter and the print head motor accuracy¹⁹. Resolution in SLA is dependent on the laser spot diameter, as well as the photoresin absorption spectra²⁰ and other properties that affect the photopolymerisation process such as resin laser penetration²¹ and photo-initiator and radical diffusion through the partially polymerised resin²⁰. Additionally, the minimum microchannel cross-sectional area made by SLA depends also on the photoresin type and viscosity²², as uncured resin must be thoroughly flushed from channels post-printing to prevent channel blockage or narrowing. Effective removal of uncured resin is the limiting factor in SLA printing of microfluidic devices, and restricts channel dimensions to values larger than the ~100 µm feature resolution possible by SLA printers²².

A related technique with submicron resolution is multiphoton stereolithography, which utilises a highly focused, high-intensity pulsed laser²³. However, as a microfluidic device fabrication method it is very expensive, with a femtosecond laser system being 3–6 times as expensive as a Nd:YAG, CO₂, etc. systems, as well as time-consuming²⁴.

2.3.2 Staircase effect

In 3D printing, due to its nature as an additive process, curved features are converted to topographies comprising straight edges. This phenomenon is a side effect of the layer-wise slicing and printing processes, and is known as the “staircase effect” (Figure 2.3). It occurs at angled part surfaces (surfaces that are not parallel or perpendicular to the build-direction) and is due to the limited geometric resolution of 3D printing making only an approximation of the intended part contour possible. The staircase effect causes greater surface roughness at angles to the build platform¹⁷, and is a major source of error in 3D printing²⁵, including SLA²⁶. The degree of stair-stepping increases with layer thickness²⁷, and with a decrease in part angle²⁶.

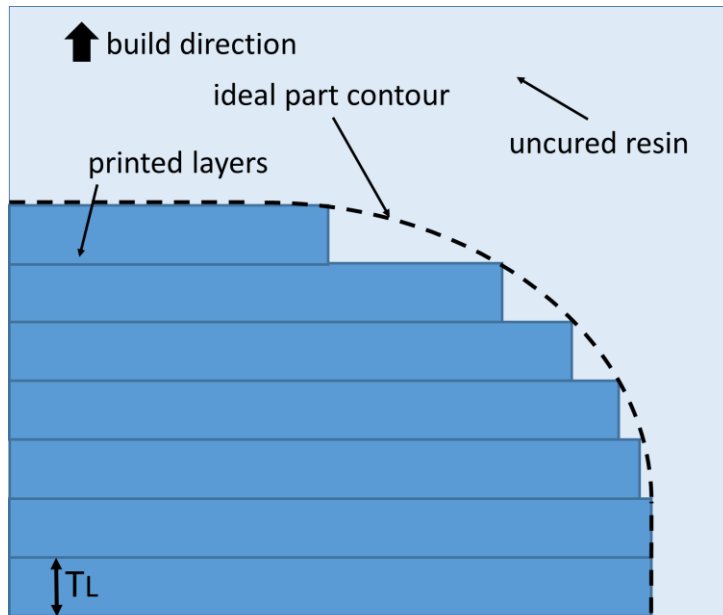


Figure 2.3 Illustration of the staircase effect occurring on a curved part surface in SLA. TL=layer height. The effect is greater at smaller part angles.

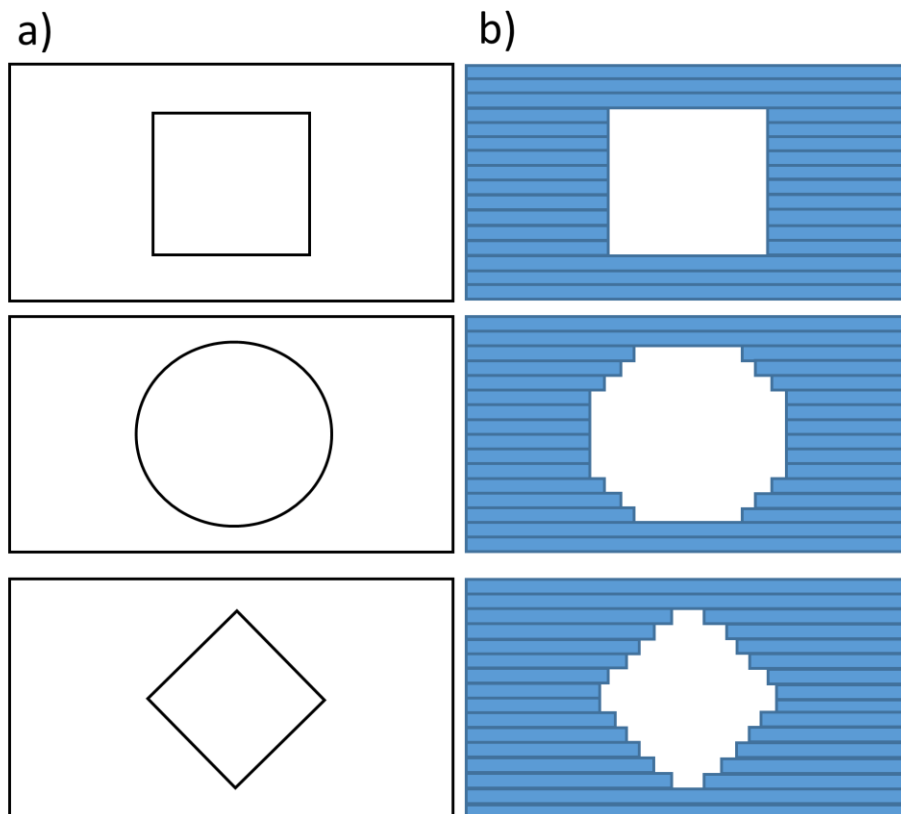


Figure 2.4 Illustration of the effects on different shapes of microchannels by AM: a) microchannel cross-sectional outlines and b) corresponding resultant AM structures, showing build layers.

In macrosized objects it affects surface roughness, but on the microscale this effect is far more significant as the dimensions are on the same scale, and so it can effectively transform the shape of very small channels²⁸. For example, it causes curved microchannels to take angular forms^{28,29}, as illustrated in Figure 2.4. Here, square microchannels are unchanged in shape by the AM process, but circular microchannels and microchannels with diagonal walls have stepped edges.

2.3.3 Support structures

Support structures prevent bulk material fall-in at overhanging sections, i.e. structures built horizontal to the build direction. They are sacrificial material used as base layers to print overhangs onto, and usually consist of thin, lattice-like structures¹⁷. They are removed post-printing, either physically (for example by snapping off and sanding, if printed in the same material as the object) or chemically (by dissolution in a solvent, if printed in a different material to the object). Their physical removal is a source of surface roughness³⁰.

AM techniques that print using powder (such as SLS and binder jetting) do not need support structures as the surrounding powder gives support during the build. Support structures in SLA require physical removal, whilst FDM is capable of both support structure types, as multi-printhead printers can build in more than one material.

2.3.4 SLA overhangs

Another source of dimensional and shape error is laser over-curing. This effect is found in overhangs built by laser-based forms of 3D printing such as SLA. These overhangs suffer from fall-in and have a lower depth than nominal that is typically at least 4x greater than the layer thickness²⁹ (Figure 2.5). Laser overcure arises due to two reasons: firstly, due to the high power of the laser involved in SLA, curing normally reaches deeper than the desired cure depth³¹. This leads to an extra, lower layer(s) being cured when curing the bottom-most layer of an overhanging part (below which is liquid resin, instead of the previously cured layer or the stage). Secondly, cured resin can be adequately transparent to the UV laser so as to permit the laser to penetrate through to the resin below the already extra cured layers³¹.

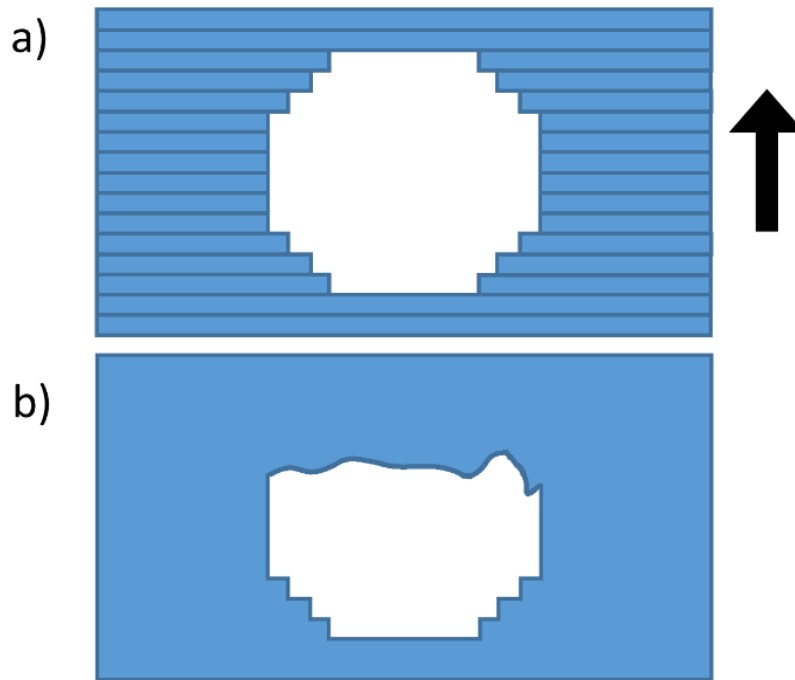


Figure 2.5 Illustration of laser overcure occurring in microchannel cross-section: a) intended build of microchannel with build direction outlined, and b) subsequent printed channel with laser-overcure occurring on microchannel ceiling²⁹.

Additionally, overhangs in SLA suffer from extra surface roughness due to gravity—polymerised resin is heavier than uncured resin, and as overhanging resin cures it sags down, causing a roughness²⁹ that makes optical microscopy harder²².

2.3.5 Build direction

Build direction, formally defined as the perpendicular vector to each of the successive layers^{32,33}, is the direction in which a part is printed in relation to the build bed. Build direction is a critical factor unique to 3D printing that affects build time^{30,34,35}, material used (due to differing support structure volumes)³⁵ and thus, part cost³⁵, therefore is an important factor in the mass production of printed parts. Furthermore however, it also affects part properties such as compressive³⁶ and tensile strength³⁷, and on the microscale, when feature sizes are of comparable size to layer thickness, it drastically affects dimensional and shape accuracy, by dictating the degree of stair-stepping³⁸, and, in SLA, laser overcure and microchannel ceiling/wall roughness. This is because build direction dictates the locations of the staircase effect and overhangs (and so, support structure volume and locations³⁹).

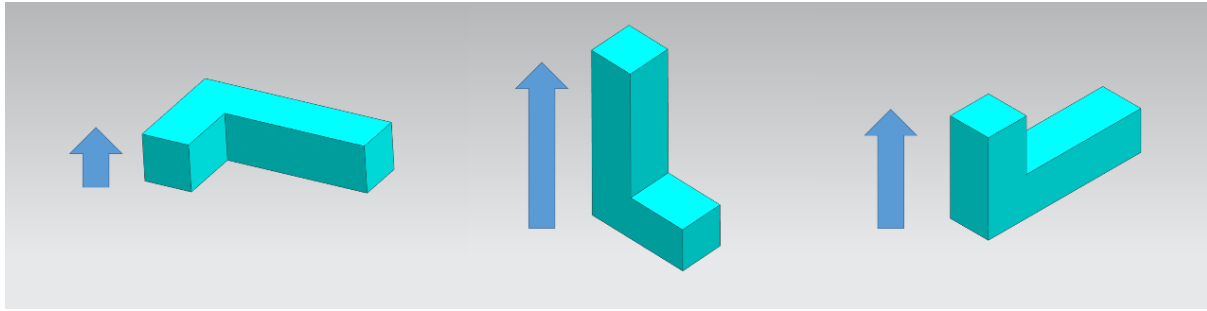


Figure 2.6 Illustration depicting the three possible build directions for an object.

An illustration of the three possible build directions for an object is shown in Figure 2.6. Note that each direction also has two further printing iterations: they can each be printed upside down.

2.3.6 Effects on laminar flow by microchannel errors

Due to the newness of the field of 3D printed microfluidics, the effects of printed dimensional errors and surface roughness on the performance of additively-manufactured microfluidic devices (in terms of how they affect laminar flow, etc.) are little-studied^{40,41}.

2.3.6.1 Dimensional errors

Dimensional errors are deviance between CAD (or .STL) file feature dimensions and the resulting printed part, caused by printer capability limitations and the aforementioned factors of the staircase effect, support structure use and removal, and laser overcure. The effect on laminar flow behaviour by microchannel dimensional errors can be insignificant if the flow rate is altered to compensate, even for deviance by a few hundred microns, as the hydrodynamic regime is dictated by Re (as in Equation 2.1). For example, the degree of fluid mixing in a 100 μm wide channel and a 500 μm wide channel will be identical as long as the flow of the latter is slowed by a factor of 5 (which would give an identical value of Re)⁴¹. However, if dimensional errors are not uniform throughout a microchannel then there will be velocity disruptions, especially with channel constrictions, which are greater with increased flow rate⁴².

2.3.6.2 Surface roughness

Microchannel surface roughness increases frictional wall shear stresses in microfluidic flow^{43,44}. Velocity perturbations are created over areas of channel roughness that can merge and combine to

create larger plumes of disturbance at distance from the channel wall⁴⁵. In addition, the presence of surface roughness lowers the critical Re number, allowing transition to turbulent flow to occur at Re values as low as ~300 instead of the usual 2300, and also narrows the transitional flow range^{46,47}. There are very few papers that investigate surface roughness effects on device performance in 3D printed microchannels. Lee, et al. measured surface roughness in printed channels and theorised that it would affect device performance⁴¹. Folch, et al. suggested that the varying topographies between two build directions create different disturbances in flow profiles in a focusing junction²². Macdonald, et al. printed simple Y-shaped mixing junctions via FDM, material jetting, and SLA, and measured the levels of mixing in each of two dyed solutions, finding that SLA had mixing that was 24x and 9x that of FDM and polyjet, respectively⁴⁸. The sole dedicated investigation into the effect of roughness on printed microchannel flow dynamics was by Lade, et al., who investigated capillary flow microchannels in FDM, SLA, SLM and multijet printing⁴⁰, and found that periodic channel roughness stemming from the AM process caused regular stop-start fluid velocity fluctuations. However, spontaneous capillary flow dynamics are not directly comparable to pump-driven microfluidic flow.

2.4 Additive manufacturing by stereolithography

There are two forms of SLA: the earliest, developed by 3D Systems, is the free surface or “bath” form (Figure 2.7 a), where the part is built at the resin/air interface at the top of the bath by a scanning laser system⁴⁹. Here, the laser scans over the bath surface and the stage translates downwards into the resin. A more recent form of SLA is the constrained surface or “bat” configuration (Figure 2.7 b), where the part is built at the bottom of the resin bath by pattern projection⁴⁹. In this form, the metal build plate is suspended inside the bath and translated upwards, with the part built upside-down before being drawn up and out. This approach is commonly used by DLP (digital light printing) SLA printers. The bath configuration has superior structural fidelity over the bat form, as the latter can cause stress fractures or feature bending as well as increased interlayer surface roughness due to its mechanical stage-separation step¹⁸. On the other hand, printing is quicker in the bat form as curing time is accelerated due to the lack of oxygen (in the bath form, photopolymerisation reaction happens at the air-resin interface and is inhibited by oxygen)¹⁸. Also, the object height is limited by the vat depth in the bath form of SLA, whilst the bat form has no such limit¹⁸.

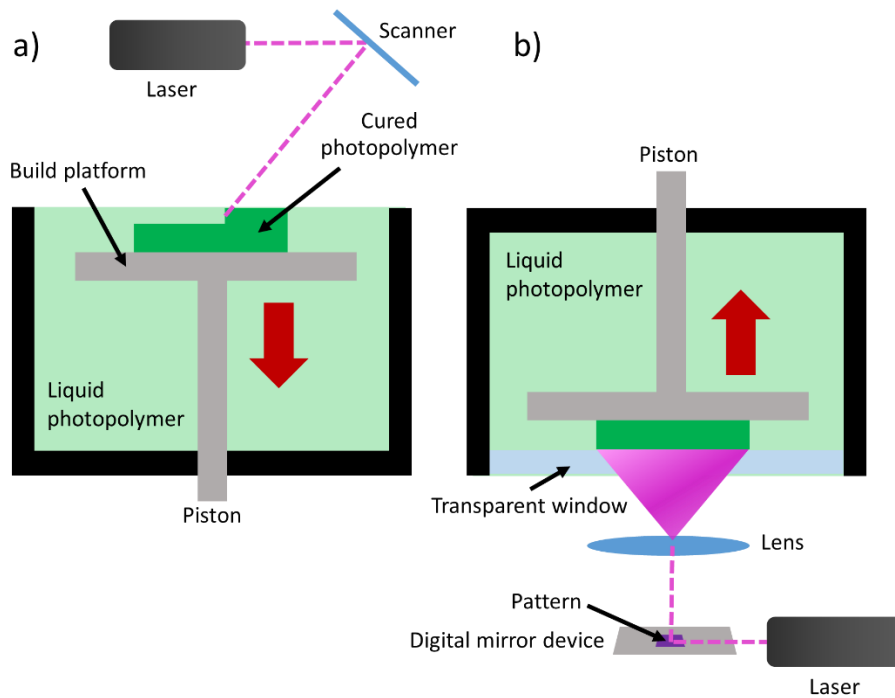


Figure 2.7 Illustration of two main configurations of SLA: a) free surface, or “bath” configuration and b) constrained surface, or “bat” configuration. Build platform movement during build is denoted by red arrow.

2.5 Optical flow cytometry

Optical flow cytometry involves two key processes: hydrodynamic focusing, where cells (or other species such as particles) are focused into single-file by flow constriction, and optical detection, which involves laser excitation and a series of optical filters and mirrors for an analysis at different wavelengths.

2.5.1 Hydrodynamic focusing

Hydrodynamic focusing is a procedure where a central (‘core’) sample stream of cells or particles is sheathed by an inert fluid, focusing the sample flow down to a single-file⁵⁰. This has two purposes: firstly, a single-file flow of sample is required for reliable measurements. Secondly, having a *sheathed* central flow prevents species sedimentation onto the channel walls. The hydrodynamic focusing process relies on the sheath and sample flows being laminar on meeting in order to ensure no mixing occurs⁵¹, and the focused core stream diameter being narrow enough relative to the species of interest to ensure formation of a single-file stream. Sample injection in flow cytometry is typically into the

centre of a 'sheath flow' inside a focusing chamber, which both narrows and accelerates the core sample flow (Figure 2.8).

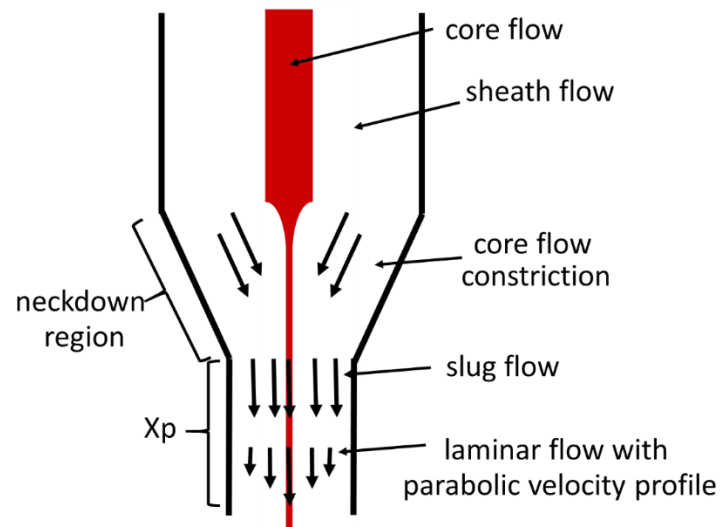


Figure 2.8 Schematic of flow cytometry hydrodynamic focusing process inside flow focusing chamber.

The flow focusing chamber has a portion where its cross-section is gradually decreased, named the neckdown region. As the cross-section narrows, the flow velocity increases. In this region, the core stream diameter can be tailored by control of the relative volume flow rates of the core and sheath flows. The aim is to form a core of narrow enough diameter to ensure that cells flow through the interrogation zone one at a time. In addition, features that will generate turbulence in the neckdown region such as sharp edges and/or sudden changes in channel diameter must be avoided, and so a gentle conical taper of 30° is usually used for this region⁵¹. Immediately after this portion is an area of flow called slug flow, where the velocity flow profile is near constant across virtually the entire cross section. This section has the length X_p , which is the distance that the fluid must flow before reestablishment of the parabolic flow profile⁵¹. For a laminar flow of water in a cylindrical capillary at 20°C, this distance in mm is defined by Equation 2.2⁵¹, where d =diameter of the constricted outlet tube (mm), v =mean fluid velocity over the tube cross-section (mm/s). Thus, X_p is longer for larger channel diameters.

$$X_p = 6 \times 10^{-5} d^2 v \quad (2.2)$$

Optical detection inside the X_p , slug flow, region is advantageous in that velocity differences between cells/particles at differing distances from the core axis will be minimised⁵¹.

2.5.2 Optical detection

After hydrodynamic focusing, the focused, single-file sample stream is analysed in a field of view called the interrogation zone or measurement region. For reliable data to be obtained, particle/cell trajectories must be almost identical as they pass the interrogation zone, and for this a stable, laminar flow pattern must be maintained⁵¹.

In benchtop flow cytometry, which commonly analyses fluorescently-labelled cells, the optical detection system can consist of a laser(s), dichroic, filters, beam stop, and a photodetector such as a photodiode. Two detection configurations are used, the first of which being FSC, where a beam stop in the form of an obstruction element or slit is used to block the detector from direct laser light, and low-angle ($\sim 0.5^\circ$) scattered light is detected⁵². By comparison with calibration beads of known size, the area or diameter of cells can be measured. Secondly, for SSC detection and fluorescence detection, light is collected at 90° to the incident laser beam and a number of optics elements are used to manipulate and process the outbound light from the sample, such as dichroic mirrors, bandpass filters and beam attenuators. SSC looks at laser light that is scattered by intracellular particulates such as the cell membrane and nucleus, thus giving a measure of cell granularity⁵². By measuring both FSC and SSC, cell subpopulations can be distinguished.

2.5.3 Microfluidic optical flow cytometry

Traditional cytometers carry out hydrodynamic focusing by the situating of a glass capillary inside a larger tube. Although this is a very effective sample introduction method into sheath flow, such a structure is extremely hard to microfabricate⁵³. Thus, hydrodynamic focusing in microfluidic flow cytometers is typically carried out by a simple four-way microchannel intersection (Figure 2.9) all on the same plane, where two incoming sheath streams squeeze a central sample flow in order to narrow it into a thinner, focused core stream^{50,53}.

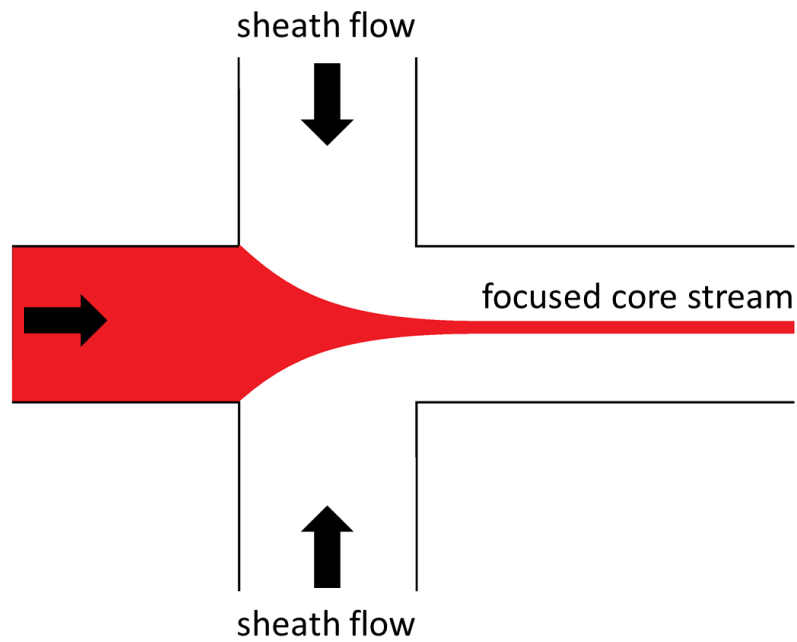


Figure 2.9 Typical two-dimensional hydrodynamic focusing junction as used in microfluidic systems.

The process of hydrodynamic focusing has been used in microfluidic systems for two decades, with Knight describing a silicon wafer device for hydrodynamic focusing in 1998⁵⁴. Since then the field of microfluidic flow cytometers has greatly expanded^{53,55,56}. Both optical⁶¹ (including that via integrated optical fibres⁶²⁻⁶⁴, and fluorescence⁶⁰) and impedance⁵⁷⁻⁵⁹ detection systems have been utilised in these devices. Microfluidic flow cytometers detect individual particles as discrete pulses, whose width and geometry are functions of the particle velocity and length of the interrogation region⁵³.

2.6 Resistive pulse sensing

Like optical flow cytometry, RPS also analyses particles in the form of signal pulses. It can determine particle size and concentration, in addition to charge characteristics⁶⁵⁻⁶⁷. Its configuration involves a small insulating orifice located between a pair of electrodes, through which there is a steady flow of electrolyte solution. This conducting solution is either driven through the orifice via a pump system or other form of applied pressure, or is left to diffuse across. Figure 2.10 shows an example of a microfluidic RPS junction, with constrictive pore channel region.

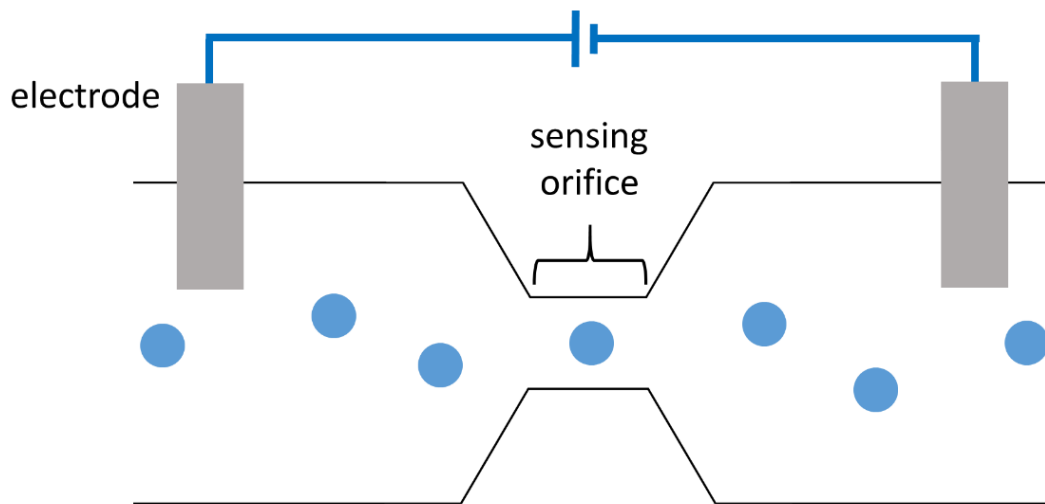


Figure 2.10 Schematic of a continuous microfluidic RPS sensing junction, including sensing orifice and electrode pair for electric field generation.

RPS relies on Maxwell's theory that the presence of non-conducting particles in a conducting medium effects an increased resistance that is proportional to the particle-excluded volume⁶⁸. When an electrical field is applied across a constrictive orifice with flowing conductive electrolyte solution running through, a particle sensing region is created: in the event of particle translocation through the orifice, a temporary change in electrical resistance across the orifice is generated. This change can be measured in the form of a current pulse, whose magnitude is proportional to the particle volume for a given sensing aperture.

2.6.1 Pulse analysis

The resistive pulse profile produced by particle translocation is dependent on both particle and pore properties. For example, 'square' pulse profiles are typical of cylindrical pores, whilst peak-shaped profiles are typical of conical pores due to their resistance gradient⁶⁹. As a general rule, pulse magnitude, shape and duration can be used to elucidate the particle size, pore and pulse shape, and particle shape respectively, whilst the pulse frequency is related to the particle concentration. However, particle and pore charges also affect pulse shape⁷⁰, and pulse duration and frequency⁷¹. Figure 2.11 illustrates an example current vs. time profile with characteristic 'square' pulses seen in cylindrical pores, and highlights the key pulse parameters that allude to particle and pore properties.

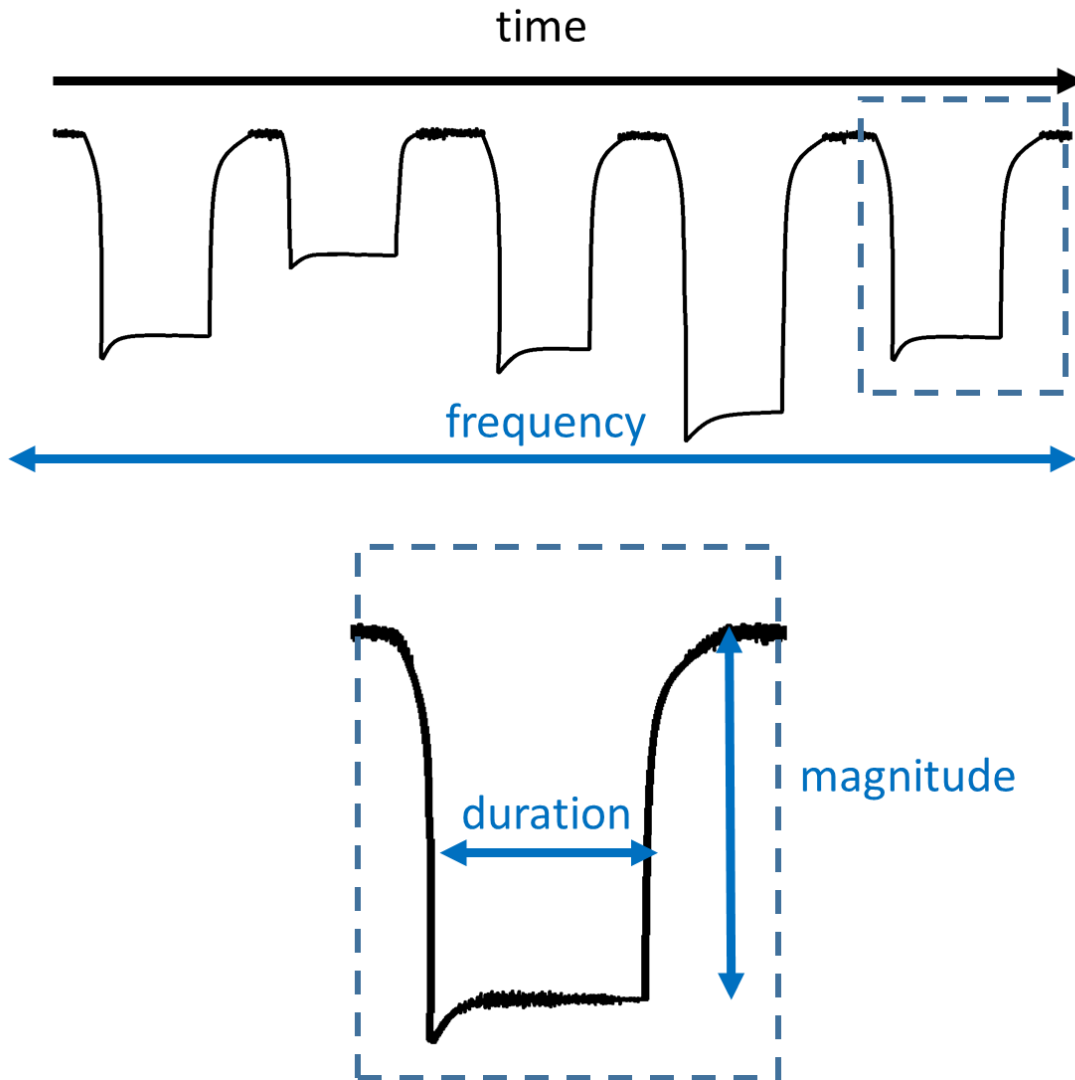


Figure 2.11 Illustration of example current vs. time profile of ‘square’ particle blockade events as typically see in a cylindrical pore. Three key characteristics are highlighted: frequency, duration and magnitude.

There are four main models for predicting pulse magnitudes for spherical particle translocations in cylindrical pores⁷², the earliest being that of Maxwell⁶⁸ (Equation 2.3, where R=resistance in Ω , d=particle diameter in m, D=pore diameter in m, L=pore length in m).

$$\frac{\Delta R}{R} = \frac{d^3}{D^2L} \quad (2.3)$$

However, this theory applies only to an infinitely small particle. Subsequently, a theory for spherical particle diameters <0.4 times the pore diameter was devised by Deblois and Bean (Equation 2.4)⁷³, who also included a correction factor ($F(d^3/D^3)$) to account for the ‘bulging’ of current streamlines around a spherical particle inside a pore.

$$\frac{\Delta R}{R} = \frac{d^3}{D^2 L} \left[\frac{D^2}{2L^2} + \frac{1}{\sqrt{1+(D/L)^2}} \right] F\left(\frac{d^3}{D^3}\right) \quad (2.4)$$

A later equation by Gregg and Steidley⁷⁴ (Equation 2.5) worked specifically with particle diameters close to the pore diameter.

$$\frac{\Delta R}{R} = \frac{D}{L} \left[\frac{\arcsin\left(\frac{d}{D}\right)}{\sqrt{1-(d/D)^2}} \right] - \left(\frac{d}{D}\right) \quad (2.5)$$

Finally, a model by Anderson and Quinn⁷⁵ (Equation 2.6) covered wide spherical particle size ranges of up to 0.9 times the pore diameter.

$$\frac{\Delta R}{R} = \frac{1}{|(d/D)^{3-0.8}| \left(\frac{L+\pi}{d^{\frac{1}{4}}}\right)} \quad (2.6)$$

However, for pore and particle shapes other than cylinders and spheres, respectively (including angular microfluidic pore channels) such equations are insufficient. For mass transfer and pulse prediction in these more advanced systems, simulations such as those generated via the finite element method (FEM) are commonly used. FEM models a body as being subdivided into an assembly of smaller sections with a certain number of behavioural degrees of freedom (thus, finite elements). This technique has been used to predict pulse magnitudes and shapes for rod-shaped particles in conical nanopores of different cone angles⁷⁶, for particles in a microfluidic device with complex electrode circuitry⁷⁷, and for particles in glass nanopores with different pore surface charges⁷⁰.

2.6.2 Ion current rectification

Ion current rectification (ICR) refers to the preferential movement of ions of a certain polarity through a charged pore constriction in an electric field. This asymmetric cation/anion transport is a physical phenomenon, brought about by pore surface charge causing the formation of an adjacent, immobile

double layer of ions, which interact with translocating ions in the form of repulsion (in the case of like-charges)⁷⁸. ICR is indicated by non-linear current-voltage relationships. Figure 2.12 a) shows a typical, linear ohmic curve seen in pore systems without ICR present, and b) departure from ohmic behaviour due to ICR, where ionic current is much higher or lower at one voltage polarity than the other.

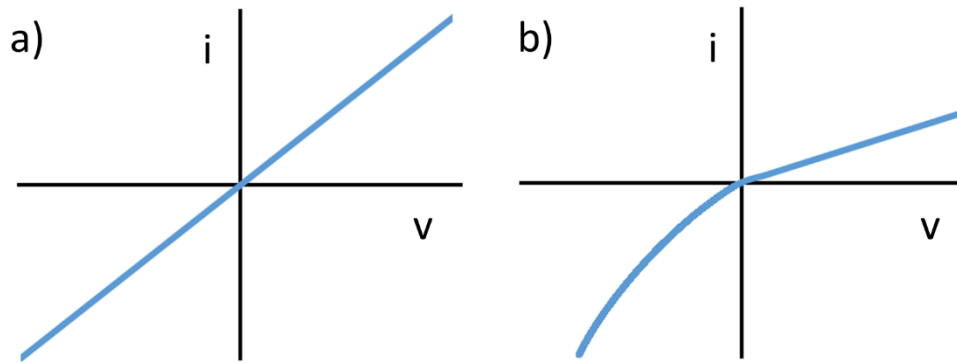


Figure 2.12 Linear current-voltage relationship as seen when no ICR is present. b) Non-linear current-voltage relationship, indicative of ICR⁷⁹.

The direction and extent of ICR is dictated by numerous factors such as pore geometry, surface charge density^{80,81} and flow-rate⁸². There are differing theories about the origin of ICR, including that of Siwy, et al. who proposes that ICR stems from a one-way, “ratchet” mechanism based on the electric potential barrier asymmetry inside the pore⁸³, and the model stated by Woermann involving an inhomogeneous conductivity near the pore orifice⁸⁴. ICR is typically observed in charged, asymmetric nanopores (most commonly, cones) when the pore diameter is of the order of the Debye length or smaller (2-10 nm), and there is low fluid flow flux. However, the phenomenon has been seen on the microscale in a small number of cases, including a 2.2 μm diameter micropore⁸⁵, 10 μm diameter micropipette⁸⁶, and a 60 μm diameter pore channel⁸⁷, when using asymmetric electrolyte solutions with different conductivities⁸⁵, or carrying out modification of the pore surface with polyelectrolytes^{81,86,87}.

2.7 Magnetophoretic separation

Separation efficiency in continuous magnetophoretic particle separation is dictated by the ability to sufficiently magnetically actuate particles away from a set trajectory. Particle trajectory involves competition between viscous drag, which sweeps the particle in the direction of flow, and magnetic

force, which migrates the particle in a transverse direction. Magnetic force (N) felt by a magnetic particle is a function of the particle volume in m^3 , V , vacuum permeability in TmA^{-1} , μ_0 , the applied magnetic field in T, B , the magnetic gradient in Tm^{-1} , $B \cdot \nabla$, and the difference in magnetic susceptibility between the particle and surrounding medium, $\Delta\chi$ (Equation 2.7)⁸⁸.

$$\vec{F} = \frac{V\Delta\chi}{\mu_0} (\vec{B} \cdot \nabla) \vec{B} \quad (2.7)$$

Separation efficiency can be defined as the proportion of magnetic particles successfully separated. In microfluidic chips, magnetic separation efficiency is dictated by many chip design and operating parameters such as channel configuration and dimensions, flow rates and ratios, fluid viscosity, and magnetic field profile and strength, in addition to properties of the magnetic particle/cell of interest such as its size, density and magnetic susceptibility.

2.8 References

- 1 L. Theodore, in *Chemical Engineering: The Essential Reference*, McGraw-Hill Education, NY, USA, 2011, pp. 1–90.
- 2 S. M. Kresta and R. S. Brodkey, in *Handbook of Industrial Mixing: Science and Practice*, eds. E. L. Paul, V. A. Atiemo-Obeng and S. M. Kresta, John Wiley & Sons, Inc., Hoboken, NJ, USA, 2004, pp. 19–88.
- 3 B. Majumdar, in *Fluid Mechanics with Laboratory Manual*, PHI Learning Private Limited, New Delhi, 2011, pp. 292–321.
- 4 B. Giri, in *Laboratory Methods in Microfluidics*, Elsevier Inc., Amsterdam, Netherlands, 2017, pp. 51–55.
- 5 W. E. Svendsen, in *Lab-on-a-Chip Devices and Micro-Total Analysis Systems: A Practical Guide*, eds. J. Castillo-León and W. E. Svendsen, Springer International Publishing, Cham, Switzerland, 2015, p. 20.
- 6 M. C. Potter and D. C. Wiggert, in *Mechanics of Fluids*, Cengage Learning, Stamford, CT, USA, 3rd edn., 2010, pp. 87–126.
- 7 J. P. Holman, in *Heat Transfer*, McGraw-Hill, NY, USA, 10th edn., 2010, pp. 215–276.
- 8 D. Moxey and D. Barkley, *Proc. Natl. Acad. Sci.*, 2010, **107**, 8091–8096.
- 9 S. Elghobashi, *Appl. Sci. Res.*, 1994, **52**, 309–329.
- 10 A. Guha, *Annu. Rev. Fluid Mech.*, 2008, **40**, 11–41.
- 11 F. Okkels, in *Micro and Nano Techniques for the Handling of Biological Samples*, eds. J.

- Castillo-León, W. E. Svendsen and M. Dimaki, CRC Press, Boca Raton, FL, USA, 2012, pp. 197–226.
- 12 W. E. Usual, H. B. Eral and P. S. Doyle, *Nat. Commun.*, 2013, **4**, 1–9.
- 13 D. Di Carlo, D. Irimia, R. G. Tompkins and M. Toner, *Proc. Natl. Acad. Sci.*, 2007, **104**, 18892–18897.
- 14 F. Babick, in *Suspensions of Colloidal Particles and Aggregates*, ed. F. Babick, Springer, Cham, Switzerland, 2016, pp. 221–284.
- 15 J. Berthier and P. Silberzan, in *Microfluidics for Biotechnology*, Artech House, Norwood, MA, USA, 1st edn., 2006, pp. 89–126.
- 16 J. Berthier and P. Silberzan, in *Microfluidics for Biotechnology*, Artech House, Norwood, MA, USA, 2nd edn., 2010, pp. 237–302.
- 17 M. Brandt, in *Laser Additive Manufacturing: Materials, Design, Technologies, and Applications*, eds. C. Emmelman, D. Herzog and J. Kranz, Woodhead Publishing, Duxford, UK, 2017, pp. 259–280.
- 18 N. Bhattacharjee, A. Urrios, S. Kang and A. Folch, *Lab Chip*, 2016, **16**, 1720–1742.
- 19 B. N. Turner and S. A. Gold, *Rapid Prototyp. J.*, 2015, **21**, 250–261.
- 20 N. Fang, C. Sun and X. Zhang, *Appl. Phys. A*, 2004, **79**, 1839–1842.
- 21 K. Bhole, P. Gandhi and T. Kundu, *J. Appl. Phys.*, 2014, **116**, 043105.
- 22 A. K. Au, W. Lee and A. Folch, *Lab Chip*, 2014, **14**, 1294–1301.
- 23 K. Sugioka and Y. Cheng, *Appl. Phys. Rev.*, 2014, **1**, 041303.
- 24 F. Bragheri, R. Martinez and R. Osellame, in *Three-Dimensional Microfabrication Using Two-Photon Polymerization (TPP)*, ed. T. Baldacchini, Elsevier Inc., Waltham, MA, USA, 1st edn., 2015, pp. 310–334.
- 25 M. Livesu, S. Ellero, J. Martínez, S. Lefebvre and M. Attene, *Comput. Graph. Forum*, 2017, **36**, 537–564.
- 26 B. Sager and D. W. Rosen, *Rapid Prototyp. J.*, 2008, **14**, 213–220.
- 27 M. Taufik and P. K. Jain, in *Proceedings of the ASME 2014 International Design Engineering Technical Conferences & Computers and Information in Engineering Conference IDETC/CIE 2014*, Buffalo, New York, USA, 2014, pp. 1–10.
- 28 J. C. Snyder, C. K. Stimpson and K. A. Thole, in *Proceedings of ASME Turbo Expo 2015: Turbine Technical Conference and Exposition*, ASME, Montréal, Canada, 2015, pp. 1–10.
- 29 R. B. Wicker, A. V. Ranade, F. Medina and J. A. Palmer, *Assem. Autom.*, 2005, **25**, 316–329.
- 30 M. Taufik and P. K. Jain, *Int. J. Manuf. Technol. Manag.*, 2013, **27**, 47–73.
- 31 L. Lü, J. Y. H. Fuh and Y.-S. Wong, in *Laser-Induced Materials And Processes for Rapid*

- Prototyping*, Springer Science+Business Media, LLC, New York, USA, 2001, pp. 9–38.
- 32 B. Khoda, in *Laser-Based Additive Manufacturing of Metal Parts: Modeling, Optimization and Control of Mechanical Properties*, eds. L. Bian, N. Shamsaei and J. M. Usher, Taylor & Francis Group, 2017, p. 15.
- 33 J. . Leitão, R. Everson, N. Sewell and M. Jenkins, in *Virtual and Rapid Manufacturing: Advanced Research in Virtual and Rapid Prototyping*, eds. P. J. Bártolo, A. J. Mateus, F. da C. Batista, H. A. Almeida, J. M. Matias and E. Al., Taylor & Francis Group, London, UK, 2008, p. 656.
- 34 P. Alexander, S. Allen and D. Dutta, *Comput. Des.*, 1998, **30**, 343–356.
- 35 M. Salmi, I. F. Ituarte, S. Chekurov and E. Huotilainen, *Int. J. Collab. Enterp.*, 2016, **5**, 218–230.
- 36 N. Alharbi, R. Osman and D. Wismeijer, *J. Prostetic Dent.*, 2016, **115**, 760–767.
- 37 K. Christiyan, U. Chandrasekhar and K. Venkateswarlu, *IOP Conf. Ser. Mater. Sci. Eng.*, 2016, **114**, 012109.
- 38 A. Armillotta, *Rapid Prototyp. J.*, 2006, **12**, 35–41.
- 39 P. Kulkarni, A. Marsan and D. Dutta, *Rapid Prototyp. J.*, 2000, **6**, 18–35.
- 40 R. K. Lade, E. J. Hippchen, C. W. Macosko and L. F. Francis, *Langmuir*, 2017, **33**, 2949–2964.
- 41 J. M. Lee, M. Zhang and W. Y. Yeong, *Microfluid. Nanofluidics*, 2016, **20**, 1–15.
- 42 M. Pan, Y. Tang, H. Yu and H. Chen, *AIChE J.*, 2009, **55**, 1969–1982.
- 43 Y.-M. Kim, W.-S. Kim, S.-H. Lee and J. Y. Baek, in *Proceedings of the 3rd Annual International IEEE EMBS Special Topic Conference on Microtechnologies in Medicine and Biology*, Kahuku, Oahu, Hawaii, pp. 292–295.
- 44 S. Yang, B. Yu, M. Zou and M. Liang, *Int. J. Heat Mass Transf.*, 2014, **77**, 208–217.
- 45 R. Jaeger, J. Ren, Y. Xie, S. Sundararajan and M. G. Olsen, *Appl. Phys. Lett.*, 2012, **101**, 184102.
- 46 J. B. Taylor, A. L. Carrano and S. G. Kandlikar, *Int. J. Therm. Sci.*, 2006, **45**, 962–968.
- 47 B. Dai, M. Li and Y. Ma, *Appl. Therm. Eng.*, 2014, **67**, 283–293.
- 48 N. P. Macdonald, J. M. Cabot, P. Smejkal, R. M. Guijt, B. Paull and M. C. Breadmore, *Anal. Chem.*, 2017, **89**, 3858–3866.
- 49 J. Wallace, M. O. Wang, P. Thompson, M. Busso, V. Belle, N. Mammoser, K. Kim, J. P. Fisher, A. Siblani, Y. Xu, J. F. Welter, D. P. Lennon, J. Sun, A. I. Caplan and D. Dean, *Biofabrication*, 2014, **6**, 015003.
- 50 M. Dziubinskim, in *Advances in Microfluidics*, ed. R. T. Kelly, InTech Inc., Rijeka, Croatia, 2012, pp. 29–54.
- 51 H. M. Shapiro, *Practical Flow Cytometry*, John Wiley & Sons Inc., Hoboken, NJ, 4th Ed., 2003.
- 52 B. Dickinson, in *Introduction to Flow Cytometry: A Learning Guide*, BD Biosciences, San Jose,

- CA, 2002, pp. 13–18.
- 53 D. A. Ateya, J. S. Erickson, P. B. Howell, L. R. Hilliard, J. P. Golden and F. S. Ligler, *Anal. Bioanal. Chem.*, 2008, **391**, 1485–1498.
- 54 J. Knight, A. Vishwanath, J. Brody and R. Austin, *Phys. Rev. Lett.*, 1998, **80**, 3863–3866.
- 55 M. I. Lapsley, L. Wang and T. J. Huang, *Biomark. Med.*, 2013, **7**, 75–78.
- 56 M. E. Piyasena and S. W. Graves, *Lab Chip*, 2014, **14**, 1044–1059.
- 57 T. Sun and H. Morgan, *Microfluid. Nanofluidics*, 2010, **8**, 423–443.
- 58 J. Chen, C. Xue, Y. Zhao, D. Chen, M.-H. Wu and J. Wang, *Int. J. Mol. Sci.*, 2015, **16**, 9804–9830.
- 59 K. C. Cheung, M. D. Berardino, G. Schade-Kampmann, M. Hebeisen, A. Pierzchalski, J. Bocsi, A. Mittag and A. Tárnok, *Cytom. Part A*, 2010, **77A**, 648–666.
- 60 J. S. Kim and F. S. Ligler, *Anal. Bioanal. Chem.*, 2010, **398**, 2373–2382.
- 61 S. H. Cho, J. M. Godin, C.-H. Chen, W. Qiao, H. Lee and Y.-H. Lo, *Biomicrofluidics*, 2010, **4**, 043001.
- 62 G. Testa and R. Bernini, *Biomed. Opt. Express*, 2015, **6**, 54–62.
- 63 L. M. Fu, R. J. Yang, C. H. Lin, Y. J. Pan and G. Bin Lee, *Anal. Chim. Acta*, 2004, **507**, 163–169.
- 64 M. Rosenauer, W. Buchegger, I. Finoulst, P. Verhaert and M. Vellekoop, *Microfluid. Nanofluidics*, 2011, **10**, 761–771.
- 65 E. L. C. J. Blundell, R. Vogel and M. Platt, *Langmuir*, 2016, **32**, 1082–1090.
- 66 E. L. C. J. Blundell, M. J. Healey, E. Holton, M. Sivakumaran, S. Manstana and M. Platt, *Anal. Bioanal. Chem.*, 2016, **408**, 5757–5768.
- 67 E. Weatherall and G. R. Wilmott, *Analyst*, 2015, **140**, 3318–3334.
- 68 J. Maxwell and J. Thompson, *A Treatise on Electricity and Magnetism*, Clarendon, Oxford, 3rd edn., 1904.
- 69 G. R. Willmott and B. E. Parry, *J. Appl. Phys.*, 2011, **109**, 094307.
- 70 W.-J. Lan, C. Kubeil, J.-W. Xiong, A. Bund and H. S. White, *J. Phys. Chem. C*, 2014, **118**, 2726–2734.
- 71 E. L. C. J. Blundell, L. J. Mayne, E. R. Billinge and M. Platt, *Anal. Methods*, 2015, **7**, 7055–7066.
- 72 I. Makra and R. E. Gyurcsányi, *Electrochem. Commun.*, 2014, **43**, 55–59.
- 73 C. P. DeBlois and R.W. Bean, *Rev. Sci. Instrum.*, 1970, **41**, 909.
- 74 E. C. Gregg and K. D. Steidley, *Biophys. J.*, 1965, **5**, 393–405.
- 75 J. L. Anderson, J. A. Quinn and R. S. Instrum., *Rev. Sci. Instrum.*, 1971, **42**, 1257–1258.
- 76 C. Y. Lee and C. Chen, *Microsyst. Technol.*, 2017, **23**, 299–304.
- 77 R. Liu, W. Waheed, N. Wang, O. Civelekoglu, M. Boya, C.-H. Chu and A. F. Sarioglu, *Lab Chip*, 2017, **17**, 2650–2666.

- 78 M. Lavalley, O. F. Schanne and N. G. Hebert, *Science*, 1969, **166**, 368–369.
- 79 D. G. Haywood, A. Saha-Shah, L. A. Baker and S. C. Jacobson, *Anal. Chem.*, 2015, **87**, 172–187.
- 80 J. Liu, D. Wang, M. Kvetny, W. Brown, Y. Li and G. Wang, *Langmuir*, 2013, **29**, 8743–8752.
- 81 E. L. C. J. Blundell, L. J. Mayne, M. Lickorish, S. D. R. Christie and M. Platt, *Faraday Discuss.*, 2016, **193**, 487–505.
- 82 W. Lan, D. A. Holden and H. S. White, *J. Am. Chem. Soc.*, 2011, **133**, 13300–13303.
- 83 Z. S. Siwy, *Adv. Funct. Mater.*, 2006, **16**, 735–746.
- 84 D. Woermann, *Phys. Chem. Chem. Phys.*, 2003, **5**, 1853–1858.
- 85 E. C. Yusko, R. An and M. Mayer, *ACS Nano*, 2010, **4**, 477–487.
- 86 X. He, K. Zhang, T. Li, Y. Jiang, P. Yu and L. Mao, *J. Am. Chem. Soc.*, 2017, **139**, 1396–1399.
- 87 F. Chang, C. Chen, X. Xie, L. Chen, M. Li and Z. Zhu, *Chem. Commun.*, 2015, **51**, 15316–15319.
- 88 W. Andrä, U. Häfeli, R. Hergt and R. Misri, in *The Handbook of Magnetism and Advanced Magnetic Materials Vol. 4: Novel Materials*, eds. H. Kronmüller and S. Parkin, John Wiley & Sons Inc., Chichester, UK, 2007, pp. 2536–2568.

Chapter 3 Microfluidic printing by stereolithography

3.1 Abstract

In recent years 3D printing has gained traction as a method for microfluidic manufacture. Of the various AM techniques, SLA has shown particular promise due to its superior resolution. However, for microfluidic LOC system printing, challenges remain concerning print methodology and sensor integration. In this chapter SLA was used to produce initial prototypes and test pieces for microfluidic particle/cell analysis platforms, including various initial features to be used in the two devices: a hydrodynamic focusing junction, RPS pore channels, sensor housing and inlet/outlet threads.

A printing style involving open, surface channels was utilised alongside subsequent cover layer sealing to enable effective flushing of uncured resin and thus improve print resolution. The effects of build direction on channel and thread quality were investigated, as well as the resolution limit of pore channel structures for RPS sensing. Additionally, an array of sensor grooves was fabricated to compare dimensional accuracy in grooves for FSC and SSC detection. Lastly, the nature of particle fouling into SLA Accura[®] 60 polymer channels was investigated: fouling onto the polymer itself was examined, as well as into channel inlets/outlets.

It was found that the Y-direction build avoided adverse channel shape deformation, roughness and other effects associated with the other two build directions. In this direction, channels with widths down to 45 μm were possible. However, below $\sim 70 \mu\text{m}$ widths, channels suffered from severe roughness and narrowing due to post-printing solidification of trapped resin residue. It was also found that channel orientation within a build was important, as diagonal, SSC sensor grooves were significantly narrower than straight, FSC grooves with the same nominal width. Finally, it was found that particle fouling onto the printed microfluidic channels was mostly due to loss into inlets and outlets, as opposed to physical trapping and adsorption onto printed steps as originally hypothesised.

3.2 Introduction

As covered in Chapter 1, fabrication of microfluidic devices by AM has a multitude of advantages over traditional photolithographic and soft-lithographic methods, including a faster prototyping process and greater three-dimensional design freedom. However, it also involves various challenges stemming from its inherent nature as an additive manufacturing process: as covered in Chapter 2, 3D printed parts are prone to dimensional and shape errors due to its layering nature, caused by aspects such as resolution limit, build direction and laser overcuring. Furthermore, surface quality and dimensional and shape inaccuracies are far more significant on the microscale.

Success in microfluidic/microscale printing varies widely across AM types¹⁻⁵. LOM had a spell of popularity as a prototyping method for microfluidic biohandling or bioassay devices in the early 2000s before being superseded by paper microfluidics⁵, and was used to build low-cost chips for applications such as immunoassays⁶, protein separation⁷ and extraction⁸. It allows printing in ceramics, metal and paper, and can print 100 μm width channels⁹. However, the laser cutting and gluing processes involved in LOM produce a large amount of debris, and so microfluidic devices made by this method require careful cleaning to prevent blockages⁵. In addition, LOM is still limited in its achievable channel network topologies^{5,10}, and involves substantial assembly and material wastage.

Use of powder metal printing techniques (SLS and SLM) for microfluidic fabrication is currently rare, due to the relatively poor resolution stemming from part surfaces comprising unprocessed metal particulates. SLM has been used to print curved 1–3 mm d. flow reactor channels¹¹, and 900 μm liquid chromatography channels^{12,13}. However, the latter had an average of 50 μm ¹² and 24 μm ¹³ Ra surface roughness. SLS test holes of approximately 1000 μm d. with 12 μm roughness¹⁴ and 508 μm d. with 8 μm roughness¹⁵ have been made. In comparison, UC, which welds together metal sheets, offers part accuracy of <50 μm ¹⁶ and a very low surface roughness of ~ 5 μm Ra (although it has a topology consisting of large, highly flat welded areas interspersed with valleys of unprocessed foil)¹⁷. However, only a single patent application for UC microfluidic channels is known to the author¹⁸. It remains a relatively new and niche technique in general, with limited exploration into process optimisation and scientific understanding of the technique¹⁹. In addition, it is unsuitable for printing parts with overhangs due to a lack of support structures¹⁶, which complicate microfluidic fabrication.

Another uncommon AM technique for microfluidic fabrication is binder jetting: there have been no whole microfluidic devices produced via this technique—only test pieces of structures such as bars,

slots and holes²⁰. Slots were produced down to 500 μm width, and walls down to 300 μm ²⁰. Smaller features are printable but are easily destroyed by the post-printing powder-blasting process for removal of excess powder, which also can still leave unbound powder in holes²⁰. In contrast, a similar technique, material jetting, has seen far greater success in microfluidic fabrication, a few examples being a device for the electrochemical detection of neurotransmitters, nitric oxide (NO) and oxygen tension²¹, a radial flow-cell for the chemiluminescence detection of hydrogen peroxide in urine and coffee samples²², and a chip for measuring blood haemoglobin via a smartphone²³. Material jetting is able to create microfluidic channels down to roughly 200–300 μm width^{4,24}, and with surface roughness of Ra 1–2 μm ^{1,14}, suffering from recurrent $\sim 6\ \mu\text{m}$ banded structures¹. It can use a wide range of materials and is able to print up to 14 types in one print³, but a critical issue is its structure removal process, which involves pressurised water jet and/or ultrasonics that can damage microchannels^{25–27}.

Microfluidic fabrication by FDM is relatively challenging due to its low printing resolution, with the technique typically unable to print channel dimensions $< 500\ \mu\text{m}$ ^{1,4}, as well as its severe macroscale channel roughness of $\sim 50\text{--}200\ \mu\text{m}$ tall bumps due to filament and nozzle diameter limitations^{1,4,14}. Additionally, devices are prone to interlayer leakages²⁸ and have low transparency, even for plastics advertised as ‘transparent’²⁸, but there are still a sizable number of papers describing FDM microfluidic devices³, from optical platforms²⁹, to ELISAs (enzyme-linked immunosorbent assays)³⁰, electronic tongues³¹ and stem cell encapsulation systems³². This area is set to grow with the introduction in 2016 of a commercial FDM printer specifically for microfluidic fabrication, able to print down to 300 μm channel widths²⁸: the Fluidic Factory³³.

In contrast, SLA has the highest resolution of the seven 3D printing types^{34,25,35}, unless comparing a desktop SLA printer to an industrial-grade material jetter²⁶. It also typically has a surface roughness of only 1 μm tall in the form of regular striped structures¹, and has the highest reproducibility and fidelity to nominal values compared to other AM types¹, due to the high spatial resolution provided by the focused laser beam spot size³⁶. SLA microstructure tests have consistently shown feature detail down to 100 μm if structures are printed open on the piece surface^{25,34,37,38}. Additionally, although SLA is slower at chip production than material jetting and FDM, its post-processing time is a fraction by comparison, making SLA quicker at microfluidic fabrication than FDM and only slightly slower than material jetting¹. SLA also has the option of highly transparent polymers³⁸.

There are six papers known to the author that describe 3D printed microfluidic devices involving particle/cell handling: four concerning magnetic capture, one covering inertial separation, and another a cell viability study. In 2013, Krejcová, et al. described an FDM chip for the magnetic capture and

indirect detection of influenza virus-CdS quantum dot magnetic particle complexes³⁹: complexes were captured in a well adjacent to a magnet, and the Cd(II) electroactivity was monitored by differential pulse voltammetry (DPV) via an embedded three-electrode set-up. Subsequently, in 2014 Lee, et al. demonstrated magnetic separation of alpha-fetoprotein (AFP) biomarker in a material jetted chip for off-chip quantification⁴⁰, as an example application for an interconnectable, modular printed microfluidic system. A second paper in 2014 reported a hollow SLA device into which a stack of magnets were placed, to carry out stop-flow magnetic separation⁴¹: antibody-magnetic particle complexes were immobilised and used to capture salmonella in a food sample. Following this in 2015, an SLA device with helical channels carried out size-based separation of *E. coli* bacteria in milk⁴², by use of antibody-functionalised nanoparticle clusters. Finally, in 2016, a study investigated the biocompatibility of different printed materials with cell cultures⁴, and in 2017 a DLP device was used to magnetically capture *E. coli* antibody-magnetic particle complexes in a well⁴³. None of these six papers looked at direct, single-particle/cell analysis, with the sole case of indirect particle detection utilising ion concentration monitoring³⁹. A 3D printed chip able to carry out single-particle/cell analysis would find application in a whole host of technologies in POC diagnostics, environmental monitoring and materials characterisation, as covered in Chapter 1. However, there are three challenges involved in the creation of such printed devices: resolution, sensor integration and particle/cell fouling.

SLA was chosen as the printing technique for this project due to its aforementioned superior resolution, feature accuracy and low surface roughness. The resolution limit was investigated, as well as the effects of build direction on various aspects of the builds (shape and dimensional accuracy, channel wall roughness and support structures) and the subsequent effects on the laminar channel flow. In order to maximise feature resolution, a printing style was used that has become popular in recent years involving open microfluidic channels and subsequent sealing via cover layer²⁴.

There have been sufficient 3D printed sensing devices of late to warrant two reviews of the subject in 2017^{44,45}. A range of additively-manufactured sensors have been developed including tactile^{46,47}, pressure⁴⁸, force⁴⁹, strain⁵⁰⁻⁵², acoustic⁵³, temperature⁵⁴⁻⁵⁶, humidity⁵⁷, gas⁵⁸, acceleration^{59,60}, ion^{61,62}, radio-frequency (RF) signal⁶³⁻⁶⁵ and electroencephalogram (EEG) signal⁶⁶ sensors. There are two main approaches for 3D printed sensor device production: 1) sensor printing/sputtering, and 2) sensor embedding either after the print or during a print pause⁶⁷. Printable sensors include waveguides^{68,69} and conductive inks and coatings in the form of commercially available mixtures⁵², or inks containing silver nanoparticles⁷⁰ or carbon nanotubes⁷¹, to make elements such as electrodes⁷⁰ and antennae⁶⁴. AM filament can also be doped with the sensing component and printed, such as PLA doped with

carbon nanotubes^{72,73} or acrylate hydrogel doped with enzymes⁷⁴. Alternatively, metal coatings can be sputtered inside printed parts⁶³. Conversely, embedded sensors include off-the-shelf electrodes in the form of wires^{21,75} or wire mesh⁴⁷, Fibre Bragg grating (FBG)^{50,51} and optical fibres^{27,37}. Over the last 6 years there have been increasing numbers of microfluidic 3D printed sensor devices, covered by a perspective piece in 2018 by Rusling⁷⁶. However, the sensing systems involved have often been off-chip, such as smart phones^{23,77} or commercial instruments such as a HPLC DAD⁷⁸. This can prevent widespread use of a technology, via the need for additional, high cost equipment and/or causing system bulkiness, thus limiting its portability and hindering it from being a genuine lab-on-a-chip. In addition, there have been publications outlining 3D printed chips for particle synthesis, but these have used off-chip analysis within UV/VIS flow cells^{79,80} or via a benchtop DLS instrument⁸⁰. In this project, we aimed to incorporate low-cost sensing systems for particle/cell analysis into microfluidic chips. Such systems could be used in a whole host of applications in portable material synthesis (especially by combination of characterisation and synthesis onto one chip) and healthcare, as covered in Chapter 1. However, challenges involved in the creation of these embedded sensor technologies are leakages and system sensitivity.

Another key challenge to address in the development of a printed microfluidic particle sensor is fouling (particle deposition onto channel surfaces). This is a significant issue in microfluidic suspension handling⁸¹⁻⁸⁵, causing sample wastage as well as decreased operational performance, and preventing conversion of batch processes involving solid suspensions to continuous-flow methods⁸². The three main mechanisms of particle fouling are sieving, bridging and aggregation⁸⁶. Sieving involves blocking of a channel constriction by a particle larger than its width⁸⁶, whilst bridging involves blocking caused by simultaneous transport of multiple particles through a constriction, causing a clog⁸⁶. Aggregation does not require a constriction to happen, and involves deposition of a particle onto a channel surface, followed by a rapid ensuing build-up due to attractive forces⁸⁶. The processes leading to particle fouling from a flowing suspension onto a surface can be triggered by a number of factors: particle behaviour in microfluidic flows is dictated by numerous forces acting upon them, such as forces exerted by the surrounding fluid (particle-fluid interactions), particle-particle interactions, particle-channel wall interactions, and in more advanced microfluidic systems: external fields and interactions with phase interfaces^{82,87}. This set of forces affects the motion pattern of a particle⁸⁷ and subsequently, the occurrence of particle sedimentation⁸¹. Gravitational forces can play a role in particle sedimentation, causing settling onto the channel floor⁸¹, but fast fluid rates have been observed to overrule interparticle electrostatic repulsion in charged particles and cause particle deposition severe enough to clog microfluidic channels^{88,89}. Particle fouling can lead to a clog, which typically causes

device performance failure. However, particle deposition onto additively manufactured channel walls has not yet been explored.

3.3 Aims and Objectives

The overall aim of this chapter was to develop and test prototypes of key features for two different particle/cell analysis devices: optical and electrochemical.

The resulting main objectives for this chapter were:

- To investigate the effects of build direction on device channel quality, as well as the focusing performance of a hydrodynamic focusing junction for the optical chip.
- To determine the smallest printable RPS pore channel dimensions, in order to maximise the electrochemical device sensitivity.
- To investigate the extent and nature of particle fouling into printed microfluidic channels, and test our hypothesis that the majority of fouling will be caused by particle trapping onto printed stair-stepping.
- To develop printed sensor grooves for sensor embedding.

3.4 Materials and Methods

3.4.1 Materials

3.4.1.1 Chemicals and reagents

Isopropyl alcohol (IPA) and methanol were both obtained from VWR. Methylene blue was obtained from Sigma-Aldrich and solochrome red was obtained from Merck. Phosphate-buffered saline (PBS) was obtained from Sigma-Aldrich (catalogue number P4417) and was made up in deionised water to the supplier-recommended concentration (phosphate buffer 0.01 M, potassium chloride 0.0027 M, sodium chloride 0.137 M), with measured pH 7.32 (taken by a FiveEasy pH meter with InLab Ultra-Micro-ISM® pH electrode, both obtained from Mettler Toledo). Polyethylenimine (PEI) and poly(acrylic acid-co-maleic-acid) (PAAMA) were obtained from Sigma-Aldrich (catalogue numbers 408727 and 416053 respectively).

3.4.1.2 Beads

1 μm Diameter Dyna[®] MyOne[™] beads (polystyrene with interspersed iron oxide, COOH surface groups) were obtained from Thermo Fisher, catalogue number 65011. 1 μm Diameter polystyrene beads (CPC1000s) were obtained from Izon Science. Carboxylated polystyrene beads of 10 μm diameter, (Fluoresbrite[®] Yellow Green microspheres, coefficient of variation (CV)=15%) were obtained from Polysciences, catalogue number 18142-2.

3.4.2 Methods

All methods were carried out at ambient room temperature (approx. 18-20°C).

3.4.2.1 Drafting and stereolithography

Siemens NX 11 software was used to draft the test pieces and device prototype CAD files and export to .STL format. The parts were fabricated in Accura[®] 60 polymer on a Viper si2 SLA printer (both obtained from 3D Systems) in its high resolution (HR) build mode. This pre-set mode uses a Nd:YV04 solid state laser at 354.7 nm, 100 mW output power, $1/e^2$ beam diameter 75 μm +/- 15 μm , and has minimum build layer height 20 μm , with elevator vertical resolution 25 μm and position repeatability 76 μm . After printing, uncured resin was removed from the parts by rinsing with IPA and methanol. Followed this, UV curing was carried out via a ProCure[™] 350 UV Chamber (3D Systems) for 4 minutes to ensure full photopolymer cross-linkage, followed by a final IPA and methanol rinsing step. Y-junctions and hydrodynamic focusing prototypes were printed in the three different build directions. One of the Y-direction hydrodynamic focusing prototypes was polished with sandpaper (grit sizes P3600, P600) and a lapping film (aluminium oxide, 9 μm , obtained from 3M). Test wafers containing arrays of sensor grooves and RPS pores were printed in the Y-direction. A block of four 1000 μm diameter, internal, circular channels were also printed in the Y-direction.

3.4.2.2 Cover layer

Device prototypes were sealed with a cover layer composed of TESA 4965 double-sided tape (obtained from 3M) and LEXAN[™] 8010PC polycarbonate (PC) film (250 μm thickness, obtained from SABIC), applied by hand and flattened using a seam roller. The external chip sensor interfaces (the parts of the

chip where the sensors protruded out from) were sealed with blobs of two-part epoxy resin (Araldite®, Rapid, obtained from Huntsman Advanced Materials).

3.4.2.3 Threads

The Y-junction chips and the hydrodynamic focusing prototypes had threads milled out of cured Accura® 60 via a tap and die kit (obtained from Tekton). Others threads were included in the device CAD file and printed as part of the chip.

3.4.3.4 Optical microscopy

All images were taken on an Optiphot-2 optical microscope using a DS-5M camera and a DS-L1 Camera Control Unit (all obtained from Nikon), with the exception of the pore channel photographs, which were taken on a DM2500 microscope (obtained from Leica).

3.4.3.5 Image analysis

Particles were counted via AxioVision (Version 4.9, Zeiss) software. Grooves, channels and dyed core streams were measured via AxioVision, whilst pore channels were sized via Image-J (Version 1.5, NIH).

Sensor groove width values and pore channel width values in the groove array and pore array wafers respectively were calculated as a mean of 15 separate width measurements spread out along the length of each groove/pore, with 5 measurements taken of the widest sections, 5 of the narrowest, and 5 of middling sections. Hydrodynamic junction channel widths built in the XYZ build direction were calculated as a mean of 10 separate width measurements spread along the length of each channel. This was done for each of three device copies for each build direction. Dyed core stream values for the XYZ build directions were calculated as a mean of 5 separate width measurements, taken in the ~400 µm after the neckdown region, in the Xp region (slug flow region—see Chapter 2.5.1).

3.4.3.6 Fluidic control

Microfluidic flows were effected by Mitos P-Pump Basic pressure-driven pumps (Dolomite) and inputted into the chip by polyether ether ketone (PEEK) microfluidic tubing (250 µm internal diameter, obtained from Dolomite) and standard Supelco® HPLC fittings and end ferrules (obtained from Sigma-

Aldrich) in printed threads. O-rings (6 mm diameter, nitrile, obtained from Rhondama) were used to prevent leakages.

3.4.3.7 Focused dye stream sizing

Methylene blue (1 mM) was focused into different-sized core streams, by using a range of applied pressures for inner flow, whilst holding sheath flows (water) steady at 200 mbar.

3.4.3.8 Particle wafer adsorption study

Positively-charged particles were produced by removal of PBS solution from a suspension of 1 μm beads (Dyna[®] MyOne[™], COOH surface groups, 1.1×10^8 particles mL^{-1} , 200 μL , in PBS) and replacement with PEI (200 μL , 10x diluted from neat) followed by sonication (2 min 40s) before being incubated for 1.5 hrs (interspersed with sonication, 2 min, every 10 min). Finally, the solution was removed and replaced with PBS (200 μL), before this itself was removed itself and replaced with fresh PBS (200 μL). The bottom 2/3 of an Accura[®] 60 wafer was incubated in PEI solution (aq. 5% w/v) for 2 hrs, followed by incubation of the other 1/3 in PAAMA solution (aq. 10% w/v) for 2 hrs. The wafer was then thoroughly rinsed with deionised water and left to dry. Next, a negatively-charged particle suspension (Dyna[®] MyOne[™], COOH surface groups, 1 μm diameter in aqueous PBS, 1.1×10^8 particles mL^{-1}) and the produced positively-charged particle suspension (above, 1.1×10^8 particles mL^{-1}) were each sonicated (1 min) before 250 μL of each was dripped onto one half of the wafer. The wafer was then left covered overnight for the solvent to dry, before being rinsed with deionised water and left to dry once more. Adsorbed particles on each wafer section were counted by eye under a microscope in 5 separate areas of 250 x 250 pixels, which equated to 40 x 40 μm .

3.4.3.9 Particle channel adsorption study

Fittings, ferrules and O-rings (as above in 3.4.3.6) were thoroughly cleaned before running by 3x alternating sonication (10 s) and water rinsing steps. Two of the four straight channels (as above in 3.4.2.1) were sawn off and bridged by a piece of tubing, fittings, etc. and ran as a pair. The two remaining channels were ran separately. Channels were each first rinsed (water, 2000 mbar, 20 s, followed by PBS buffer, 1000 mbar, 5 s), before PBS (1000 mbar) was collected into an Eppendorf (~1.5 mL) as a control run. Subsequently, an initial suspension of 1 μm beads (CPC1000s in PBS, 100 μL , 2.0×10^7 particles mL^{-1}) was run through at 500 mbar and the output collected, followed by another

suspension (CPC1000s in PBS, 500 μL , 2.0×10^7 particles mL^{-1} , 500mbar). For the bridged channel pair, particle suspensions were doubled to 200 μL and 1000 μL , respectively. One of the lone channels was sliced open after running with a band-saw for microscopic inspection.

3.4.3.10 Particle quantification by TRPS

Collected control (PBS) and particle suspensions after flowing through printed devices channels were counted by a QNano TRPS instrument via an NP1000 pore (both Izon Science) at +0.1 V, 45.50 mm applied pore stretch, with a CPC1000, 2.0×10^7 particles mL^{-1} PBS calibration suspension, controlled by Izon Control Suite software (Version 3.1, Izon Sciences). Subsequently, efficiencies were calculated from these gained concentration values, as a percentage of the total number of particles outputted by the device, over the total number inputted, using measured volumes.

3.4.3.11 Particle suspension flow in X-direction hydrodynamic junction

A suspension of 10 μm beads (9.1×10^4 particles mL^{-1} in aqueous solution, carboxylated polystyrene, Fluoresbrite® Yellow Green microspheres, CV=15%, obtained from Polysciences, catalogue no. 18142-2), was fed into one of the Y-direction hydrodynamic junctions at 100 mbar inner flow, with 200 mbar water sheath flows.

3.4.3.12 Statistical methods

Standard deviation for a data set was calculated via Equation 3.1, where N=the total number of values in the set, x_i =an individual value and μ =the mean of the set.

$$\sigma = \sqrt{\frac{1}{N} \sum_{i=1}^N (x_i - \mu)^2} \quad (3.1)$$

3.5 Results & Discussion

3.5.1 Device design

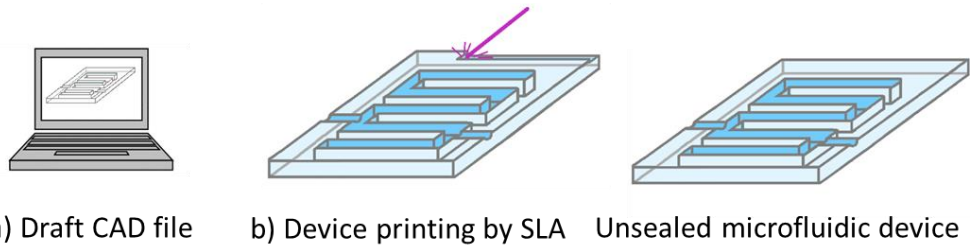
In microfluidic fabrication by SLA, a microchannel is built by photopolymerisation of the channel walls and subsequent draining of uncured resin from the channel cavity after printing completion. This

technique has been around for nearly 15 years⁹⁰. However, in recent years a trend has been emerging where microfluidic channels are printed at the device surface and then sealed with a cover layer, as opposed to being printed internally²⁴. This open-channel printing style allows superior channel resolution, as uncured resin is far easier and quicker to flush out, and laser overcuring is avoided. Figure 3.1 illustrates the fabrication process for the open-style microfluidic LOC devices produced in this thesis. Even with post-printing rinsing, curing and sealing steps, this process is significantly shorter than the conventional photolithographical or soft-lithographical microfluidic process (Figures 1.10 and 1.11, respectively). Channels are printed open on the device topmost surface, and have square or rectangular cross-sections as opposed to round, in order to minimise the staircase effect and maximise repeatability and uniformity, as well as aid the alignment of the optical fibres with the microchannel walls.

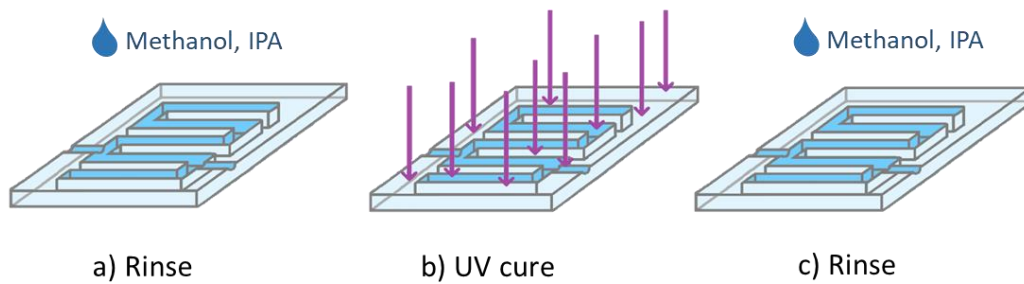
The device is sealed with a transparent cover layer consisting of 250 µm thickness polycarbonate film, and double-sided tape. TESA[®] 4965 double-sided acrylic adhesive tape was chosen for its high adhesive water and pressure resistance, removal ease, and optical transparency^{37,91}. Another, lower-cost acrylic adhesive tape (Gorilla Clear Repair Tape, obtained from Gorilla Glue Inc) also marketed as waterproof but only single-sided was trialled, but lost grip and suffered leaks within 10s of exposure to 500 mbar pressure water fluid flow, and released a large amount of adhesive residue that blocked channels, preventing chip cleaning and reuse. In comparison, the TESA[®] 4965 double-sided tape could withstand 2500 mbar pressure water fluid flow for at least 10s without leakages forming. In-depth fluid pressure-resistance testing of this tape is covered by Monaghan, et al⁹².

As well as microfluidic channels, grooves were also printed on device surfaces to enable sensor embedding. As illustrated in Figure 3.1, sensor end faces were placed in direct contact with chip fluid flow. This contact is required for RPS sensing (Chapter 5), and, in the optical chip (Chapter 4), prevents reflection, scattering, and absorption light losses stemming from the light waves having to traverse through two extra material interfaces. Additionally, this open channel configuration allows ease of chip cleaning and re-use, as the cover layer and sensors are quickly and easily removed and replaced by hand.

1) Device drafting and fabrication



2) Device post-processing



3) Embedding of sensors and device sealing

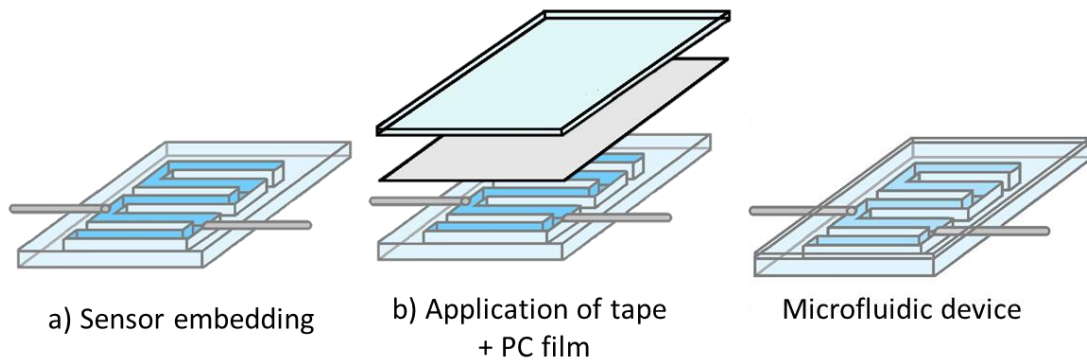


Figure 3.1 Schematic of microfluidic device production, encompassing printing, rinsing, sensor embedding and sealing steps.

3.5.2 Optical chip prototype

The optical detection device working principles were based on those of a flow cytometer, with the chip design having two key features: a hydrodynamic focusing junction and an optical fibre detection system (Figure 3.2).

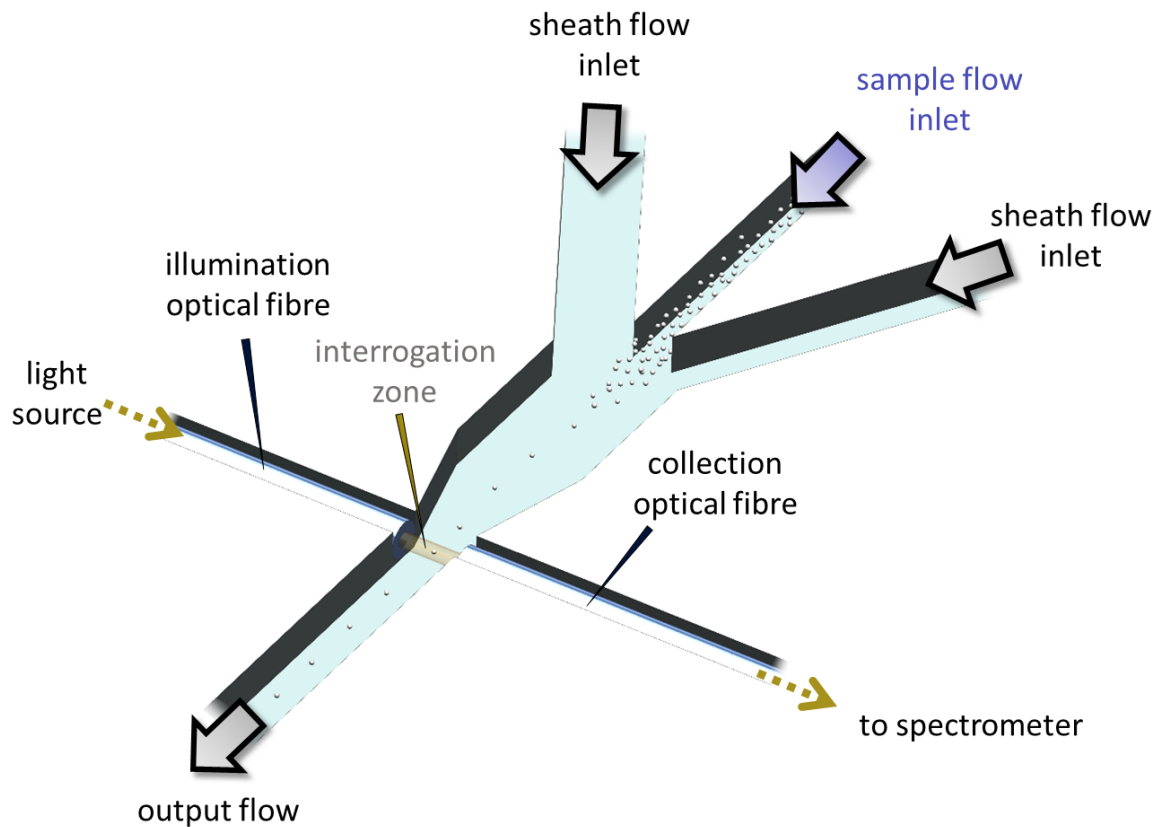


Figure 3.2 Schematic illustrating hydrodynamic focusing and detection processes in the 3D printed optical device.

As covered in Chapter 2.5.1, optical detection inside the flow cytometer slug flow region is advantageous as velocity differences between cells/particles at differing channel positions is minimised⁹³. Thus, the optical fibre junction was placed immediately after the focusing junction in our chip design.

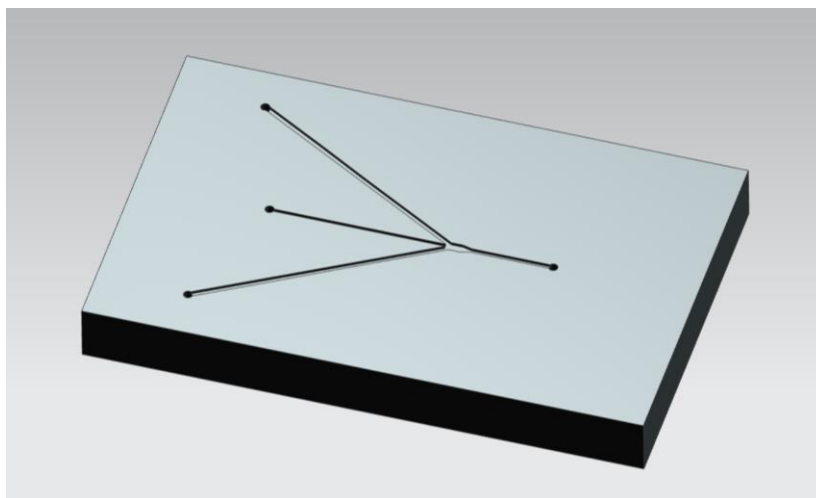


Figure 3.3 CAD file of optical chip prototype.

Figure 3.3 shows the CAD file for the prototype optical chip. A shallow 30° angle was chosen for the hydrodynamic focusing junction neckdown region to prevent creation of turbulences⁹³. Channel dimensions were 250 μm width depth, and 250 μm width for the sample flow inlet, 400 μm width for the sheath flow inlets, and 400 μm width for the outlet channel. After printing, M6 threads were tapped in the fluid inlets and outlets, to allow attachment of fluid fittings.

3.5.2.1 Build direction effects: channel quality

As covered in Chapter 2, dimensional inaccuracies are more significant in microscale 3D printed detail than macroscale parts^{34,94}, with build direction being especially critical. To investigate the effects of build direction on channel quality, simple Y-junctions and hydrodynamic focusing junction prototypes were printed in the three different build directions (Figure 3.4). Figures 3.5 and 3.6 show the resulting printed prototypes. Junctions built in the X-direction had residual wedge-shaped support structures present in the focusing junction (Figure 3.6), due to the printer attempting to build the topmost channel on top of a cavity. Additionally, as expected, stair-stepping was present on all angled channels (channels not parallel or perpendicular to the build bed), such as the sheath inlet channels. Also, due to laser-overcuring, the channels had an extremely rough ceiling, and the junction shape was deformed and non-symmetrical. Laser overcure greater than 4x the layer thickness has been observed in parts made by the SLA Viper si2⁹⁵.

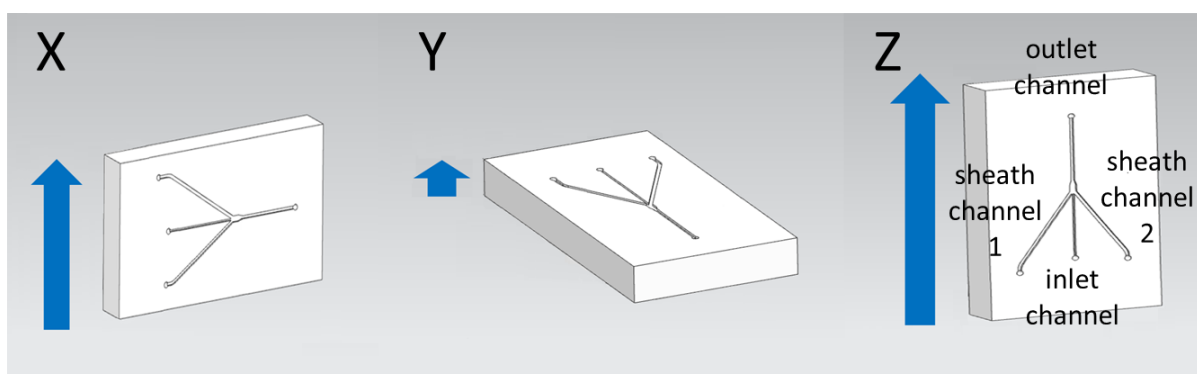


Figure 3.4 Illustration showing the build directions used in hydrodynamic junction prototype printing. Printing directions are given in blue. The different channels are labelled.

For the Z-direction build, 1 of the 3 copies was printed outlet-down (Z3) and the others (Z1, Z2) outlet-up. All junctions built in the Z-direction suffered from sample inlet channel constriction due to cave-in of the thin vertical walls around it, but the extent was less severe in the Z3 direction. The Z-direction

build direction gave smoother channels than the X-direction build, as laser-overcuring was limited to the sheath inlet channels and slightly on the neckdown region.

In contrast, the Y-direction build gave far smoother channel walls than the other two build directions as they were built parallel with the build direction, and laser-overcuring was absent (instead, it was found on the device underside, thus making the chips less transparent, but this is easily remedied by polishing³⁴, as can be seen in Figure 3.5). This build direction gave very good shape conformity and dimensions compared to the other two (see Table 3.1), the only significant difference being the slight constriction of the sample inlet channel adjacent to the junction mouth, again due to the thinness and weakness of the surrounding walls.

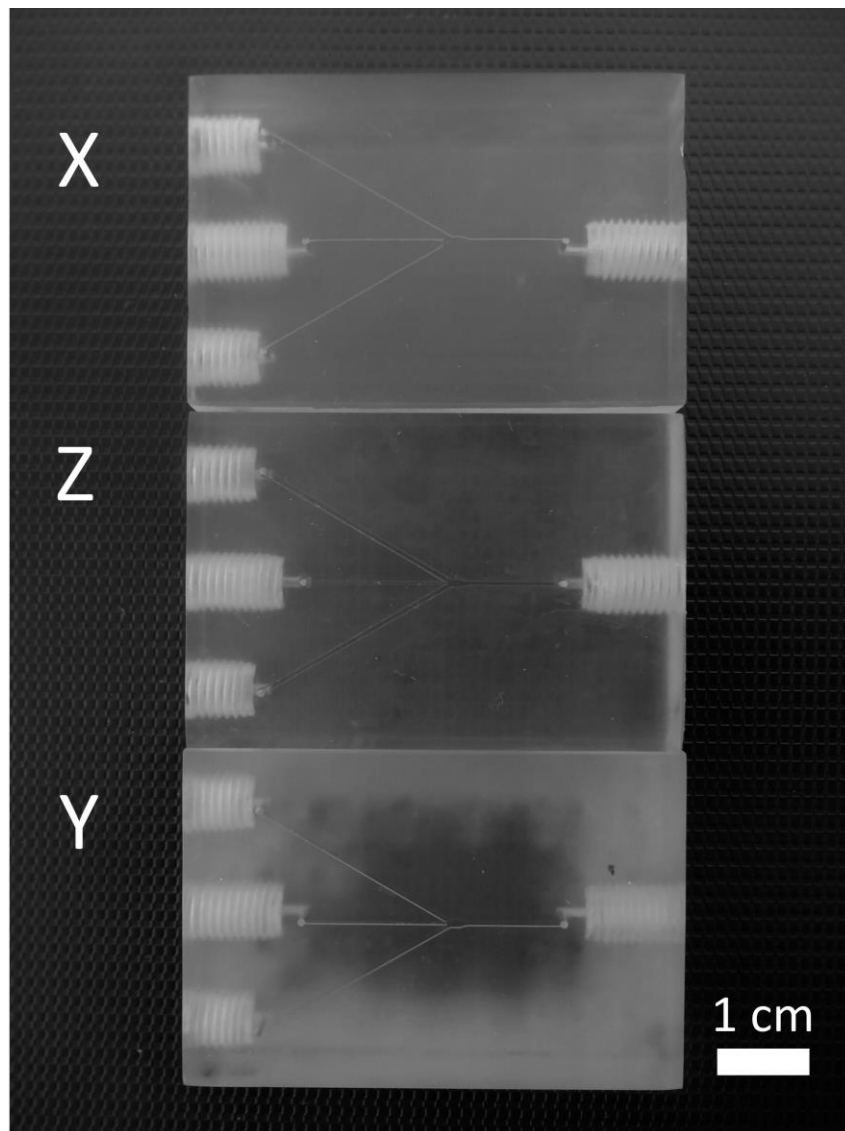


Figure 3.5 Hydrodynamic focusing junction prototypes printed in the three build directions (top-to-bottom, X, Y and Z), and after thread tapping.

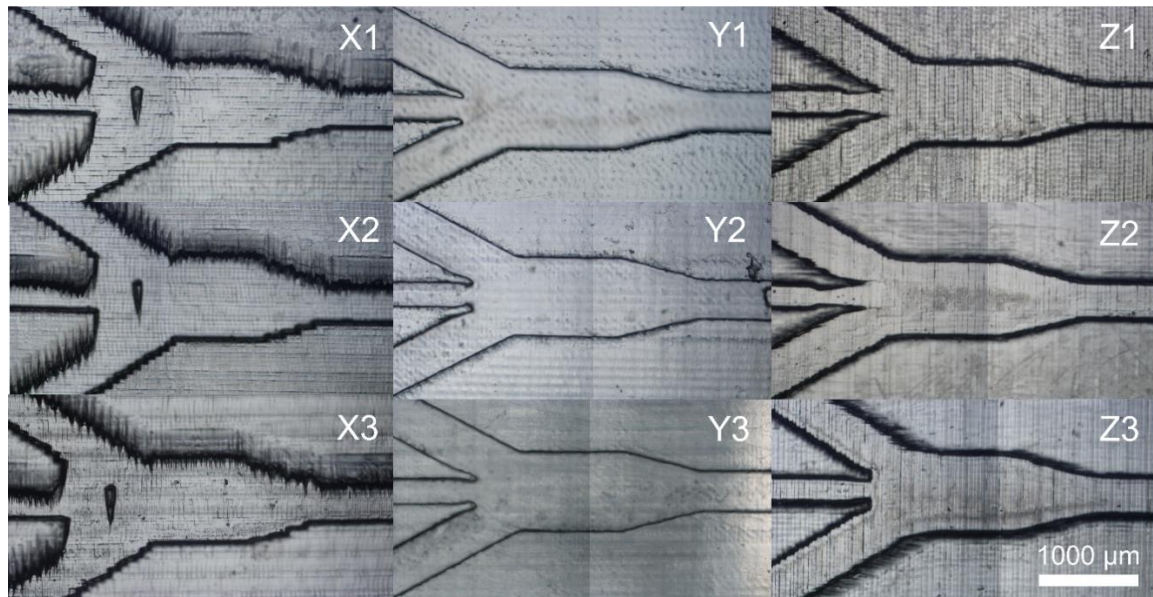


Figure 3.6 Photographs of hydrodynamic focusing junctions built in the three build directions: X-direction build (1st column), Y-direction build (2nd column), Z-direction build (3rd column).

Table 3.1 gives the mean measured channel widths for the prototype hydrodynamic focusing junctions across the 3 build directions from the three separate device repeats (Figure 3.6) for each. The majority of channels across the three build directions came out narrower than nominal. We believe this narrowing to be due to a number of reasons: post-print solidification of residual SLA resin trapped in the channels, laser-overcuring, and stair-stepping.

The smallest channel, the 250 μm width sample inlet, is significantly narrowed from nominal in all three build directions due to the aforementioned adjacent wall thinness in the Y-direction build, laser-overcuring on the ‘ceiling’ wall in the X-direction, and cave-in of adjacent walls in the Z-direction. With the exception of one of the two Y-direction channels, sheath inlet channels were $\sim 40\text{--}84$ μm narrower (X-direction) or wider (Y- and Z-directions) or than nominal. The latter discrepancy is thought to be due to widening during the splicing process of these diagonal surfaces. The large degree of narrowing in the X-direction chip channels is due to the aforementioned severe stair-stepping. The Y-direction gave the closest widths to nominal values for all channels, with its two largest channels (the junction chamber and the outlet channel) having mean widths only 2–9 μm smaller, and the others 16–40 μm smaller. The Y-direction build also gave the lowest channel width variation between the three chip copies by far, with standard deviation (SD) being only 2–6 across chip repeats for all channels. In contrast, the other two build directions had SD values ranging up to 49.

Table 3.1 Measured mean channel widths of focusing junctions in the three build directions, averaged over 3 device copies, 10 measurements taken of each channel.

Junction part	Nominal length	Measured aspect	Build direction		
			X	Y	Z
Focusing junction width	800 μm	Mean width / μm	802	798	782
		SD	2	2	22
Sample inlet channel width	250 μm	Mean width / μm	143	229	182
		SD	49	4	13
Sheath inlet channel 1 width	400 μm	Mean width / μm	351	440	441
		SD	16	6	23
Sheath inlet channel 2 width	400 μm	Mean width / μm	345	416	456
		SD	25	5	9.7
Outlet channel width	400 μm	Mean width / μm	316	391	360
		SD	2	2	9

There have been a number of Y-direction SLA straight microchannel test pieces reported in literature, but results vary and there is no study similar to ours (non-DLP-SLA, open channels): Shallan, et al. produced open channels with widths ranging from 300–500 μm via DLP-SLA, and found them to be 50–100 μm narrower than nominal³⁸. Folch, et al. produced internal channels with 300–1000 μm widths and found widths to vary from nominal by only a few percent either way (narrower or wider)³⁴. However, MacDonald, et al. also produced internal channels ranging from 300–500 μm , by DLP-SLA, and found them to be consistently wider than nominal by $\sim 25 \mu\text{m}$, which corresponds to half a pixel¹.

As well as comparing chip reproducibility in the form of channel width variation across chip copies, we also looked at channel width variation *within* chip copies as a measure of channel roughness. Table 3.2 gives the mean %CV of the channel width measurements taken for each channel across the chips, along with the mean channel width range. With the exception of the sheath channels, the Y-direction channel variation was a fraction of the others. Overall, the Y-direction build had significantly smaller ranges than those of the other directions, at times (for the focusing junction and the outlet channel) being $\sim 6\times$ smaller than the X-direction build. The X-direction variation was particularly bad due to laser-overcuring.

Table 3.2 Measured mean variation within hydrodynamic focusing junction channels built in the 3 build directions (averaged over three device copies, 10 measurements taken of each channel): an indication of channel wall roughness.

Junction part	Nominal length	Measured aspect	Build direction		
			X	Y	Z
Focusing junction width	800 μm	Mean %CV	2.4	0.5	1.5
		Mean width range / μm	63	12	32
Sample inlet channel width	250 μm	Mean %CV	30	7.2	12.6
		Mean width range / μm	106	50	64
Sheath inlet channel 1 width	400 μm	Mean %CV	4.9	1.8	3.7
		Mean width range / μm	50	23	50
Sheath inlet channel 2 width	400 μm	Mean %CV	7.2	2.4	2.3
		Mean width range / μm	63	29	31
Outlet channel width	400 μm	Mean %CV	6.0	0.8	1.6
		Mean width range / μm	58	9	16

3.5.2.2 Build direction effects: dye testing

Two dye solutions (methylene blue and solochrome red, aqueous) were used to investigate the effects of build direction on the resulting laminar flow quality of the hydrodynamic focusing junction prototypes, as well as the Y-junctions (Figure 3.7). The Y-direction build gave the most laminar flow, as evidenced by having the sharpest dye stream interfaces. This was attributed to being due to its highly smooth channel walls. In contrast, rough channel walls as found in the X- and Z-directions gave more indistinct dye stream interfaces, thought to be due to laminar flow disruption from frictional wall shear stresses^{96,97} and velocity perturbations⁹⁸ as covered in Chapter 2 (however, the exact nature of impact of additively-manufactured stepping and other surface roughnesses on microfluidic performance has yet to be clearly understood³). These observations build on those of Folch, et al. and Macdonald, et al., who carried out similar printed flow studies^{1,34}. Folch, et al. compared dye streams in SLA-made flow focusing junctions in the Y- and Z-directions and noted a difference in flow profile but gave no further comment³⁴. Macdonald, et al. printed Y-junctions in the Y-direction in 3 different

AM types (DLP, material-jetting and FDM) and measured increased levels of stream mixing for higher instances of channel roughnesses¹.

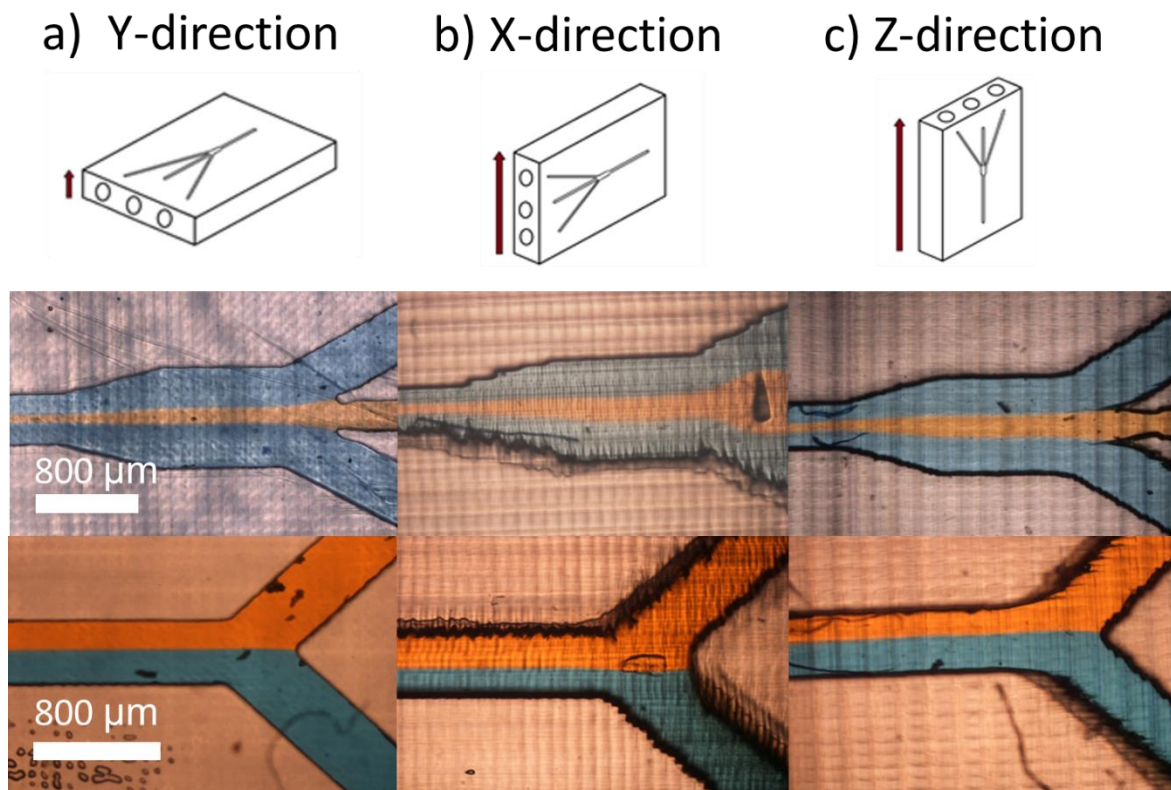


Figure 3.7 Dye solution flows in hydrodynamic focusing junctions (middle row) and Y-junctions (bottom row) printed in the three build directions (top row) a) Y-direction, b) X-direction and c) Z-direction.

However, for our study only single copies of each build direction were investigated, and the effects of changing temperature and humidity were also not looked into.

3.5.2.3 Build direction effects: minimum core stream size

The focusing behaviour of hydrodynamic junctions made in the three build directions was compared over a range of inner/sheath flow ratios: the sheath flow rate was kept constant with its applied pressure kept at 200 mbar, whilst the inner flow rate was varied. The resulting focused core streams were photographed and their widths measured (Figure 3.8). Figure 3.8 has no y or x axes intercepts, the former due to core streams failing to be formed at low inner/sheath flow rate ratios due to significant back pressure from the sheath flows, the latter reflecting the thinnest core stream diameter possible for the inner/sheath flow ratio in question. As would be expected by the high quality laminar

flows witnessed in the Y-direction focusing junction and Y-inlet junction (Figure 3.7), the Y-direction build gave the narrowest stable core stream diameter (18 μm). This value is critical because it is very closely related to the limit of detection for the device, as this value effectively dictates the smallest particle/cell diameter that can be focused into a single-file. An 18 μm diameter covers larger cells such as monocytes ($\sim 17\text{--}20\ \mu\text{m}$)⁹⁹, but not smaller cells such as red blood cells⁹⁹ ($\sim 6\ \mu\text{m}$) and bacteria ($\sim 0.5\text{--}1\ \mu\text{m}$ diameter and $\sim 2\text{--}5\ \mu\text{m}$ length)¹⁰⁰.

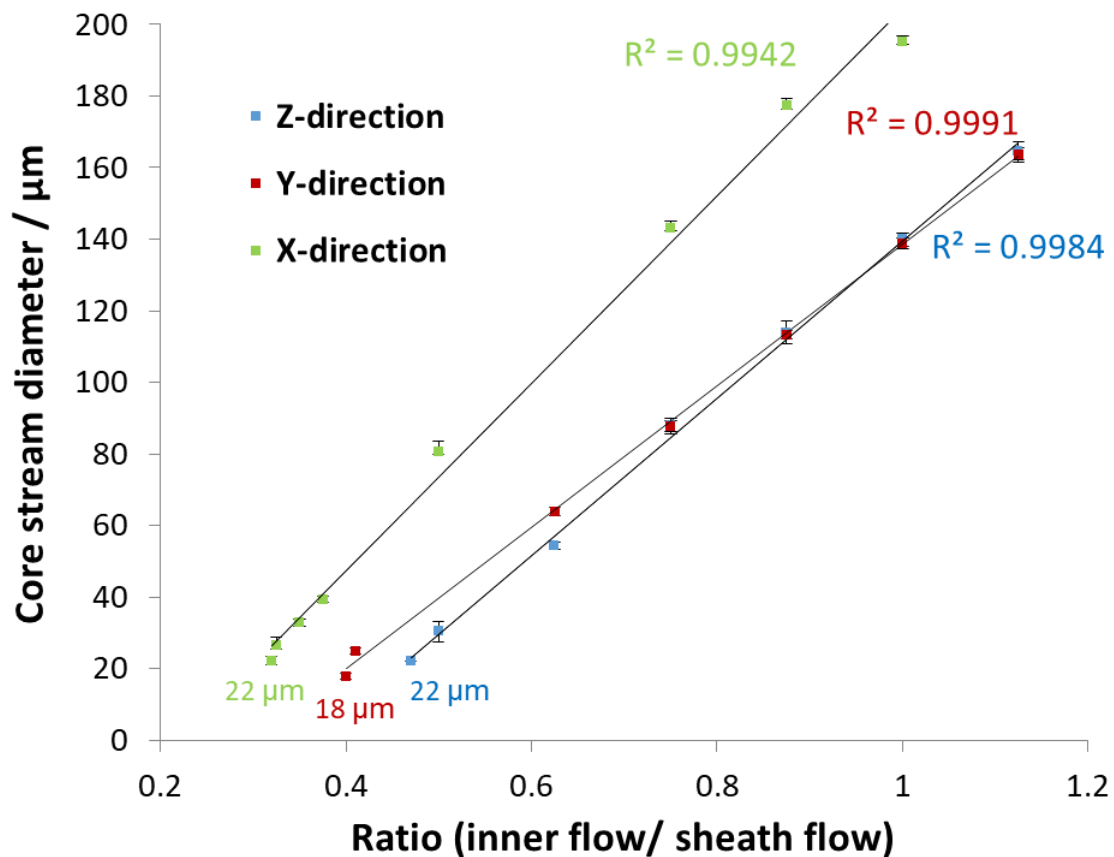


Figure 3.8 Plots of measured dyed core stream diameters created with different inner/sheath flow rate ratios for hydrodynamic focusing prototypes printed in the 3 different build directions at a 200 mbar inner flow. The smallest possible stable core stream diameters are indicated. Error bars denote standard deviation of five separate width measurements taken from one image.

The gradients for the three build directions in Figure 3.8 were similar (indicating a similar degree of widening/narrowing with differing flow rate ratios). The X-direction hydrodynamic junction required relatively higher sheath flow rates to produce the same core stream widths as the other two junctions, possibly due to disruption of the core stream due to the residual artefact. The error bars denote the

standard deviation of five separate width measurements made from a single image of each core stream, taken up to $\sim 400 \mu\text{m}$ after the neckdown section, in the slug flow region (see Chapter 2.5.1).

3.5.3 Sensor grooves

Three main approaches to AM microfluidic sensor integration have been utilised: pausing of the build either for sensor printing^{31,72} or embedding of commercially available fittings^{21,75,101,102}, or dedicated printed housing grooves followed by sealing^{27,37}. The build-pausing methods are time-consuming in SLA. However, printed sensor grooves must strike a balance between being too large and too tight, or the device will be prone to fluid leakages, or sensor embedding will be prevented, respectively. Thus, the nominal accuracy and reproducibility of 3D printed grooves were investigated: grooves with semicircle-like cross-sections (Figure 3.9) were fabricated in a range of diameters (200, 230, 235, 240, 250 and $300 \mu\text{m}$) in triplicate repeat sets on 3 mm thick wafers in a Y-direction build. This groove shape is based on those of Monaghan, et al³⁷.

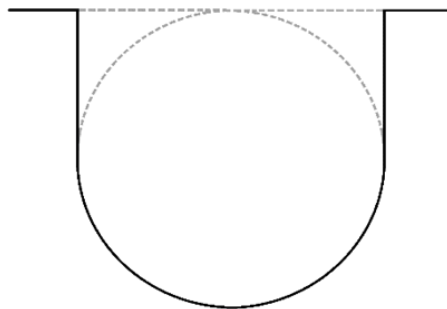


Figure 3.9 Illustration of a fibre/electrode groove cross-section on a printed part surface. The groove allows full fitting of a circular waveguide/wire whose edge is flush with the part surface, impossible with semi-circular grooves, but is susceptible to leaks on either side.

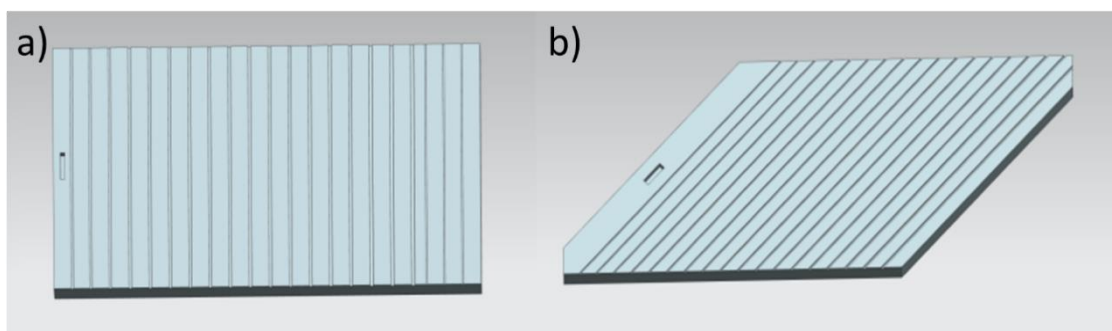


Figure 3.10 CAD files of 3D printed wafers made with surface a) straight and b) diagonal, 45° grooves.

The CAD file for the wafers are shown in Figure 3.10. Grooves were printed straight (Figure 3.10a), or diagonal (grooves built at 45°, Figure 3.10 b) on the build bed, and the resulting effects on dimensional accuracy were measured. The reason for the diagonal grooves was two-fold: to investigate the effect on nominal accuracy, and because optical fibres at an angle to the microchannel could be used to measure side scatter (SSC), and so allow fluorescence detection.

Figure 3.11 shows measured widths for straight-printed (blue) and diagonally-printed (red) grooves compared against theoretical grooves with widths identical to nominal (black). Straight grooves printed slightly wider than nominal widths (Figure 3.11 and Table 3.3). This disparity to the narrowing seen in the microfluidic channels in Chapter 3.5.2.2 is believed to stem from the curved shape of the grooves, as narrower channel widths than nominal were later seen for square cross-section pore channels (Chapter 3.5.5.1). In comparison, diagonal grooves came out significantly narrower (Table 3.4) due to stair-stepping superseding this effect¹⁰³.

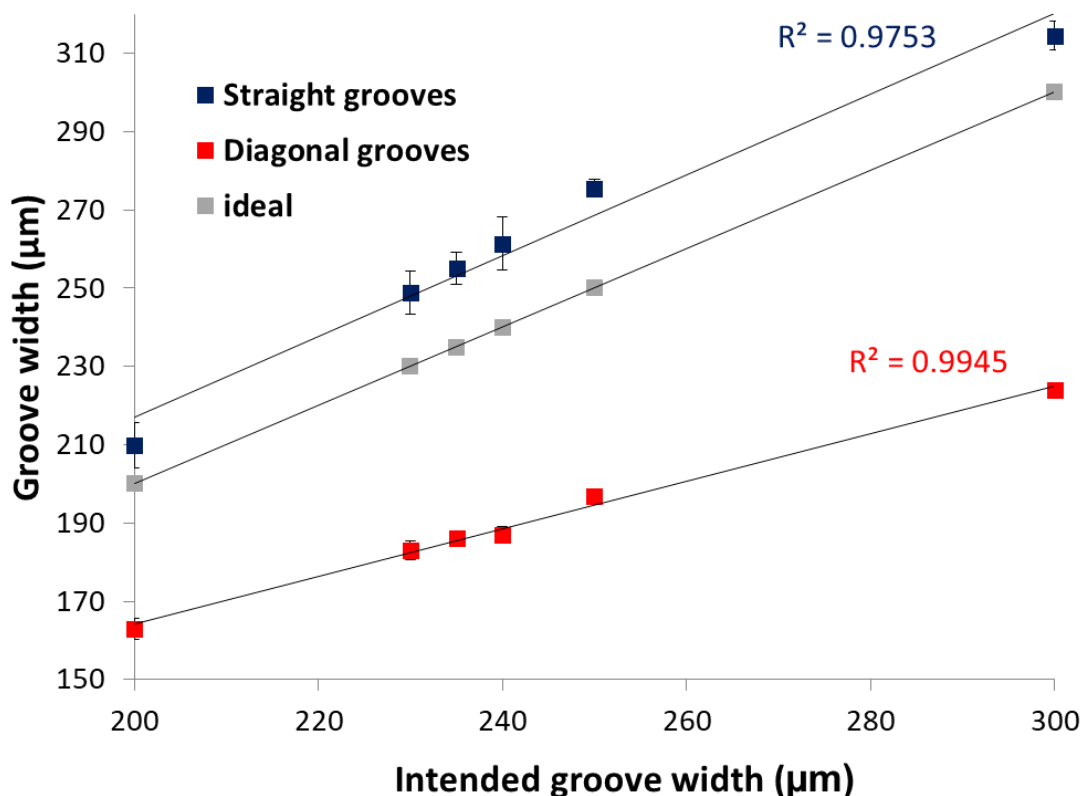


Figure 3.11 Deviation from nominal groove width as in STL file (grey) by straight (blue) and diagonal (red) grooves. Points denote mean width of sets of three groove repeats, with 15 measurements taken of each pore. Error bars denote the standard deviation of the mean pore widths in each set of three repeats.

A large gap between the fibre/electrode and the groove can cause fluid leakage. Thus, a groove diameter value of 235 μm gave the best fit for our 250 μm diameter fibres, being only 5 μm wider. Tables 3.3 and 3.4 give the resulting groove widths for each dimension, along with the % difference from nominal, and the SD between groove repeats and between measurements taken within grooves. Straight grooves had widths $\sim 10\text{--}20$ μm larger than nominal and diagonal grooves $\sim 40\text{--}50$ μm smaller than nominal, with the exception of the largest, 300 μm widths, which were ~ 70 μm smaller. There is no similar SLA groove study known to the author to compare to. The closest is that of Walczak, et al., who printed semicircle sensor grooves with nominal diameters of 1500 and 2400 μm via two material jetting printers, and gained resulting diameters 4% and 5% larger respectively for Projet printing, and 16% and 8% smaller respectively for Objet.

Table 3.3 Mean widths (stemming from sets of three groove repeats, with 15 separate measurements taken of each pore), difference from nominal values, and SD between grooves and within grooves of printed straight grooves.

Nominal groove width / μm	200	230	235	240	250	300
Mean groove width / μm	210	249	255	261	276	315
Difference from nominal as % of nominal	5.0	8.3	8.5	8.8	10.4	5.0
Inter-groove mean SD	5.9	5.6	4.1	6.7	2.2	3.5
Intra-groove mean SD	3.1	4.0	4.1	2.7	3.8	3.8

Table 3.4 Mean widths (stemming from sets of three groove repeats, with 15 separate measurements taken of each pore), difference from nominal values, and SD between grooves and within grooves of printed diagonal grooves.

Nominal groove width / μm	200	230	235	240	250	300
Mean groove width / μm	163	183	186	187	197	224
Difference from nominal as % of nominal	-18.5	-20.4	-20.9	-22.1	-21.2	-25.3
Inter-groove mean SD	2.7	2.4	2.0	2.2	0.9	1.8
Intra-groove mean SD	2.1	3.1	3.7	2.8	3.8	2.8

The mean variance between groove repeats was found to be $\sim 4\text{--}6$ μm for 200–240 μm straight grooves and 3 μm for bigger (250–300 μm) straight grooves. Interestingly, diagonal grooves only had 1–3 μm mean variance between repeats.

As seen in Figure 3.9 the grooves had gaps on either side of the fibre/electrode, so there were concerns about fluid leakages. It was found that the Tesa® tape adhesive was flexible enough and strong enough to seal these gaps if the cover layer was firmly applied. However, to fully prevent incidence of leakages, Araldite® resin was used around the sensor/chip interface.

3.5.4 Threads

Fluidic inlets and outlets of the initial optical chip prototypes and the Y-junction chips consisted of tapped M6, 1/16" threads for interfacing to standard HPLC fittings. These threads were milled out of the plastic body via a tap and die kit. The grinding action involved in this tapping process created a large amount of debris in the form of Accura® 60 swarf, which caused blockages during experiments. To remedy this, threads were instead incorporated into subsequent CAD designs. It can be challenging to produce mating parts with 3D printing due to dimensional errors¹⁰⁴. Indeed, the quality of the resulting printed threads were greatly affected by the build direction (Figure 3.12): horizontally-printed threads had a sunken ceiling due to laser over-curing (Figure 3.12 a). Use of these printed threads created swarf from the fittings grinding the deformed threads. In contrast, vertically printed threads were of a relatively very high quality (Figure 3.12 b). As a result, subsequent optical chip configurations incorporated vertically-printed threads on the device underside. However, this made holding of the device and tubing into a system somewhat awkward, culminating in the incorporation of custom juts into the chip design (see Chapter 4.5.1) to steady it within our microscope set-up.

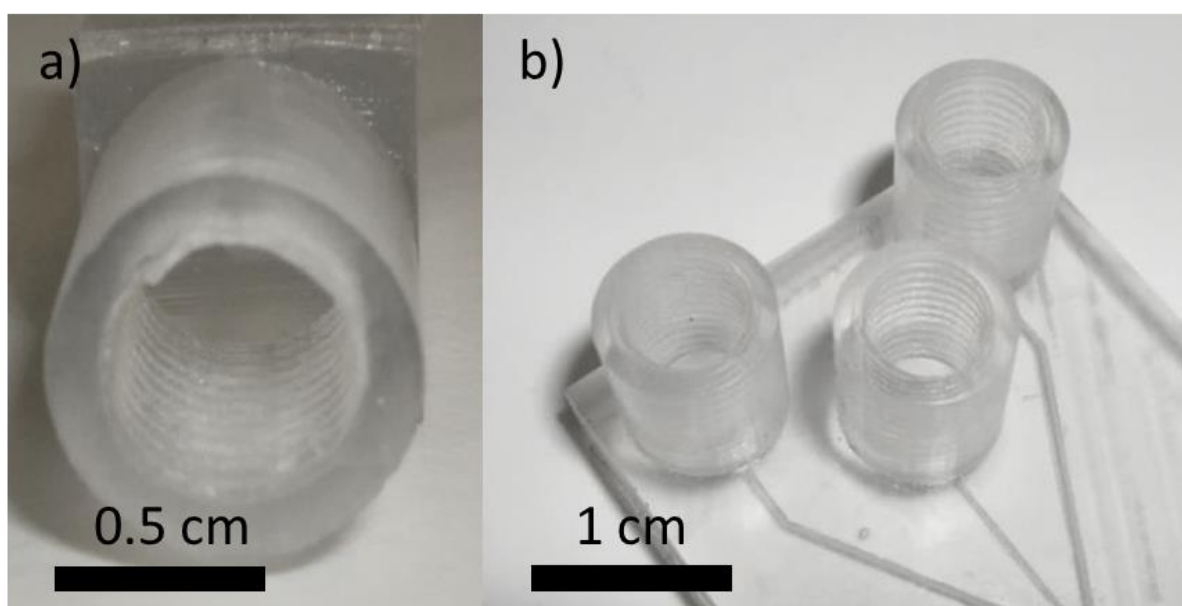


Figure 3.12 3D printed 1/16" threads printed a) horizontally and b) vertically, the former displaying laser overcure present on the thread 'ceiling'.

3.5.5 Resistive pulse sensing chip

A pore/channel constriction is required in RPS in order to generate the current pulses that indicate particle/cell size and other properties, as well as ensure a more uniform electric field. Due to the open printing style used in this project, the pore channel was placed at the device surface, with ramps being added to prevent particle trapping at the sudden vertical wall face.

3.5.5.1 Pore resolution study

Smaller pore dimensions give higher RPS sensitivities in terms of lower minimum detectable particle size, as the particle to pore volume ratio is higher. Thus, we investigated the smallest pore channel width possible via a Viper si2 SLA printer in Accura® 60 in HR mode by printing of a series of different pore widths on a test wafer. The CAD file of this pore array wafer is shown in Figure 3.13. Pore channel length was held constant at 500 μm , whilst square cross-sectional (channel depth=channel width) dimensions were decreased from 110 μm down to 40 μm in 10 μm increments. Six repeats were made of each pore width. Pore ramps were included with 100 μm lengths.

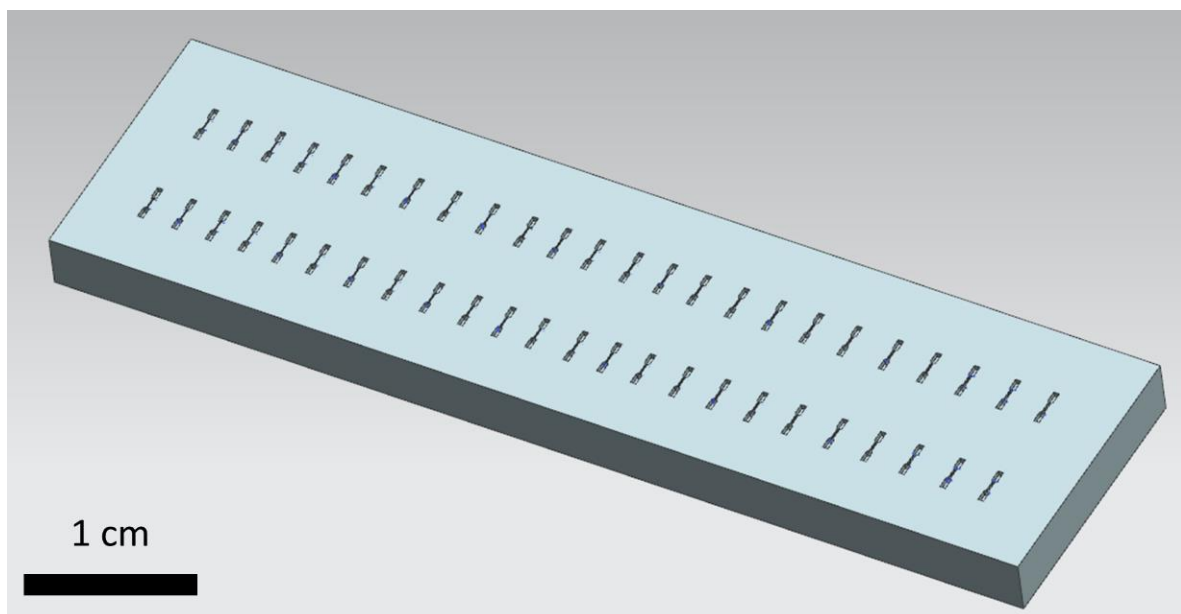


Figure 3.13 CAD file of RPS pore channel array. Pores had lengths of 500 μm , and square width and depth cross-sections of 110 μm , 100 μm , 90 μm , 80 μm , 70 μm , 60 μm , 50 μm and 40 μm . There were six repeats made of each pore dimension.

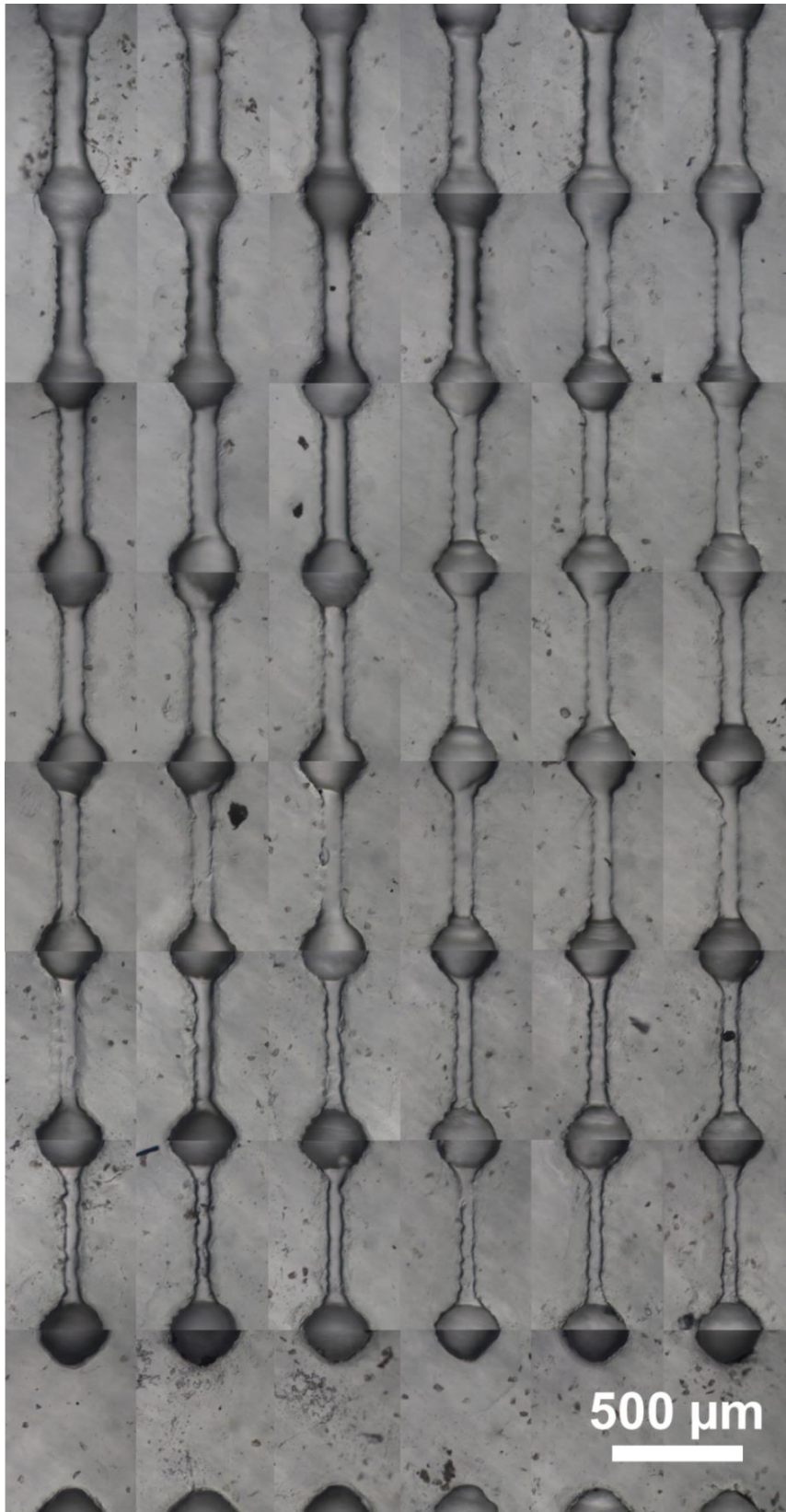


Figure 3.14 Photographs of RPS open pore channels, made by SLA in Accura® 60 in the Y-direction build, in HR mode, showing a range of nominal widths (rows, top-to-bottom): 110 μm , 100 μm , 90 μm , 80 μm , 70 μm , 60 μm , 50 μm , 40 μm .

Figure 3.14 shows the resulting pore channels formed in the pore array wafer. All pore channels had jagged edges, but the 50 and 60 μm width pores had particularly rough walls. At 40 μm nominal pore channel widths, the pore channels did not form at all.

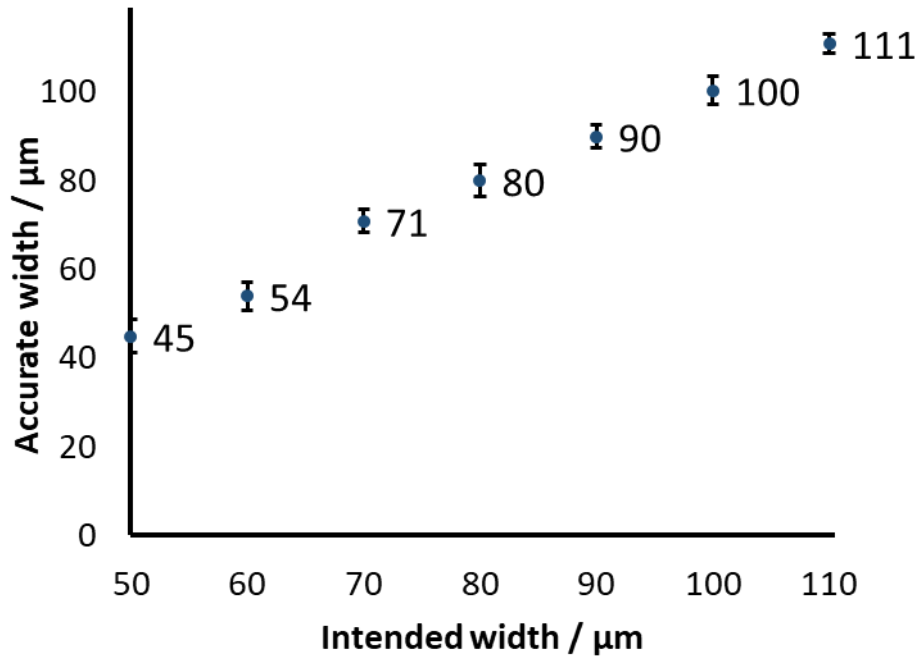


Figure 3.15 Mean measured pore widths in printed pore array wafer, calculated from the mean widths of each pore in a set of six repeats, with 15 separate width measurements made on every pore repeat. Error bars denote the standard deviation of the mean pore widths in each set of six repeats.

Figure 3.15 shows the resulting mean measured pore widths from the pore array wafer. The measurement technique accuracy was ± 1 pixel, which corresponded to $\pm 0.92 \mu\text{m}$. Similar to the microfluidic channels in Chapter 3.5.2.1, the pore channels were narrower than nominal. With the exception of widths smaller than 70 μm , the mean pore widths were $\leq 1 \mu\text{m}$ off nominal values. At 50 μm and 60 μm widths the pores are 10% thinner than nominal. Figure 3.16 shows the mean channel width variation (in the form of channel width SD). The seemingly low values for the 60 and 70 μm widths are due to having only a small number of very large protruding bumps. This is corroborated by Figure 3.17, which shows the mean channel width ranges for the pores in the wafer array.

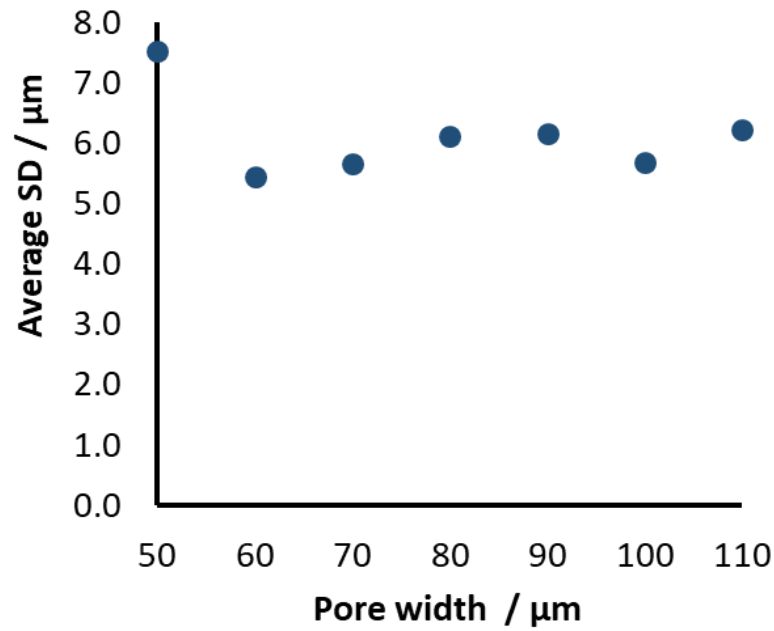


Figure 3.16 Mean measured width variation within pore channels in printed pore array wafer.

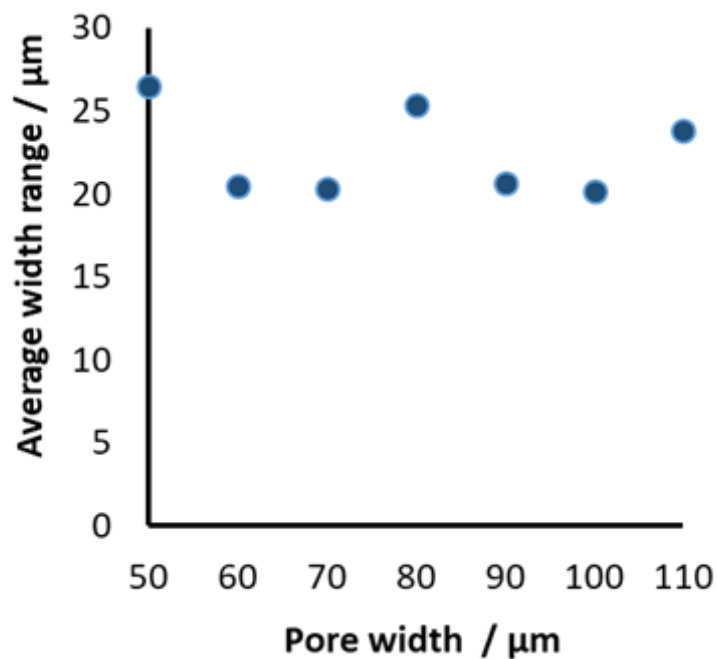


Figure 3.17 Mean measured pore channel width ranges found in printed pore array wafer.

We believed that the observed channel width narrowing from nominal, along with the wall roughness seen especially in the smallest channels, was due to trapped uncured resin residues curing post-printing. The jaggedness seen in the pore channel walls is not due to stair-stepping as the walls were built parallel with the build directions. Regular roughness in SLA-made microchannels have been

observed by Lade, et al.¹⁰⁵ and Folch, et al.³⁴, who both theorised that they stem from the Gaussian energy profile of the laser resulting in vertical sidewalls being generated as a series of stacked parabolas^{34,105}. Striped surfaces in non-microfluidic Accura[®] 60 parts have also been witnessed¹⁰⁶. However, these marks or ‘ripples’ are ~300 μm wide¹⁰⁵, far larger than the widths of these pore channels. Our roughness is similar to the small-scale 50–100 μm irregularities reported by Lade, et al.¹⁰⁵, who simply described it as being polymer roughness.

3.5.6 Particle fouling investigation

3.5.6.1 Cured Accura[®] 60 structure

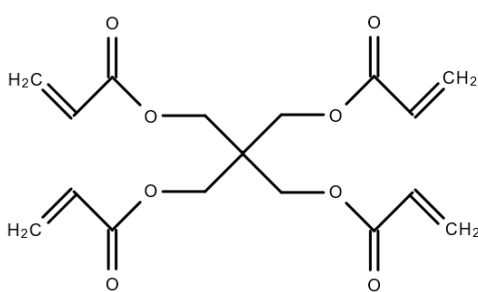
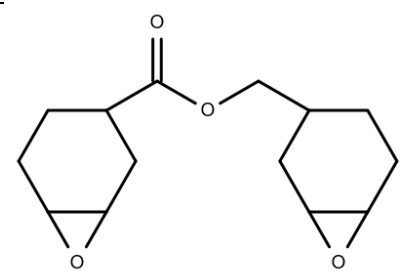
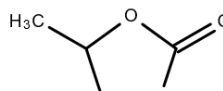
SLA photopolymerisation resins consist of monomers, photoinitiators, and additives, and can be classified into three categories based on their monomer type: free radical, cationic or hybrid. Epoxide (which polymerise via photocationic mechanisms) and acrylate (which polymerise via free radical polymerisation) monomers are the most common types of SLA resin³ due to their high photosensitivity and polymerisation speed, but they require anhydrous conditions and suffer from poor dimensional stability, respectively¹⁰⁷. Hybrid resins, which contain a mixture of the two types of monomer, benefit from a synergistic effect between the two, being slower in photospeed but having lower viscosities, higher build accuracies and impact strengths¹⁰⁸.

Accura[®] 60, a commercially available epoxy/acrylate hybrid resin produced by 3D Systems, was selected as the printing polymer for all of the test pieces and devices in this work, due to its high optical transparency, resistance to swelling in the presence of water¹⁰⁹, stiffness, durability and its ongoing success in microfluidic fabrication^{11,37,109}. It is made to mimic PC in its optical transparency. The exact composition of Accura[®] 60 is proprietary information, but it contains epoxy and acrylate monomers, a triarylsulfonium salt mixture and propylene carbonate (Table 3.5)¹¹⁰.

The reaction mechanism of both free radical polymerisation of acrylates and photocationic polymerisation of epoxides is highly complex^{111,112} and form large, cross-linked networks. When a hybrid epoxy/acrylate resin polymerises an interpenetrating network (IPN) of the two is formed¹¹³. IPNs are a type of polymer blend as opposed to a copolymerisation, as the two polymerisation processes occur independently of each other¹¹³. However, despite consisting of two separate networks, IPNs act as a uniphase material¹¹³. The degree of interlinking or separation of these two networks, i.e. the size

of the epoxy and acrylate regions, is affected by the monomer concentration ratio^{107,114}. The two networks do not chemically bond unless a coupling agent with both functional groups is included in the resin¹⁰⁷.

Table 3.5 Chemical components found in uncured 3D Systems Accura[®] 60 photopolymer resin.

Component	Chemical structure	Function
Ethoxylated pentaerythritol tetraacrylate		Tetra acrylate monomer
3,4-Epoxy cyclohexylmethyl 3',4'-epoxycyclohexane carboxylate		Diepoxide monomer
Mixture of triarylsulfonium salts	Unknown (proprietary information)	UV initiator
Propylene carbonate		Non-reactive diluent

3.5.6.2 Cured Accura[®] 60 wafer adsorption study

One factor that can cause microfluidic particle adsorption is electrostatic attraction between particles and the channel wall material. This attraction can cause adsorption to happen if the trajectory of a slow-moving particle moves it close enough to a channel wall to interact with it. As mentioned earlier, when Accura[®] 60 resin is cured via SLA, it forms a striped surface¹⁰⁶. This striped microstructure is a result of the laser-based SLA manufacturing process¹⁰⁶. We carried out a simple study to measure particle adsorption onto a cured Accura[®] 60 polymer wafer using negatively-charged and positively-charged 1 μm polystyrene beads. We applied two charged polyelectrolyte coatings, polyethylenimine (PEI) and poly(acrylic acid co-maleic acid (PAAMA) (Figure 3.18) to sections of the Accura[®] 60 surface for comparison. We hoped that this study might give some indication of polymer charge magnitude, based on simple laws of electrostatic repulsion (like-charges repel, opposite-charges attract). A negatively-charged polymer can be expected to repel negatively-charged beads but attract positively-

charged beads, and vice versa for a positively-charged polymer^{115,116}. We postulated that cured Accura® 60 would be highly negatively-charged due to the high number of oxygen atoms in its constituent monomers. This theory is somewhat backed up by X-ray photoelectron spectroscopy (XPS) measurements by Wilhelm, et al. on the surface of an Accura® 60 part, which showed that it was 24.3% oxygen, 73.6% carbon and 2.1% silicon¹⁰⁶. However, XPS of a charged, uncoated surface is not usually viable, but it is unclear from this paper the nature of the method used for this measurement.

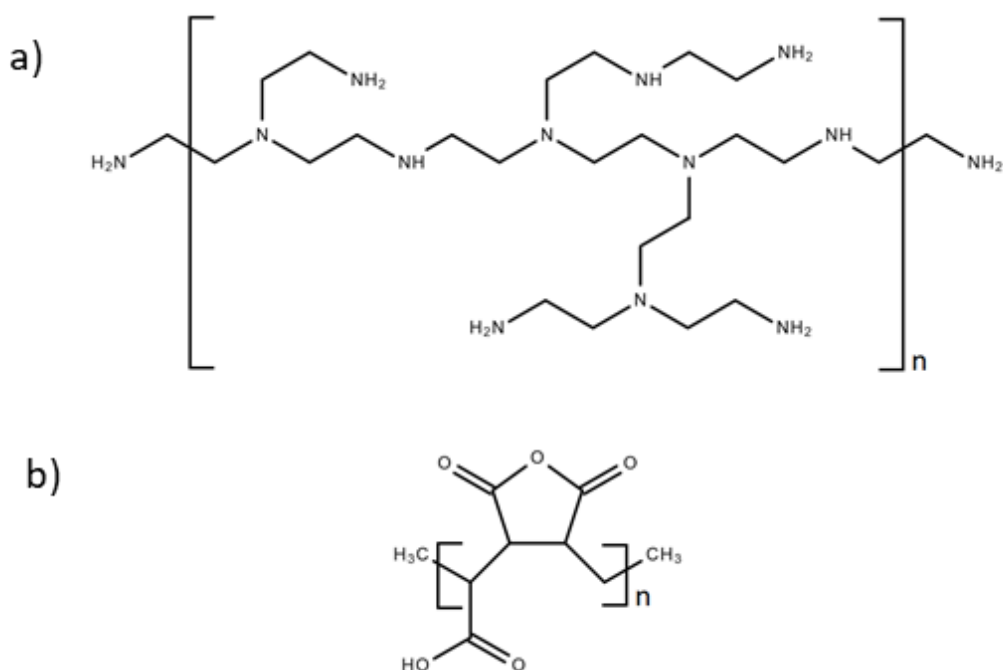


Figure 3.18 Structures of charged polymers: a) PEI, positively-charged polymer and b) PAAMA, negatively-charged polymer.

After coating application, two suspensions of 1 μm beads (1.1×10^8 particles mL^{-1} , 250 μl) were dripped onto each half of the wafer and left to incubate—the left half having COOH-coated, negatively-charged beads, and the right half having PEI-coated, positively-charged beads. Figure 3.19 shows the wafer during overnight incubation. The sections with opposite coating and particle charges have suspensions that lie flatter against the wafer surface, whilst those with like charges have suspensions that sit in bubbles on the surface due to repulsion. Following rinsing and drying, adsorbed beads were counted, with the results summarised in Table 3.6.

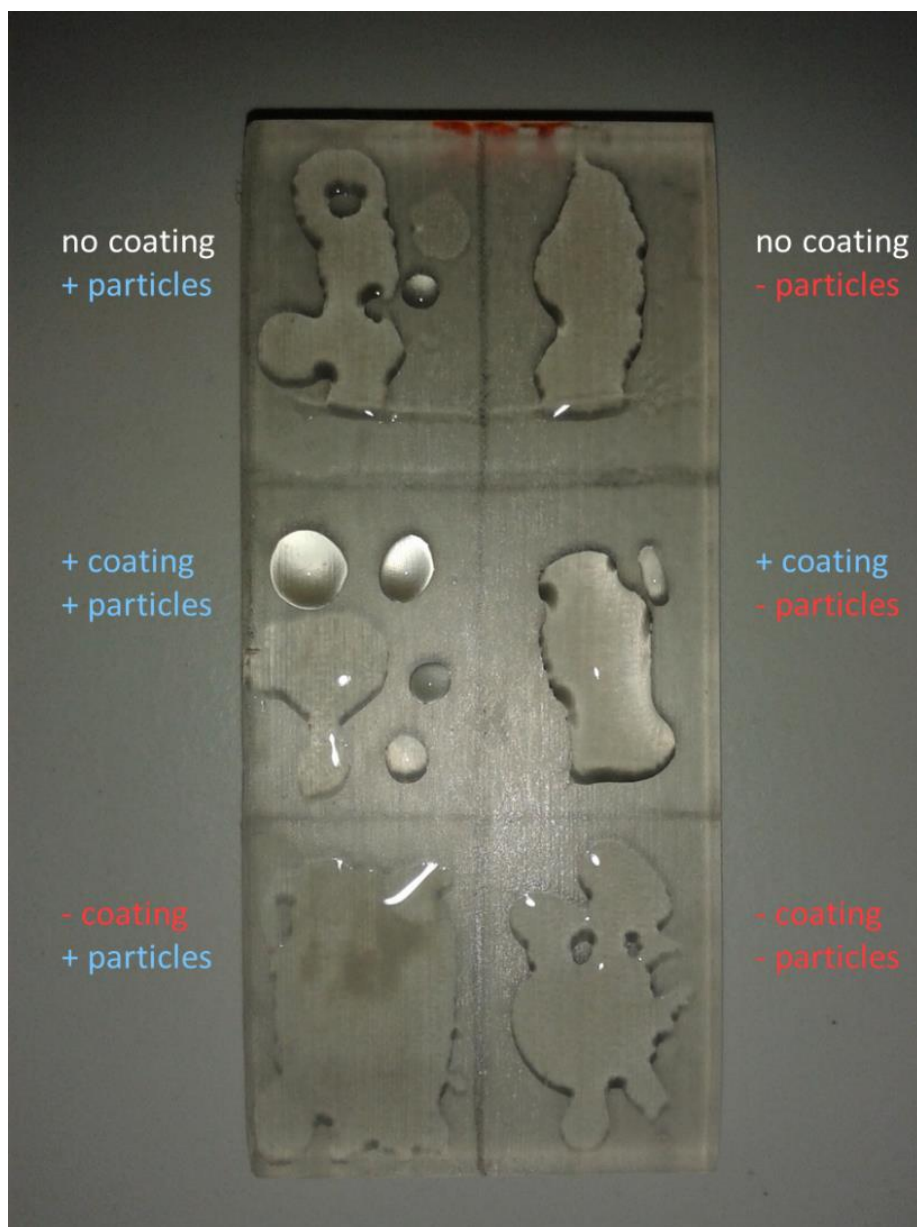


Figure 3.19 Photograph of printed Accura® 60 wafer during particle adsorption study. Aliquots (250 μ L) of different particle suspensions have been added to each wafer section to incubate.

Table 3.6 Mean counted adsorbed beads of opposite charge on the varying uncoated and coated sections of an Accura® 60 wafer, averaged from five separate 40 x 40 μ m sections.

Surface coating charge Particle coating charge	None		Positive		Negative	
	Positive	Negative	Positive	Negative	Positive	Negative
Mean no. of particles per 40 μ m ²	151	123	118	210	138	7
SD	33.0	62.2	27.0	111.3	71.9	1.1
%RSD	21.9	50.6	22.8	53.0	52.2	15.0

Unexpectedly, the uncoated Accura® 60 wafer surface adsorbed both positively and negatively-charged particles. We theorise that this may be due to chemical heterogeneity in the IPN, which can increase particle fouling¹¹⁷. If heterogeneity is present in microsystems its effects can be significant, especially in the small feature scales found in 2PP¹¹⁸. There is no literature investigating the chemical heterogeneity of Accura® 60.

3.5.6.3 Fouling into Accura® 60 microfluidic channels

A secondary particle adsorption study was carried out, to investigate if particles were also being trapped by stair-stepping inside channels. Four straight, 1000 µm diameter cylindrical channels were printed internally into a block (Figure 3.20 a). Two of the channels were first rinsed with water at 2000 mbar to remove polymer swarf or other debris, before being rinsed in PBS. Following this, outputted PBS was collected for use as a control. Subsequently, two suspensions of 1 µm polystyrene beads were swept through and collected separately. Counting via a QNano instrument against a calibration suspension showed a 34% recovery of the original particle concentration, followed by 97% recovery for the second. This loss decrease after the initial run seems to indicate that the majority of the fouling sites available were filled by the first particle run. The PBS control runs showed no particles within 30 s.

The other channel was sliced into two using a band saw and the channels examined under a microscope. Less than four particles were seen in each half. This indicated that either large numbers of particles had been adsorbed onto channel surfaces and became dislodged and lost during the sawing process, or particles had been trapped into device inlets and outlets instead. Particle fouling into or immediately after inlets/outlets has been observed in PDMS microfluidic devices and can be due to a sudden settling force experienced by particles on entering into a device⁸⁵.

To attempt to confirm if particle loss was due to inlet/outlet fouling, we carried out a bridged channel study: two straight channels were connected (Figure 3.20 b) and the same PBS and particle runs carried out, but using double the particle suspension volumes: thus, the number of inputted particles per channel surface area was kept constant but the number of inlets/outlets was doubled. Again, the PBS control run showed no particles in 30s, but found percentage recovery for the particle runs were 15% and 33%, respectively. These higher losses indicate particle loss into inlets/outlets is likely.

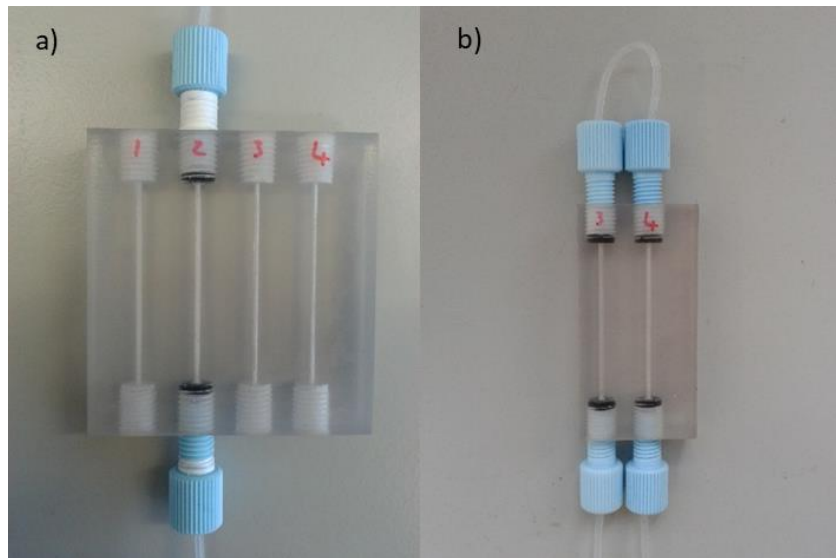


Figure 3.20 Photographs of 1000 μm diameter, internal, X-direction channels in Accura® 60 for second particle fouling study. a) Set of 4 solo channels and b) bridged pair of channels.

3.5.6.4 Particle adsorption onto support structures

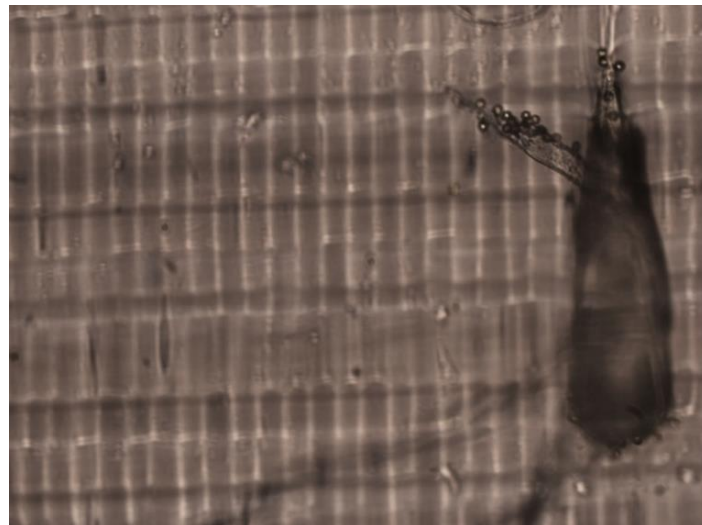


Figure 3.21 Photograph of support structure artefact inside X-direction build flow cytometer device, showing adsorbed particles.

A particle suspension was driven through one of the X-direction hydrodynamic focusing junctions in Chapter 3.5.2.1. It was observed that the particles are carried around the support structure by the laminar flow, but that they were also decelerated by this, allowing some to adsorb onto the support artefact. The particles seemed to be strongly attracted to the rough strands of the support structure (Figure 3.21).

3.6 Conclusions

Initial prototypes and pieces for the optical and RPS particle/cell analysis devices in this project were fabricated and investigated regarding three challenges: channel and part quality effects caused by build direction, particle fouling and sensor embedding. An open, surface-channel printing style as made popular in recent years was utilised to produce sensor junctions, Y-junctions, and hydrodynamic focusing junctions and pore channels for the optical and RPS chips, respectively. This printing style increases the print resolution by easing the flushing of uncured resin, allowing comfortable printing of channel diameters $<300\ \mu\text{m}$, usually unattainable for internally-printed channels.

Hydrodynamic focusing junctions were produced in the three build directions, and wall roughness, accuracy (in terms of shape quality and closeness to nominal dimensions), and reproducibility measured. The Y-direction build gave the highest quality channels regarding these parameters, as it minimised stair-stepping, laser-overcuring and support structure artefacts. It also had diminished transparency due to laser-overcuring on the part underside, but this was easily amended by polishing. This build direction gave the most ordered laminar flow interfaces, as turbulences from surface roughnesses were reduced. The Y-direction was then used to print subsequent device parts, including high quality device threads for fluidic input and output, preventing swarf production by tapping.

A range of sensor groove widths ($200\text{--}300\ \mu\text{m}$) were printed for $250\ \mu\text{m}$ diameter optical fibre and electrode embedding, manufactured parallel and diagonal to the build bed, for FSC and SSC sensing, respectively. Straight grooves were 5–10% wider and diagonal grooves $\sim 20\%$ narrower than nominal. A $235\ \mu\text{m}$ nominal width groove was determined to give the best fit for a $250\ \mu\text{m}$ diameter sensor.

The RPS pore channel resolution limit was investigated and found that below $70\ \mu\text{m}$ channel cross-section, channel quality rapidly erodes, and that the minimum channel width formable is $\sim 45\ \mu\text{m}$. Channel widths printed narrower than nominal due to solidification of residual resin.

Lastly, we investigated the nature of particle fouling into printed Accura[®] 60 devices, and found that trapping onto printed steps is probably insignificant, with loss into channels being mainly due to fouling into inlets/outlets. However, we also found that both positively- and negatively-charged particles will adsorb onto Accura[®] 60 polymer, possibly due to chemical heterogeneity from its IPN structure—this could lead to adsorption if particles are able to slow down sufficiently during flow.

3.7 References

- 1 N. P. Macdonald, J. M. Cabot, P. Smejkal, R. M. Guijt, B. Paull and M. C. Breadmore, *Anal. Chem.*, 2017, **89**, 3858–3866.
- 2 Y. Zhou, *J. Biomed. Sci.*, 2017, **24**, 1–22.
- 3 S. Waheed, J. M. Cabot, N. P. Macdonald, T. Lewis, R. M. Guijt, B. Paull and M. C. Breadmore, *Lab Chip*, 2016, **16**, 1993–2013.
- 4 J. M. Lee, M. Zhang and W. Y. Yeong, *Microfluid. Nanofluidics*, 2016, **20**, 1–15.
- 5 A. K. Au, W. Huynh, L. F. Horowitz and A. Folch, *Angew. Chem. Int. Ed.*, 2016, **55**, 3862–3881.
- 6 A. Hatch, A. E. Kamholz, K. R. Hawkins, M. S. Munson, E. A. Schilling, B. H. Weigl and P. Yager, *Nat. Biotechnol.*, 2001, **19**, 461–465.
- 7 K. Macounová, C. R. Cabrera and P. Yager, *Anal. Chem.*, 2001, **73**, 1627–1633.
- 8 E. A. Schilling, A. E. Kamholz and P. Yager, *Anal. Chem.*, 2002, **74**, 1798–1804.
- 9 D. Bartholomeusz, R. W. Boutté and J. D. Andrade, *J. Microelectromech. Syst.*, 2005, **14**, 1364–1374.
- 10 D. Prasad, *Int. J. Adv. Ind. Eng.*, 2015, **3**, 115–119.
- 11 A. J. Capel, S. Edmondson, S. D. R. Christie, R. D. Goodridge, R. J. Bibb and M. Thurstans, *Lab Chip*, 2013, **13**, 4583–90.
- 12 S. Sandron, B. Heery, V. Gupta, D. A. Collins, E. P. Nesterenko, P. N. Nesterenko, M. Talebi, S. Beirne, F. Thompson, G. G. Wallace, D. Brabazon, F. Regan and B. Paull, *Analyst*, 2014, **139**, 6343–6347.
- 13 V. Gupta, M. Talebi, J. Deverell, S. Sandron, P. N. Nesterenko, B. Heery, F. Thompson, S. Beirne, G. G. Wallace and B. Paull, *Anal. Chim. Acta*, 2016, **910**, 84–94.
- 14 W. S. Tan, S. R. Suwarno, J. An, C. K. Chua, A. G. Fane and T. H. Chong, *J. Memb. Sci.*, 2017, **537**, 283–296.
- 15 J. C. Snyder, C. K. Stimpson and K. A. Thole, in *Proceedings of ASME Turbo Expo 2015: Turbine Technical Conference and Exposition*, ASME, Montréal, Canada, 2015, pp. 1–10.
- 16 D. R. White, *Adv. Mater. Process*, 2003, **161**, 64–65.
- 17 R. J. Friel, K. E. Johnson, P. M. Dickens and R. A. Harris, *Mater. Sci. Eng. A*, 2010, **527**, 4474–4483.
- 18 C. Schalansky, Method of using additive materials for production of fluid flow channels, United States, Patent number: US20150137412A1, 21/05/2015.
- 19 P. J. Wolcott and M. J. Dapino, in *Additive Manufacturing Handbook: Product Development for the Defense Industry*, eds. A. B. Badiru and V. V Valencia, CRC Press, Boca Raton, FL, USA,

- 2017, pp. 275–313.
- 20 C. Polzin, S. Spath and H. Seitz, *Rapid Prototyp. J.*, 2013, **19**, 37–43.
- 21 J. L. Erkal, A. Selimovic, B. C. Gross, S. Y. Lockwood, E. L. Walton, S. McNamara, R. S. Martin and D. M. Spence, *Lab Chip*, 2014, **14**, 2023–2032.
- 22 V. Gupta, P. Mahbub, P. N. Nesterenko and B. Paull, *Anal. Chim. Acta*, 2018, **1005**, 81–92.
- 23 K. Plevniak, M. Campbell, T. Myers, A. Hodges and M. He, *Biomicrofluidics*, 2016, **10**, 054113.
- 24 M. J. Beauchamp, G. P. Nordin and A. T. Woolley, *Anal. Bioanal. Chem.*, 2017, **409**, 4311–4319.
- 25 L. J. Y. Ong, A. B. Islam, R. DasGupta, N. G. Iyer, H. L. Leo and Y. C. Toh, *Biofabrication*, 2017, **9**, 1–12.
- 26 S. Knowlton, C. H. Yu, F. Ersoy, S. Emadi, A. Khademhosseini and S. Tasoglu, *Biofabrication*, 2016, **8**, 1–13.
- 27 R. Walczak and K. Adamski, *J. Micromech. Microeng.*, 2015, **25**, 1–13.
- 28 N. Bhattacharjee, A. Urrios, S. Kang and A. Folch, *Lab Chip*, 2016, **16**, 1720–1742.
- 29 A. Tothill, M. Partridge, S. James and R. Tatam, *J. Micromech. Microeng.*, 2017, **27**, 1–16.
- 30 M. Bauer and L. Kulinsky, *Micromachines*, 2018, **9**, 1–20.
- 31 G. Gaal, M. Mendes, T. P. De Almeida, M. H. O. Piazzetta, Â. L. Gobbi, A. Riul Jr and V. Rodrigues, *Sens. Actuators B Chem.*, 2017, **242**, 35–40.
- 32 A. J. L. Morgan, L. H. San Jose, W. D. Jamieson, J. M. Wymant, B. Song, P. Stephens, D. A. Barrow and O. K. Castell, *PLoS One*, 2016, **11**, 1–17.
- 33 Dolomite Microfluidics, Rapid Microfluidic Prototyping—Fluidic Factory [online], 2016 [Accessed 02/10/2017]. Available from: <https://www.dolomite-microfluidics.com/product/fast-microfluidic-prototyping/>.
- 34 A. K. Au, W. Lee and A. Folch, *Lab Chip*, 2014, **14**, 1294–1301.
- 35 B. Bhushan, in *Biomimetics: Bioinspired hierarchical-structured surfaces for green science and technology*, Springer International Publishing, Cham, Switzerland, 2nd edn., 2016, pp. 327–382.
- 36 S. Ligon, R. Liska, J. Stampfl, M. Gurrll and R. Mulhaun, *Chem. Soc. Rev.*, 2017, **117**, 10212–10290.
- 37 T. Monaghan, M. J. Harding, R. A. Harris, R. J. Friel and S. D. R. Christie, *Lab Chip*, 2016, **16**, 3362–3373.
- 38 A. I. Shallan, P. Smejkal, M. Corban, R. M. Guijt and M. C. Breadmore, *Anal. Chem.*, 2014, **86**, 3124–3130.
- 39 L. Krejcova, L. Nejdil, M. A. M. Rodrigo, M. Zurek, M. Matousek, D. Hynek, O. Zitka, P. Kopel, V.

- Adam and R. Kizek, *Biosens. Bioelectron.*, 2014, **54**, 421–427.
- 40 K. G. Lee, K. J. Park, S. Seok, S. Shin, D. H. Kim, J. Y. Park, Y. S. Heo, S. J. Lee and T. J. Lee, *RSC Adv.*, 2014, **4**, 32876–32880.
- 41 W. Lee, D. Kwon, B. Chung, G. Y. Jung, A. Au, A. Folch and S. Jeon, *Anal. Chem.*, 2014, **86**, 6683–6688.
- 42 W. Lee, D. Kwon, W. Choi, G. Y. Jung and S. Jeon, *Sci. Rep.*, 2015, **5**, 1–6.
- 43 C. Park, J. Lee, Y. Kim, J. Kim, J. Lee and S. Park, *J. Microbiol. Methods*, 2017, **132**, 128–133.
- 44 Y. Xu, X. Wu, X. Guo, B. Kong, M. Zhang, X. Qian, S. Mi and W. Sun, *Sensors*, 2017, **17**, 1–37.
- 45 Y. Ni, R. Ji, K. Long, T. Bu, K. Chen and S. Zhuang, *Appl. Spectrosc. Rev.*, 2017, **52**, 1–31.
- 46 S.-Z. Guo, K. Qiu, F. Meng, S. Hyun Park and M. C. McAlpine, *Adv. Mater.*, 2017, **29**, 1701218.
- 47 C. Shemelya, F. Cedillos, E. Aguilera, D. Espalin, D. Muse, R. Wicker and E. MacDonald, *IEEE Sens. J.*, 2015, **15**, 1280–1286.
- 48 Y. Lin, T. Hsieh, L. Tsai, S. Wang and C. Chiang, *Sens. Mater.*, 2016, **28**, 389–394.
- 49 M. Saari, B. Xia, B. Cox, P. Krueger, A. Cohen and E. Richer, *3D Print. Addit. Manuf.*, 2016, **3**, 136–141.
- 50 R. Zelený and J. Včelák, *Procedia Eng.*, 2016, **168**, 1338–1341.
- 51 M. G. Zubel, K. Sugden, D. Saez-Rodriguez, K. Nielsen and O. Bang, in *Proceedings of SPIE: Sixth European Workshop on Optical Fibre Sensors*, ed. E. Lewis, SPIE, Limerick, Ireland, 2016, vol. 9916, pp. 1–4.
- 52 J. T. Muth, D. M. Vogt, R. L. Truby, Y. Mengüç, D. B. Kolesky, R. J. Wood and J. A. Lewis, *Adv. Mater.*, 2014, **26**, 6307–6312.
- 53 M. Mannoor, Z. Jiang, T. James, Y. Kong, K. Malatesta, W. Soboyejo, N. Verma, D. Gracias and M. McAlpine, *Nano Lett.*, 2013, **13**, 2634–2639.
- 54 M. Sajid, J. Z. Gul, S. W. Kim, H. B. Kim, K. H. Na and K. H. Choi, *3D Print. Addit. Manuf.*, 2018, **5**, 160–169 .
- 55 S. L. Marasso, M. Cocuzza, V. Bertana, F. Perrucci, A. Tommasi, S. Ferrero, L. Scaltrito and C. F. Pirri, *Rapid Prototyp. J.*, 2018, **24**, 739–743.
- 56 M. F. Farooqui, M. A. Karimi, K. N. Salama and A. Shamin, *Adv. Mater. Technol.*, 2017, **2**, 1700051.
- 57 F. Salamone, L. Belussi, L. Danza, M. Ghellere and I. Meroni, *Sensors*, 2015, **15**, 13012–13027.
- 58 M. Paknahad, J. S. Bachhal, A. Ahmadi and M. Hoorfar, *Sens. Actuators B Chem.*, 2017, **241**, 55–64.
- 59 J. van Tiem, J. Groenesteijn, R. Sanders and G. Krijnen, in *2015 IEEE Sensors Proceedings*, Piscataway, Busan, South Korea, pp. 1430–1433.

- 60 E. MacDonald, R. Salas, D. Espalin, M. Perez, E. Aguilera, D. Muse and R. B. Wicker, *IEEE Access*, 2014, **2**, 234–242.
- 61 M. Banna, K. Bera, R. Sochol, L. Lin, H. Najjaran, R. Sadiq and M. Hoorfar, *Sensors*, 2017, **17**, 1–17.
- 62 Y. Hong, M. Wu, G. Chen, Z. Dai, Y. Zhang, G. Chen and X. Dong, *ACS Appl. Mater. Interfaces*, 2016, **8**, 32940–32947.
- 63 A. Hadarig, S. Ver Hoeye, C. Vázquez, R. Camblor, M. Fernandez, G. Hotopan, L. Alonso and F. Las-Heras, in *Global Symposium on Millimeter-Waves (GSMM 2015)*, Curran Associates, Inc., Montréal, Canada, pp. 3–6.
- 64 J. Kimionis, M. Isakov, A. Georgiadis, B. S. Koh and M. M. Tentzeris, *IEEE Trans. Microw. Theory Tech.*, 2015, **63**, 4521–4532.
- 65 I. T. Nassar, T. M. Weller and J. L. Frolik, *IEEE Trans. Microw. Theory Tech.*, 2012, **60**, 3309–3316.
- 66 S. Krachunov and A. J. Casson, *Sensors*, 2016, **16**, 1–18.
- 67 E. MacDonald and R. Wicker, *Science*, 2016, **353**, 1512–1522.
- 68 K. Willis, E. Brockmeyer, S. Hudson and I. Poupyrev, in *Proceedings of the 25th Annual ACM Symposium on User Interface Software and Technology—UIST’12*, 2012, pp. 589–598.
- 69 M. Weidenbach, D. Jahn, A. Rehn, S. F. Busch, F. Beltrán-Mejía, J. C. Balzer and M. Koch, *Opt. Express*, 2016, **24**, 28968–28976.
- 70 H. Yang, M. T. Rahman, D. Du, R. Panat and Y. Lin, *Sens. Actuators B Chem.*, 2016, **230**, 600–606.
- 71 K. Chen, W. Gao, S. Emaminejad, D. Kiriya, H. Ota, H. Y. Y. Nyein, K. Takei and A. Javey, *Adv. Mater.*, 2016, **28**, 4397–4414.
- 72 L. C. Duarte, C. L. S. Chagas, L. E. B. Ribeiro and W. K. T. Coltro, *Sens. Actuators B Chem.*, 2017, **251**, 427–432.
- 73 G. Postiglione, G. Natale, G. Griffini, M. Levi and S. Turri, *Compos. Part A Appl. Sci. Manuf.*, 2015, **76**, 110–114.
- 74 C. A. Mandon, L. J. Blum and C. A. Marquette, *Procedia Technol.*, 2017, **27**, 1–2.
- 75 G. W. Bishop, J. E. Satterwhite-Warden, I. Bist, E. Chen and J. F. Rusling, *ACS Sens.*, 2016, **1**, 197–202.
- 76 J. F. Rusling, *ACS Sens.*, 2018, **3**, 522–526.
- 77 H. N. Chan, Y. Shu, B. Xiong, Y. Chen, Y. Chen, Q. Tian, S. A. Michael, B. Shen and H. Wu, *ACS Sens.*, 2016, **1**, 227–234.
- 78 A. J. Capel, A. Wright, M. J. Harding, G. W. Weaver, Y. Li, R. A. Harris, S. Edmondson, R. D.

- Goodridge and S. D. R. Christie, *Beilstein J. Org. Chem.*, 2017, **13**, 111–119.
- 79 O. Okafor, A. Weilhard, J. A. Fernandes, E. Karjalainen, R. Goodridge and V. Sans, *React. Chem. Eng.*, 2017, **2**, 129–136.
- 80 P. J. Kitson, M. H. Rosnes, V. Sans, V. Dragone and L. Cronin, *Lab Chip*, 2012, **12**, 3267–3271.
- 81 F. Scheiff and D. Agar, in *Micro-Segmented Flow: Applications in Chemistry and Biology*, eds. Köhler, J. Michael and B. P. Cahill, Springer-Verlag, Berlin, Germany, 2013, pp. 123–127.
- 82 K. Wu and S. Kuhn, *Chim. Oggi.*, 2014, **32**, 62–66.
- 83 R. L. Hartman, *Org. Process Res. Dev.*, 2012, **16**, 870–887.
- 84 B. S. Flowers and R. L. Hartman, *Challenges*, 2012, **3**, 194–211.
- 85 D. H. Lee and J. K. Park, *Electrophoresis*, 2013, **34**, 3119–3125.
- 86 E. Dressaire and A. Sauret, *Soft Matter*, 2017, **13**, 37–48.
- 87 R. Johnson, *Handbook of Fluid Dynamics*, Taylor & Francis, London, UK, 1998.
- 88 V. Ramachandran and H. S. Fogler, *J. Fluid Mech.*, 1999, **385**, 129–156.
- 89 G. C. Agbangla, É. Climent and P. Bacchin, *Sep. Purif. Technol.*, 2012, **101**, 42–48.
- 90 H.-W. Kang, I. H. Lee and D.-W. Cho, *J. Manuf. Sci. Eng.*, 2005, **126**, 766–771.
- 91 A. Weltin, K. Slotwinski, J. Kieninger, I. Moser, G. Jobst, M. Wego, R. Ehret and G. A. Urban, *Lab Chip*, 2014, **14**, 138–146.
- 92 T. Monaghan, PhD thesis, Loughborough University, 2017.
- 93 H. M. Shapiro, *Practical Flow Cytometry*, John Wiley & Sons Inc., Hoboken, NJ, 4th Ed., 2003.
- 94 T. R. Neitzert, *Key Eng. Mater.*, 2015, **661**, 113–118.
- 95 R. B. Wicker, A. V. Ranade, F. Medina and J. A. Palmer, *Assem. Autom.*, 2005, **25**, 316–329.
- 96 Y.-M. Kim, W.-S. Kim, S.-H. Lee and J. Y. Baek, in *Proceedings of the 3rd Annual International IEEE EMBS Special Topic Conference on Microtechnologies in Medicine and Biology*, Kahuku, Oahu, Hawaii, pp. 292–295.
- 97 S. Yang, B. Yu, M. Zou and M. Liang, *Int. J. Heat Mass Transf.*, 2014, **77**, 208–217.
- 98 R. Jaeger, J. Ren, Y. Xie, S. Sundararajan and M. G. Olsen, *Appl. Phys. Lett.*, 2012, **101**, 184102.
- 99 R. V Krstic, *Human Microscopic Anatomy: An Atlas for Students of Medicine and Biology*, Springer Berlin Heidelberg, Berlin, Germany, 1991.
- 100 S. Srivastava, *Understanding Bacteria*, Springer Science+Business Media, LLC, Dordrecht, Netherlands, 2003.
- 101 G. W. Bishop, J. E. Satterwhite, S. Bhakta, K. Kadimisetty, K. M. Gillette, E. Chen and J. F. Rusling, *Anal. Chem.*, 2015, **87**, 5437–5443.
- 102 M. E. Snowden, P. H. King, J. A. Covington, J. V Macpherson and P. R. Unwin, *Anal. Chem.*, 2010, **82**, 3124–3131.

- 103 P.-T. Lan, S.-Y. Chou, L.-L. Chen and D. Gemmill, *Comput. Des.*, 1997, **29**, 53–62.
- 104 D. D. Hernandez, *Int. J. Aviat. Aeronaut. Aerosp.*, 2015, **2**, Article 2.
- 105 R. K. Lade, E. J. Hippchen, C. W. Macosko and L. F. Francis, *Langmuir*, 2017, **33**, 2949–2964.
- 106 E. Wilhelm, K. Deshpande, F. Kotz, D. Schild, N. Keller, S. Heissler, K. Sachsenheimer, K. Länge, C. Neumann and B. E. Rapp, *Lab Chip*, 2015, **15**, 1772–1782.
- 107 S. Lantean, I. Roppolo, M. Sangermano, C. F. Pirri and A. Chiappone, *Inventions*, 2018, **3**, 1–13.
- 108 T. H. Pang, presented in part at the 1993 North American Users Group Meeting, Atlanta, Georgia, March, 1993.
- 109 C. Neumann, E. Wilhelm, T. Düttenhofer, L. Pires and B. E. Rapp, *Microfluidics, BioMEMS, and Medical Microsystems XII*, eds. B. L. Gray and H. Becker, SPIE, San Francisco, CA, US, 2014, vol. 8976, p. 89760E–1.
- 110 3D Systems, Accura® 60 Safety Data Sheet [online], 2017 [Accessed 15/07/2017]. Available from: <http://infocenter.3dsystems.com/materials/sla/accura-60>.
- 111 C. Barner-Kowollik, *Macromol. Rapid Commun.*, 2009, **30**, 1961–1963.
- 112 C. E. Corcione, A. Greco and A. Maffezzoli, *J. Appl. Polym. Sci.*, 2004, **92**, 3484–3491.
- 113 I. Gibson, D. Rosen and B. Stucker, in *Additive Manufacturing Technologies: 3D Printing, Rapid Prototyping, and Direct Digital Manufacturing*, Springer Science+Business Media, LLC, New York, USA, 2nd edn., 2015, pp. 66–73.
- 114 M. Sangermano, W. Carbonaro, G. Malucelli and A. Priola, *Macromol. Mater. Eng.*, 2008, **293**, 515–520.
- 115 S. McBain, H. Yiu, A. El Haj and J. Dobson, *Langmuir*, 2017, **17**, 2561–2565.
- 116 L. Grøndahl, B. Battersby, J. Keen, M. Lorentzen, P. Surawski and M. Trau, *Langmuir*, 2006, **22**, 497–505.
- 117 Y. Kim, S. Lee, J. Kuk and S. Hong, *Desalination*, 2015, **367**, 154–160.
- 118 D. Hernandez and J. Shear, in *Three-Dimensional Microfabrication Using Two-Photon Polymerization*, ed. T. Baldacchini, William Andrew Applied Science Publishers, Norwich, NY, USA, 2016, pp. 102–118.

Chapter 4 3D printed microfluidic lab-on-a-chip device with integrated optical detection for particle counting and analysis

4.1 Abstract

This chapter covers the development and optimisation of an additively manufactured LOC particle analyser device that utilises optical sensing. The device is based on flow cytometry and comprises two main features: a hydrodynamic focusing chamber to streamline particles into single-file to allow single-particle analysis, and an optical fibre sensing system, for particle counting and sizing. The chip is low-cost, having a total materials cost of approximately £12, bringing it within the scope of disposal POC devices. Its detection system is embedded, allowing a more compact, integrated LOC device. Particle sizing was achieved by relating drops in intensity of occluded light to the diameter of spherical particles.

Initially, the optical detection system and the hydrodynamic focusing stability was tested using dyed core streams. Following this, the signal-to-noise ratio and reproducibility of the device particle analysis was optimised by use of a genetic algorithm (GA). The GA explored various combinations of five experimental parameters (overall flow rate, core flow rate/sheath flow rate ratio, particle concentration and optical fibre core diameter, presence or lack of dye) and optimised them towards three objectives (pulse magnitude, pulse uniformity and pulse periodicity). Once optimised, the chip was able to count particles up to 5.5×10^4 particles mL^{-1} , and differentiate between $10 \mu\text{m}$ and $30 \mu\text{m}$ particles in a mixture.

4.2 Introduction

Fast, accurate particle/cell characterisation is crucial in a broad range of areas ranging from health, environmental monitoring, food safety, and all kinds of industries. Currently, a call exists for particle/cell detection devices in portable health diagnostics for resource-limited settings¹⁻³, pharmaceutical manufacturing quality control (QC) systems^{4,5} and environmental applications^{6,7}. One solution for these needs is microfluidic LOC systems, which use unique fluid behaviour and high surface-to-volume ratios to enable precise sample handling and detection, and controlled, reproducible conditions^{8,9}. Their continuous-flow nature also allows high throughput processing with in-line detection and easy integration of other sample preparation processes^{9,10}.

Optical detection methods have an extensive record of successful integration into microfluidic LOC devices¹¹⁻¹⁴, ranging from those utilising UV/VIS absorption¹⁵ or obscuration¹⁶, to fluorescence detection¹⁷⁻¹⁹, through to more specialised techniques such as chemiluminescence^{20,21}, Raman²² and surface plasmon resonance (SPR)²³ detection. Microfluidic LOC optical systems can be classified into two main groups based on the light property used for sensing: those that monitor a direct change in light intensity such as absorbance, fluorescence or chemiluminescence, and those that detect an induced change in light wavelength, phase or polarisation. The latter method is more sensitive, but more susceptible to light source and temperature fluctuations¹³. An alternative way of classifying optical microfluidic systems is by their configuration: in free-space wave sensing, all of the incoming light (minus losses due to scattering, etc.) interacts with the fluid/sample, whereas in evanescent wave sensing, only the evanescent field does^{24,25}. The free-space wave method has a higher sensitivity but higher light losses, which can decrease the signal-to-noise ratio¹³. There are also a vast array of miniaturised optical elements integratable into microfluidic systems, including waveguides¹⁴ (in the form of either optical fibres or planar waveguides), microlenses^{26,27}, mirrors²⁷, prisms²⁸, laser diodes²⁶, and detectors, such as organic photodiodes (OPDs)²⁹. These elements can be fabricated on-chip, or mass-produced in low-cost polymer materials and embedded into devices, allowing the creation of highly versatile and sensitive technologies with complex integrated optical functionality^{26,27} and potential for commercialisation that can extend to single-use chips. Lastly, as well as these optical elements, device sensitivity and selectivity can be enhanced by a wide selection of labels, including fluorescent organic dyes, quantum dots³⁰ and fluorescent proteins³¹.

However, conventional microfluidic fabrication methods are long and expensive, involving creation of a master mould under cleanroom conditions, formation of chip layers, assembly and etching, and

bonding³². This has led to the exploration over the last decade of 3D printing as an alternative³³. AM has a number of advantages over conventional techniques, including the potential for one-step chip fabrication from an STL file³³, and three-dimensional freedom³⁴. 3D printing is able to produce optically transparent chips to easily facilitate optical analysis of samples^{35–37}. In addition, various optical elements have been printed (albeit not in microfluidics yet): waveguides³⁸, including 'light pipes' by Disney for children's toys³⁹, prisms⁴⁰, reflective air pockets³⁹ and lenses⁴¹ (although currently microscale lenses have only been achieved via 2PP⁴²). However, so far, optical sensing in 3D printed microfluidics has been limited to liquid^{36,37,43,44} and protein samples³⁵, and particles and cells have not been studied. Furthermore, in 3D printed chips, optical sensing has commonly been carried out via smartphones^{35,45}, which greatly limits their implementation in many portable and low-cost applications.

In this chapter we detail the development, testing and optimisation of a microfluidic optical particle characterisation LOC chip fabricated by SLA. It is the first 3D printed microfluidic system to feature integrated particle detection. Hitherto, additively manufactured microfluidic systems requiring particle analysis have used completely external, off-chip UV/VIS flow cells, such as by Okafor, et al. and Kitson, et al. for their silver⁴⁶ and gold⁴⁷ nanoparticle synthesis chips, respectively. The LOC device presented here uses embedded optical fibres to carry out particle-by-particle counting and analysis. It incorporates a hydrodynamic focusing junction to arrange the particles into single-file, grooves for fibre housing, and printed inlet and outlet threads. It was printed with open channels and sealed with a cover layer in order to increase channel resolution.

For initial testing, the embedded optical fibre system was first used to size focused dye solution core streams, by measurement of the dye stream absorption at its λ_{\max} . Core stream stability (in terms of its fluctuation in diameter over time) was observed and found to vary depending on the fluid flow rates used. Following this, sample suspensions comprising 30 μm diameter polystyrene beads were analysed by the device, and the experimental conditions optimised by a genetic algorithm (GA). Five experimental conditions in total were investigated: the fibre core area, particle concentration, sample/sheath flow rate ratio, overall flow rate and the use of a dye in the sample core stream. These parameters were explored and ranked according to three objectives: pulse magnitude, pulse magnitude variance and pulse regularity. The GA was run for three generations, searching for the set of conditions that maximised these three objectives. Once an optimal set of conditions was found, it was used to carry out particle quantification across a range of concentrations over two orders of magnitude, and analyse a mixture of 10 μm and 30 μm beads.

The chip took approximately 5 hours to print and assemble, which is far quicker than conventional photolithography methods if pattern and master mould creation are taken into account. It could also be reused dozens of times, by stripping of the tape layer, cleaning, and seal replacement.

4.3 Aims and Objectives

The aim of this chapter was to develop a 3D printed microfluidic particle analysis device utilising a low-cost, label-free optical detection system.

The above aim was facilitated by the following objectives:

- To investigate the focused core stream stability under different flow parameters.
- To assess the sizing accuracy of the optical detection system.
- To optimise the device particle analysis in terms of its signal-to-noise ratio and signal reproducibility, by use of a genetic algorithm.
- To demonstrate quantification and sizing of particles and cells.

4.4 Materials and Methods

4.4.1 Materials

4.4.1.1 Chemicals and reagents

IPA and methanol were both obtained from VWR. Methylene blue was obtained from Sigma-Aldrich.

4.4.1.2 Beads

Carboxylated polystyrene beads of 10 μm diameter, (Fluoresbrite® Yellow Green microspheres, CV 15%, obtained from Polysciences, catalogue no. 18142-2) and 30 μm diameter (SD<0.4 μm , CV<1%, obtained from Sigma-Aldrich, catalogue number 84135) were used in aqueous suspension for counting and sizing studies.

4.4.2 Methods

All methods were carried out at ambient room temperature (approx. 18-20°C).

4.4.2.1 Device drafting

NX software (Version 11.0, obtained from Siemens) was used to draft device CAD files and export to .STL format.

4.4.2.2 Stereolithography and post-print processing

The device was printed in Accura® 60 polymer on a Viper si2 SLA printer (both obtained from 3D Systems) in its HR build mode (Nd:YVO4 solid state laser at 354.7 nm, 100 mW output power, $1/e^2$ beam diameter 75 μm +/- 15 μm , minimum build layer height 20 μm , elevator vertical resolution 25 μm and position repeatability 76 μm) in the Y build-direction, washed with IPA and methanol, cured with a ProCure™ 350 UV Chamber (3D Systems) for 4 minutes to ensure full photopolymer cross-linkage, and washed again with IPA and methanol.

4.4.2.3 Optical fibre embedding

Light was transmitted via two multimode fibre diameters: 105 μm (core: silica, core diameter 105 μm $\pm 2\%$, 0.22 NA, cladding: glass, cladding diameter 125 μm $\pm 1 \mu\text{m}$, coating: acrylate, acrylate diameter 250 μm $\pm 4\%$, wavelength range 250–1200 nm, catalogue number FG105UCA) and 50 μm (core: silica, core diameter 50 μm $\pm 2\%$, 0.22 NA, cladding: acrylate, cladding diameter 250 μm $\pm 4\%$, coating: acrylate, coating diameter 250 μm $\pm 4\%$, wavelength range 250–1200 nm, catalogue number FG050UGA). Both obtained from Thorlabs. Before embedding, optical fibres were cut with scissors and polished by hand whilst held firm in a bare fibre terminator (BFT1, obtained from Thorlabs) via a series of lapping films (aluminium oxide, particulate sizes 9 μm , 5 μm , 3 μm , 1 μm , 0.3 μm , obtained from 3M). Optical alignment was accomplished by the inclusion of open grooves in the device CAD file for optical fibre housing. Optical fibres were pushed into the grooves via a rubber nub, and alignment carried out manually under a microscope.

4.4.2.4 Device sealing

Finally, the device was sealed with a cover layer consisting of LEXAN™ 8010PC polycarbonate film (obtained from SABIC, 250 µm thickness) attached via TESA 4965 double-sided tape (obtained from 3M), applied by hand and flattened via seam roller. The fibre optic grooves were sealed with blobs of two-part epoxy resin (Araldite®, Rapid, obtained from Huntsman Advanced Materials).

4.4.2.5 Fluidic control

Microfluidic flows were effected by Mitos P-Pump Basic pressure-driven pumps (Dolomite) and inputted into the chip by PEEK microfluidic tubing (250 µm internal diameter, obtained from Dolomite) and standard Supelco® HPLC fittings and end ferrules (obtained from Sigma-Aldrich) in printed threads.

4.4.2.6 Microscopy and image processing

Photos of chip and experiments were taken via an Optiphot-2 optical microscope with DS-5M Camera Head controlled by a DS-L1 Digital Sight Camera Control Unit (all obtained from Nikon). Captured dye stream images were sized via AxioVision software (Zeiss).

4.4.2.7 UV/visible spectroscopy

Light supply and collection was carried out via a MINI-D2T Miniature Deuterium Tungsten Light Source and an S2000 Miniature Fibre Optic Spectrometer, respectively (both obtained from Ocean Optics), the latter controlled via SpectraSuite software (Ocean Optics). Light intensity was measured at a single wavelength at a 15 ms acquisition period and an integration time of 3 ms.

4.4.2.8 Dye analysis procedure

Methylene blue dye solution (1.0M) was focused under different sheath flow/sample flow rate ratios and total overall pressures using water as sheath fluid, and the resulting focused core stream monitored at 665 nm via the aforementioned optical detection system.

4.4.2.9 Particle analysis procedure

Immediately preceding running, particle suspensions were vortexed (5 s) and sonicated (1 min) to ensure monodispersity. Water sheath flows were used. Data was captured for 100 s.

Videos of particle focusing were recorded via a Meros high-speed digital microscope (Dolomite).

4.4.2.10 Signal processing

Particle pulse spectra were attained by recording of collected light at 650 nm (the wavelength of intensity maxima of the tungsten light source) as raw counts, followed by smoothing of signal noise via Origin software (OriginLabs, Version 9.0) using either a 220-point or 50-point smooth (see Table 4.1), non-weighted, adjacent-averaging smooth function. Peak calling was carried out either with a moving window background of 50 data points for suspensions of 10 μm beads, or from a threshold set from an overall mean baseline for a study of differently-sized beads (see Table 4.1). Peaks were designated as significant if the drop in intensity was greater than either 5 or 3 SDs from the mean of this window, or from the mean baseline.

Table 4.1 Signal processing procedure for the two different sets of experiments for the optical particle counter chip.

Sample	Data points averaged in adjacent-average smoothing method	Peak-calling threshold, distance from mean intensity	Moving window of 50 points
30 μm beads homogenous suspension	50	5 SDs for GA study 3 SDs for counting study	Yes
10 μm and 30 μm bead mixture	220	3 SDs	No

4.4.2.11 Genetic algorithm optimisation

Evolutionary optimisation was carried out over 3 generations, with 20, 16 and 19 experiment runs in the first, second and third generations, respectively (see Tables 4.3, 4.4 to 4.5). The first generation consisted of conditions randomly generated within defined boundaries for five different variables: two

intrinsic variables in the form of a) either 50 or 105 μm optical fibre core diameters, b) the use of either water or methylene blue solution (aqueous, 1.0M) for the bead suspension solvent, and three continuous variables: c) particle concentrations ranging between 5.0×10^3 and $2.5 \times 10^5 \text{ mL}^{-1}$, d) 1–3.5 inner flow/sheath flow applied pressure ratios, and e) 100–375 mbar total applied pressure (the sum of the pressures used across the three pumps).

Figure 4.1 shows a flowchart outlining the GA process. The algorithm PESA-II was implemented as described as in Jarvis, et al.⁴⁸ to select the best experimental conditions from the preceding generation, and then modify these variables to generate the next generation. Each generation involved sets of conditions that were modifications of runs from the previous generation, with the exception of a group of the highest-ranked sets of conditions (selected from the Pareto front) from the previous generation: these 4 best sets of conditions were left unchanged, serving as both controls and a metric of progress. Variables were mutated with a probability of $2/L$ (where L =the total number of variables). When mutation was applied, each of the variables was modified (increased or decreased) by up to 20%, by a uniform random number between 0 and 20% of the original value. The core diameter and presence of MB dye were encoded as a decimal x : for example, if $x > 0.5$, dye was added to the solution, and if $x \leq 0.5$ dye was omitted.

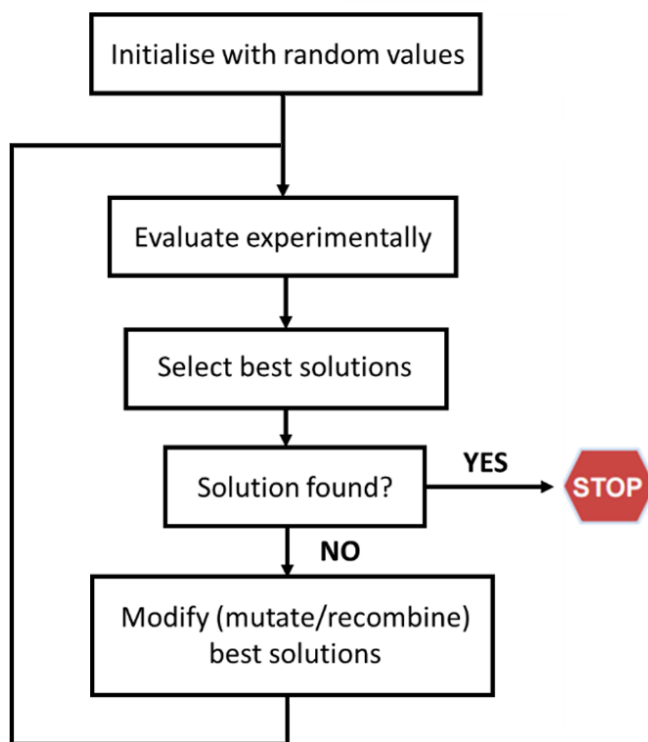


Figure 4.1 Flow chart illustrating the closed-loop optimisation of experimental conditions described in this chapter.

60% of the experiments in the second and third generations were generated through uniform crossover by combining variables from the best solutions. The GA also included repeats to check run reproducibility, by generating a number of runs in the second and third generations that had near identical conditions to certain 1st generation runs.

In order to allow direct inputting of experimental settings without requirement for calculation steps, flow rates were inputted in the form of applied pressures across inlets (see Chapter 4.5.2). For all non-dyed, 105 μm core streams, a baseline light intensity of was 125 counts was used. On the occasion of a chip being assembled and its fibres giving <125 count baseline intensity at 659 nm, the run was registered in the GA as a 'null' (failed) result.

4.4.2.12 Statistical Methods

Standard deviation of data sets was calculated using Equation 3.1. Coefficient of variation of data sets was calculated by Equation 4.1, where σ =the SD of the set, and μ =the mean of the set.

$$CV = \left(\frac{\sigma}{\mu}\right) \times 100 \quad (4.1)$$

Non-weighted adjacent averaging was used for particle pulse spectra smoothing in 4.4.2.10: each value in a data set was calculated as the average of the data points within the moving window as denoted by Table 4.1.

4.5 Results and Discussion

4.5.1 Final flow cytometer design

After the device initial development in Chapter 3, the final optical chip design is shown in Figure 4.2 a and includes vertical threads, as well as four side juts to hold the piece in place whilst being used under a microscope. The printed device, including embedded optical fibres, is shown in Figure 4.2 b.

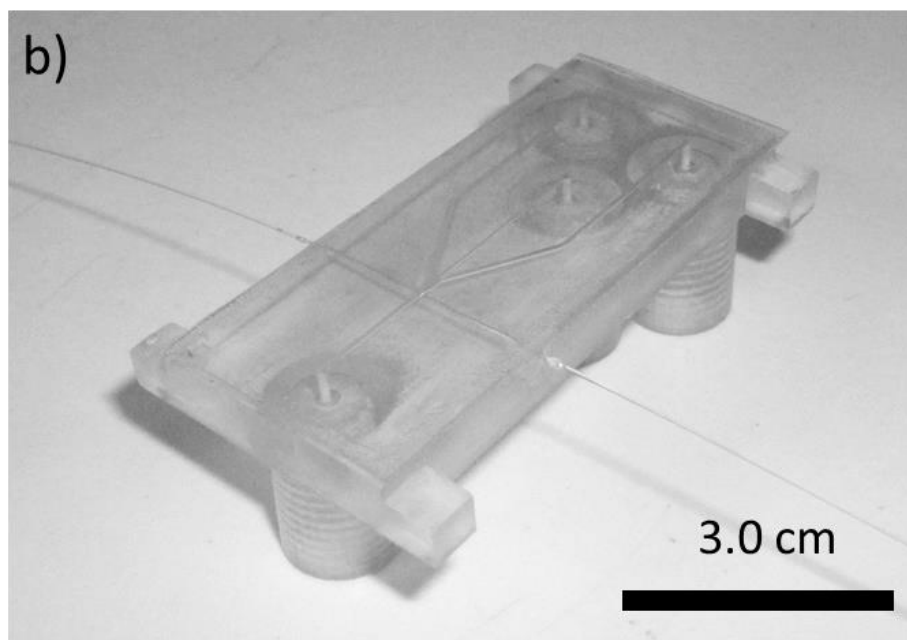
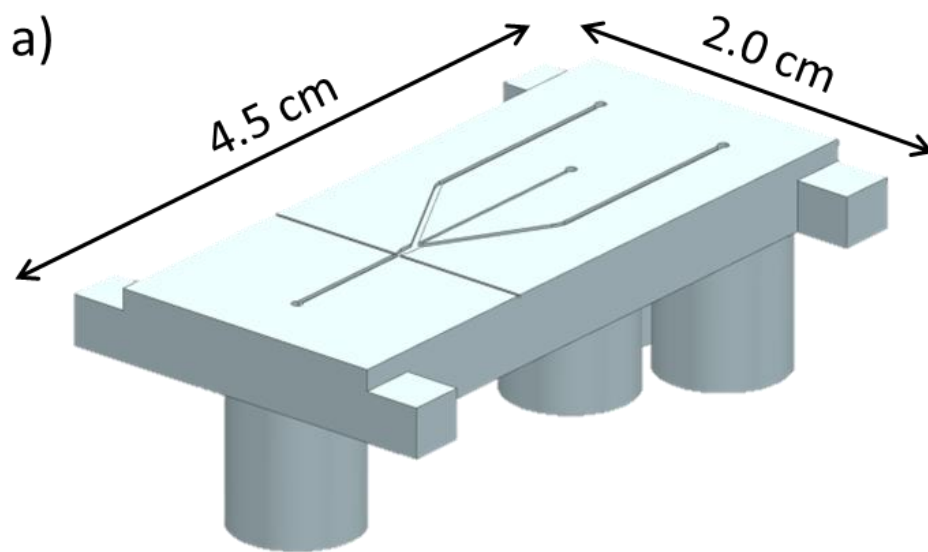


Figure 4.2 a) CAD design of final optical flow cytometer design, featuring juts to hold the device inside the Nikon Optiphot microscope system used. b) Photograph of printed optical flow cytometer device. Embedded optical fibres protrude out of the side of the device.

As covered in Chapter 3, the chip was printed in the Y build direction due to the channel quality issues associated with the other two directions, and channels were printed open on the surface of the device to improve printing resolution, as well as printed square to minimise the staircase effect and make the fibre faces flush with the channel walls.

The flow cytometric processes of hydrodynamic focusing and optical detection are illustrated in Figure 3.2. Sample suspension flow is directed into a flow focusing chamber, where it is compressed by two flanking sheath flows into a single file. This allows individual particles to be characterised as they traverse through an optical interrogation zone located between a pair of transmitting and receiving optical fibre core faces. The passage of a particle between these fibres should cause a drop in the transmitted light signal across the interrogation region, and thus continuous monitoring of the transmitted light intensity over time during particle suspension flow should give a number of pulses that is proportional to particle concentration. As the fibre cores (105 and 50 μm diameters) used do not capture the entire 250 μm channel height, some particles will inevitably be missed, thus giving a count efficiency <100%. However, comparison to a known calibration suspension can correct for this.

4.5.2 Chip experimental parameters

The pump system used in this project does not have integrated flow rate sensors, and instead uses applied fluid pressures and not fluid flow rate values, and so flow rate was equated to the applied pressure as per Equation 4.1, (where P =applied pressure from pump, mbar, μ =viscosity of flowing fluid, mPa.s, and R =flow resistance, μm^{-3}).

$$\text{Flow rate} = \frac{P}{\mu R} \quad (4.1)$$

Thus, the total flow rate was taken to be (2x1 sheath flow pressure) + inner flow pressure.

4.5.3 Dye stream testing

Before particle analysis was carried out, the performance of the hydrodynamic focusing junction and optical detection system were explored via focused dye solution streams. Methylene blue dye streams of differing diameters were focused, and the resulting core streams analysed by the chip optical detection system. Stream stability was measured over ranges of two flow conditions: inner/sheath flow ratio and total flow rate, and the ability of the optical system to accurately size streams tested.

4.5.3.1 Effects of inner/sheath flow ratio and total flow rate on core stream width

Figure 4.3 shows resulting dye core streams at a range of inner/sheath flow ratios and total flow rates, using methylene blue solution (1 mM) as the inner flow, and water as the sheath fluid. The

inner/sheath flow ratio dictates the core stream diameter: as the sheath stream flow rates are increased relative to the inner stream flow rate, the inner stream is constricted and accelerated into a fast, narrow core stream. Meanwhile, the total flow rate dictates the overall speed of the flow streams. The transmitted light intensity passing through the focused core streams was monitored at 665 nm, the λ_{max} of methylene blue, and a mean taken over 10 s. Decreasing the inner/sheath flow ratios gave narrower core streams, whilst changing the total flow rate should not affect the core stream width if the inner/sheath flow ratio is kept constant. However, for all but the narrowest streams (those with inner/sheath ratios of 0.75 and 1.0), increasing the overall flow rate gave increased measured light intensities, which would indicate narrower core streams.

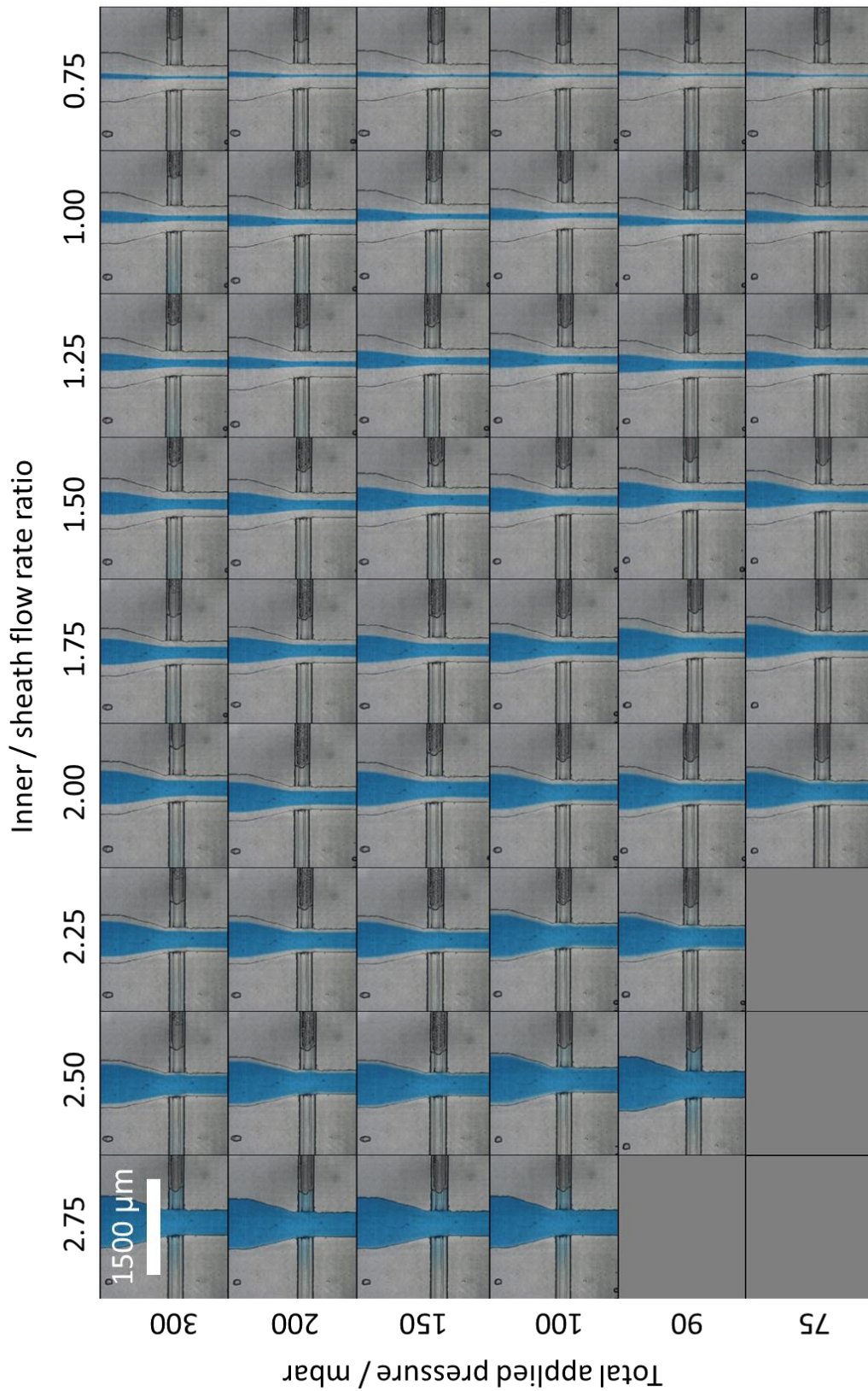


Figure 4.3 Focusing of a central stream of methylene blue (aq. solution) across a range of inner/sheath flow ratios and total flow rates. The grey boxes indicate pressures beyond the working range of the pump system.

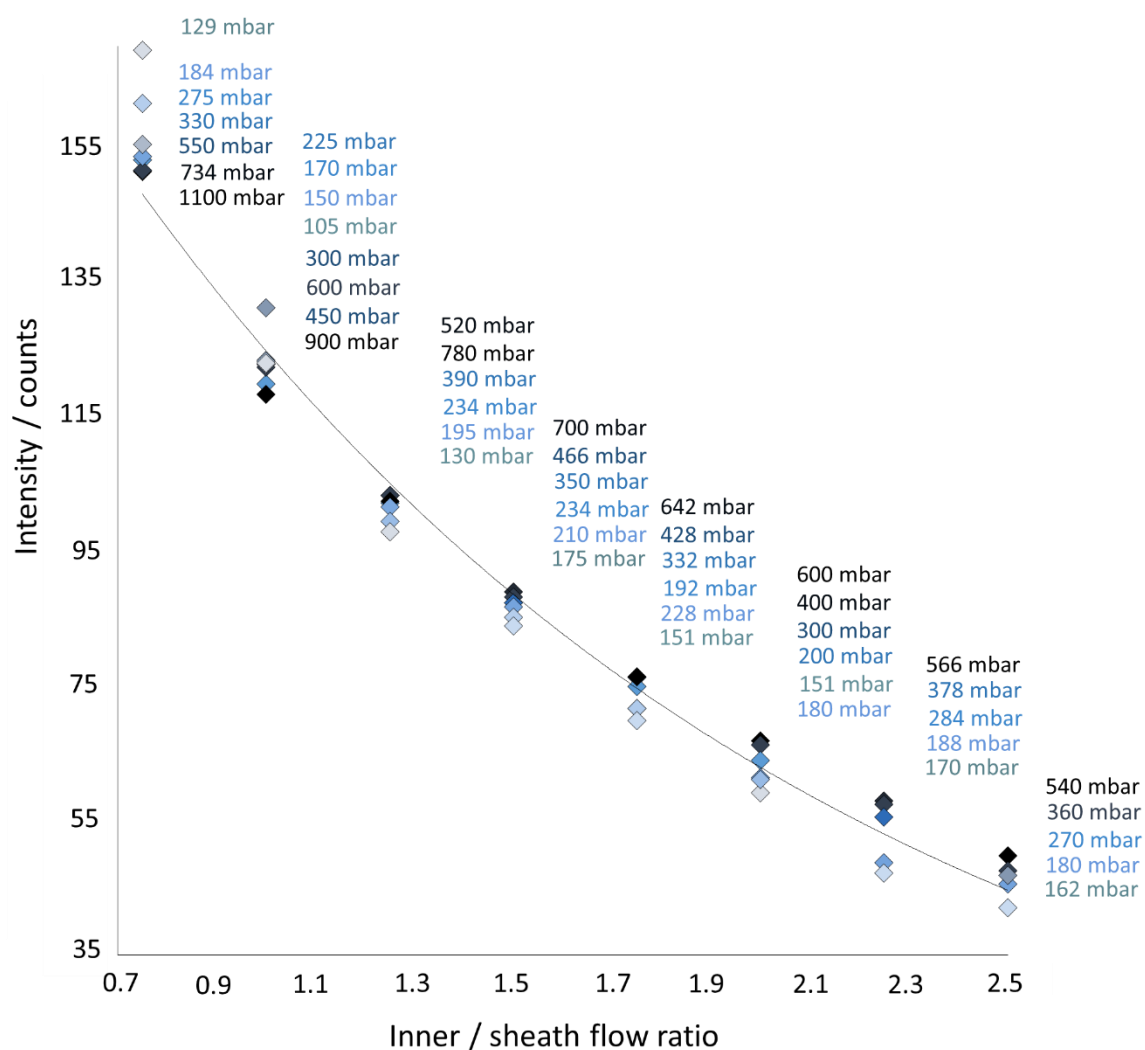


Figure 4.4 Decrease in measured output light intensity at 665 nm with increase in inner/sheath flow ratio (due to the increasing width of the focused dye stream). Variance in core stream width due to different total overall flow rate also shown.

4.5.3.1 Effect of inner/sheath flow ratio on core stream stability

By holding the sheath flows constant at 200 mbar and decreasing the inner/sheath flow ratio, a linear plot of measured absorbance vs. core stream width was gained (Figure 4.5 a) after conversion of raw intensity counts to absorbance values. This linear graph indicated good ($R^2=0.09986$) sizing ability by the chip. Figure 4.5 b shows the measured absorbance values recorded over time. Fluctuations in core stream thickness (indicated by absorbance instabilities) are attributed to fluctuations in the applied pressures as supplied by the pumps, and not due to the chip itself, as the flows are laminar. Streams

could be focused and detected down to $\sim 3 \mu\text{m}$ thickness, determined by measuring of stream photographs via image sizing software.

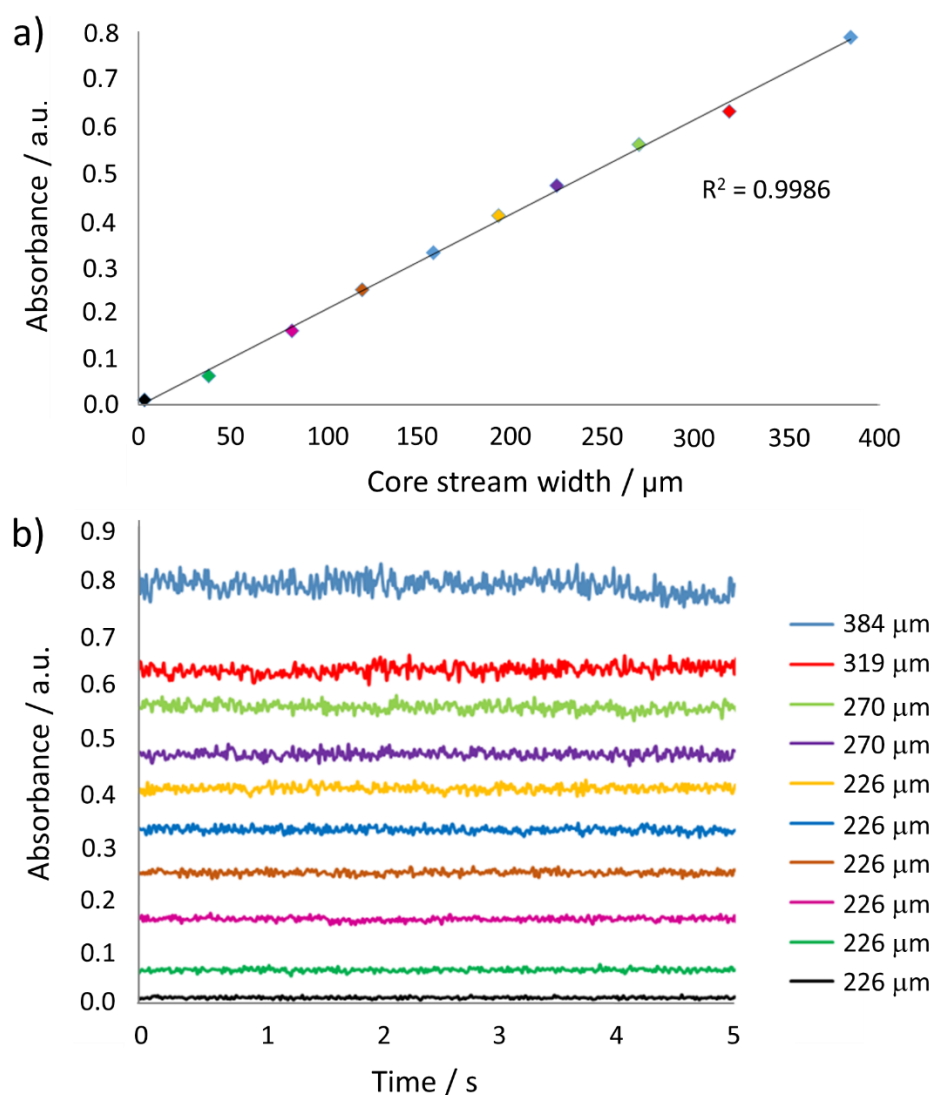


Figure 4.5 Shows a linear plot of the measured absorbance at 665 nm (aqueous methylene blue λ_{max}) for different thicknesses of dye core streams, with the sheath flow held steady under 200 mbar pressure. Plot and R2 value include a (0,0) value. b) Shows the corresponding λ_{max} absorbance signal over time for the different core stream thicknesses. Absorbance fluctuation increases with core stream width.

4.5.3.2 Effect of overall flow rate on core stream stability

Figure 4.6 Shows a plot of all measured values for core stream width SD over time for the total overall flows in Figure 4.5. An overall slight increase in stream width stability (decrease in width SD) is

observed as the total overall flow rate increases. However, these points encompass many core stream widths (inner/sheath flow rate ratios), which also affect the stream stability as found in Chapter 4.5.3.1.

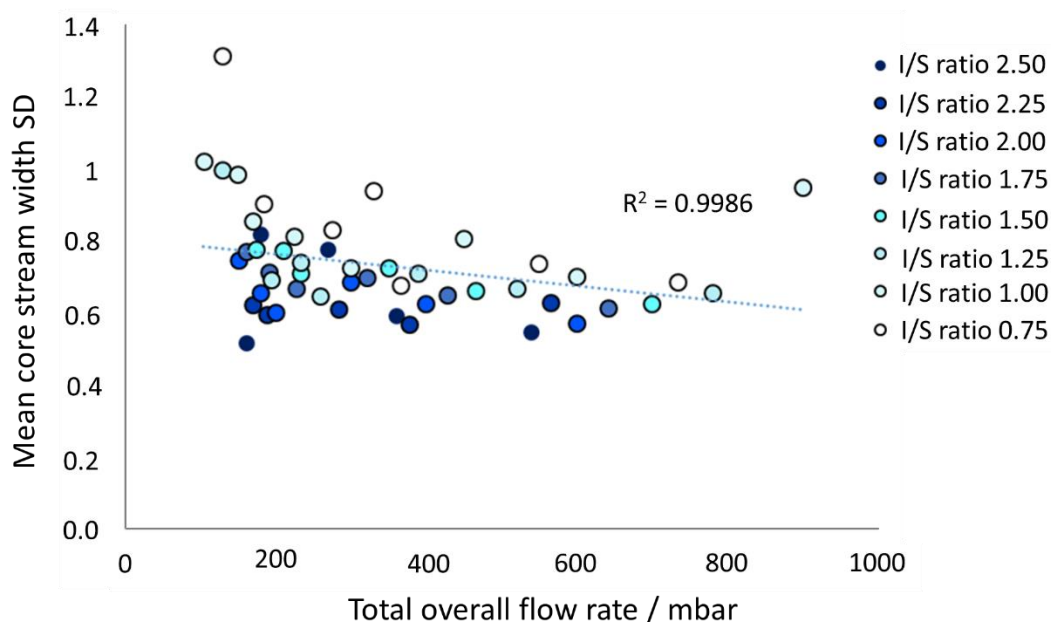


Figure 4.6 Scatter plot of mean measured dyed core stream width SD versus total overall flow rate, for different inner/sheath ratios.

4.5.3.3 Core stream absorbance comparison to theoretical values

The measured absorbance values in Figure 4.5 a) were used to calculate corresponding core stream widths via the Beer–Lambert Law (Equation 4.2), where A =absorbance in arbitrary units, ϵ =molar absorption coefficient in $\text{L mol}^{-1} \text{cm}^{-1}$, c =dye concentration in mol L^{-1} and l =path length, i.e. the core stream width, in cm. Rearrangement of this equation gives $l=A/\epsilon c$.

$$A = \epsilon l c \quad (4.2)$$

Calculated core stream widths were compared to widths gained from image analysis of dye stream photographs from Figure 4.3 (Figure 4.7). The core stream width values measured by the optical chip were roughly half the values gained by photograph image analysis. This is believed to be due to either the core stream being of thin height parallel to the optical fibre faces, and/or diffusion happening along the dye stream/sheath stream interface, effectively diluting the streams. The lower limit of the

plots at ~ 0.6 inner/sheath ratio reflects the minimum stable core stream width for this set of conditions.

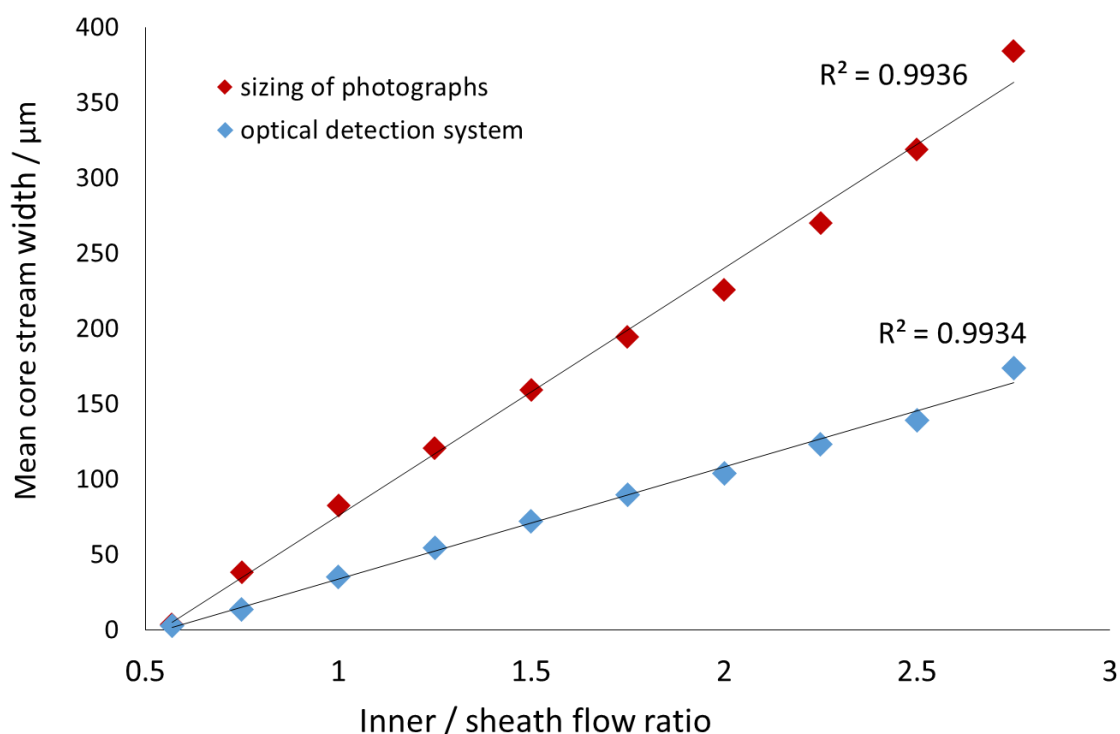


Figure 4.7 Plot of core stream sizes gained from absorbance measurements and application of Beer–Lambert Law, for MB core streams over a range of inner/sheath flow ratios at 200 mbar sheath flow (red), in comparison to core stream sizes gained by image analysis of dye stream photographs (blue).

4.5.4 Optimisation of particle flow cytometry by genetic algorithm

After verifying that the core stream width could be accurately controlled, optimisation of the system experimental conditions was carried out for the counting and analysis of 30 μm diameter spherical polystyrene particles. This was challenging as numerous parameters affect the detection performance, and some are interrelated: firstly, particle concentration is important as too low a concentration lowers the analysis throughput, whilst too high a concentration increases the likelihood of pulse overlap, decreasing the pulse magnitude repeatability, and can cause signal saturation (where the pulse rate exceeds the maximum acquisition rate for the detection system). Secondly, fibre core diameter greatly affects the pulse magnitude and signal-to-noise ratio, as it dictates the size of the light intensity drop relative to the baseline intensity by changing the particle-to-core ratio. However, although smaller fibre cores can be expected to give a higher signal-to-noise ratio, in our system they

would also have a lower counting efficiency, unless particles are aligned correctly into a very narrow stream. In addition, two flow parameters are critical: the total overall flow and the sample flow/sheath flow ratio. The former affects the analysis throughput: very low values also give very low throughputs, until eventually flow stops, whilst high values cause pulses to be missed as their speed is greater than the spectrometer acquisition speed. The latter dictates the width of the resulting focused sample core stream, and so affects many aspects of the analysis: too wide a core stream causes >1 particle to be detected at the same time, which leads to a decrease in pulse size uniformity (due to pulse overlap) and pulse periodicity (as now particles are now spread out across the cross-section of the channel as opposed to being in a single-file in one plane) as well as the analysis throughput (as the inner/sheath flow ratio affects the core stream acceleration by extension). Meanwhile, too low a ratio will prevent particle passage. These two flow parameters are interlinked, as changing the inner/flow ratio will also change the total flow rate, unless it is scaled. Lastly, a fifth and final parameter was added: methylene blue (MB) dye (1 mM) was used as the particle core stream solvent in a number of runs, as it was hypothesised that when at single-file, the particle pulses could instead be observed as a sudden, sharp increase in light intensity, improving the sensitivity.

Due to the aforementioned variable interlinkage, a multiobjective, evolutionary optimisation algorithm was used, as a simple optimisation algorithm such as simplex would be likely to walk to a local, rather than global minimum—it has a high risk of finding and stopping at a local optimum as opposed to searching the entire parameter space and finding the true optimum value for the given parameter limits. In contrast, genetic algorithms (GAs) explore latent search space in experimental scenarios by applying Darwinian practises of mutation and natural selection in a closed-loop evolutionary process⁴⁹. They have been used in aptamer⁵⁰, airfoil⁵¹ and adaptive robotic⁵² development. The GA used in this chapter was multiobjective: it rated recorded pulse spectra on three aspects. Evolutionary multiobjective optimisation (EMO) facilitates the simultaneous optimisation of multiple objectives⁴⁸. Previously, this entailed combination of objectives into a single unary value, but now algorithms such as Pareto envelope-based selection algorithm (PESA-II) can select sets of conditions evenly from the Pareto front (see Figure 4.8)⁴⁹. Unlike simplex optimisation, EMO is able to optimise in scenarios that exhibit non-linear interaction of variables—it has demonstrated effectiveness in a range of real world optimisation challenges, including proving effective in maximisation of experimental conditions to enhance signal and reproducibility in SERS measurements⁴⁸. The experimental variables were modified by the Pareto Envelope-based Selection Algorithm II (“PESA-II”), a multi-objective evolutionary optimisation algorithm⁵³. PESA-II was used to

modify ('evolve') the variables: the algorithm was adapted such that the conditions generated in generations two and three were modifications of the previous generation.

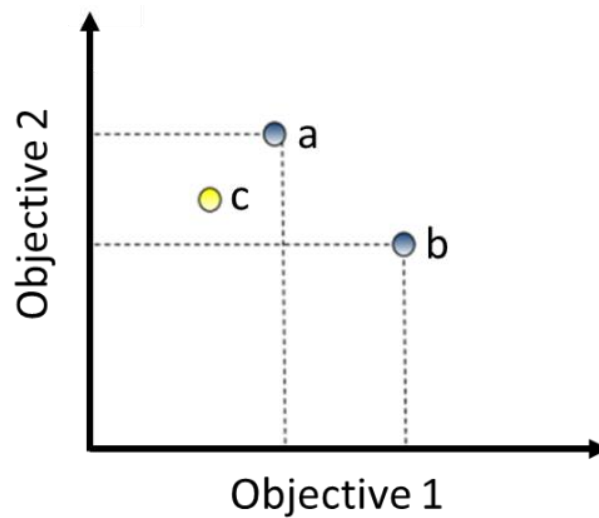


Figure 4.8 Diagram illustrating Pareto optimality. Point a dominates point c, as it is superior in both objectives. Additionally, point a is inferior to point b in terms of objective 1, but it is superior in terms of objective 2. In this situation neither point is superior. As neither point is inferior to any other point in the dataset, they are said to be non-dominated; they form the Pareto front.

The three objectives that the GA optimised towards (and ranked each recorded pulse spectrum by) were: 1) Signal reproducibility (in the form of variation in the light intensity drop produced by particle transport through the fibre optic junction. An ideal system would have no variance in pulse magnitude for a sample of uniform size particles. Thus, the GA was instructed to minimise this value of variance, which decreases the more steady and stable the particle stream is in the interrogation zone), 2) signal periodicity (variation in time between pulses. To maximise the number of particles that could be counted per unit time the GA was instructed to minimise this value) and 3) the signal-to-noise ratio (pulse magnitude, i.e. the drop in intensity from the baseline value. The GA was instructed to maximise this value). A summary is given in Table 4.2.

Table 4.2 A summary of the three objectives used by the GA to rank experiment runs, listing how they were measured and the instruction of the GA for each.

Objective	Measured as	GA instruction
Signal reproducibility	Light pulse variation / CV%	Minimise
Signal periodicity	Variation in time between pulses / CV%	Minimise
Signal-to-noise ratio	Pulse intensity drop from baseline / counts	Maximise

The GA coding was carried out by a collaborator (William Rowe, Loughborough University, Department of Chemistry) and so comprehensive detail is omitted in this thesis. However, a general overview including predefined experimental parameter limits, variable mutation process and value inputs are given in Methods 4.4.2.11. There are only two papers known to the author that describe the use of design of experiments (DoE) inside AM microfluidic systems, both from Loughborough University and concerning organic synthesis optimisation: the first utilising a simplex algorithm to optimise temperature and flow rate⁵⁴, and the other response surface methodology (RSM) and central composite face-centred (CCF) DoE for temperature and residence time optimisation⁴³. Synthetic yield optimisation is non-comparable to the focused particle stream analysis however, due to the aforementioned non-linear variable interrelation of the latter.

4.5.4.1 Genetic algorithm particle runs

The same chip was used for the entirety of the GA. An initial set of 20 runs, with varying combinations of the five aforementioned experimental conditions, was randomly generated by the GA (Table 4.3) within the boundaries given in Methods (4.4.2.11), forming the GA first generation. The resulting pulse spectra were analysed and rated according to each of the three objectives. During this first generation of experiments it was quickly determined that use of dye in the core stream was not conducive to observing peaks: dye presence caused severe peak spectral disruption in the form of both greatly reduced baseline light intensity (well below the 125-count threshold) and pulse obscuration (Figure 4.9). It was deduced that dye would give no useful data unless in very thin core streams, and thus, the decision was made to drop this parameter option in subsequent generations (Table 4.4 and 4.5), as it was deemed more appropriate to be explored in a separate study.

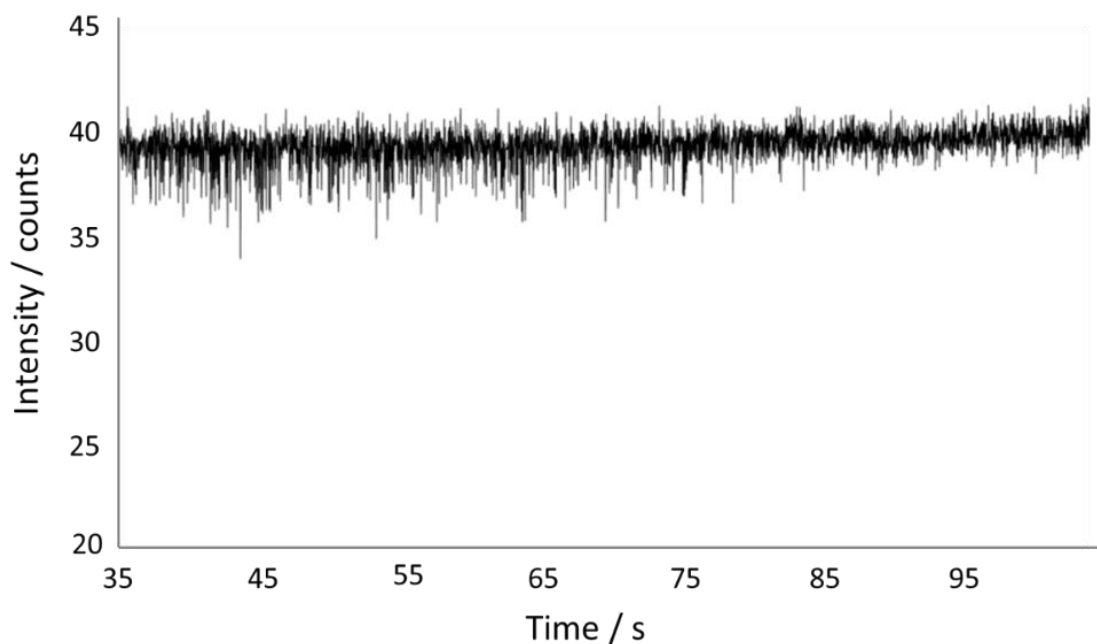


Figure 4.9 Recorded pulse spectrum for run 'H1' in genetic algorithm (see Table 4.3), involving a 30 μm particle core stream (1.91×10^5 particles mL^{-1}) dyed with MB and analysed via a 105 μm core optical fibre. A very low baseline light intensity of approximately 39 counts was measured, which is significantly below the minimum 125 count threshold set. Particle pulses are obscured by the resultant signal-to-noise ratio.

Additionally, the smaller optical fibre core size was extremely difficult to align reproducibly, thus preventing a reproducible counting efficiency in addition to making it very hard to gain a sufficiently high enough baseline intensity. On event of a run being set up and the fibres giving <125 count baseline intensity at 665 nm, the run was registered in the GA as a 'null' (failed) result. As this happened often, the GA rapidly decreased the number of runs using a 50 μm fibre core size. Furthermore, although the pulse magnitude relative to the baseline intensity was higher, the signal-to-noise ratio for the 50 μm fibre core was inferior to the 105 μm core, as the smaller fibre core gave far lower baseline intensities (for example, compare 'P1', a 50 μm fibre core run, Figure 4.10, to '11', a 105 μm fibre core run with similar experimental parameters, Figure 4.11).

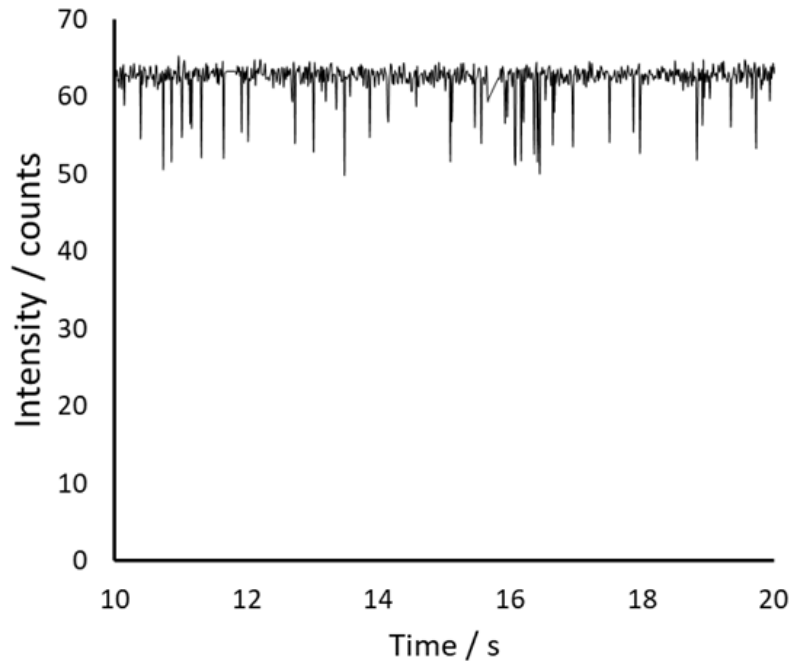


Figure 4.10 Sample of recorded pulse spectrum for run 'P1' in genetic algorithm (see Table 4.3), involving a 1.35×10^5 particles mL^{-1} $30 \mu\text{m}$ particle core stream analysed via a $50 \mu\text{m}$ core optical fibre at 2.40 inner/sheath flow ratio and 304 mbar total pressure.

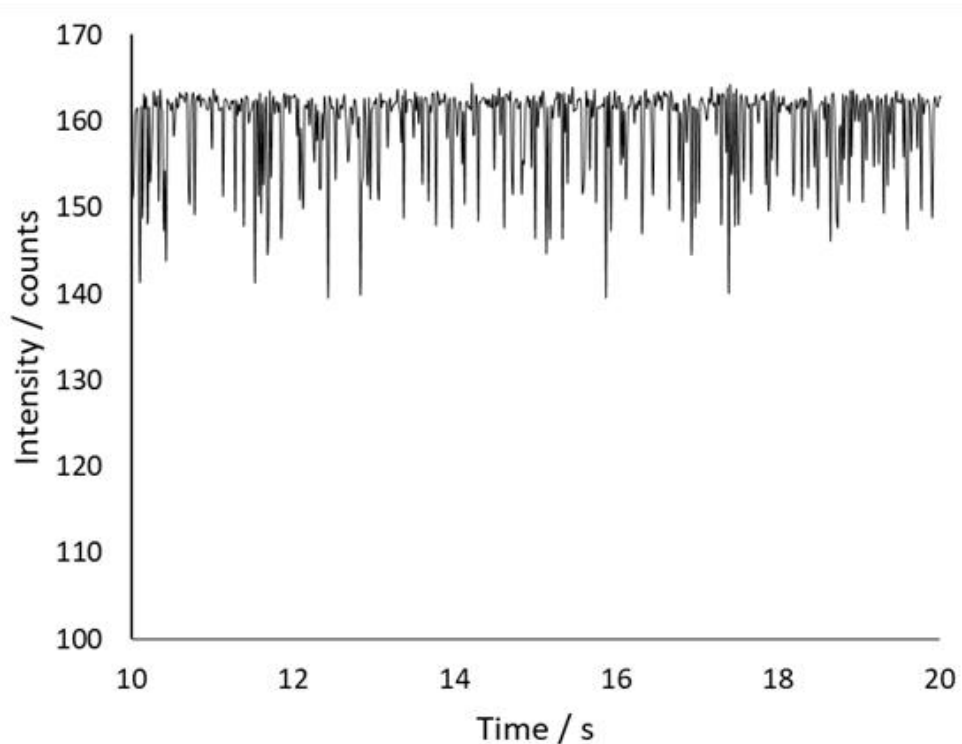


Figure 4.11 Sample of recorded pulse spectrum for run 'I1' in genetic algorithm (see Table 4.3), involving a 1.97×10^5 particles mL^{-1} $30 \mu\text{m}$ particle core stream analysed via a $105 \mu\text{m}$ core optical fibre at 2.65 inner/sheath flow ratio and 303 mbar total pressure.

Table 4.3 Particle runs generated by the GA, first generation, as carried out by William Rowe (Loughborough University, Department of Chemistry).

Generation	Reference	Fibre core diameter / μm	Bead conc. / beads mL^{-1}	Inner/sheath ratio	Total flow rate / mbar	Dye yes/no
1 st	A1	105	8.06×10^3	2.63	241	no
	B1	105	9.88×10^3	2.22	115	no
	C1	105	1.96×10^4	2.25	101	yes
	D1	105	4.91×10^4	1.36	182	yes
	E1	105	1.00×10^5	1.13	288	no
	F1	105	1.22×10^5	1.14	122	no
	G1	105	1.88×10^5	1.09	354	yes
	H1	105	1.91×10^5	3.45	247	yes
	I1	105	1.97×10^5	2.65	303	no
	J1	50	2.99×10^4	2.14	240	no
	K1	50	3.56×10^4	1.94	341	no
	L1	50	6.10×10^4	1.92	333	no
	M1	50	7.54×10^4	1.97	227	no
	N1	50	1.12×10^5	1.41	253	no
	O1	50	1.13×10^5	2.82	261	no
	P1	50	1.35×10^5	2.40	304	no
	Q1	50	1.38×10^5	2.86	301	no
	R1	50	1.45×10^5	1.97	180	no
	S1	50	1.69×10^5	1.73	355	no
	T1	50	2.21×10^5	1.67	108	no

Table 4.4 Particle runs generated by the GA, second generation, as carried out by William Rowe (Loughborough University, Department of Chemistry).

Generation	Reference	Fibre core diameter / μm	Bead conc. / beads mL^{-1}	Inner/sheath ratio	Total flow rate / mbar	Dye yes/no
2 nd	A2	105	8.06×10^3	2.63	207	no
	B2	105	8.06×10^3	1.94	241	no
	C2	105	8.06×10^3	2.63	241	no
	D2	105	8.42×10^3	2.63	241	no
	E2	105	2.99×10^4	2.63	243	no
	F2	105	2.99×10^4	2.78	240	no
	G2	105	1.00×10^5	1.13	253	no
	H2	105	1.35×10^5	2.72	304	no
	I2	105	1.15×10^5	1.13	253	no
	J2	50	8.17×10^3	2.40	287	no
	K2	50	3.59×10^4	1.94	355	no
	L2	50	6.10×10^4	1.33	288	no
	M2	50	6.10×10^4	1.98	333	no
	N2	50	6.17×10^4	1.92	396	no
	O2	50	9.88×10^4	1.92	333	no
	P2	50	1.00×10^5	1.48	288	no

Table 4.5 Particle runs generated by the GA, third generation, as carried out by William Rowe (Loughborough University, Department of Chemistry).

Generation	Reference	Fibre core diameter / μm	Bead conc. / beads mL^{-1}	Inner/sheath ratio	Total flow rate / mbar	Dye yes/no
3rd	A3	105	6.99×10^3	1.98	333	no
	B3	105	8.05×10^3	2.63	207	no
	C3	105	8.06×10^3	2.02	241	no
	D3	105	8.06×10^3	2.63	180	no
	E3	105	8.06×10^3	1.94	241	no
	F3	105	9.65×10^3	1.94	238	no
	G3	105	2.99×10^4	1.14	243	no
	H3	105	2.99×10^4	2.63	243	no
	I3	105	2.99×10^4	2.77	242	no
	J3	105	2.99×10^4	3.27	240	no
	K3	105	3.13×10^4	2.63	243	no
	L3	105	6.10×10^4	2.63	333	no
	M3	105	9.88×10^4	1.92	333	no
	N3	105	1.00×10^5	2.63	252	no
	O3	105	1.03×10^5	1.13	253	no
	P3	50	8.06×10^3	1.98	210	no
	Q3	50	2.99×10^4	2.11	243	no
	R3	50	6.10×10^4	1.98	333	no
S3	50	9.88×10^4	1.92	333	no	

The GA then carried out a further two generations of evolutionary optimisation, comprising 16 and 19 experiment runs respectively (Tables 4.4 and 4.5). Recorded particle runs from the three GA generations are plotted in Figure 4.12. Note that this figure omits runs utilising MB dye and 50 μm core fibre diameters. Each cube plot gives the rating (by colour) according to one of the three objectives for each of the different runs. It was apparent that sets of conditions with low overall flow rates, low particle concentrations, and low sheath/inner flow ratios yielded insufficient numbers of pulses to analyse, if at all (blue-coloured runs in Figure 4.12 represent spectra lacking any pulses). In contrast, a region of high performance around point "A2" was observed. The GA quickly converged to this region after the first generation, and explored the surrounding parameter space in subsequent generations. Figure 4.12 e) shows an example of a non-optimised particle spectra (point "I2"), with weak pulses occurring in bursts as opposed to periodic intervals. In contrast, Point "A2", the deduced optimum set of experimental conditions, gives a profile (Figure 4.12 f) with relatively strong pulses and low time interval variation.

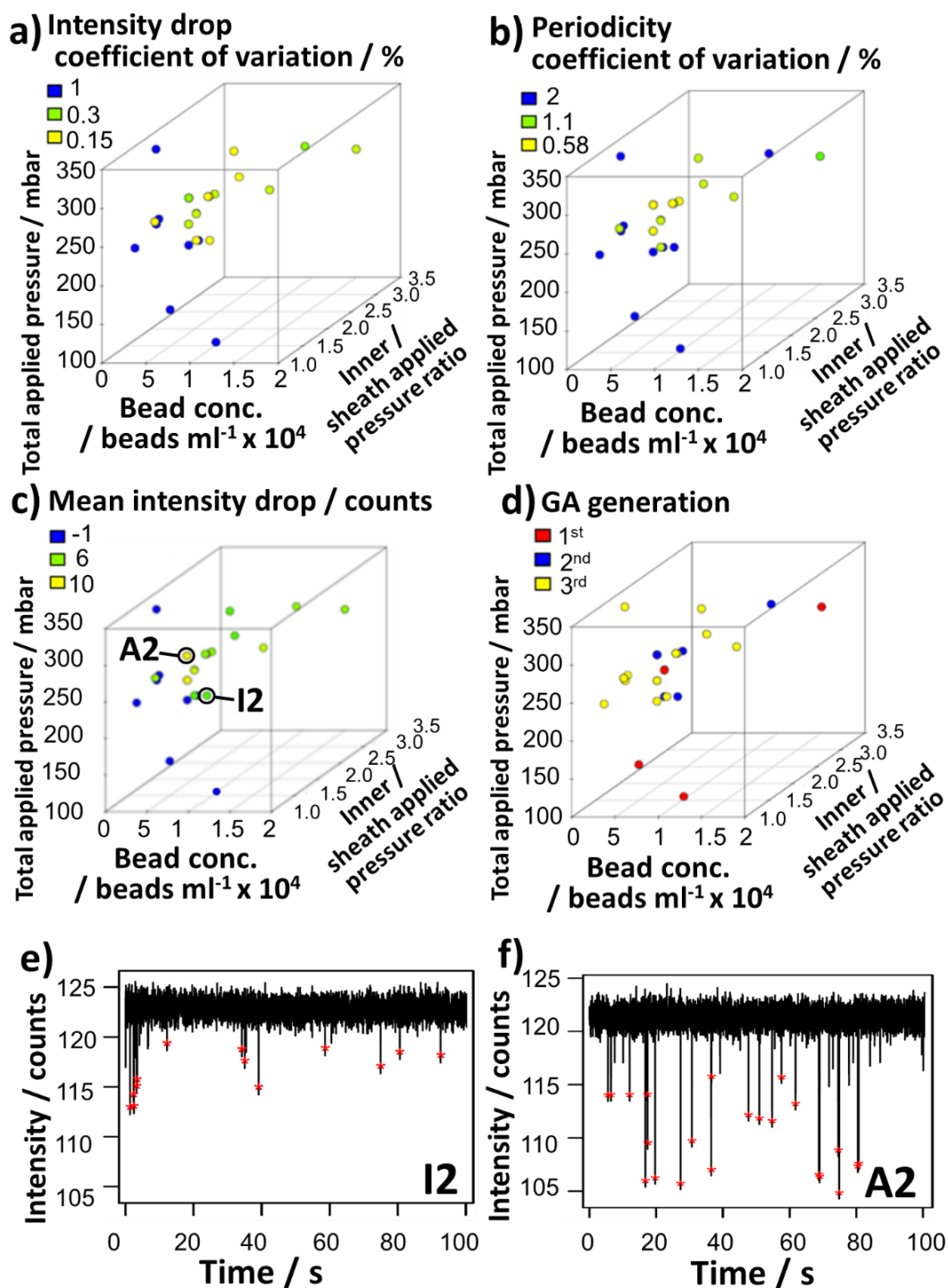


Figure 4.12 Findings of GA optimisation of optical particle analysis experimental parameters. Plots a)–c) denote the same evaluated experimental parameters coloured by performance in terms of a) pulse magnitude variation, b) pulse periodicity variation (time between pulses) and b) mean pulse magnitude. d) Denotes the same points coloured by algorithm generation. e) Example pulse spectrum gained under non-optimised conditions (“I2”), versus f) that gained under optimum conditions “A2”. Plots a)–d) created by William Rowe (Loughborough University, Department of Chemistry).

As another example, found optimum run A2 (Figure 4.13) has far more uniform pulse sizes and periods than run H2 (Figure 4.14), which features large bursts of simultaneous particle pulses.

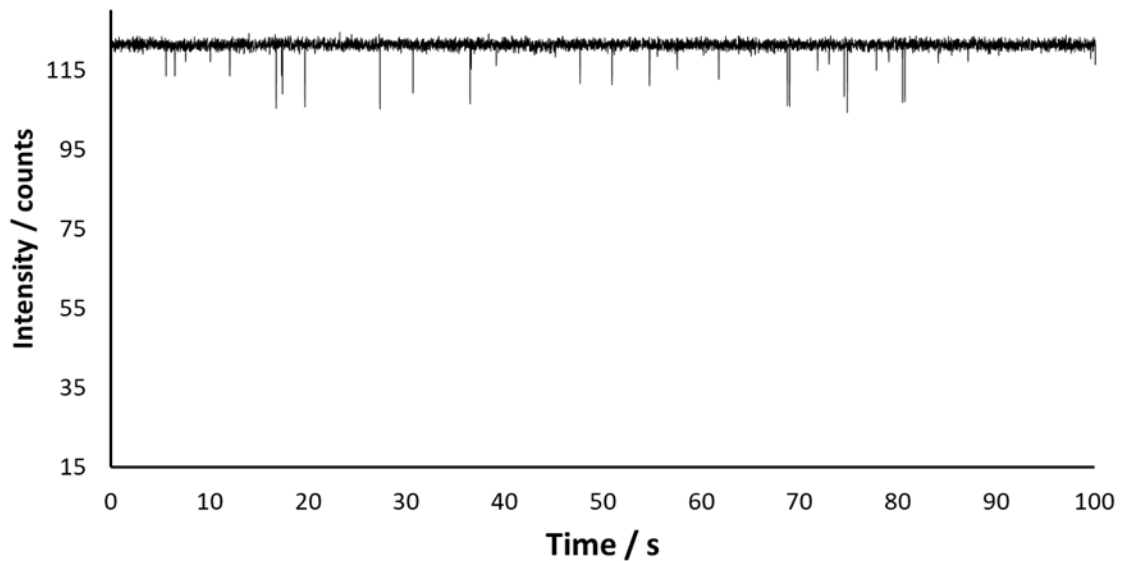


Figure 4.13 Recorded pulse spectrum for found optimum run 'A2' in genetic algorithm (see Table 4.4), involving a 8.06×10^3 particles mL^{-1} $30 \mu\text{m}$ particle core stream analysed via a $105 \mu\text{m}$ core optical fibre at 2.63 inner/sheath flow ratio and 207 mbar total pressure.

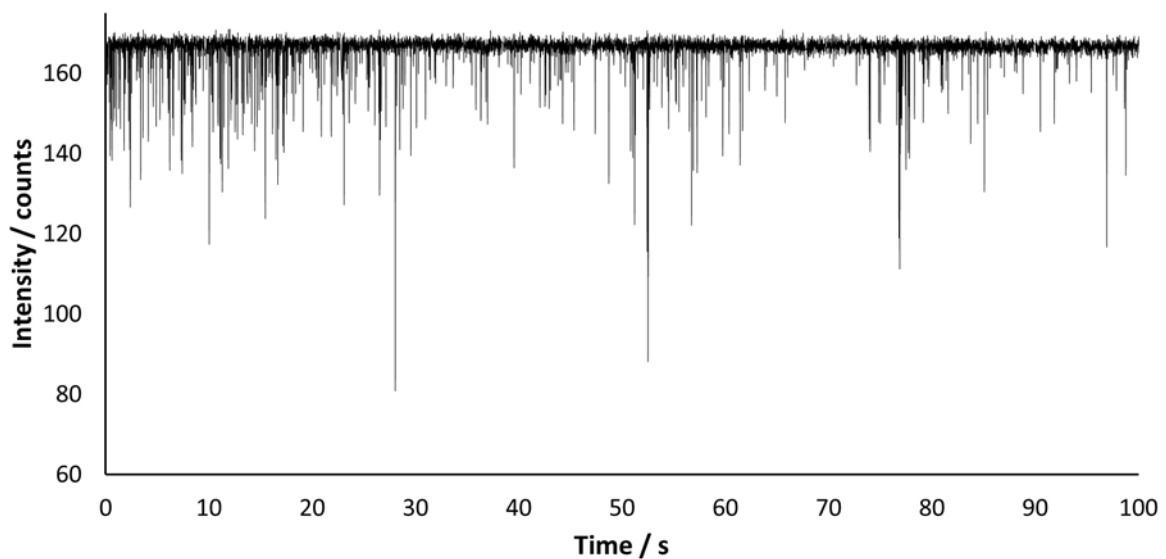


Figure 4.14 Recorded pulse spectrum for run 'H2' in genetic algorithm (see Table 4.4), involving a 1.35×10^5 particles mL^{-1} $30 \mu\text{m}$ particle core stream analysed via a $105 \mu\text{m}$ core optical fibre. Sample suspension flow appears unstable, as indicated by large bursts of pulses.

It should be noted that a number of pulses with magnitudes of approximately 6–7 counts were not called by the genetic algorithm in Figure 4.12 f), but 4 count pulses of this magnitude were called in Figure 4.12 e). This was due to the method of peak-calling, where pulses were called if their magnitude was $> 5xSDs$ from the baseline intensity; higher pulse numbers and magnitudes decrease the baseline intensity, effectively increasing the threshold for peak-calling.

4.5.5 Particle counting

To determine if device pulse frequency was proportional to particle concentration, a range of $30\ \mu\text{m}$ bead concentrations was analysed under the optimum conditions set “A2” identified by the GA. This allowed us to produce a plot of pulse frequency versus particle concentration (Figure 4.15). Each point is a mean of 2 run repeats performed after device dismantling and reassembly. A high correlation coefficient of 0.998 was gained, comparable to soft-lithography devices utilising electrochemical sensing with a relatively costly set-up⁵⁵.

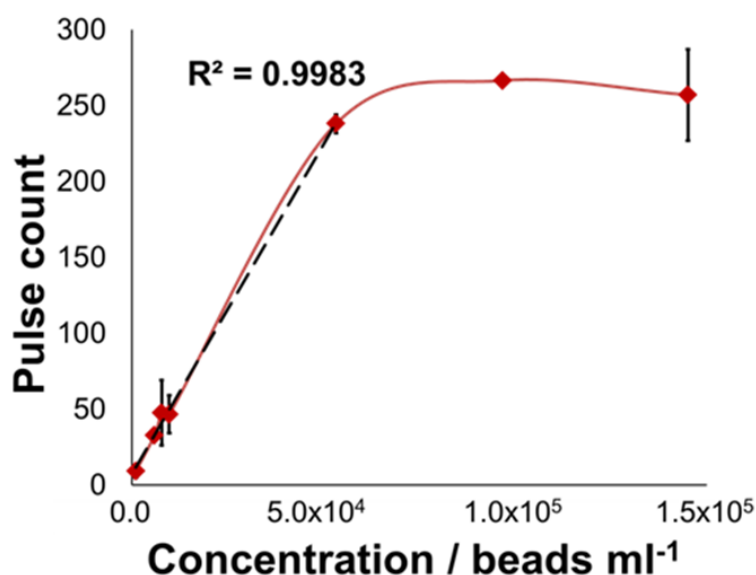


Figure 4.15 Plot of pulse count measured versus particle concentration by the printed optical chip, each count captured over 100 s at the deduced optimised conditions for $30\ \mu\text{m}$ beads.

It was found that pulse count increased linearly with bead concentration up to 5.5×10^4 particles mL^{-1} , at which point the number of counted pulses plateaus at approximately 270 particles min^{-1} (Figure 4.15). The reason for the lack of increase in measured pulse frequency beyond this concentration for this set of conditions is, like the missed pulses in Figure 4.12 f) compared to Figure 4.12 e), attributed to the automated process for peak-calling used: a 50-point moving average

baseline light intensity was calculated across a particle run duration, and an intensity drop threshold of $3 \times \text{SDs}$ from this value was set for pulse calling. At greater bead concentration the high numbers of pulses decreases the calculated baseline intensity value, whilst increasing the intensity SD value, causing pulses to be missed. Figure 4.16 illustrates this effect. An alternative pulse-calling method that uses a threshold for the baseline intensity calculation to eliminate pulse values being included could alleviate this, but for the purposes of this project the graph linear section was adequate, and the found optimum concentration for $30 \mu\text{m}$ diameter beads fell well within this range.

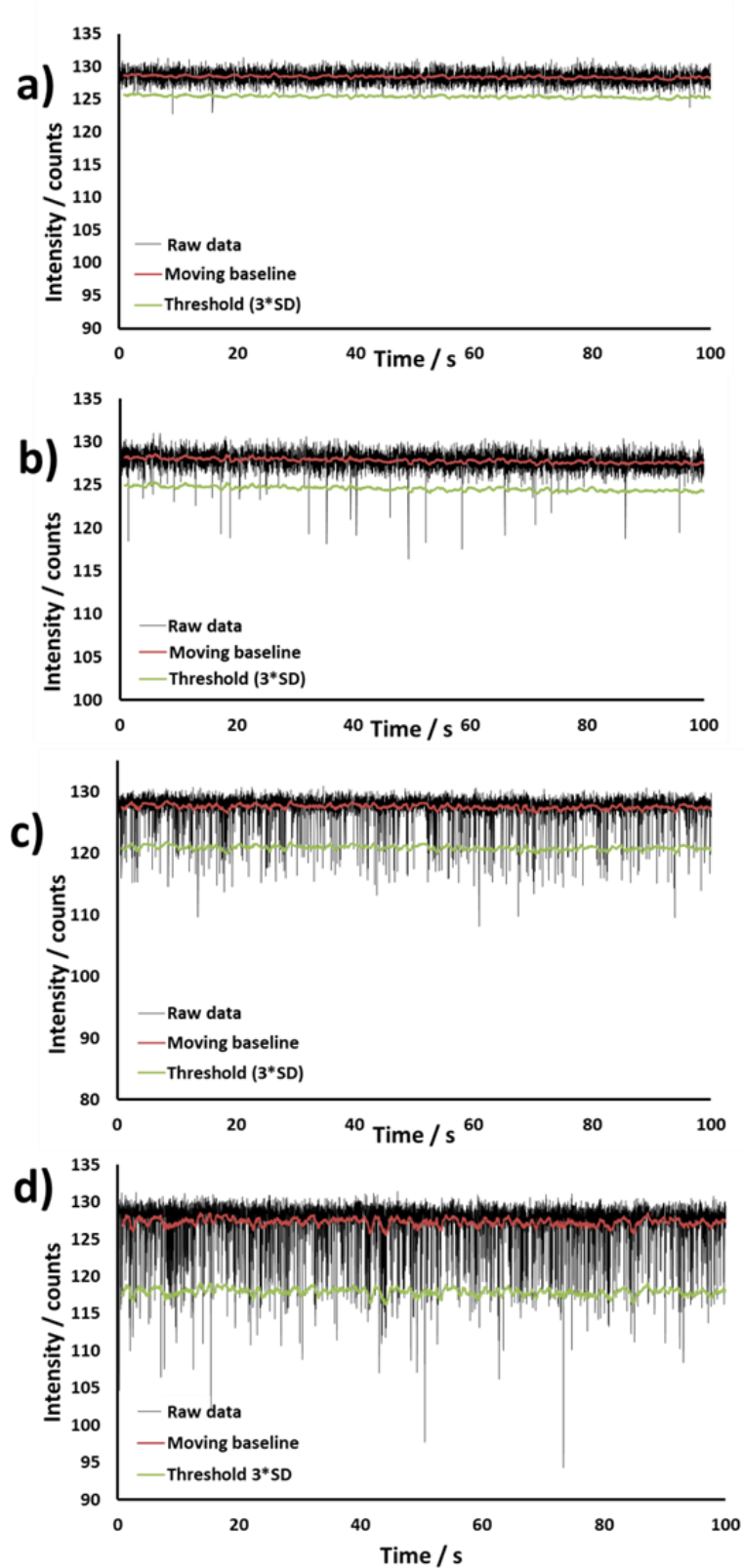


Figure 4.16 Examples of particle runs from the 30 μm bead count calibration graph: a) 1×10^3 particles mL^{-1} b) 1×10^4 particles mL^{-1} c) 5.5×10^4 particles mL^{-1} d) 1.0×10^5 particles mL^{-1} , all run under the found optimum conditions. a)–c) Fall in the calibration graph region. d) Falls in the graph plateau region.

4.5.6 Particle sizing

Finally, we wished to ascertain if device pulse magnitude was proportional to particle diameter. Suspensions containing $10\ \mu\text{m}$ (2.5×10^4 beads mL^{-1}), and $30\ \mu\text{m}$ (2.5×10^4 beads mL^{-1}) polystyrene beads were analysed by the optical chip at the found optimum conditions, followed by a mixture of the two (1.25×10^4 beads mL^{-1} each). Figure 4.17 shows the pulse spectra attained from the suspensions of a) $30\ \mu\text{m}$ beads c) $10\ \mu\text{m}$ beads and d) the mixture.

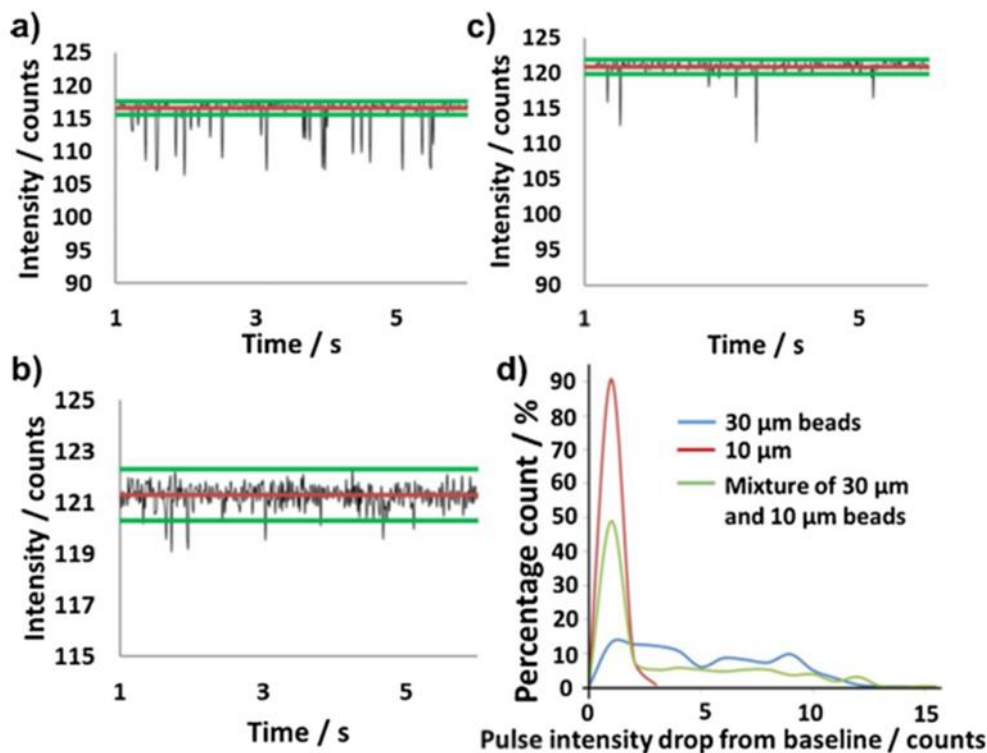


Figure 4.17 Recorded pulse spectra at found optimised conditions ('A2') for a) $30\ \mu\text{m}$ beads (2.5×10^4 beads mL^{-1}) b) $10\ \mu\text{m}$ beads (2.5×10^4 beads mL^{-1}) c) a 1:1 mixture of the two beads (each 1.25×10^4 beads mL^{-1}). The red line denotes the mean baseline light intensity, with the green lines denoting $3 \times \text{SD}$ of the noise from a blank run. d) Histogram showing percentage of pulses vs. signal intensity for $10\ \mu\text{m}$ beads (2.5×10^4 beads mL^{-1}), $30\ \mu\text{m}$ beads (2.5×10^4 beads mL^{-1}), and the 1:1 mixture (1.25×10^4 beads mL^{-1}).

The pulses from the $10\ \mu\text{m}$ beads (with intensities 1–3 counts lower than baseline, Figure 4.17 b) have a significantly smaller magnitude than those of $30\ \mu\text{m}$ beads (1–14 counts lower than baseline, Figure 4.17 a). This pulse magnitude reduction is due to the $10\ \mu\text{m}$ beads blocking less light from the illumination fibre. A challenge in sizing heterogeneous mixtures via light obscuration is the steep decrease in pulse magnitude with particle size, as the method involved effectively capturing particle

circular surface area, which scales with particle diameter via πr^2 . Thus, for a 105 μm fibre optic core, which has a surface area of 1964 μm^2 , a 30 μm spherical particle will cover 707 μm^2 : 36% of the core face, whilst a 10 μm particle will cover 4.0% and a 4 μm particle only 0.7%. Thus, the signal-to-noise ratio diminishes rapidly as particle diameter decreases. Table 4.6 gives the percentage of optical fibre face coverage for three particle sizes and the two optical fibre faces used. It is not probable that the optical chip could measure particles smaller than 10 μm in its current form.

Table 4.6 Circular surface areas of three particle sizes (30 μm , 10 μm and 4 μm) and the percentage area they cover of two optical fibre areas (50 μm and 105 μm).

Optical fibre core diameter, area	30 μm particle diameter, 707 μm^2	10 μm particle diameter, 79 μm^2	4 μm particle diameter, 13 μm^2
	% of optical fibre diameter		
50 μm , 1964 μm^2	36.0%	4.0%	0.7%
105, 8659 μm^2	8.2%	0.9%	0.2%

Pulse magnitudes for the 3 runs were plotted as pulse percentage histograms (Figure 4.17 d). The bead mixture histogram had peaks coinciding with those of the individual 10 and 30 μm bead suspensions. The broad pulse intensity range of the 30 μm beads is likely to be due to the nature of data acquisition and particle movement: particles in the process of entering or exiting the light path during data acquisition will give a lower signal than those captured in the beam centre. This could be alleviated by increasing the number of data points captured per second, ensuring particle measurement throughout its passage through the interrogation zone. However, this does not prevent particles at different heights in the channel causing pulse variation. We also cannot exclude multiple beads being simultaneously detected.

Due to the aforementioned poor pulse uniformity for 30 μm beads, it was thought that the device resolving power would be insufficient to be able to characterise a cell population.

4.6 Conclusions

The first 3D printed optical particle analysis device was fabricated in roughly 5 hours, with only ~ 1 h fabrication time spent on manual work (consisting of rinsing, optical fibre polishing and cover layer application). It utilises an integrated optical detection system that is simpler, cheaper and more user-friendly than those of current microflow cytometers, as well as being able to discriminate particles by

size (to a certain extent) without requiring sample labelling. The chip cost only £12 in materials to produce, bringing it into the realm of disposable sensors.

Initial dye stream focusing studies found that core stream width stability was lower at lower overall flow rates. Good linearity ($R^2=0.9986$) was found between core stream width and measured absorbance, although core stream sizing via the Beer–Lambert Law was not possible as there appears to be interface diffusion and/or non-uniform vertical focusing occurring.

Particle analysis experimental parameters were optimised in terms of signal reproducibility and strength via three generations of an evolutionary multiobjective optimisation algorithm. The GA identified an optimised set of five parameters (particle concentration, inner flow/sheath flow ratio and thus core stream width, overall flow rate, optical fibre core diameter and the presence or lack of dye in core stream), eliminating the use of smaller, 50 μm optical fibre core due to alignment failures, and dye due to pulse obscuration. Using these optimised conditions, particle counting and sizing experiments were carried out, finding a linear dynamic range up to 5×10^4 particles mL^{-1} for 30 μm particles, and being able to discriminate between 10 and 30 μm beads. However, it was thought that resolving power was insufficient for cell population characterisation.

During this work numerous issues were discerned, a key one being that pulse uniformity was poor, not just relative to that of similar, albeit non-printed, optical particle analysis microfluidic chips^{56–58}, but also to the printed RPS chip in Chapter 5. In comparison to other optical LOC papers, we have a significant number of reduced pulses stemming from only partial capturing of whole particle surface area during measurement. This is made worse by the fibre core not encompassing the entire microchannel height. The smaller, 50 μm optical fibre core is especially prone to partial particle imaging, and thus its signal reproducibility is worse. Additionally, the device sensitivity was much lower than similar, non-printed optical chips^{56–58}, with 10 μm particle sizes being its detection limit. Other issues include the GA failing to take into account throughput or counting efficiency except for runs showing 0 particles, and difficulty in fibre alignment, especially for the smaller, 50 μm wave guide.

4.7 References

- 1 M. E. Natoli, R. A. Schwarz, M. Bond, C. E. Majors, B. A. Rohrman, C. A. Smith and R. R. Richards-Kortum, in *Frugal Innovation in Bioengineering for the Detection of Infectious Diseases*, eds. A. K. Chavali and R. Ramji, Springer International Publishing AG, Basel,

- Switzerland, 2018, pp. 1–22.
- 2 M. D. Perkins, C. Dye, M. Balasegaram, C. Bréchet, J.-V. Mombouli, J.-A. Røttingen, M. Tanner and C. C. Boehme, *Lancet*, 2017, **390**, 2211–2214.
- 3 A. M. Urdea, L. A. Penny, S. S. Olmsted, M. Y. Giovanni, P. Kaspar, A. Shepherd, P. Wilson, C. A. Dahl, S. Buchsbaum, G. Moeller and D. C. H. Burgess, *Nature*, 2006, **422**, 412–418.
- 4 S. Colombo, M. Beck-Broichsitter, J. P. Bøtker, M. Malmsten, J. Rantanen and A. Bohr, *Adv. Drug Deliv. Rev.*, 2018, **128**, 115–131.
- 5 J. Rantanen and J. Khinast, *J. Pharm. Sci.*, 2015, **104**, 3612–3638.
- 6 R. Dragone, G. Grasso, M. Muccini and S. Toffanin, *Front. Public Heal.*, 2017, **5**, 1–6.
- 7 K. A. Koehler and T. Peters, *Curr. Environ. Health Rep.*, 2015, **2**, 399–411.
- 8 D. T. Chiu, A. J. DeMello, D. Di Carlo, P. S. Doyle, C. Hansen, R. M. Maceiczkyk and R. C. R. Wootton, *Chem*, 2017, **2**, 201–223.
- 9 S. Shoji and K. Kawai, in *Microfluidic Technologies and Applications*, ed. B. Lin, Springer-Verlag, Berlin, Germany, 2011, pp. 1–25.
- 10 M. Karle, S. K. Vashist, R. Zengerle and F. von Stetten, *Anal. Chim. Acta*, 2016, **929**, 1–22.
- 11 N. M. M. Pires, T. Dong, U. Hanke and N. Hoivik, *Sensors*, 2014, **14**, 15458–15479.
- 12 M. Estevez, M. Avarez and L. Lechuga, *Laser Photonics Rev.*, 2012, **6**, 463–487.
- 13 H. Gai, Y. Li and E. Yeung, in *Microfluidics Technologies and Applications*, ed. B. Lin, Springer-Verlag, Berlin, Germany, 2011, pp. 171–201.
- 14 K. B. Mogensen and J. P. Kutter, *Electrophoresis*, 2009, **30**, 92–100.
- 15 V. Srinivasan, V. K. Pamula and R. B. Fair, *Anal. Chim. Acta*, 2004, **507**, 145–150.
- 16 G.-B. Lee, C.-H. Lin and G.-L. Chang, *Sens. Actuators A Phys.*, 2003, **103**, 165–170.
- 17 A. Acharya, M. Packirisamy and R. Izquierdo, *Micromachines*, 2015, **6**, 1406–1420.
- 18 M. Yao, G. Shah and J. Fang, *Micromachines*, 2012, **3**, 462–479.
- 19 J.-L. Fu, Q. Fang, T. Zhang, X.-H. Jin and Z.-L. Fang, *Anal. Chem.*, 2006, **78**, 3827–3824.
- 20 Z. A. K. Wang, S. Y. Chin, C. D. Chin, J. Sarik, M. Harper, J. Justman and S. K. Sia, *Anal. Chem.*, 2010, **82**, 36–40.
- 21 S. L. Zhao, X. T. Lia and Y. M. Liu, *Anal. Chem.*, 2010, **81**, 3873–3878.
- 22 G. Perozziello, P. Candeloro, A. De Grazia, F. Esposito, M. Allione, M. L. Coluccio, R. Tallerico, I. Valpapuram, L. Tirinato, G. Das, A. Giugni, B. Torre, P. Veltri, U. Kruhne, G. Della Valle and E. Di Fabrizio, *Opt. Express*, 2016, **24**, 180–190.
- 23 M. Furuki, J. Kameoka, H. G. Craighead and M. S. Isaacson, *Sens. Actuators B Chem.*, 2001, **79**, 63–69.
- 24 N. Punjabi, J. Satija and S. Mukherji, in *Sensing Technology: Current Status and Future Trends*

- III, eds. A. Mason, S. C. Mukhopadhyay and K. P. Jayasundera, Springer International Publishing, Basel, Switzerland, 2015, pp. 25–45.
- 25 X. Li, J. Wu, A. Liu, Z. Li, Y. Soew, H. Huang, K. Xu and J. Lin, *Appl. Phys. Lett.*, 2008, **93**, 193901.
- 26 X. Liang, A. Liu, C. Lim, T. Ayi and P. Yap, *Sens. Actuators A Phys.*, 2007, **133**, 349–354.
- 27 T. Ngernsutivorakul, C. M. Cipolla, C. E. Dugan, S. Jin, M. D. Morris, R. T. Kennedy and F. W. L. Esmonde-White, *Anal. Bioanal. Chem.*, 2017, **409**, 275–285.
- 28 F. Xing, G.-X. Meng, Q. Zhang, L.-T. Pan, P. Wang, Z.-B. Liu, W.-S. Jiang, Y. Chen and J.-G. Tian, *Nano Lett.*, 2014, **14**, 3563–3569.
- 29 O. Hofmann, P. Miller, P. Sullivan, T. S. Jones, J. C. DeMello, D. D. C. Bradley and A. J. DeMello, *Sens. Actuators B Chem.*, 2005, **106**, 878–884.
- 30 J.-T. Cao, Z.-X. Chen, X.-Y. Hao, P.-H. Zhang and J.-J. Zhu, *Anal. Chem.*, 2012, **84**, 10097–10104.
- 31 A. H. Tkaczyk, E. R. Tkaczyk, T. B. Norris and S. Takayama, *J. Mech. Med. Biol.*, 2011, **11**, 1–4.
- 32 K. F. Lei, in *Microfluidics in Detection Science*, eds. F. H. Labeed and H. O. Fatoyinbo, RSC, Cambridge, UK, 2014, pp. 1–28.
- 33 A. Waldbaur, H. Rapp, K. Länge and B. E. Rapp, *Anal. Methods*, 2011, **3**, 2681–2716.
- 34 W. Lee, D. Kwon, W. Choi, G. Y. Jung and S. Jeon, *Sci. Rep.*, 2015, **5**, 1–6.
- 35 H. N. Chan, Y. Shu, B. Xiong, Y. Chen, Y. Chen, Q. Tian, S. A. Michael, B. Shen and H. Wu, *ACS Sens.*, 2016, **1**, 227–234.
- 36 G. W. Bishop, J. E. Satterwhite-Warden, I. Bist, E. Chen and J. F. Rusling, *ACS Sens.*, 2016, **1**, 197–202.
- 37 A. I. Shallan, P. Smejkal, M. Corban, R. M. Guijt and M. C. Breadmore, *Anal. Chem.*, 2014, **86**, 3124–3130.
- 38 M. Weidenbach, D. Jahn, A. Rehn, S. F. Busch, F. Beltrán-Mejía, J. C. Balzer and M. Koch, *Opt. Express*, 2016, **24**, 28968–28976.
- 39 K. Willis, E. Brockmeyer, S. Hudson and I. Poupyrev, in *Proceedings of the 25th Annual ACM Symposium on User Interface Software and Technology—UIST’12*, 2012, pp. 589–598.
- 40 S. S. Hinman, K. S. McKeating and Q. Cheng, *Anal. Chem.*, 2017, **89**, 12626–12630.
- 41 B. G. Assefa, T. Saastamoinen, M. Pekkarinen, J. Bishop, M. Kuittinen and J. S. Turunen, in *Proceedings Volume 10554, Light-Emitting Diodes: Materials, Devices, and Applications for Solid State Lighting XXII*, ed. SPIE, San Francisco, CA, US, 2018, p. 105541J.
- 42 B. Stender, W. Mantei, R. Houbertz and B. Hall, *Laser Tech. J.*, 2017, **2**, 20–23.
- 43 T. Monaghan, M. J. Harding, R. A. Harris, R. J. Friel and S. D. R. Christie, *Lab Chip*, 2016, **16**,

- 3362–3373.
- 44 R. Walczak and K. Adamski, *J. Micromech. Microeng.*, 2015, **25**, 1–13.
- 45 G. Comina, A. Suska and D. Filippini, in *Proceedings Volume 10061 Microfluidics, BioMEMS, and Medical Microsystems XV*, San Francisco, US, 2017, vol. 100610E.
- 46 O. Okafor, A. Weilhard, J. A. Fernandes, E. Karjalainen, R. Goodridge and V. Sans, *React. Chem. Eng.*, 2017, **2**, 129–136.
- 47 P. J. Kitson, M. H. Rosnes, V. Sans, V. Dragone and L. Cronin, *Lab Chip*, 2012, **12**, 3267–3271.
- 48 R. M. Jarvis, W. Rowe, N. R. Yaffe, R. O'Connor, J. D. Knowles, E. W. Blanch and R. Goodacre, *Anal. Bioanal. Chem.*, 2010, **397**, 1893–1901.
- 49 J. Knowles, *IEEE Comput. Intell. Mag.*, 2009, **4**, 77–91.
- 50 C. G. Knight, M. Platt, W. Rowe, D. C. Wedge, F. Khan, P. J. R. Day, A. Mcshea, J. Knowles and D. B. Kell, *Nucleic Acids Res.*, 2009, **37**, e6.
- 51 A. Hacıoğlu and İ. Özkol, *Aircr. Eng. Aerosp. Technol.*, 2003, **75**, 350–357.
- 52 J. Bongard, V. Zykov and H. Lipson, *Science*, 2006, **314**, 1118–1121.
- 53 D. Corne, N. Jerram, J. D. Knowles, M. Oates and J. Martin, in *Proceedings of the Genetic and Evolutionary Computation Conference (GECCO 2001)*, ed. L. Spector, Morgan Kaufmann Publishers, San Francisco, CA, US, 2001, pp. 283–290.
- 54 A. J. Capel, A. Wright, M. J. Harding, G. W. Weaver, Y. Li, R. A. Harris, S. Edmondson, R. D. Goodridge and S. D. R. Christie, *Beilstein J. Org. Chem.*, 2017, **13**, 111–119.
- 55 Y. Song, H. Zhang, C. H. Chon, S. Chen, X. Pan and D. Li, *Anal. Chim. Acta*, 2010, **681**, 82–86.
- 56 M. Rosenauer, W. Buchegger, I. Finoulst, P. Verhaert and M. Vellekoop, *Microfluid. Nanofluidics*, 2011, **10**, 761–771.
- 57 C. Song, T.-D. Luong, T. F. Kong, N.-T. Nguyen and A. K. Asundi, *Opt. Lett.*, 2011, **36**, 657–659.
- 58 L. M. Fu, R. J. Yang, C. H. Lin, Y. J. Pan and G. Bin Lee, *Anal. Chim. Acta*, 2004, **507**, 163–169.

Chapter 5 Additive manufacture of a resistive pulse sensing microfluidic device

5.1 Abstract

Following on from the optical-based sensing chip, a chip was designed that utilised an alternative, electrochemical mode of detection: RPS. RPS particle analysis varies in its advantages and setbacks from optical methods as covered in Chapter 1.3.2, critical differences being its superior resolving power, and susceptibility to blockages. The RPS chip detection system comprised a constrictive pore channel and embedded electrode pair. During the RPS process, particles/cells in a conductive solution traverse the pore channel and cause measurable, transient drops in ionic current, whose frequency allows counting, and whose magnitude and profile elucidates particle/cell size and other information.

The same fabrication method as previous chapters was used, again making it possible for the sensor to be quickly assembled, disassembled, cleaned and reused relative to conventional lithography methods. Due to their smaller size, the chips were lower-cost than the optical chip, costing approximately £6.50 and £8.50 to produce. Building on the pore channel resolution and reproducibility study in Chapter 3.5.5.1, we compared the behaviour reproducibility of different pore device copies, and investigated the effects of the cover layer sealing process on analysis. Additionally, three different pore channel dimensions were produced, and their I-V responses, particle throughputs and pulse morphologies investigated under a range of flow conditions.

Particle quantification linearity ($R^2=0.9981$) was similar to that of the optical chip ($R^2=0.9983$), but counting throughout was significantly higher: $\sim 1380 \text{ min}^{-1}$ under unoptimised conditions, in comparison to the $\sim 270 \text{ min}^{-1}$ throughput of the optical chip under optimised parameters. Resolving power was also higher, with the RPS device being able to differentiate between $20 \mu\text{m}$ and $30 \mu\text{m}$ beads in a mixture (in comparison to the 10 and $30 \mu\text{m}$ bead mixture differentiated by the optical chip in Chapter 4), as well as characterise a population of skeletal muscle cells. However, chip detection sensitivity was lower, with the RPS device only able to detect $10 \mu\text{m}$ beads under certain cover layer conditions, due to electrical noise. This noise susceptibility requires further improvement.

5.2 Introduction

RPS is a type of ionic current sensing technology that relies on Maxwell's theory that the presence of non-conducting particles in a conducting medium causes an increased resistance proportional to the particle-excluded volume¹. RPS sensors are a subset of Coulter counters, relying on the Coulter principle which states that particles traversing an orifice concurrent with an electric current produce an impedance change that is proportional to the volume of the particle². By comparison of measured impedance changes (also recordable as sudden drops in baseline current, or increases in resistance, i.e. *resistive pulses*) to those of calibration beads of known size, particle sizing is possible. The magnitude of these pulses give information on the particle size as it is related to the excluded ion volume, and pulse shape and duration also allude to the shapes and charges of the particle and pore (see Chapter 2.6.1). Thus, RPS can both quantify particle concentration as well as characterise them, deducing particle size as well as charge/zeta information^{3,4}.

The basic RPS set-up comprises a pore orifice with electrodes situated on either side. There are two main pore categories: solid-state pores and biological pores. Solid-state pores are fabricated in synthetic materials and include glass, quartz and carbon pipettes⁵. The original nanopore sensor as made by Coulter in 1953 was a solid-state pore, and consisting of a glass tube with a microscopic hole that counted translocating blood cells². Other solid-state pore materials include silicon nitride⁶, polymers⁷, graphene⁸, boron nitride⁹ and MoS₂¹⁰. Biological pores are naturally-occurring pore-forming proteins, such as α -hemolysin and Mycobacterium smegmatis porin A (MspA), embedded into a lipid bilayer¹¹. These systems can be relatively low-cost, quick to prepare and reproducible, but their size choice is highly restricted to a very narrow range of $\sim 1\text{--}6$ nm¹¹, severely limiting their use to analysis of very small analytes such as DNA¹¹, and they also typically require narrow temperature and pH ranges¹². In contrast, solid-state pores can be produced to diameters across the entire nm to μm range and in a range of shapes, the most common being cones¹³ and cylinders^{14,15} due to their fabrication ease and most biological pores being cylindrical, but other shapes such as pyramids¹⁶ are possible. Solid-state fabrication techniques depend on the material involved¹⁷ but include focused ion beam (FIB)¹⁸, electron beam¹⁹ and wet etching²⁰. In addition, a subset RPS technique, tunable resistive pulse sensing (TRPS), involves a stretchable pore whose diameter can be tuned in order to maximise population resolution in heterogeneous samples²¹, and has emerging biosensing applications²²⁻²⁴.

RPS has been successfully incorporated into a large array of microfluidic systems as covered in a review by Song, et al.²⁵, who notes its value as a high-throughput, high-sensitivity, label-free platform for

continuous-flow analysis. Many papers describing microfluidic RPS systems are either proof-of-concept studies demonstrating bead analysis^{26–28}, or demonstrate bacteria detection for healthcare application^{29,30}, whilst others have been developed for niche applications as broad as measuring space radiation effects on cells³¹, bacteria detection in ship ballast water³², and biopharmaceutical product characterisation³³, to name a few. A small number of fluidic devices feature embedded pore structures such as silicon nitride pore membranes^{34,35}, but typically ‘pores’ take the form of planar, angular channel constrictions^{26,28,32,36–38}, although unique pore channel geometries and configurations have also been produced, including planar circular pores³⁹ to enable further analysis, and pores with additional fluid streams^{40,41} for sensitivity enhancement. Multiple pores can also be used in tandem within microfluidic devices to vastly increase throughput, as in the seven-channel RPS chip produced by Song, et al.²⁷ that counted 7140 particles min⁻¹ with a flow rate of 10 $\mu\text{L min}^{-1}$. Microfluidic pores can also be used in series to further resolve two populations of similar size (such as two strains of HBV capsids with diameters differing by 3 nm³⁷) by electrophoretic mobility. The most common material for microfluidic RPS systems has been PDMS^{28,29,32,36,38,39}, with pore dimensions ranging from tens of microns to single microns, but there are a small number of papers describing other materials such as glass^{37,42}, in which 300x100 nm cross-section pores are produced by FIB milling.

Unlike optical flow cytometry, RPS is not affected by the optical properties of the particles/cells, or of the solution. It can also detect translucent particles, a challenge for light obscuration methods⁴³. However, RPS involves a number of challenges. Due to the flow constrictions involved, RPS is highly susceptible to blockages, which waste both sample and time, and require instrument cleaning. Blockages typically occur when an initial particle becomes attached to a wall either inside the pore or at its mouth, followed by a rapid ensuing build-up of more particles due to attractive forces at a short distance⁴⁴. Alternatively, pore blockages can form due to large particle aggregates⁴⁵ or particle bridging at the pore mouth⁴⁵. This tendency to block limits the measurable size range of RPS and prevents analysis of highly polydisperse samples⁴⁶, as pores must be of a similar size to particle/cells of interest to ensure adequate sensitivity. It also hinders sensitivity when retaining high throughputs as pulse frequency is directly related to pore size. Additionally, RPS has a further limitation in that samples must be analysed in electrolyte buffer, adding an extra sample preparation step as well as being unsuitable for certain biological samples, and can cause a build-up of salt crystals in the pore⁴⁷. In addition, due to the electrochemical nature of the technique, shielding of the RPS set-up from electrical noise is required⁴⁸.

This chapter concerns a 3D printed microfluidic RPS sensor, fabricated via SLA using the facile cover layer method as used in Chapters 3–4, and featuring embedded silver wire electrodes for single

particle analysis and counting. The effects of sensing zone parameters (pore channel cross-section and length) on current-voltage response, pulse morphology and counting throughput were investigated. The effects of the cover layer application process on the two latter aspects were also investigated, along with reproducibility between device copies. Finally, RPS chips were used to count particles at a range of concentrations and flow rates, analyse a 20 μm and 30 μm bead mixture, detect 10 μm beads, and analyse a population of skeletal muscle cells. Like the optical device covered in Chapter 4, this chip took approximately 5 hrs to print and assemble, and was relatively low cost to produce.

5.3 Aims and Objectives

The aim of this chapter was to develop a 3D printed microfluidic particle analysis device utilising an electrochemical low-cost, label-free detection system.

Towards this end, this chapter had the following objectives:

- Investigate the effects of the pore channel dimensions on current-voltage behaviour, particle throughput and the resulting RPS pulses.
- To demonstrate quantification and sizing of particles and cells.

5.4 Materials and Methods

5.4.1 Materials

5.4.1.1 Chemicals and reagents

IPA, methanol and potassium chloride (KCl) were both obtained from VWR. KCl solutions were made up in deionised water to the following concentrations and measured pH values: 0.1 mM (pH 6.08), 0.25 mM (pH 6.41), 0.5 mM (pH 6.34), 1.0 mM (pH 6.25), 2.5 mM (pH 6.45), 5.0 mM (pH 6.33) and 10.0 mM (pH 6.15). Phosphate-buffered saline (PBS) was obtained from Sigma-Aldrich (catalogue number P4417) and was made up in deionised water to the supplier-recommended concentration (phosphate buffer 0.01 M, potassium chloride 0.0027 M, sodium chloride 0.137 M), with measured pH 7.32. All pH measurements taken by a FiveEasy pH meter with InLab Ultra-Micro-ISM[®] pH electrode, both obtained from Mettler Toledo.

5.4.1.2 Beads

Spherical polystyrene beads of 30 μm diameter (COOH-coated, $\text{SD}<0.4\mu\text{m}$, $\text{CV}<1\%$, obtained from Sigma-Aldrich, catalogue number 84135), 20 μm diameter (micromer[®], COOH-coated, $\text{CV}<5\%$, obtained from Micromod Partikeltechnologie GmbH, catalogue no. 01-02-204), 10 μm diameter, (Fluoresbrite[®] Yellow Green microspheres, COOH-coated, $\text{CV}=15\%$, obtained from Polysciences, catalogue no. 18142-2), and 4 μm diameter (CPC4000s, COOH-coated, obtained from Izon Science) were used for counting and sizing studies.

5.4.1.3 Cells

Skeletal muscle cells of roughly 30 μm diameter were fixated via formaldehyde by Rowan Rimmington, Loughborough University, School of Sport, Exercise and Health Sciences.

5.4.2 Methods

All methods were carried out at ambient room temperature (approx. 18-20°C).

5.4.2.1 Device drafting

NX software (Version 11.0, obtained from Siemens) was used to draft device CAD files and export to .STL format.

5.4.2.2 Stereolithography and post-print processing

The device was printed in Accura[®] 60 polymer on a Viper si2 SLA printer (both obtained from 3D Systems) in its HR build mode (Nd:YV04 solid state laser at 354.7 nm, 100 mW output power, $1/e^2$ beam diameter 75 μm +/- 15 μm , minimum build layer height 20 μm , elevator vertical resolution 25 μm and position repeatability 76 μm) and in the Y build-direction (see Chapter 3), before being cured and washed in IPA and methanol.

5.4.2.3 Electrode embedding

Silver wire (0.25 mm diameter, silver wire, 0.25 mm diameter, purity 99.99%, catalogue number AG5485) was obtained from Advent Research Materials. Electrode alignment was accomplished by the inclusion of open grooves in the device CAD file for wire housing. Wires were pressed into the grooves via a rubber nub, and alignment carried out manually under a microscope.

5.4.2.4 Device sealing

The device was sealed with a cover layer consisting of LEXAN™ 8010PC polycarbonate film (obtained from SABIC, 250 µm thickness) attached via TESA 4965 double-sided tape (obtained from 3M), applied by hand and flattened via seam roller. The electrode grooves were sealed with blobs of two-part epoxy resin (Araldite®, Rapid, obtained from Huntsman Advanced Materials).

5.4.2.5 Fluidic control

Microfluidic flows were effected by Mitos P-Pump Basic pressure-driven pumps (Dolomite) and inputted into the chip by PEEK microfluidic tubing (250 µm internal diameter, obtained from Dolomite) and standard Supelco® HPLC fittings and end ferrules (obtained from Sigma-Aldrich) in printed threads.

5.4.2.6 Noise shielding and set-up

A custom-built Faraday cage (steel, 1 mm thick) was obtained from Nanopore Solutions and used to shield the system from electrical noise. Gold-plated crocodile clips (obtained from Maplins) were used to link electrode wires to circuitry.

5.4.2.7 Data collection

A current amplifier (eOne-XS, obtained from Elements) was utilised for current-voltage response measurements. A second current amplifier (QSensing3) was controlled by Izon Control Suite Software Version 3.1 (both obtained from Izon Science) and current-voltage responses and RPS data recorded. RPS experiments utilised a 15 kHz sampling rate and default 0.05 nA minimum blockade height for particle detection.

5.4.2.8 Current-voltage response measurements

Current-voltage responses were recorded in 3 different printed pores (100 μm cross-section with 500 μm length, 100 μm cross-section with 100 μm length, and 80 μm cross-section with 500 μm length) over a range of KCl electrolyte concentrations and flow rates. A 10 s stabilisation time was used before taking each current measurement.

5.4.2.9 Particle runs

Particle flow was left to stabilise at the flow rate used for 7 s, before being recorded for 60 s. Particle suspensions were ran via the same method as used in Chapter 4.

5.4.2.10 Cell runs

A cell suspension (skeletal muscle cells, $5 \times 10^3 \text{ mL}^{-1}$, prepared by Rowan Rimington) was monitored using the Hp,Wp=100 μm , Lp=500 μm RPS device in Figure 5.6 a (i) for 60 s under 75 mbar in KCl (0.25 mM) and PBS (made up to the recommended concentration), and calibrated against 30 μm beads ran under the same concentration and conditions using Izon Control Suite software (Version 3.1, Izon Sciences).

5.4.2.11 Photography and microscopy

Device photographs were taken via an Exmor R digital camera (obtained from Sony). Microscope photos of chips taken via an Optiphot-2 optical microscope with DS-5M Camera Head controlled by a DS-L1 Digital Sight Camera Control Unit (all obtained from Nikon). Subsequent sizing was carried out via AxioVision software (Zeiss).

5.4.2.12 FEM modelling

FEM modelling of electric field lines and pulse magnitude and shape within a printed Hp,Wp=105 μm , Lp=545 μm pore channel, for particle diameter=30 μm , voltage=+5.64 V, $\sigma=3.675 \text{ mS m}^{-1}$ (KCl, 0.5 mM) was carried out by Peter Hauer, Victoria University of Wellington, School of Chemical and Physical Sciences, via COMSOL. Full details are given in the Supporting Information of Hampson, et al⁴⁹.

5.4.2.13 Statistical methods

Standard deviation for a data set was calculated via Equation 3.1.

5.5 Results & discussion

5.5.1 Chip concept

Figure 5.1 illustrates the RPS sensing principle of the printed pore device. Figure 5.1 a) shows particle translocation through the pore constriction, guided by microfluidic flow over ramps included in the CAD file. The act of this translocation causes a drop in the baseline ionic current running across the pore, whose intensity is related to the size of the particle (see Chapter 2.6.1). Figure 5.1 b) illustrates the change in pulse magnitude with particle size, reflecting the different relative volumes occupied of the pore channel by the particle.

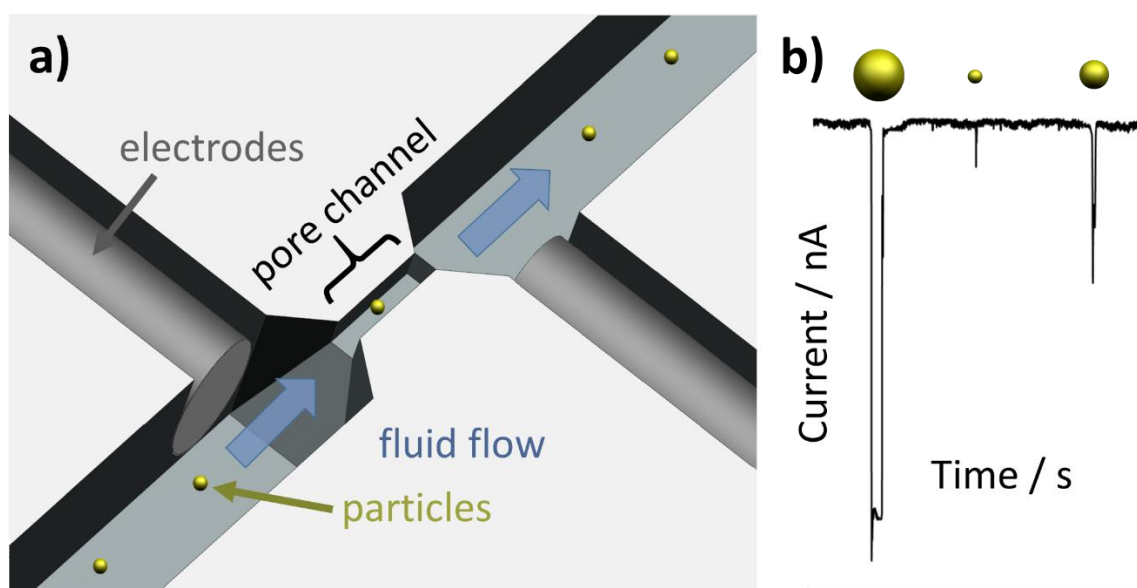


Figure 5.1 Schematic illustrating a) particle translocation through the pore channel under microfluidic flow, and b) resulting pulses from different-sized particles.

As pulse magnitude scales linearly with particle volume, sample sizing can be enabled by a single point calibration with beads of a known size. This process does not require the accurate, printed pore dimensions to be known.

5.5.2 Device parameters

Like the optical chip in Chapter 4, the microfluidic channels of the RPS chips in this chapter were printed open on the device surface. This includes the pore channel, which takes the form of a channel constriction upwards, towards the chip surface. The pore channel features two ramps at each opening to gently guide particle-laden flow, as opposed to using a shear vertical surface face perpendicular to flow, and is flanked by two Ag/AgCl electrodes. The channels are sealed by a cover layer consisting of adhesive and PC film. These different sections of the pore device are illustrated in Figure 5.2.

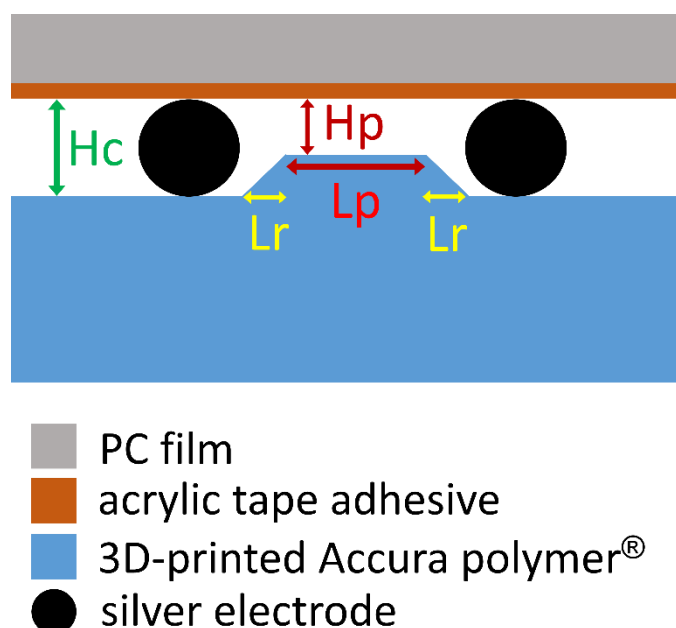


Figure 5.2 Illustration of pore device channel cross-section. H_c (channel height), H_p (pore channel height), L_p (pore channel length), L_r (ramp length).

White space represents the microfluidic channel. Microfluidic channel height, H_c , is the same as the channel width, W_c (not shown in figure as this parameter comes towards the viewer, perpendicular to the page) as the channel is of a square cross-section ($H_c=W_c=250\ \mu\text{m}$). The sensing zone has three dimensions: pore channel length (L_p), pore channel height (H_p), and pore channel width (W_p , not shown, which is equal to H_p as the pore channel has a square cross-section). These three pore channel dimensions were varied. Ramps found at either pore end had length L_r , which was kept constant at $100\ \mu\text{m}$.

Two device configurations were trialled: a more compact design (Figure 5.3 a) and a larger one (Figure 5.3 b), both utilising surface, Y-directionally printed microfluidic channels but differing in thread

direction. The latter device design was produced after discovery of the problems associated with horizontally-printed threads (Chapter 3.4.2.3).

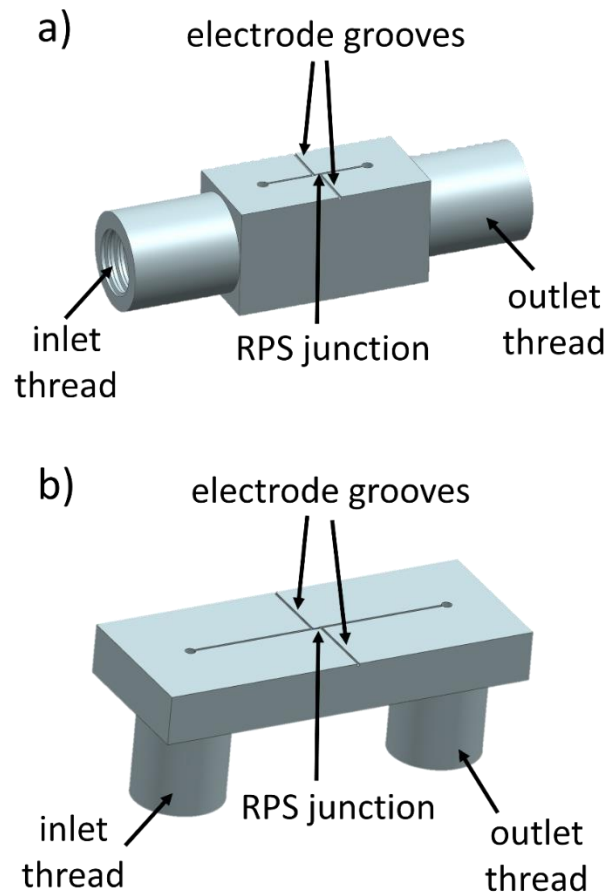


Figure 5.3 CAD files of the two device configurations used for the microfluidic RPS device, with features labelled: a) more compact design featuring horizontal threads, and b) larger design featuring vertical threads.

Figure 5.4 shows a finished, printed, sealed device, showing embedded silver electrodes protruding out of the device sides.

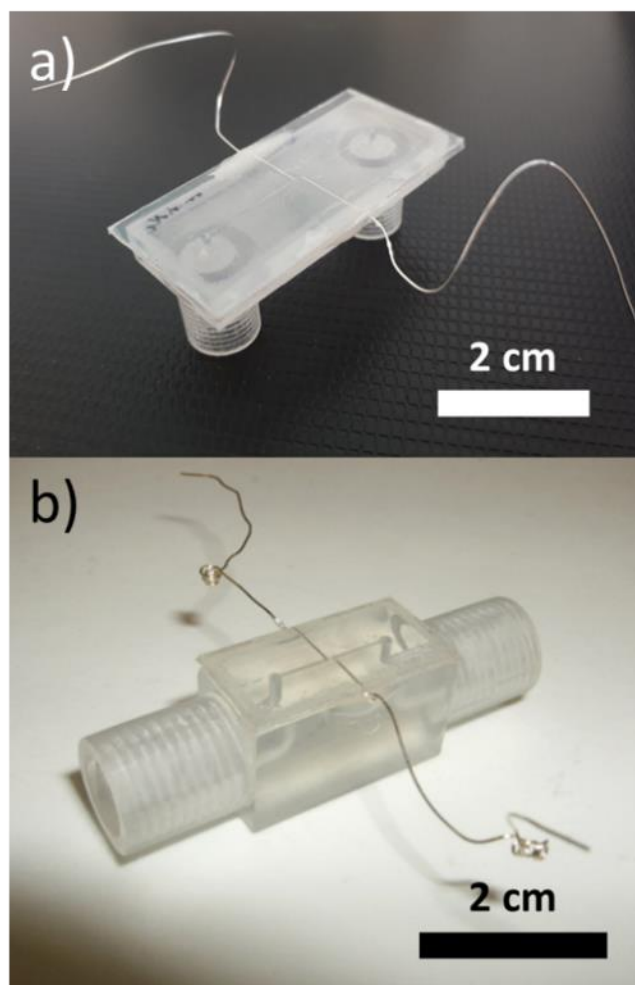


Figure 5.4 Photographs of two different pore device configurations, with embedded electrodes and cover layer. *a) A larger chip design with vertical threads, and b) a more compact chip but with horizontal threads.*

5.5.2.1 Pore channel dimensions

Three dimensions of pore channel were investigated, all with square-cross sections ($H_p=W_p$) but different pore aspect ratios. Pore aspect ratio, that is, pore length divided by its diameter, is an important factor in RPS^{50,51}. Low-aspect pores give sharp, short duration, high magnitude pulses⁵² and have excellent spatial resolution, being able to carry out in-depth particle/cell shape analysis⁵², and having the potential to enable nanoscale scanning of particle morphologies. However, in such short pores, ion transport is no longer defined straightforwardly by pore resistance as it is in high aspect ratio pores, but by the access resistance: the ionic resistivity at the orifice, which greatly complicates pulse interpretation as the effective translocation length extends out of the pore due to this effect^{51,53}. In contrast, higher-aspect pores give longer duration pulses due to the longer translocation time⁸ and can much better differentiate sample surface charges⁸. Early RPS pores were of this type^{15,54} and their

pulse interpretation is relatively simple, with pulse width denoting the translocation time-of-flight. We fabricated two chips with high aspect ratio pore channels of varying cross-section (Figure 5.5 a and b) and a chip with a lower-aspect pore channel with a 100 μm square pore channel ($H_p=W_p=L_p=100 \mu\text{m}$, Figure 5.5 c). The thickness of the tape adhesive was 54 μm . As this thickness was over half that of the pore channels, there was concern that the adhesive could block or partially block pore channels by shifting and/or swelling when wetted.

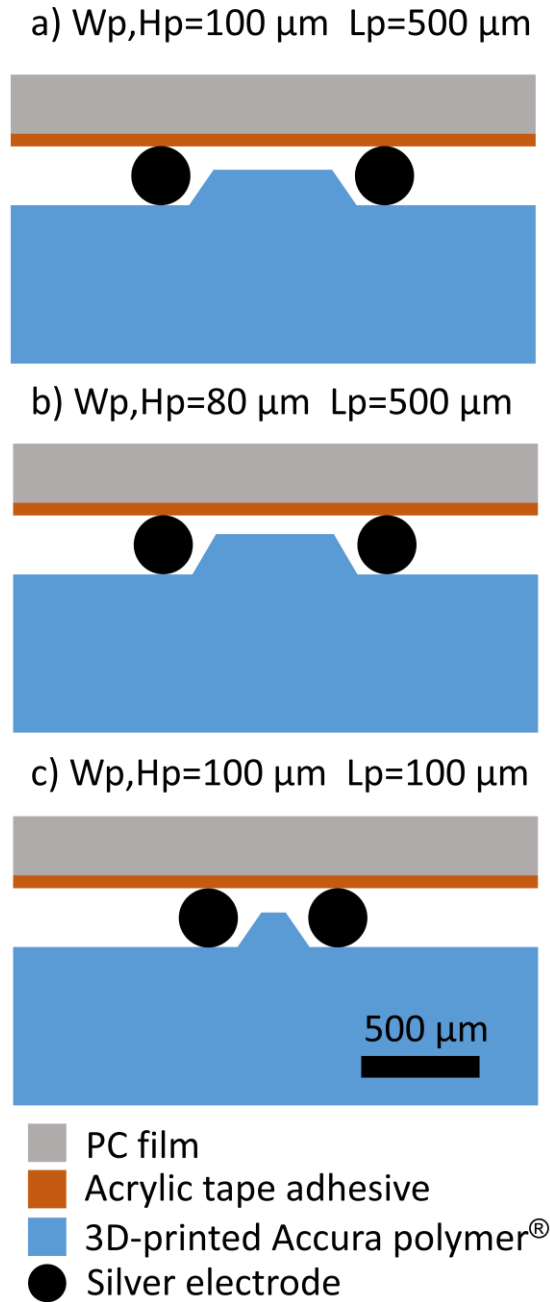


Figure 5.5 Dimensions of the three different pore channels investigated: two high aspect-ratio pore channels a) $H_p, W_p = 100 \mu\text{m}$ and $L_p = 500 \mu\text{m}$ and b) $H_p, W_p = 80 \mu\text{m}$ and $L_p = 500 \mu\text{m}$, and one lower aspect-ratio pore channel c) $H_p, W_p, L_p = 100 \mu\text{m}$.

Figure 5.6 shows photographs of pore junctions inside different printed RPS chips. Figure 5.6 a) (i)–(iii) show $H_p, W_p = 100 \mu\text{m}$, $L_p = 500 \mu\text{m}$ pore channels inside separate pore device copies, Figure 5.6 b) shows a $H_p, W_p, L_p = 100 \mu\text{m}$ pore channel, and Figure 5.6 c) shows a $H_p, W_p = 80 \mu\text{m}$, $L_p = 500 \mu\text{m}$ pore channel with electrodes embedded. The photograph in Figure 5.6 a) (i) was taken after multiple uses of the pore channel, hence the darkened channel floors and rougher channel walls.

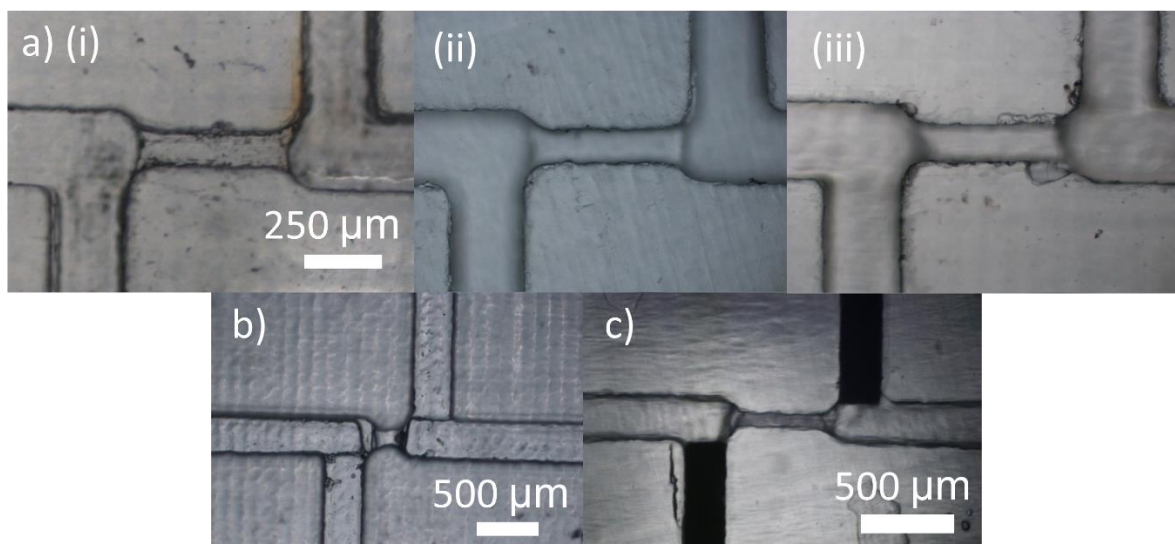


Figure 5.6 Photograph of the three pore sizes printed in Accura® 60: a) $H_p, W_p=100 \mu\text{m}$, $L_p=500 \mu\text{m}$, 3 separate device repeats (i)–(iii), b) $H_p, W_p, L_p=100 \mu\text{m}$, c) $H_p, W_p=80 \mu\text{m}$, $L_p=500 \mu\text{m}$.

5.5.3 Current-voltage response

The electrochemical response of the three different dimensions of pore channel was investigated over a range of flow rates and electrolyte concentrations. For the $H_p, W_p=100 \mu\text{m}$, $L_p=500 \mu\text{m}$ pore, the copy in Figure 5.6 a) (i) was used. Initial I-V curves taken via an eOne current amplifier (obtained from Elements) appeared to show non-linear behaviour that would indicate ICR occurring (Figures 5.7 a, 5.8, 5.9 a), although other data (Figures 5.7 b, 5.9 b) showed linear plots. This was highly unusual as ICR is usually only witnessed in pore diameters of the order of the Debye length or below (2-10 nm), and exceptions reported are still only in the $\sim 2\text{--}60 \mu\text{m}$ pore diameter range^{55–57}. In many of the recorded current-voltage curves produced currents were of large enough magnitudes (at one or both extremes) so as to saturate the electronics, witnessed in the form of flat regions at the end of the I-V curve (for example: at voltages lower than -500 mV at 30 and 50 mbar flow rates in Figure 5.7).

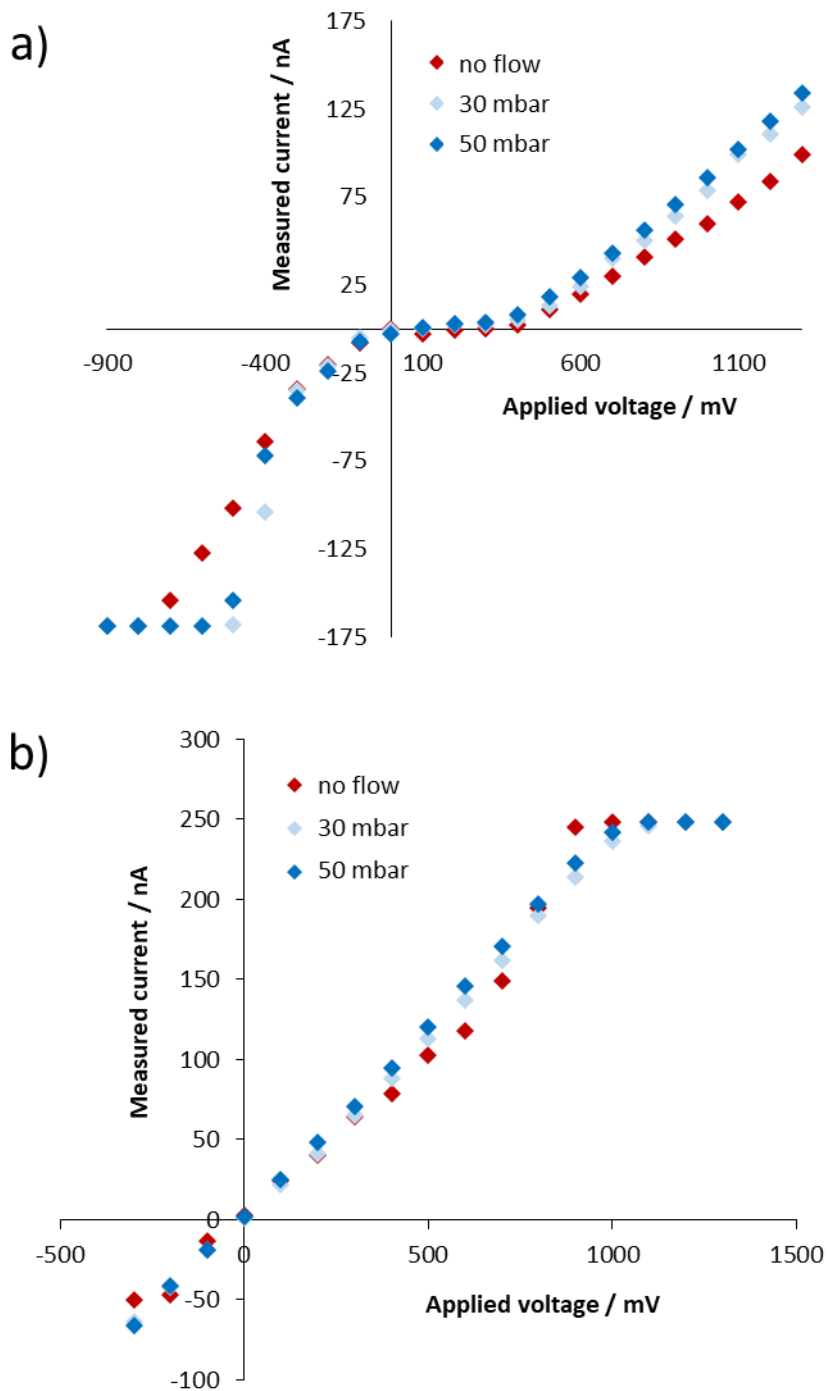


Figure 5.7 Effect of flow rate on I-V curves for pore channel $H_p, W_p=100 \mu\text{m}$, $L_p=500 \mu\text{m}$ at a) KCl (0.5 mM) and b) KCl (1.0 mM).

The effect of flow rate on the I-V curves of a $H_p, W_p=100 \mu\text{m}$, $L_p=500 \mu\text{m}$ pore was investigated at two KCl concentrations: 0.5 mM (Figure 5.7 a) and 1.0 mM (Figure 5.7 b). The former, lower electrolyte concentration gave non-linear curves at all 3 pressures, whilst the higher concentration gave linear curves for all 3. This is thought to be due to the larger concentrations of ions shielding the ionic layer

formed at the pore surface⁵². It was also noted that for KCl, 0.5 mM the gained currents are slightly lower in magnitude for 0 mbar applied pressure—this is due to the lack of pressure-driven flow to supersede the effects on flow by the pore surface ion layer⁵³. However, there was little difference between 30 and 50 mbar applied pressure data.

The effect of flow rate on the I-V curves of a short pore ($H_p, W_p, L_p=100 \mu\text{m}$) at KCl, 0.5 mM concentration were also measured and very similar results gained (Figure 5.8), with slight ICR at all pressures. Current downticks were observed at negative applied voltages, which were believed to either be due to current reading abnormalities at these high voltages, or perhaps be caused by air bubbles or debris, which would encompass a higher proportional pore volume than the larger $H_p, W_p=100 \mu\text{m}$, $L_p=500 \mu\text{m}$ pores.

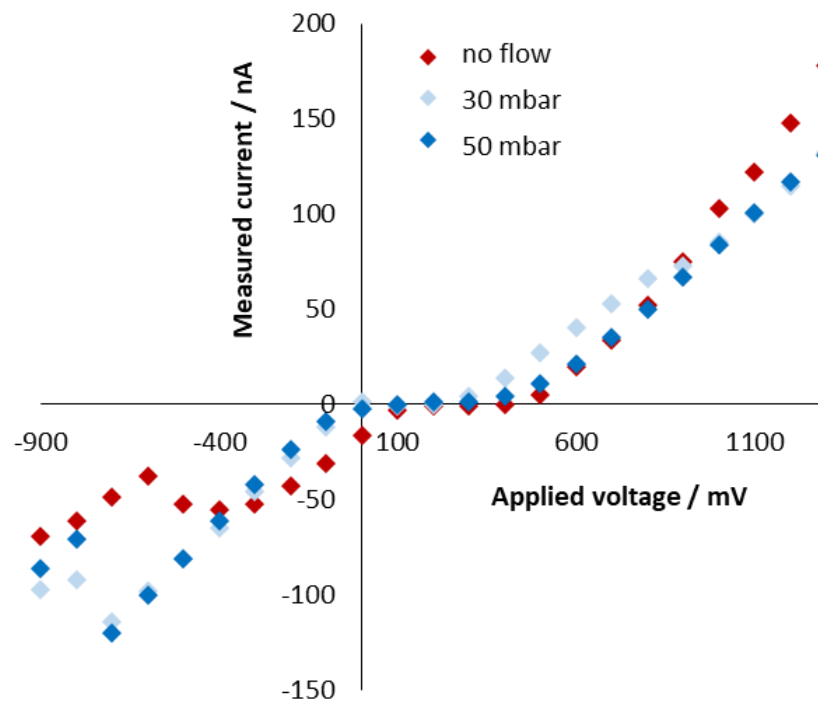


Figure 5.8 Effect of flow rate on I-V curves for pore channel $H_p, W_p, L_p=100 \mu\text{m}$ in KCl (0.5 mM)

Subsequently, we investigated the effect of electrolyte concentration in a $H_p, W_p=100 \mu\text{m}$, $L_p=500 \mu\text{m}$ pore at 50 mbar applied pressure. Two repeats were carried out: in one run, increasing the KCl concentration decreased the I-V non-linearity by the aforementioned pore surface ion layer shielding⁵² (Figure 5.9 a). However, a repeat run (Figure 5.9 b) gave only linear I-V curves for the lower concentrations. It was also noted that current amplifier saturation occurred at 2.5 mM and higher concentrations of KCl, at voltages of $\sim 200\text{--}500 \text{ mV}$.

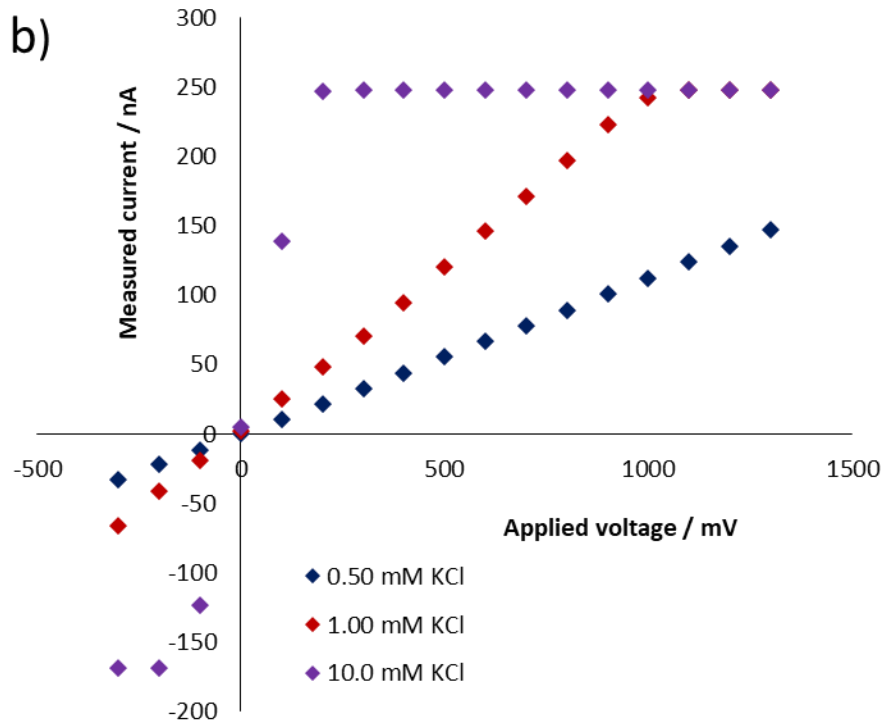
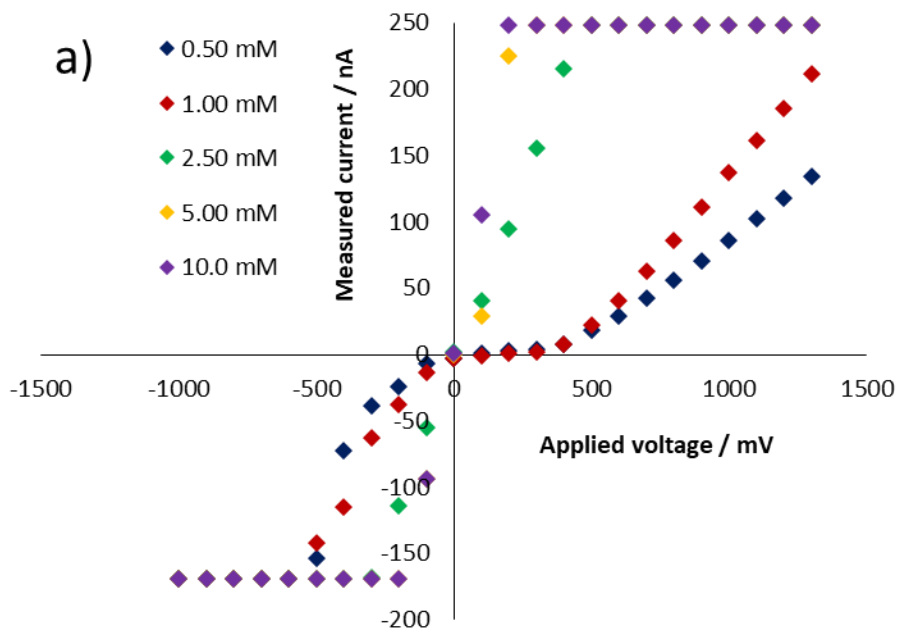


Figure 5.9 Effect of electrolyte concentration on I-V curves of $H_p, W_p=100 \mu\text{m}$, $L_p=500 \mu\text{m}$ pore at 50 mbar. a) And b) are repeat runs.

Consequently, to check the non-linearity, I-V curves were recorded using a second current amplifier (QSensing3, obtained from IzonScience), and typical linear responses (Figures 5.10–5.12) were gained. For these secondary data sets, a third, higher aspect pore (Hp,Wp=80 μm , Lp=500 μm) was also analysed. As expected for microscale pores, I-V curves gained using this current amplifier were linear, at all flow rates and KCl concentrations, with the exception of nonlinearity seen in the Hp,Wp,Lp=100 μm pore at low electrolyte concentrations and flow rates: KCl (0.25 mM), 0 mbar, Figure 5.11 a, and KCl (0.1 mM), 55 mbar, Figure 5.11 b, as well as the Hp,Wp=100 μm , Lp=500 μm pore, KCl (0.25 mM), 55mbar (Figure 5.10 a). Excluding these exceptions, there was no significant difference seen in the I-V curves with flow rate variation. Higher flow rates can be expected to produce steeper I-V curves due to higher ionic conductance through the pore⁶⁰. We believe that the flow rates used were insufficient to effect significantly higher ionic currents, as a 250 mbar applied pressure increased the current for a 165 nm diameter nanotip by only $\sim 0.03\text{--}0.05$ nA across a range of pressures⁶⁰.

The Hp,Wp=80 μm , Lp=100 μm pore had the smallest I-V curve gradients, with the Hp,Wp=100 μm , Lp=500 μm and Hp,Wp,Lp=100 μm pore having the second and most steep I-V curves, respectively. The slope of pore I-V curves alludes to the ionic conductance, which increases with pore diameter^{61,62}, and decreases with pore length (as the ion path through the pore is longer, giving higher system resistivity)^{63,64}. Thus, our findings are as expected, as the small Hp,Wp,Lp=100 μm pore should have the lowest resistance, and the Hp,Wp=80 μm , Lp=100 μm pore can be expected to have the highest due to its long length and small diameter. Pore conductance also increases with electrolyte concentration⁶⁵ (as expected as there are more ions present in flow), hence the increase in I-V curve gradient witnessed as the KCl concentration was increased.

Current amplifier saturation was not witnessed at all despite the higher voltages (-8V–7V) applied, and thus the non-reproducible ICR behaviour observed using the previous current amplifier was dismissed as being due to the detector. Figure 5.13 overlays the I-V curves for KCl (1.0 mM) in the Hp,Wp=100 μm , Lp=500 μm pore for both current amplifiers, and it can be seen that the eOne current amplifier gave far steeper I-V gradients and its current signal saturated rapidly.

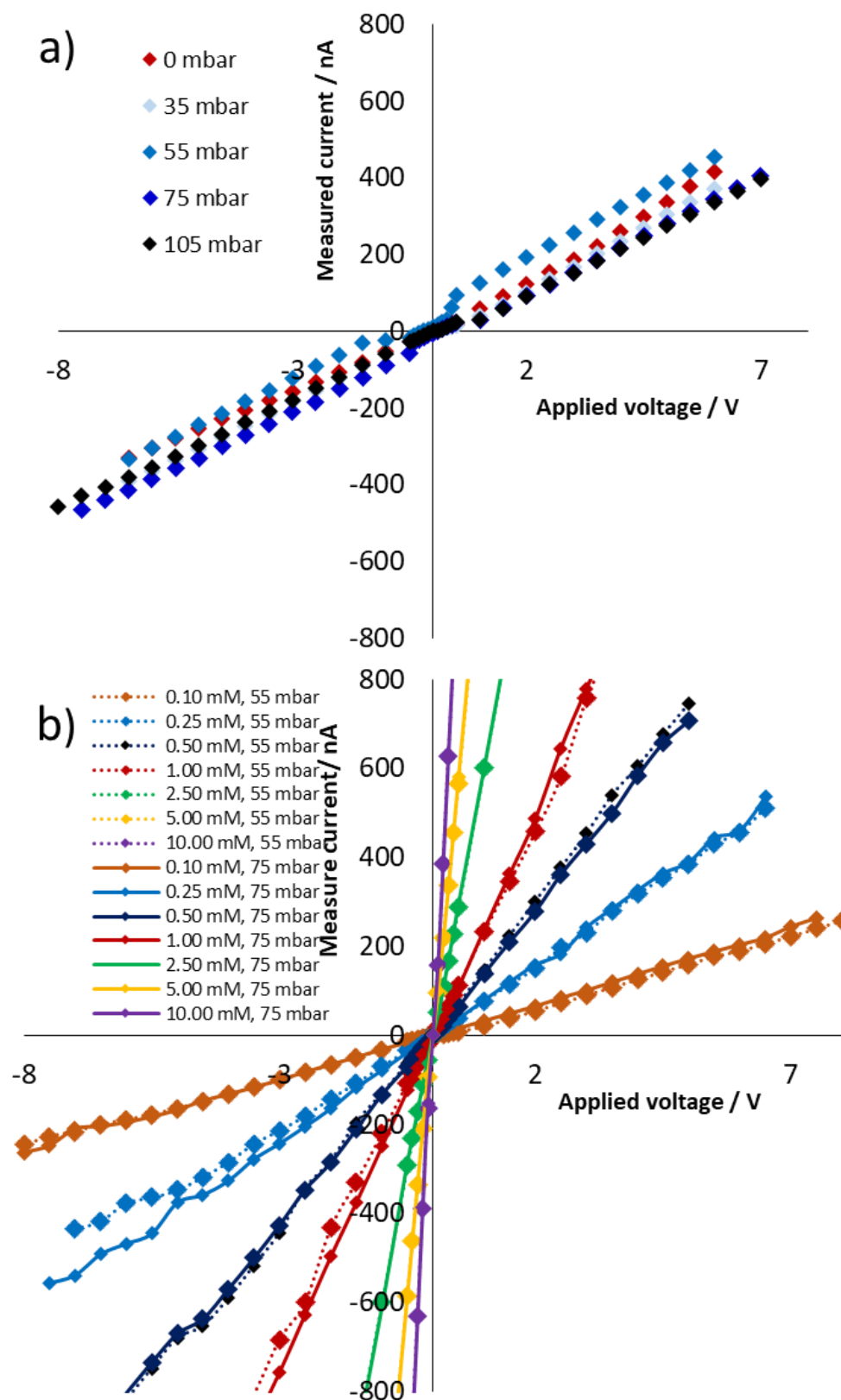


Figure 5.10 Current-voltage responses for a printed $H_p, W_p=100 \mu\text{m}, L_p=500 \mu\text{m}$ pore channel, for a) a range of flow rates and KCl (0.25 mM), and b) for a range of KCl concentrations at 2 different flow rates (55 mbar and 75 mbar).

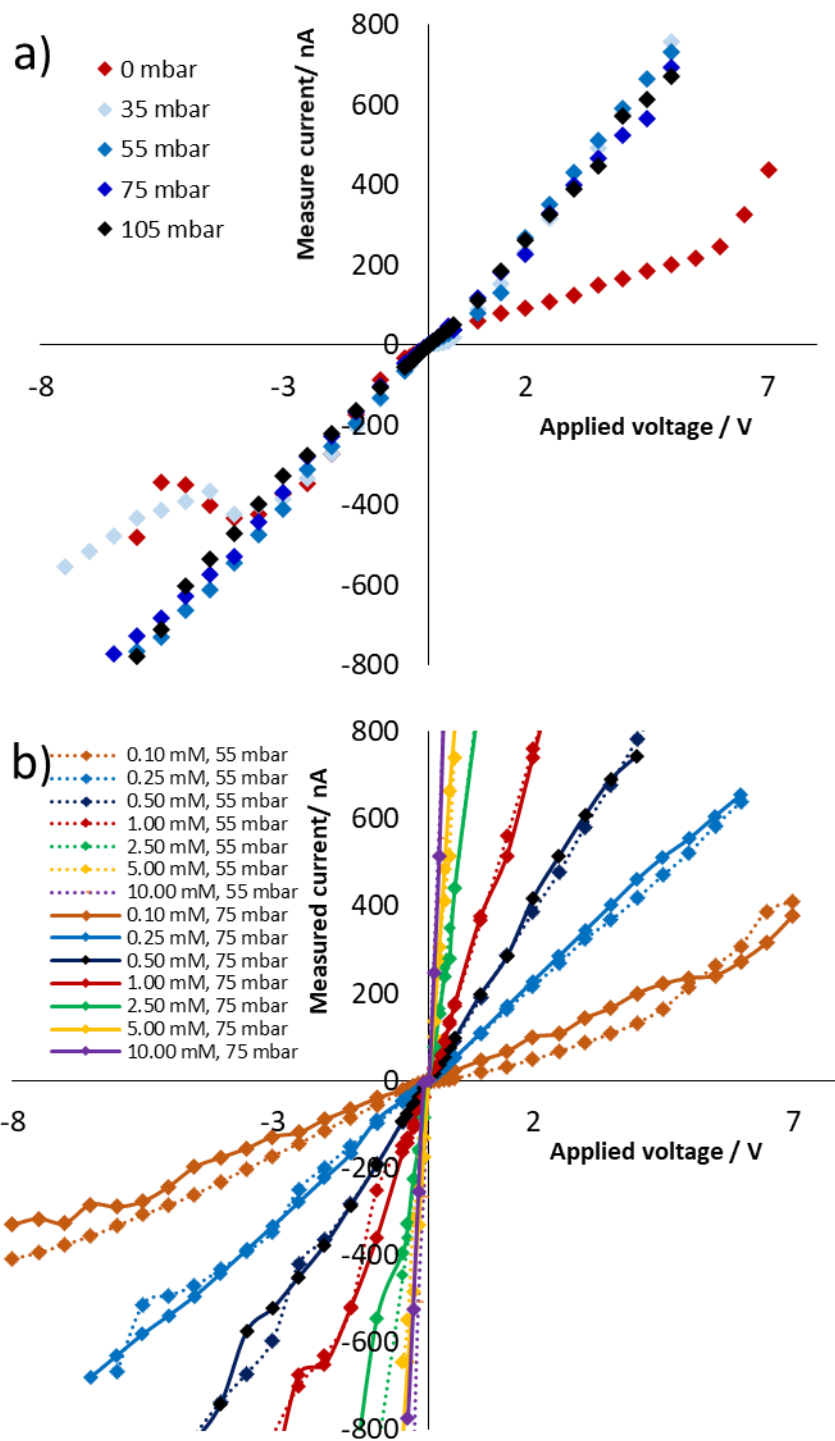


Figure 5.11 Current-voltage responses for a printed $H_p, W_p, L_p=100 \mu\text{m}$ pore channel, for a) a range of flow rates and KCl (0.25 mM), and b) for a range of KCl concentrations at 2 different flow rates (55 mbar and 75 mbar).

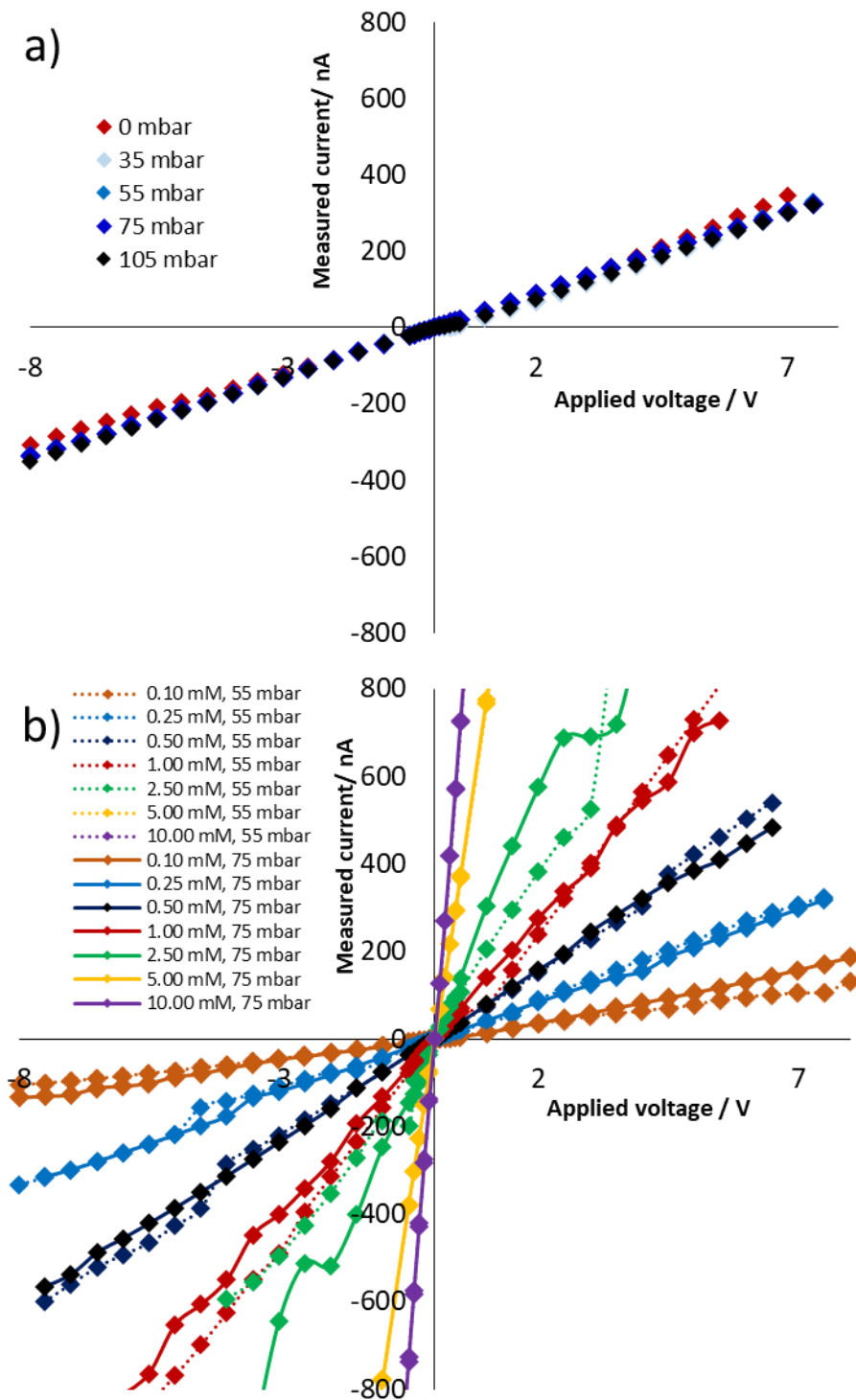


Figure 5.12 Current-voltage responses for a printed $H_p, W_p=80 \mu\text{m}$, $L_p=500 \mu\text{m}$ pore channel, for a) a range of flow rates and KCl (0.25 mM), and b) for a range of KCl concentrations at 2 different flow rates (55 mbar and 75 mbar).

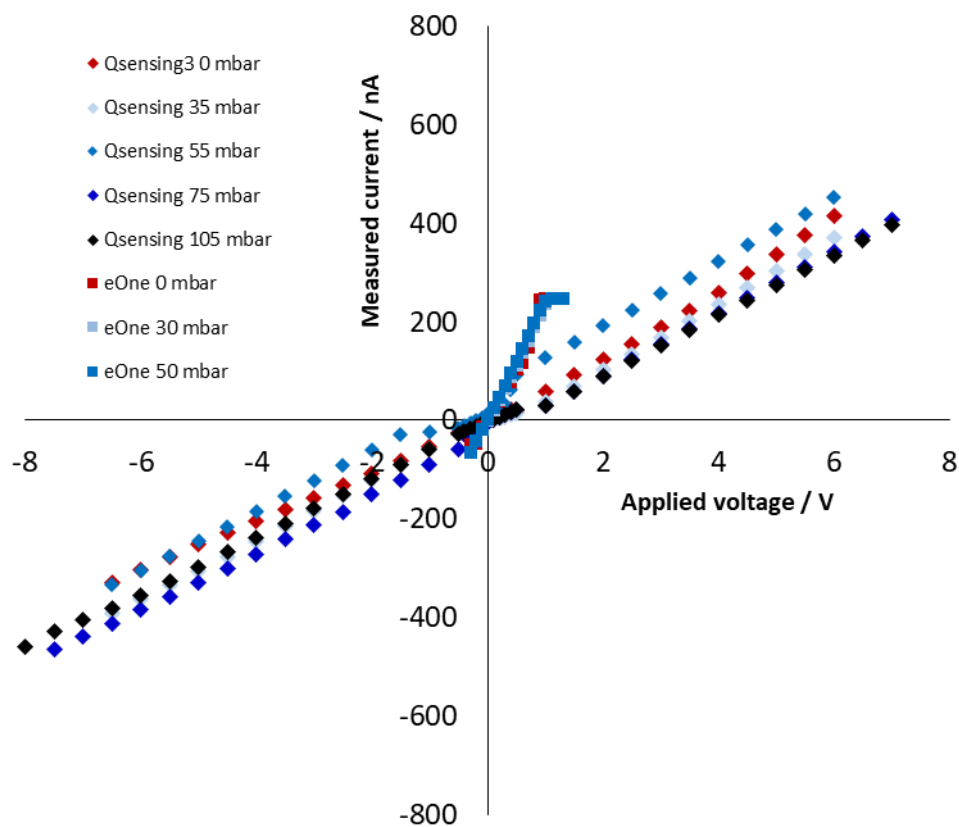


Figure 5.13 Overlaid I-V curves for KCl (1.0 mM) in the Hp, Wp=100 μm, Lp=500 μm pore for the two current amplifiers used: the eOne (Elements) and QSensing3 (Izon Science). The former saturates rapidly.

5.5.4 Predicted pulse magnitudes

In contrast to the optical detection chip covered in Chapter 4, which effectively measures the two-dimensional, circular surface area of particles, the RPS chip measures particles by their three-dimensional volume. Table 5.1 lists the percent pore volume occupied by 4 particle diameters: 30 μm, 20 μm, 10 μm and 4 μm. Whilst cross-sectional particle area increases by x^2 for an x increase in particle diameter, particle volume increases by x^3 .

Table 5.1 Percent pore volume occupation of 30 μm , 20 μm , 10 μm , 4 μm diameter particles for the three different pores used.

Pore dimensions, volume	30 μm particle diameter, 14137 μm^3	20 μm particle diameter, 4189 μm^3	10 μm particle diameter, 524 μm^3	4 μm particle diameter, 34 μm^2
	% Of pore volume occupied			
100 x 100 x 500 μm 5.00x10 ⁶ μm^3	0.283%	0.084%	0.010%	0.001%
80 x 80 x 500 μm 3.20x10 ⁶ μm^3	0.442%	0.131%	0.016%	0.001%
100 x 100 x 100 μm 1.00x10 ⁶ μm^3	1.414%	0.419%	0.052%	0.003%

5.5.5 Faraday cage shielding

In order to shield the RPS system from background electrical noise, a custom Faraday cage (Figure 5.14) was designed by the author and Nanopore Solutions, that was produced by welding of steel sheets (1 mm thick) into a box with lid, and subsequent drilling of holes for microfluidic tubing and wiring.

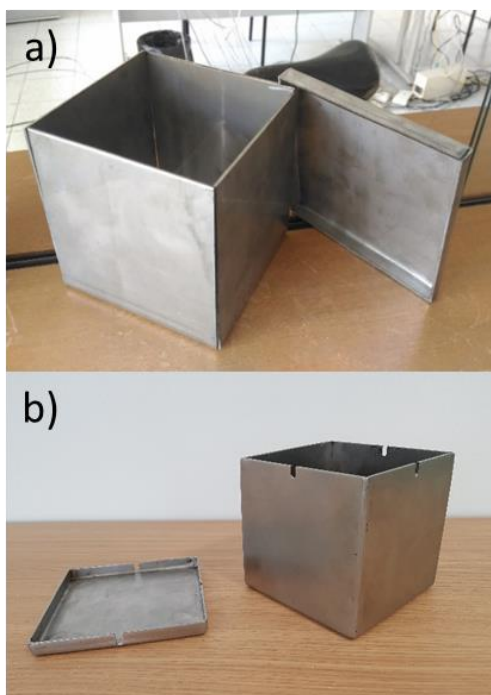


Figure 5.14 Photographs of the custom-made Faraday cage obtained by Nanopore Solutions that was used for RPS particle/cell studies. a) Shows the initial steel sheets (1 mm thickness) before welding and drilling of holes, and b) shows the finished Faraday cage (box and lid).

5.5.6 Particle quantification

The quantification ability of the printed RPS chip was tested via measurement of a series of 7 concentration standards of 30 μm beads at two different flow rates, with the recorded pulse frequencies displayed in Figure 5.15. It was noted that the highest counted throughput observed was 1380 counts min^{-1} —considerably higher than the 270 counts min^{-1} optical chip throughput.

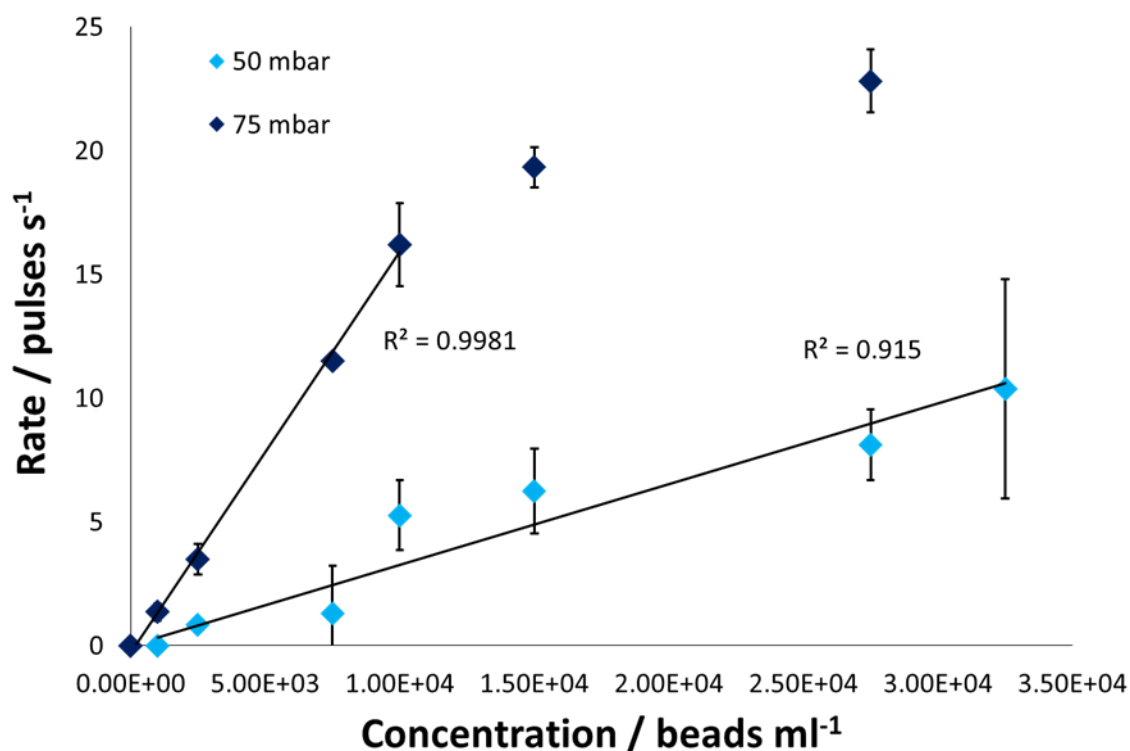


Figure 5.15 Correlation curve of pulse frequency measured by the $H_p, W_p=100 \mu\text{m}, L_p=500 \mu\text{m}$ printed RPS pore channel with increasing particle concentration for particle diameter=30 μm , 50 mbar and 75 mbar applied pressure. Points represent means of 3 repeat runs. Trendlines were forced through the origin (0,0). Error denote standard deviation of triplicate runs.

Linearity at 75 mbar was on par with the optical chip, with $R^2=0.9981$ versus 0.9983 for the previous chip, and was superior to that of 1–2 μm bacteria quantification by a PDMS chip developed by Song, et al²⁵., who also used averages of 3 repeats. To the knowledge of the author this is the only other paper reporting an R^2 value for a concentration calibration curve in an RPS microfluidic chip. However, linear dynamic range was narrower at 75 mbar, with a concentration range of 0– 1.25×10^4 beads m^{-1} , versus a range of 0 to 3.25×10^4 beads m^{-1} at 50 mbar. The plateauing of measured rate at

concentrations beyond 1.25×10^4 beads m^{-1} at 75 mbar is due to increasing incidences of simultaneous detection of ≥ 2 beads.

5.5.7 Particle throughput

Figure 5.16 compares plots of measured particle rate against flow rate for $30 \mu m$ bead suspensions (7.5×10^3 beads mL^{-1}) in a range of pores: pores 1–3 being the separate $H_p, W_p=100 \mu m, L_p=500 \mu m$ device copies in Figure 5.6 a) (i), (ii) and (iii) respectively, and pore 4 being the $H_p, W_p, L_p=100 \mu m$ pore in Figure 5.6 b. All rate plots were linear, with similar gradients. Pore copies 2 and 3 (red and purple respectively) gave relatively similar rate values, whilst copy 1 (blue) was an outlier, giving faster rates than even the $H_p, W_p, L_p=100 \mu m$ pore.

Removal and reapplication of a fresh cover layer onto 1 of the $H_p, W_p=100 \mu m, L_p=500 \mu m$ copies ('pore 3', purple, square points) gave relatively little change in particle rates ('pore 3 repeat', purple, circular points). However, omission of the flattening step, where the tape is pressed with a rubber nib, in a subsequent cover layer reapplication onto the same pore ('pore 3, rubber nib not used', purple, cross points) almost doubled the observed particle rates. This affirmed the significance of the cover layer on the chip performance, with application reproducibility being required to ensure data repeatability. The points in the $H_p, W_p, L_p=100 \mu m$ pore rate plot in Figure 5.16 are means of 3 repeat runs at each flow rate. The points for all of the $H_p, W_p=100 \mu m, L_p=500 \mu m$ pore rate plots represent single runs, as repeats runs inside the same pore set-up were prevented by frequent pore blockages. The sole similar study known to the author is that of Song, et al., whose PDMS RPS chip recorded a rate plot with linearity of $R^2=0.997$, although an average of at least 4 points were used for each point²⁷. A plot of pulse frequency measurements was attempted in the $H_p, W_p=80 \mu m, L_p=500 \mu m$ pore but blockages occurred often, even at the lowest applied pressure of 35 mbar.

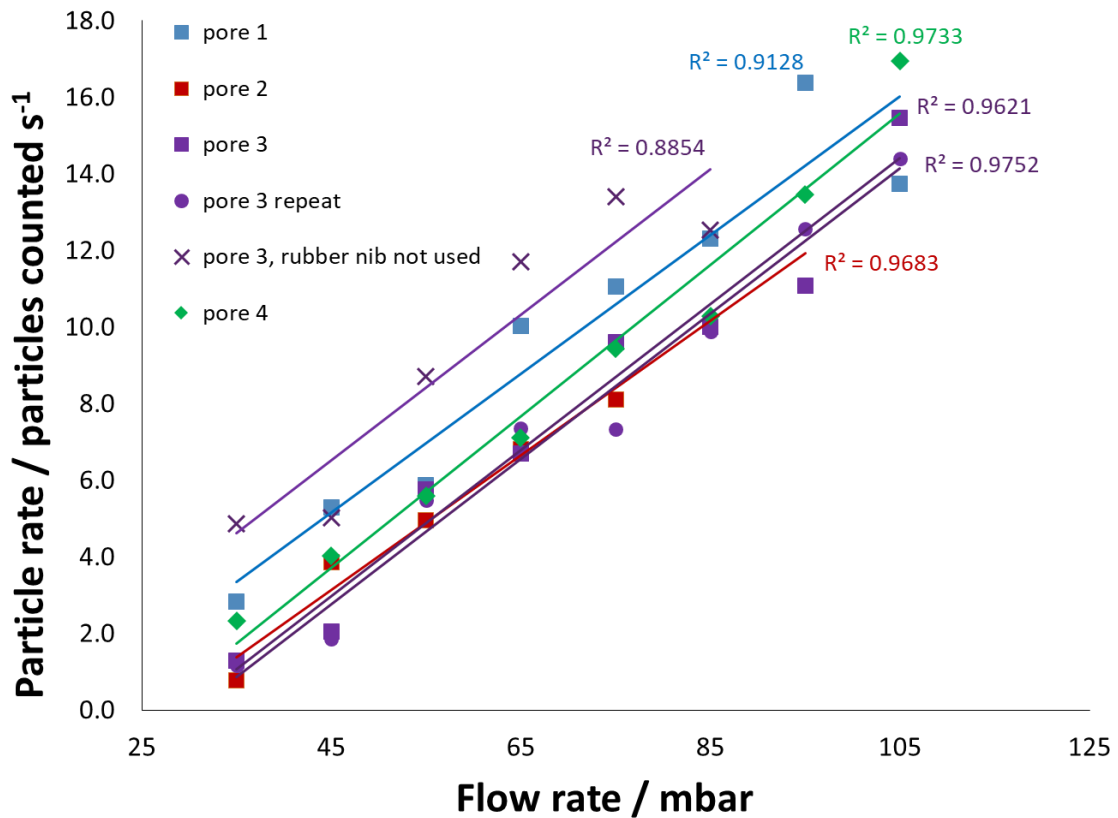


Figure 5.16 Plots of measured particle rate (pulse frequency) over a range of flow rates for 30 μm bead suspensions (7.5×10^3 beads mL^{-1}), in different printed RPS pore devices: pores 1–3=Hp,Wp=100 μm , Lp=500 μm , pore 4=Hp,Wp,Lp=100 μm . Data for pores 1–3 are from singular runs across the flow rate range. Pore 4 data is a mean of three repeat runs.

5.5.8 Particle pulse shapes

Frequency histograms of recorded pulse magnitude and duration at different flow rates of 45 mbar (blue), 65 mbar (orange), 85 mbar (grey) and 105 mbar (yellow) for the Hp,Wp=100 μm , Lp=500 μm pore, pore copy 1, are shown in Figures 5.17 a) and b), respectively. Increasing the flow rate gives a small decrease in mean pulse size, from 1.1 to 0.9 nA, and decreases pulse duration, as the particles traverse the sensing zone in less time. A scatter plot of pulse magnitude versus duration is given in Figure 5.17 c), and example pulses given in Figure 5.17 d). It was noted that the recorded pulse shapes comprised a relatively symmetrical pair of current drops: a drop in current, followed by a small increase, followed by a drop in current similar to the first.

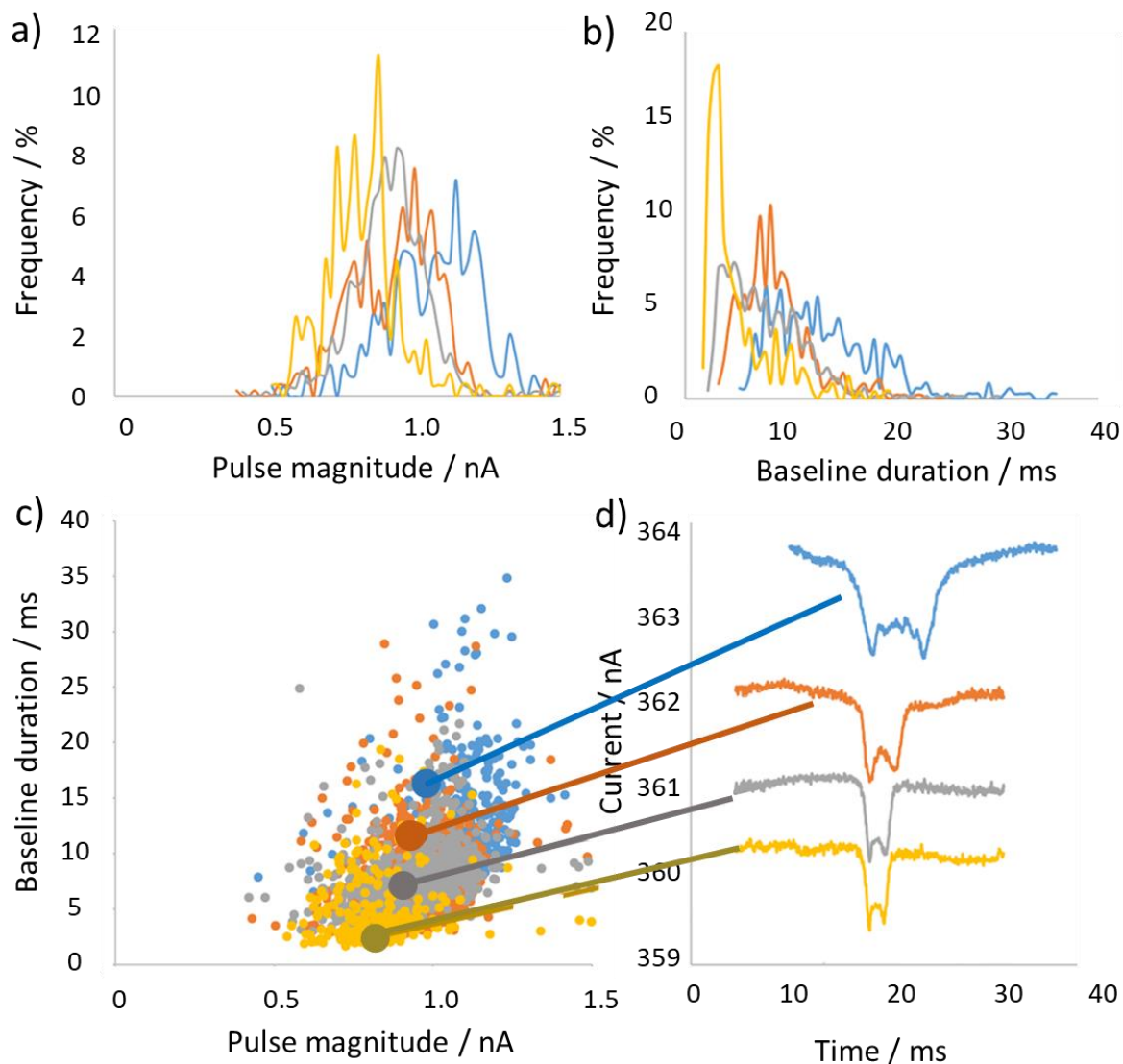


Figure 5.17 Gained pulse information from a $H_p, W_p=100 \mu\text{m}$, $L_p=500 \mu\text{m}$ pore channel RPS chip, using $30 \mu\text{m}$ beads (7.5×10^3 particles mL^{-1}), KCl (0.25 mM), +5.64 V applied voltage at applied pressures: blue=45 mbar, orange=65 mbar, grey=85 mbar, yellow=105 mbar: a) pulse magnitude distribution, b) pulse duration, c) scatter plot of pulse duration versus magnitude, and d) example pulse shapes for the different flow rates.

Corresponding data for the lower aspect $H_p, W_p, L_p=100 \mu\text{m}$ pore is shown in Figure 5.18. Pulse magnitudes have a similar spread and relationship with flow rate (decrease with an increase in flow rate, but cannot be compared directly with values from the $H_p, W_p=100 \mu\text{m}$, $L_p=500 \mu\text{m}$ pore as the baseline current was significantly different. Pulse durations were significantly shorter, which is to be expected for a shorter pore length (although not for nanoscale pores, where greater access resistance significance in low aspect ratio pores causes pulse widening⁵¹). Also, the increase in pulse magnitude and duration with increasing flow rate (Figure 5.18 c) was less obvious in the square pore than the

longer pore. The pulse shapes witnessed using this lower aspect pore channel did not feature the double spikes, consisting only of a simple, Gaussian-like profile (Figure 5.18 d). Song, et al. reported similar pulse shapes for a microfluidic pore channel with a comparable aspect ratio³⁸.

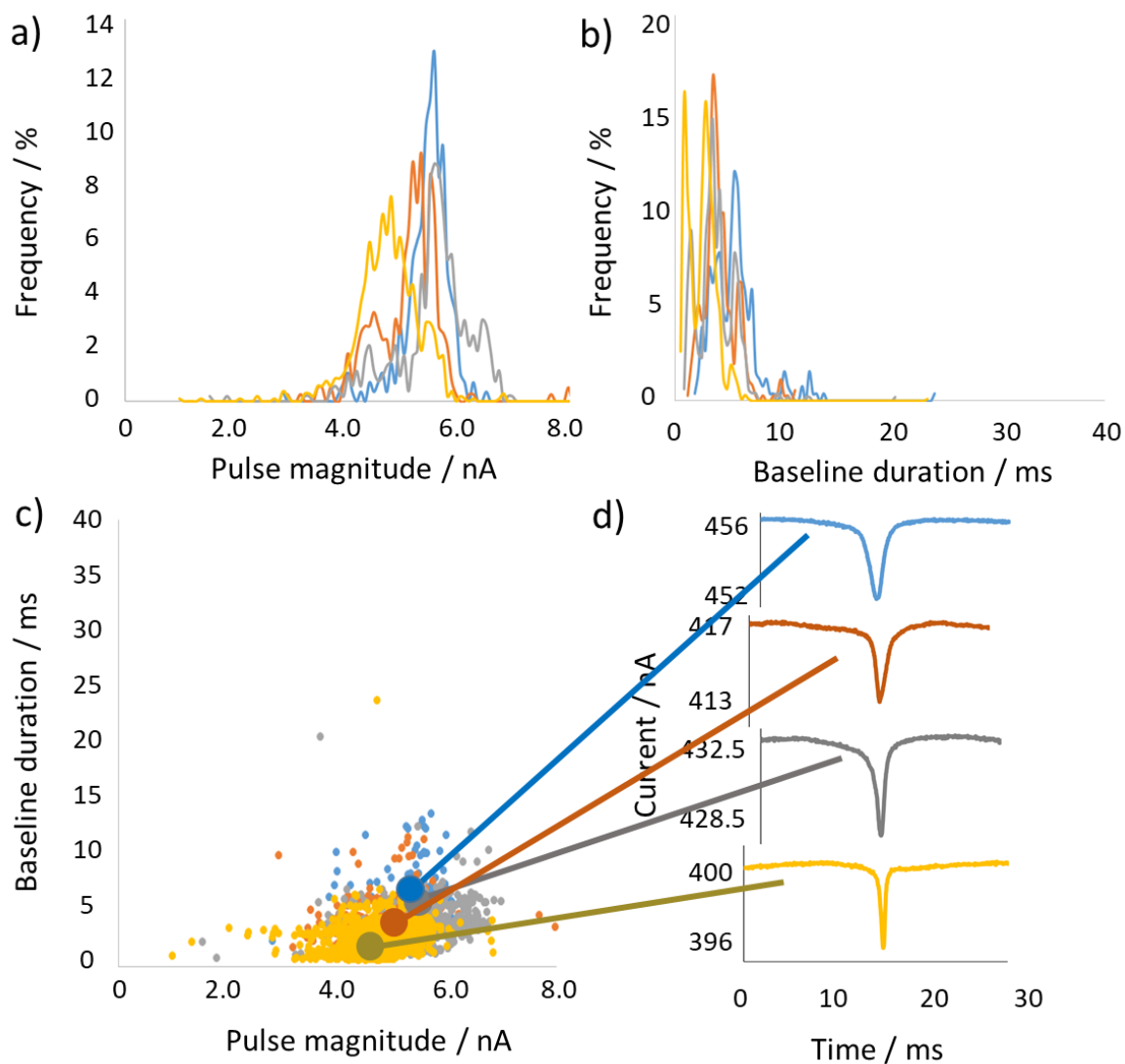


Figure 5.18 Gained pulse information from a $H_p, W_p, L_p=100 \mu\text{m}$ pore channel RPS chip, using $30 \mu\text{m}$ beads ($7.5 \times 10^3 \text{ particles mL}^{-1}$), KCl (0.25 mM), $+5.64 \text{ V}$ applied voltage at applied pressures: blue=45 mbar, orange=65 mbar, grey=85 mbar, yellow=105 mbar: a) pulse magnitude distribution, b) pulse duration, c) scatter plot of pulse duration versus magnitude, and d) example pulse shapes for the different flow rates.

As a strong tendency for pore blockages prevented flow rate runs being carried out in the $H_p, W_p=80 \mu\text{m}$, $L_p=500 \mu\text{m}$ pore, only a single 35 mbar run was collected. Example pulse shapes gained from this run are shown in Figure 5.19. These have a complex but repeating morphology, believed to

reflect the profile of the tape adhesive found in the device in the specific build used at the time. At this narrow pore cross-section, the tape adhesive profile would be greatly significant (see Figure 5.5).

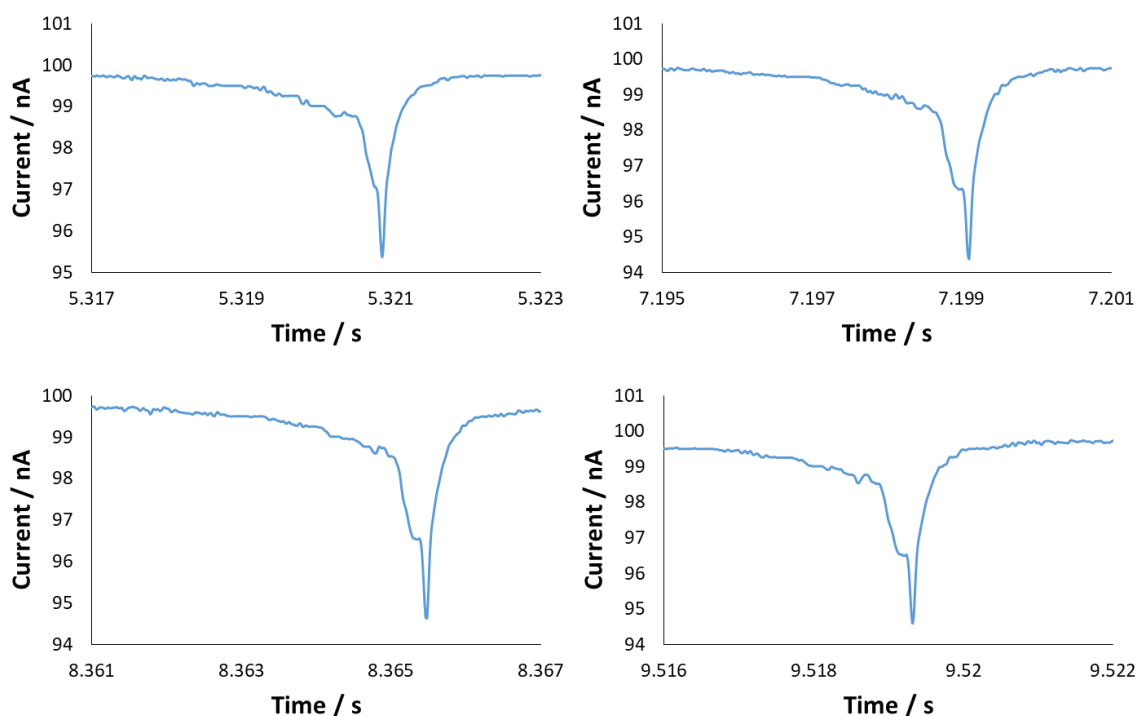


Figure 5.19 Examples of pulse shapes gained from a run of 30 μm beads (7.5×10^3 particles mL^{-1}) in a $H_p, W_p=80 \mu\text{m}$, $L_p=500 \mu\text{m}$ pore, applied pressure: 35 mbar, KCl (0.25 mM), +5.64 V applied voltage.

5.5.9 Finite element method pulse simulation

Predicted pulse shapes for the $H_p, W_p=100 \mu\text{m}$, $L_p=500 \mu\text{m}$ pore channel were calculated via FEM simulation, as pulse prediction equations for simple cylindrical pores such as those given in Chapter 2.6.1 were not applicable, due to the unusual pore geometry of the printed channel, and its perpendicular electrode configuration. FEM simulation was carried out by a collaborator (Peter Hauer, School of Chemical and Physical Sciences, Victoria, University of Wellington, Wellington 6140, New Zealand) via Comsol. Full parameters and results are detailed in Hampson, et al⁴⁹. Pulse modelling involved simulation of the electric field lines and subsequent particle disturbance. Particle and pore charges were assumed to be negligible as the pore channel dimensions were on the order of 100 μm . The accurate pore dimensions of the pore in Figure 5.6 a) (i) were used: $H_p, W_p=105 \mu\text{m}$, $L_p=545 \mu\text{m}$. Electric field simulation determined that the field lines first bend close to the electrodes due to their perpendicular orientation to the pore channel, before straightening out within the channel and

running predominantly parallel to the channel walls, with a uniform field and field potential across the channel. Following this, pulse shape simulation for 30 μm spherical beads predicted a square-shaped pulse with rounded sides (Figure 5.20), with the long, flat pulse bottom reflecting the long particle translocation time through the channel. This shape matches pulses observed in high aspect ratio microfluidic pore channels^{39,41}. The relatively long rounded pulse sections in our simulation relative to these pulses are thought to be due to the ramp structures at the pore mouths.

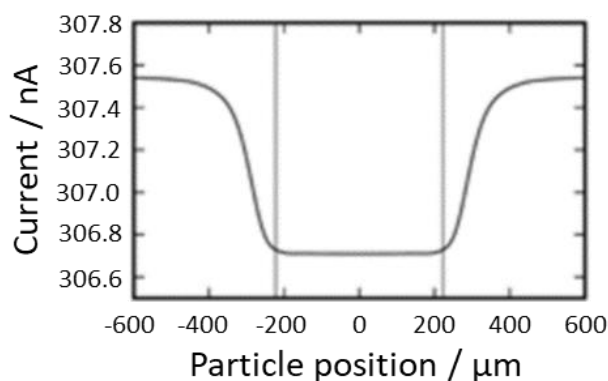


Figure 5.20 Predicted pulse shape generated by FEM by Peter Hauer, University of Wellington, School of Chemical and Physical Sciences, for a $H_p, W_p=105 \mu\text{m}$, $L_p=545 \mu\text{m}$ pore channel, particle diameter=30 μm , voltage=+5.64 V, $\sigma=3.675 \text{ mS/m}$ (KCl, 0.5 mM). The vertical lines indicate the beginning of the ramp structures.

However, observed pulses in the $H_p, W_p=100 \mu\text{m}$, $L_p=500 \mu\text{m}$ pore channels featured central, upward spikes of current. Papers describing microfluidic RPS pore channels either overlook reporting on pulse shape^{27,30-32}, or have pulses featuring non-symmetrical spikes but omit scrutinisation^{28,36}. Pulse profiles can be affected by electric field non-uniformity^{51,66}, off-axial particle translocations^{39,51,67}, particle charge or double-layer effects⁶⁸, or channel dimension irregularities⁶⁸. Electric field non-uniformity was ruled out as the cause of the current spikes as electric field simulation had determined a uniform field and potential across the pore channel. Particle or pore charge effects were ruled out as insignificant due to the microscale channel and particle dimensions, as substantiated by the collected ICR data. Thus, it was first hypothesised that the observed pulse shape was likely a result of the pore channel shape, with the upward spike in current being indicative of channel widening³⁹.

5.5.10 Pore channel scanning electron microscopy imaging

Pore channel shape was investigated via SEM. SEM imaging of the $H_p, W_p=100\ \mu\text{m}$, $L_p=500\ \mu\text{m}$ pore channel, copy 1, (Figure 5.21 a–d) indicated straight channel walls and generally smooth floor and wall surfaces within the pore channel (roughness in the form of scratches in the pore channel and on the ramps were due to previous incidents of manual cleaning of the device with a wire), and no widening of channel width/depth. Thus, we concluded that the pore channel widening may be occurring due to the PC cover layer—the tape adhesive may be collecting at the pore mouths. SEM imaging of tape adhesive from cover layers removed following particle runs was attempted but the adhesive settled to being flat before images could be taken.

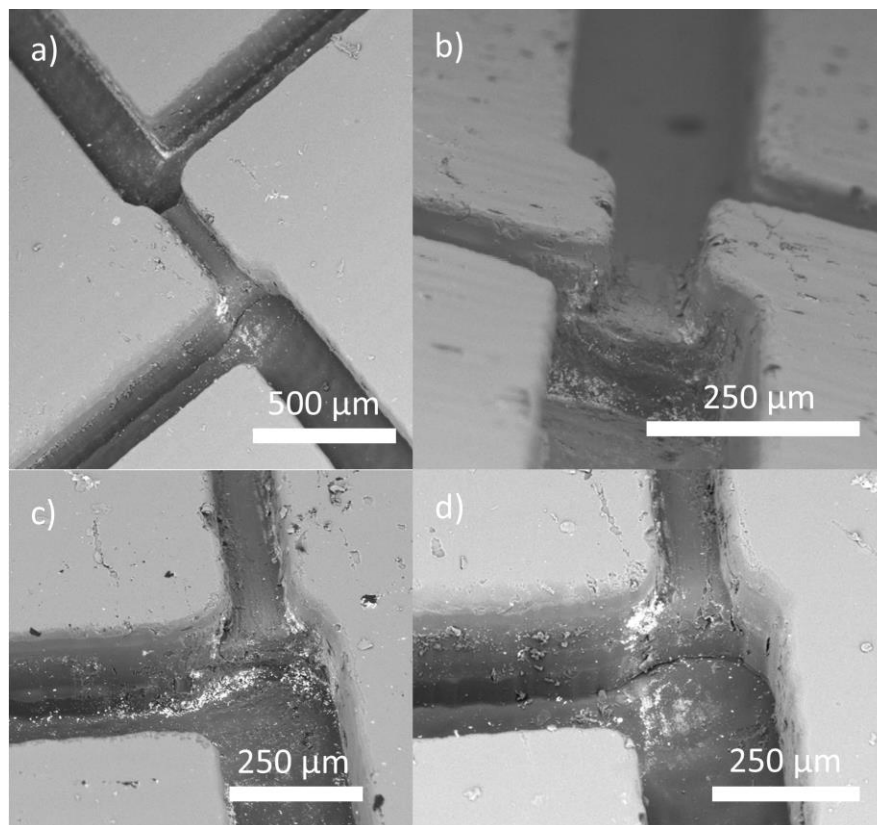


Figure 5.21 SEM images taken of ‘pore copy 1’, a $H_p, W_p=100\ \mu\text{m}$, $L_p=500\ \mu\text{m}$ pore (accurate dimensions: $H_p, W_p=105\ \mu\text{m}$, $L_p=545\ \mu\text{m}$). a) Pore channel profile, b) view looking down pore channel, c) view of one of the ramps, d) view of other ramp.

5.5.11 20 and 30 μm bead mixture analysis

Mixtures containing 20 μm and 30 μm beads were analysed in the $H_p, W_p=80\ \mu\text{m}$, $L_p=100\ \mu\text{m}$ pore, to ascertain the ability of the RPS chip to resolve them. Measured data is shown in Figure 5.22. Three

different electrolyte solutions were used: KCl, 0.25 mM (Figure 5.22 a), KCl, 0.50 mM (Figure 5.22 b) and PBS, 5.00 mM (Figure 5.22 c). PBS was investigated as it allows cells to be analysed with reduced lysis. The chip was able to clearly resolve the two bead sizes in the two KCl concentrations, but not the PBS buffer, where the 20 μm beads were not detected. Increasing the electrolyte concentration increases the pulse magnitude, but the ratio of pulse magnitude to the baseline current should remain the same; the baseline current will be higher with higher electrolyte concentrations due to a higher number of ions flowing per volume of solution, but the ratio of particle volume to the pore volume remains constant.

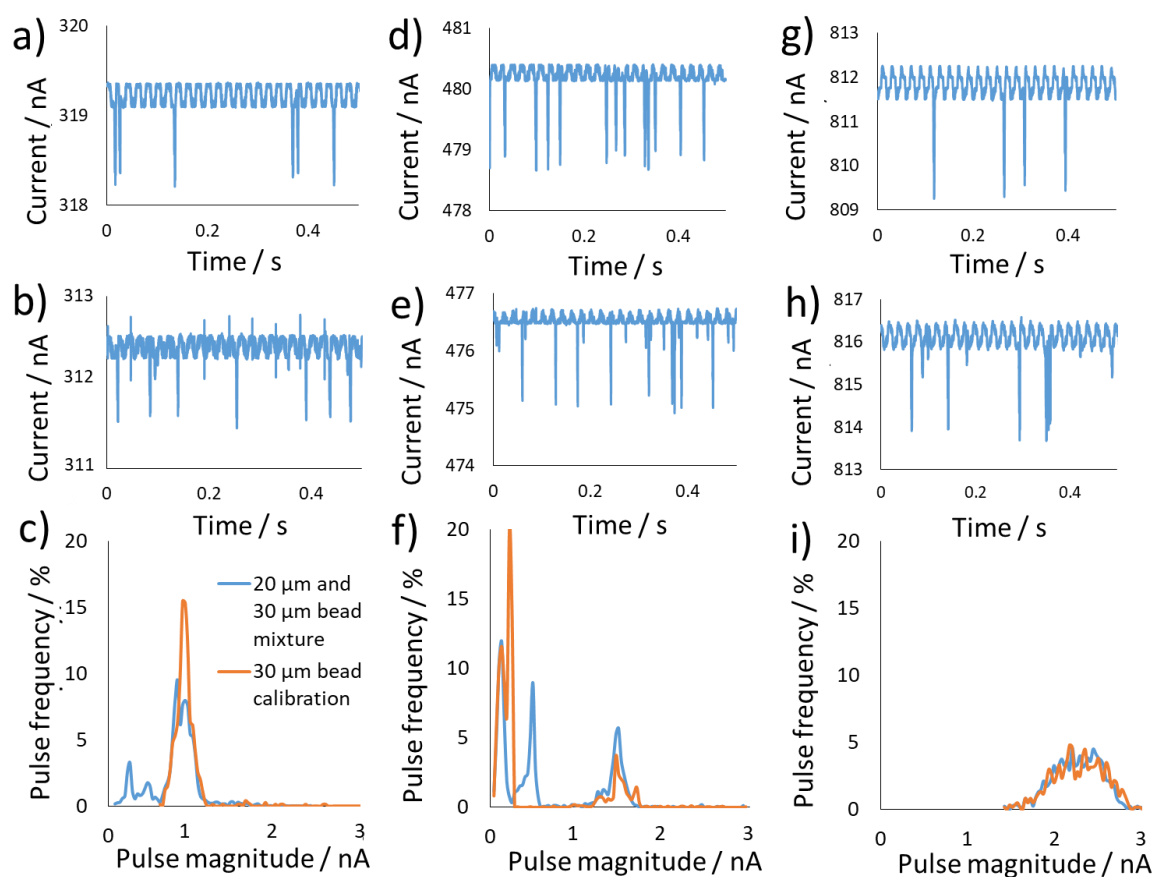


Figure 5.22 Results of analysis of 20 μm and 30 μm bead mixtures by a printed $H_p, W_p=80 \mu\text{m}$, $L_p=100 \mu\text{m}$ RPS chip in KCl (0.25 mM), +4.5 V, 100 mbar (a–c), KCl (0.5 mM), +3.58 V, 100 mbar (d–f), PBS (5.0 mM), +1.30 V, 100 mbar (g–i). a), d) and g) Show obtained pulse spectra for 20 μm and 30 μm bead mixtures (5.0×10^3 particles mL^{-1}). c) d) and (i) Show corresponding pulse magnitude frequency histograms.

A broader pulse size distribution was gained in PBS electrolyte. This may be due to aggregation of particles being enhanced by the high ionic strength, but such an effect usually takes place at the nm

scale, where the effect on the ion clouds surrounding the particles are significant⁶⁹. Also, the 20 μm beads were undetected in PBS—the pulses were below the minimum blockade height threshold for a pulse to be registered as being due to a particle (0.05 nA) by the software used.

Noise in the form of sharp conductive and resistive pulses were seen in KCl, 0.25 mM electrolyte (Figure 5.22 a). Also, a large number of low magnitude pulses were recorded in the KCl, 0.5 mM electrolyte. It is believed that these pulses are due to debris, and that their pulse magnitudes were sufficient to be detected by the software.

5.5.12 Analysis of 10 μm beads

Attempts to detect 10 μm beads in the three pore channel dimensions were unsuccessful due to the insufficient signal-to-noise ratio against background electrical noise. Attempts in $H_p, W_p=60 \mu\text{m}$, $L_p=500 \mu\text{m}$ and $H_p, W_p=70 \mu\text{m}$, $L_p=500 \mu\text{m}$ pore channel devices were also unsuccessful due to channel blockages by the cover layer tape adhesive. However, during one run in a $H_p, W_p=80 \mu\text{m}$, $L_p=500 \mu\text{m}$ pore channel, the sensing zone was effectively narrowed to $\sim 35 \mu\text{m}$ diameter by the tape adhesive (Figure 5.23 a) and pulses were recorded (Figure 5.23 b) with magnitudes centering around 0.8 nA (Figure 5.23 c). Figure 5.23 d shows examples of recorded pulses. Pulse shapes varied more than those of the 30 μm particle runs, although a number had a large shoulder on the right-hand side, possibly reflecting the pocket unfilled by tape adhesive on the right-hand side of the pore channel. This data reflects that analysis of particles $<20 \mu\text{m}$ is possible by these printed devices, but is made difficult to reproduce due to high risk of blockages at channel dimensions $<80 \mu\text{m}$.

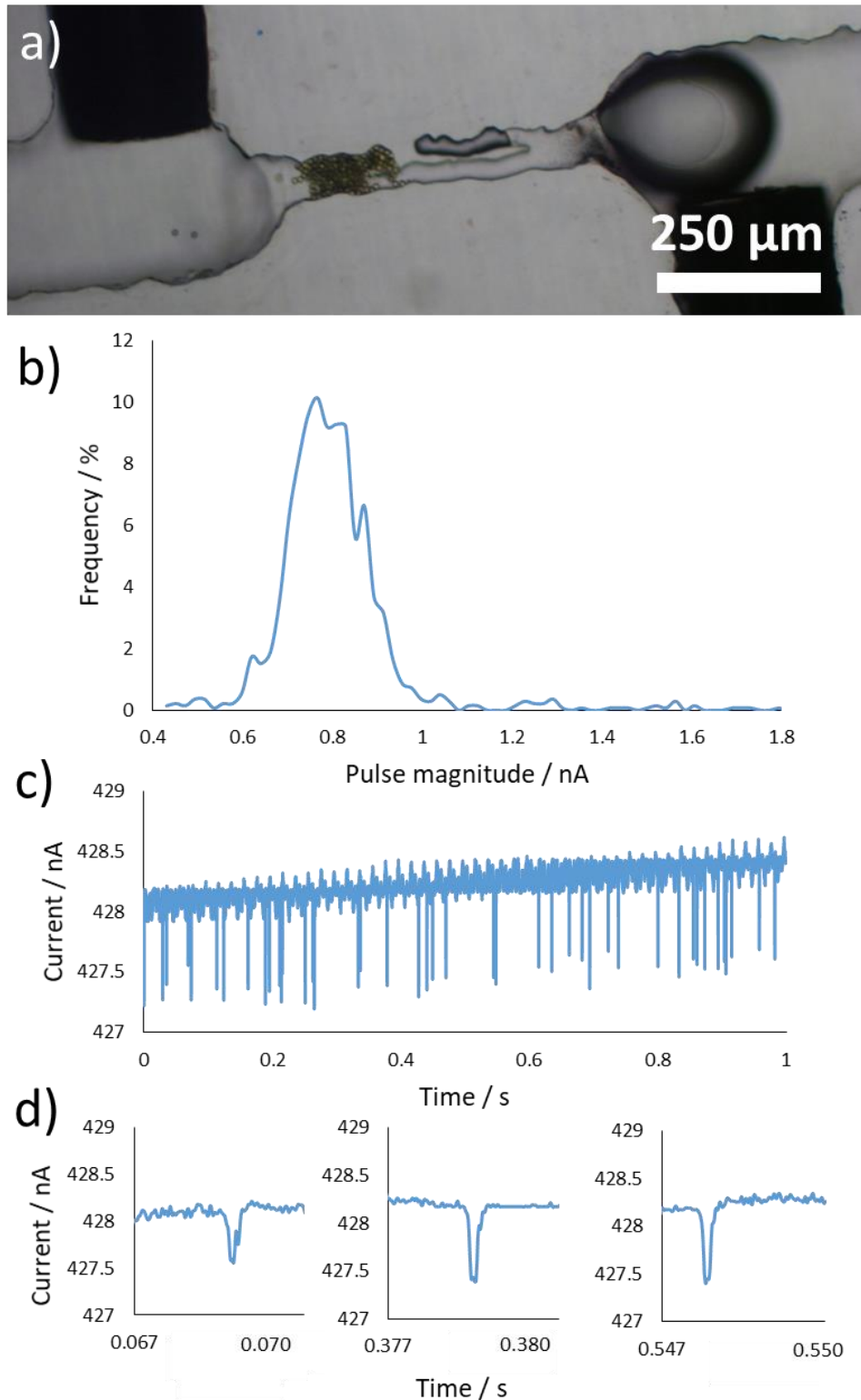


Figure 5.23 Analysis of 10 μm beads via $H_p, W_p=80 \mu\text{m}, L_p=500 \mu\text{m}$ pore channel, 300 mbar applied pressure, 3.0×10^4 beads mL^{-1} in PBS (5 mM), +4.24V applied voltage: a) Photograph of pore channel after run ended due to bead blockage, showing that channel was effectively blocked off by tape to be ~35 μm diameter. b) Frequency plot of measured pulse magnitudes centred around mean of 0.8 nA. c) Section of recorded pulse spectrum. d) Examples of recorded pulses.

5.5.13 Analysis of skeletal muscle cells

Finally, Figure 5.24 shows size data recorded by the Hp,Wp=100 μm , Lp=500 μm RPS device in Figure 5.6 a (i) for a population of human skeletal muscle cells in KCl (0.25 mM) electrolyte. Three repeat measurements were carried out (denoted by 'cells 1', 'cells 2' and 'cells 3': red, pink and beige, respectively) of separate suspensions produced by dilutions from the same stock sample. A suspension of 30 μm beads, also in KCl (0.25 mM), was ran through the device under the same conditions for calibration purposes (blue): the cells were sized using this run via Izon Control Suite software and found to range approximately 16–40 μm in size. This matches well with human skeletal muscle cells typically ranging between 10–50 μm in diameter⁷⁰. Despite the polydisperse nature of the cell samples, the individual repeats showed good overlap, with the exception of a small number of larger cells (45–55 μm) in the third sample. These may also possibly be aggregates of approximately 25 μm cells.

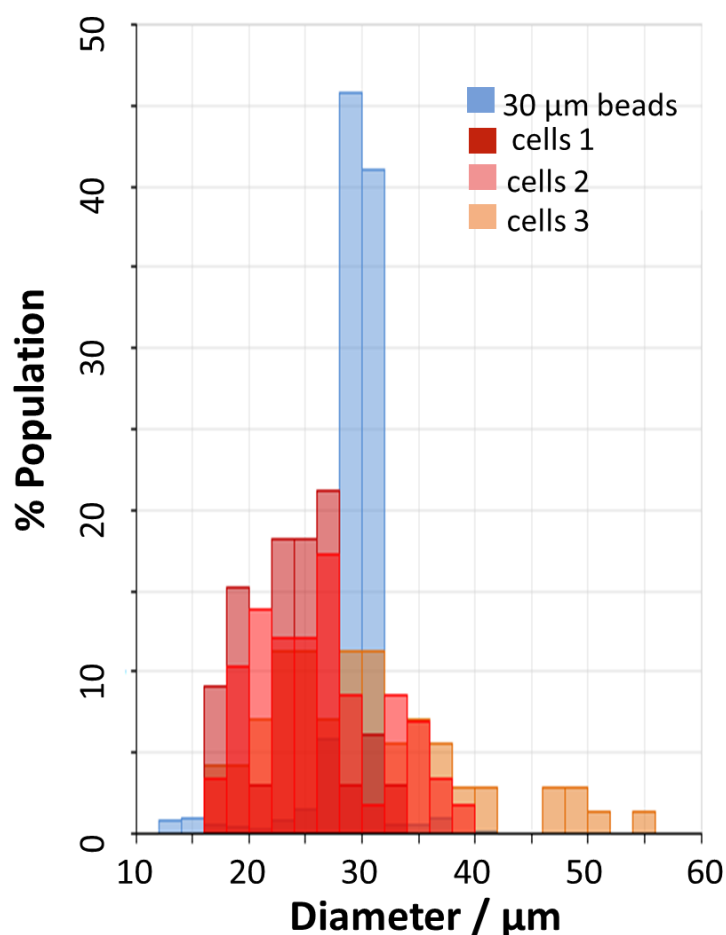


Figure 5.24 Gained size data measured by the printed RPS chip of a population of skeletal muscle cells (5×10^3 cells mL^{-1} , 75 mbar, KCl, 0.25 mM). Repeat runs are denoted as 'cells 1', 'cells 2' and 'cells 3'. Blue histogram denotes 30 μm calibration bead run (5×10^3 bead m^{-1} , 75 mbar, KCl, 0.25 mM).

Repeat measurements in PBS buffer were also carried out to hopefully prevent cell lysis, but the higher noise levels obscured pulses.

5.5 Conclusions:

A microfluidic LOC chip featuring embedded electrodes for particle/cell RPS sensing was fabricated by SLA. Like the optical chip covered in Chapter 4, single-particle analysis is carried out via pulses, which allow label-free counting and elucidate particle/cell information. The RPS chip sizes particles by measuring volume as opposed to cross-sectional surface area, by monitoring of ion displacement. Fabrication time was also 5 hours, but the chip was lower cost than the optical chip, being ~£6.50 and £8.50 for the two different device configurations, due to the more compact designs of the devices.

Linear I-V curves were gained for three different pore dimensions at a range of flow rates and electrolyte concentrations, the exception being in the $H_p, W_p, L_p = 100 \mu\text{m}$ pore at very low KCl concentrations and flow rates. Furthermore, it was found that the $H_p, W_p, L_p = 100 \mu\text{m}$ and $H_p, W_p = 100 \mu\text{m}, L_p = 500 \mu\text{m}$ pores had similar particle throughput, with the cover layer application being more significant. However, the $H_p, W_p = 80 \mu\text{m}, L_p = 500 \mu\text{m}$ pore had a large tendency for blocking and could only be used at low flow rates. The $H_p, W_p = 100 \mu\text{m}, L_p = 500 \mu\text{m}$ pore produced symmetrical double-humped pulses, which were deduced by FEM simulation and SEM imaging to likely be due to the tape adhesive settling at the pore mouths, as opposed to the pore channel morphology.

Particle quantification across a range of particles concentrations up to 3.5×10^4 particles mL^{-1} was carried out at two flow rates (55 and 75 mbar applied pressures), with the linear dynamic range being lower for the higher flow rate due to earlier saturation. Linearity was on par with the optical chip ($R^2 = 0.9983$ versus 0.9981 , respectively), but counting throughput was significantly superior ($\sim 1380 \text{ min}^{-1}$ versus $\sim 270 \text{ min}^{-1}$, respectively) due to faster data acquisition and higher sample volume throughput, making this chip more effective at analysing relatively low sample concentrations. Additionally, resolving power was better, with the RPS chip able to more clearly differentiate between 20 and 30 μm beads in a mixture, and characterise a population of skeletal muscle cells. This was due to the better signal reproducibility of RPS in comparison with light obscuration⁴⁷, a large part of which involves the faster data acquisition, which allows recording of full pulses for each particle, in contrast to the large number of partial pulses recorded by the optical chip in Chapter 4. However, a key challenge associated with the RPS device was a susceptibility to electrical noise, requiring use to be carried out within a Faraday cage, and limiting sensitivity. This decreases device portability and hinders

device implementation to POC/in-field applications, and prevented the detection of 10 μm beads unless under certain cover layer conditions, respectively. Additionally, due to the restrictive pore channels, the RPS chips were highly susceptible to blockages, limiting the use of narrow (≤ 80 μm dimensions) pores.

5.6 References

- 1 J. Maxwell and J. Thompson, *A Treatise on Electricity and Magnetism*, Clarendon, Oxford, 3rd edn., 1904.
- 2 W.H. Coulter, Means for counting particles suspended in a fluid, United States, Patent number: 2656508A, 27/08/1953.
- 3 E. L. C. J. Blundell, M. J. Healey, E. Holton, M. Sivakumaran, S. Manstana and M. Platt, *Anal. Bioanal. Chem.*, 2016, 408, 5757–5768.
- 4 E. L. C. J. Blundell, R. Vogel and M. Platt, *Langmuir*, 2016, **32**, 1082–1090.
- 5 Y. Wang, D. Wang and M. V Mirkin, *Proc. R. Soc. A*, 2017, **473**, 1–19.
- 6 J. B. Heng, A. Aksimentiev, C. Ho, P. Marks, Y. V Grinkova, S. Sligar, K. Schulten and G. Timp, *Biophys. J.*, 2006, **90**, 1098–1106.
- 7 G. S. Roberts, D. Kozak, W. Anderson, M. F. Broom, R. Vogel and M. Trau, *Small*, 2010, **6**, 2653–2658.
- 8 T. Ito, L. Sun, R. R. Henriquez and R. M. Crooks, *Acc. Chem. Res.*, 2004, **37**, 937–945.
- 9 Z. Gu, Y. Zhang, B. Luan and R. Zhou, *Soft Matter*, 2016, **12**, 817–882.
- 10 J. Feng, K. Liu, R. D. Bulushev, S. Khlybov, D. Dumcenco, A. Kis and A. Radenovic, *Nat. Nanotechnol.*, 2015, **10**, 1070–1076.
- 11 Y. Feng, Y. Zhang, C. Ying, D. Wang and C. Du, *Genom. Proteom. Bioinf.*, 2015, **13**, 4–16.
- 12 C. Durrieu, F. Lagarde and N. Jaffrezie-Renault, in *Nanomaterials: A Danger or a Promise? A Chemical and Biological Perspective*, eds. R. Brayner, F. Fievet and T. Coradin, Springer-Verlag, London, 2013, p. 169.
- 13 W.-J. Lan, D. A. Holden, B. Zhang and H. S. White, *Anal. Chem.*, 2011, **83**, 3840–3847.
- 14 T. Ito, L. Sun and R. M. Crooks, *Anal. Chem.*, 2003, **75**, 2399–2406.
- 15 R. W. DeBlois, C. P. Bean and R. K. A. Wesley, *J. Colloid Interface Sci.*, 1977, **61**, 323–335.
- 16 N. Arjmandi, W. Van Roy, L. Lagae and G. Borghs, *Anal. Chem.*, 2012, **84**, 8490–8496.
- 17 Z. Tang, D. Zhang, W. Cui, H. Zhang, W. Pang and X. Duan, *Nanomater. Nanotechnol.*, 2016, **6**, 1–12.
- 18 B. Schiedt, L. Auvray, L. Bacri, G. Oukhaled, A. Madouri, E. Bourhis, G. Patriarche, J. Pelta, R.

- Jede and J. Gierak, *Microelectron. Eng.*, 2010, **87**, 1300–1303.
- 19 M. D. Fischbein and M. Drndić, *Appl. Phys. Lett.*, 2008, **93**, 1–11.
- 20 C.-L. Lee, K. Tsujino, Y. Kanda, S. Ikeda and M. Matsumura, *J. Mater. Chem.*, 2008, **18**, 1015–1020.
- 21 R. Vogel, G. Willmott, D. Kozak, S. G. Roberts, W. Anderson, L. Groenewegen, B. Glossop, A. Barnett, A. Turner and M. Trau, *Anal. Chem.*, 2011, **83**, 3499–3506.
- 22 E. L. C. J. Blundell, L. J. Mayne, M. Lickorish, S. D. R. Christie and M. Platt, *Faraday Discuss.*, 2016, **193**, 487–505.
- 23 E. L. C. J. Blundell, L. J. Mayne, E. R. Billinge and M. Platt, *Anal. Methods*, 2015, **7**, 7055–7066.
- 24 E. R. Billinge and M. Platt, *Y. Biosens. Bioelectron.*, 2015, **68**, 741–748.
- 25 Y. Song, J. Zhang and D. Li, *Micromachines*, 2017, **8**, 1–19.
- 26 R. Peng and D. Li, *Talanta*, 2018, **184**, 418–428.
- 27 Y. Song, J. Yang, X. Pan and D. Li, *Electrophoresis*, 2015, **36**, 495–501.
- 28 Y. Song, H. Zhang, C. H. Chon, X. Pan and D. Li, *Sens. Actuators, B*, 2011, **155**, 930–936.
- 29 J.-L. Fraikin, T. Teesalu, C. M. McKenney, E. Ruoslahti and A. N. Cleland, *Nat. Nanotechnol.*, 2011, **6**, 308–313.
- 30 Y. Song, H. Zhang, C. H. Chon, S. Chen, X. Pan and D. Li, *Anal. Chim. Acta*, 2010, **681**, 82–86.
- 31 J. Wang, Z. Fan, Y. Zhao, Y. Song, H. Chu, W. Song, Y. Song, X. Pan, Y. Sun and D. Li, *Sci. Rep.*, 2016, **6**, 1–8.
- 32 M. M. Maw, J. S. Wang, K. Z. Yu, Y. J. Wang, B. W. Dai, X. D. Wu and X. X. Pan, *IOP Conf. Ser. Earth Environ. Sci.*, 2018, **171**, 1–9.
- 33 A. D. Grabarek, D. Weinbuch, W. Jiskoot and A. Hawe, *J. Pharm. Sci.*, 2018, in press.
- 34 R. Tahvildari, E. Beamish, V. Tabard-Cossa and M. Godin, *Lab Chip*, 2015, **15**, 1407–1411.
- 35 T. Jain, J. S. Guerrero, C. A. Aguilar and R. Karnik, *Anal. Chem.*, 2013, **85**, 3871–3878.
- 36 J. Wang, J. Zhao, Y. Wang, W. Wang, Y. Gao, R. Xu and W. Zhao, *Micromachines*, 2016, **7**, 1–17.
- 37 Z. D. Harms, D. G. Haywood, A. R. Kneller, L. Selzer, A. Zlotnick and S. C. Jacobson, *Anal. Chem.*, 2015, **87**, 699–705.
- 38 Y. Song, R. Peng, J. Wang, X. Pan, Y. Sun and D. Li, *Electrophoresis*, 2013, **34**, 684–690.
- 39 P. Hinkle, T. M. Westerhof, Y. Qiu, D. J. Mallin, M. L. Wallace, E. L. Nelson, P. Taborek and Z. S. Siwy, *Sci. Rep.*, 2017, **7**, 1–14.
- 40 Z. Liu, J. Li, J. Yang, Y. Song, X. Pan and D. Li, *Microfluid. Nanofluidics*, 2017, **21**, 1–11.
- 41 H. Yasaki, T. Yasui, T. Yanagida, N. Kaji, M. Kanai, K. Nagashima, T. Kawai and Y. Baba, *J. Am. Chem. Soc.*, 2017, **139**, 14137–14142.

- 42 P. Kondylis, J. Zhou, Z. D. Harms, A. R. Kneller, L. S. Lee, A. Zlotnick and S. C. Jacobson, *Anal. Chem.*, 2017, **89**, 4855–4862.
- 43 J. G. Barnard, M. N. Rhyner and J. F. Carpenter, *J. Pharm. Sci.*, 2012, **101**, 140–153.
- 44 B. Dersoir, M. Robert de Saint Vincent, M. Abkarian and H. Tabuteau, *Microfluid. Nanofluidics*, 2015, **19**, 953–961.
- 45 Z. B. Sendekie and P. Bacchin, *Langmuir*, 2016, **32**, 1478–1488.
- 46 W. Anderson, D. Kozak, V. A. Coleman, Å. K. Jämting and M. Trau, *J. Colloid Interface Sci.*, 2013, **405**, 322–330.
- 47 M. N. Rhyner, *AAPS J.*, 2011, **13**, 54–58.
- 48 I. Makra and R. E. Gyurcsányi, *Electrochem. Commun.*, 2014, **43**, 55–59.
- 49 S. M. Hampson, M. Pollard, P. Hauer, H. Salway, S. D. R. Christie and M. Platt, *Anal. Chem.*, 2019, **91**, 2947–2954.
- 50 M. Davenport, K. Healy, M. Pevarnik, N. Teslich, S. Cabrini, A. P. Morrison, Z. S. Siwy and S. E. Létant, *ACS Nano*, 2012, **6**, 8366–8380.
- 51 Z. Qin, J. Zhe and G.-X. Wang, *Meas. Sci. Technol.*, 2011, **22**, 045804.
- 52 S. Ryuzaki, M. Tsutsui, Y. He, K. Yokota, A. Arima, T. Morikawa, M. Taniguchi and T. Kawai, *Nanotechnology*, 2017, **28**, 155501.
- 53 J. Wang, J. Ma, Z. Ni, L. Zhang and G. Hu, *RSC Adv.*, 2014, **4**, 7601–7610.
- 54 C. P. DeBlois and R. W. Bean, *Rev. Sci. Instrum.*, 1970, **41**, 909.
- 55 X. He, K. Zhang, T. Li, Y. Jiang, P. Yu and L. Mao, *J. Am. Chem. Soc.*, 2017, **139**, 1396–1399.
- 56 F. Chang, C. Chen, X. Xie, L. Chen, M. Li and Z. Zhu, *Chem. Commun.*, 2015, **51**, 15316–15319.
- 57 E. C. Yusko, R. An and M. Mayer, *ACS Nano*, 2010, **4**, 477–487.
- 58 H. S. White and A. Bund, *Langmuir*, 2008, **24**, 2212–2218.
- 59 W. Lan, D. A. Holden and H. S. White, *J. Am. Chem. Soc.*, 2011, **133**, 13300–13303.
- 60 L. Jubin, A. Poggioli, A. Siria and L. Bocquet, *Proc. Natl. Acad. Sci.*, 2018, **115**, 4063–4068.
- 61 C. Wen, Z. Zhang and S.-L. Zhang, *ACS Sensors*, 2017, **2**, 1523–1530.
- 62 M. J. Kim, J. W. F. Robertson and J. J. Kasianowicz, in *Nanofluidics: Nanoscience and Nanotechnology*, eds. J. Edel and A. DeMello, Royal Society of Chemistry, Cambridge, UK, 2009, p. 129.
- 63 H. Ghosh and C. Roychaudhuri, in *COMSOL Conference Puna, India*, 2015, pp. 1–5.
- 64 K. Kant, C. Priest, J. G. Shapter and D. Losic, *Sensors*, 2014, **14**, 21316–21328.
- 65 R. Smeets, U. Keyser, D. Krapf, M. Wu, N. Dekker and C. Dekker, *Nano Lett.*, 2006, **6**, 89–95.
- 66 R. Liu, W. Waheed, N. Wang, O. Civelekoglu, M. Boya, C.-H. Chu and A. F. Sarioglu, *Lab Chip*, 2017, **17**, 2650–2666.

- 67 O. A. Saleh and L. L. Sohn, *Rev. Sci. Instrum.*, 2002, **73**, 4396–4398.
- 68 J. Menestrina, C. Yang, M. Schiel, I. Vlassiouk and Z. S. Siwy, *J. Phys. Chem. C*, 2014, **118**, 2391–2398.
- 69 R. A. French, A. R. Jacobson, B. Kim, S. L. Isley, R. L. Penn and P. C. Baveye, *Environ. Sci. Technol.*, 2009, **43**, 1354–1359.
- 70 H. Lodish, A. Berk, S. L. Zipursky, P. Matsudaira, D. Baltimore, and J. Darnell, *Molecular Cell Biology*, W.H. Freeman & Co Ltd, New York, USA, 4th edn., 2000, Chapter 18, 201-245.

Chapter 6 3D printed devices for particle magnetic separation

6.1 Abstract

This final chapter covers the development of 3D printed microfluidic devices for continuous magnetic separation. Such separators could be incorporated into a microfluidic LOC system as means of sample preparation before in-line detection, for example for matrix separation in POC or environmental applications.

A number of continuous magnetic separator prototypes were printed and initial particle magnetic separation trials carried out. The devices incorporated commercially-available, macro-sized, external magnets to migrate magnetic particles away from a main path into a separate, secondary flow. Preliminary prototypes were linear in format and two configurations were trialled: an internal T-junction and an open, surface Y-junction. Further prototypes utilised the three-dimensional freedom of AM, comprising of internal, spiral, multibridged microfluidic channels surrounding a magnet cavity, and would be extremely difficult or impossible to produce using conventional photolithographic microfluidic fabrication methods. It was hoped that these configurations would give higher separation efficiencies than T- or Y- separator designs. A number of spiral separators were produced varying in pitch, diameter and number of spirals/bridges. Combined linear magnetic separator chips with integrated hydrodynamic focusing junctions (as produced in Chapter 4) as well as RPS pore channels (as produced in Chapter 5) included in outlet lines were also produced, but suffered from pore clearance and reproducibility issues.

Due to the ending of this project the work described in this chapter did not extend beyond initial studies and proposed prototype designs, with a great deal of further work and optimisation still being required.

6.2 Introduction

Magnetophoresis can sort species by magnetic susceptibility¹, and can be used to magnetically separate a species out of a matrix², sort magnetic particles/cells from non-magnetic particles/cells³, or separate out different sized sub-populations of magnetic particles/cells^{4,5}. Particles/cells may be naturally magnetic, as in the case of magnetotactic bacteria⁶ or deoxygenated red blood cells⁷, but often, magnetic labelling of a sample is used to carry out a separation⁸. Magnetic bead assays are a mainstay technique in the biomedical sciences⁹, for example in cell analysis and immunoassays¹⁰, but are also used in areas like food safety, where they are used to extract pathogenic bacteria^{11,12}, environmental pollutant detection, such as in water quality measurement¹³ or bacteria quantification in natural environments¹⁴, and mining and waste purification¹⁵.

Magnetic separation has numerous advantages over other separation techniques such as filtration and centrifugation: magnetic labelling can greatly facilitate the separation of particles/cells of interest from a bulk mixture by simple application of an external magnetic field, as magnetic particles can be precisely guided to a target location¹⁶. Thus, direct separation from crude matrices like food samples, blood, faecal matter and culture mediums can be carried out without the need for washing and buffer replacement steps¹⁷. In addition, as almost all biological cells are magnetically neutral, separation via magnetic labels is independent of in situ biological and chemical processes. Furthermore, magnetic beads are an effective medium for immunomagnetic reaction, offering large, selective surfaces for cell or other biomolecular target binding^{18,19}. Immunomagnetic separation (IMS) is a technique in its own right, in which magnetic beads are coated with surface-immobilised antibodies to capture target cells, toxins or other molecules of interest²⁰.

Magnetic separation has been utilised in a multitude of microfluidic devices; there have been a wide range of microfluidic magnetic separation systems since the seminal ones by Pamme from the mid-2000s^{5,21,22}, in many configurations²³⁻²⁶, but there are two overall modes of separation: trapping and continuous. The former involves entrapment or 'enrichment' of the sample, followed by subsequent release for analysis to be carried out^{27,28}. This is a batch process, with associated low throughput. In contrast, continuous magnetic separation offers higher throughputs and is complimentary to microfluidic flow, giving it the potential for unification into a wider LOC system alongside in-line functionalities such as continuous monitoring^{5,26,29}. Continuous microfluidic devices have been designed to magnetically separate cells, including red³⁰ and white blood cells² from whole human blood, and magnetotactic bacteria³. Its gentleness is an advantage of LOC magnetic separation for cell

separation^{5,29}, and it has also been used to separate CTCs³¹. In addition, magnetic microbeads are an effective means to remotely manipulate and position samples inside microfluidic systems^{19,32}, allowing use in areas such as protein bead-based assays³³ and IMS^{34,35}.

The simplest configuration for continuous microfluidic magnetic separation is a Y-junction with an external magnet in close proximity to one of the outlets, but this can suffer from poor efficiency³⁶. More advanced iterations of this basic design feature an extra fluid stream(s) to focus the sample mixture stream for more effective separation—either one adjacent stream^{3,37}, or two (in the same manner as hydrodynamic focusing³⁸). An example of less common configuration is a spiral, such as those of Dutz, et al^{39,40}. This shape allows additional separation by size and density in addition to magnetic susceptibility, by generation of inertial lift forces.

Magnetic particle motion when subject to a magnetic field in a microfluidic channel is influenced by a large combination of forces and both particle-fluid and particle-particle interactions; magnetic force, hydrodynamic force, Brownian force, gravitational force, fluid drag, viscosity and velocity all affect particle/cell trajectory³⁶. At high concentrations, magnetic particles interact with each other, creating undesired clusters of aggregates and chains which have different transport behaviour³⁶. These factors all affect device magnetic separation performance. In addition, various chip parameters must be optimised: channel dimensions, especially at the separation junction³⁶, and magnetic field gradient and position (as magnetic field strength is strongly inverse with distance, with magnetic actuation greatly weakening within a very short distance)²⁹. This is a large number of factors requiring optimisation, or else magnetic particles/cells can fail to be actuated, or can undergo sedimentation. Separation efficiency is a function of all of these operating and design parameters. These practical challenges prevent the widespread use of microfluidic magnetic separators beyond the proof-of-concept stage²⁰.

One way to improve magnetic separation efficiency is to use multiple magnetic separators in series, as a 'cascade'³⁶. By using multiple separators in tandem, n number of separators in series can achieve up to 2^n folds sample enrichment³⁶. For example, Jung, et al. developed a six-stage cascade magnetophoretic separation system for separation of red blood cells from whole blood with an efficiency of 86%⁴¹, and Lee, et al. used multiple microfluidic devices in series to magnetically extract *E. coli* from whole blood, with nearly 100% clearance⁴². As an alternative to these bulky, planar multi-separator microfluidic systems, 3D printing offers the possibility for advanced, compact, LOC magnetic separation devices due to its three-dimensional freedom. 3D printing has been utilised to produce milli- and microfluidics with complex 3D configurations that are extremely hard, or unattainable with

conventional PDMS fabrication methods, including a number of intricate reactor designs^{43,44} and a spiral separator for inertial separation of bacteria⁴⁵.

There are only a handful of reported 3D printed devices featuring magnetic separation, all involving stop-flow, batch separation, except for one simple Y-junction module⁴⁶. In 2013, Krejčová, et al. fabricated an FDM chip for the capture and indirect detection of influenza viruses, that magnetically held them inside a reaction chamber well⁴⁷. The following year, Lee, et al. outlined a hollow vessel for containing sample suspension, into which a stack of magnets was held⁴⁸. Also in 2014, Lee, et al. produced a proof-of-concept, material-jetted, planar Y-junction module for separation of magnetically-captured alpha-fetoprotein (AFP), but did not give any obtained data⁴⁶. Similarly, in 2015 Zhang, et al. printed a device for magnetic bead nucleic acid isolation that had separate chambers for magnetic capture, and finally, in 2017 a DLP device that magnetically captured *E. coli*-antibody-magnetic bead complexes into a well was reported⁴⁹. As yet, continuous magnetic separation of particles/cells in a printed LOC device has not been achieved. This would allow the opportunity for incorporation of magnetic separation into a more complete, printed LOC system with the option for in-line detection.

6.3 Aims and Objectives

The aim of this chapter was to develop 3D printed modules for continuous magnetic separation, with the motive being to ultimately combine them with the particle/cell analysis chips covered earlier in this thesis, as means of sample preparation.

This above aim raised the following core chapter objectives:

- Compare the magnetic separation efficiency of standard, linear T- or Y-separator designs with that of 3D-printed, three-dimensional, multi-bridged spiralled designs.
- Demonstrate continuous magnetic separation of a non-magnetic and magnetic particle mixture followed by subsequent RPS detection within the same printed microfluidic chip.

6.4 Materials and Methods

6.4.1 Materials

6.4.1.1 Chemicals and reagents

Methylene blue was obtained from Sigma-Aldrich, and solochrome red obtained from Merck. TWEEN 20 was obtained from Sigma-Aldrich. Phosphate-buffered saline (PBS) was obtained from Sigma-Aldrich (catalogue number P4417) and was made up in deionised water to the supplier-recommended concentration (phosphate buffer 0.01 M, potassium chloride 0.0027 M, sodium chloride 0.137 M), with measured pH 7.32 (taken by a FiveEasy pH meter, with InLab Ultra-Micro-ISM[®] pH electrode, both obtained from Mettler Toledo).

6.4.1.2 Beads

Large magnetic particles (30 µm mean diameter, 20–50 µm diameter range, PLA matrix, iron oxide 40% w/w, COOH-coated, catalogue number 12-02-304) and non-magnetic particles (20 µm, micromer[®], polystyrene, COOH-coated, CV<5%, catalogue number 01-02-204) were both obtained from Micromod Partikeltechnologie GmbH. Small magnetic particles (1 µm, Dyna[®] MyOne[™], polystyrene matrix, iron oxide 37% w/w, COOH-coated, catalogue number 65011) were obtained from Thermo Fischer Scientific. Small non-magnetic particles (CPC1000, 1 µm) were obtained from Izon Science, and fluorescent particles (10 µm, Fluoresbrite[®] Yellow Green microspheres, CV=15%, catalogue no. 18142-2) were obtained from Polysciences.

Two different rod magnets were used: 5 mm diameter, 10 mm length, Neodymium, grade N42, 0.95kg pull, NiCuNi plated, catalogue number EP642, obtained from e-Magnets UK, and 5 mm diameter, 50 mm length, Neodymium, grade N52, 6.9 kg pull, NiCuNi plated, catalogue number F550DM-2, obtained from First4Magnets.

6.4.2 Methods

All methods were carried out at ambient room temperature (approx. 18-20 °C).

6.4.2.1 Magnetic field measurements of small rod magnet

B-field readings of the small Neodymium rod magnet were measured via a DX-103 Gaussmeter, obtained from Dexing Magnet Tech Company). Measurements were taken parallel to the end of the magnet, at increasing distances. A background reading of 14 mT was measured and was subtracted from all measured values to give the accurate reading.

6.4.2.2 Device fabrication

Device designs and hollow cylinders were produced and converted to .STL format on NX Version 9.0 CAD software (Siemens). Fabrication was carried out in Accura[®] 60 resin (obtained from 3D Systems) via an SLA[®] Viper si2 (3D Systems), in HR mode (Nd:YV04 solid state laser at 354.7 nm, 100 mW output power, 1/e² beam diameter 75 μm +/- 15 μm , minimum build layer height 20 μm , elevator vertical resolution 25 μm and position repeatability 76 μm) in the Y build-direction (device built upwards whilst positioned on the build-bed in the configuration for use). Followed this, UV curing was carried out via a ProCure[™] 350 UV Chamber (3D Systems) for 4 minutes to ensure full photopolymer cross-linkage, followed by a final IPA and methanol rinsing step. Device channels were cleared using a methanol:water mixture (50:50). Certain device inlets, outlets, and magnetic chambers were produced by M6 tapping via a tap and die kit (obtained from Tekton). Devices with open, surface channels were sealed using a cover layer consisting of LEXAN[™] 8010PC polycarbonate film (obtained from SABIC, 250 μm thickness) attached via TESA 4965 double-sided tape (obtained from 3M), applied by hand and flattened via seam roller. As in Chapter 5, electrodes (silver wire, 0.25 mm diameter, purity 99.99%, catalogue number AG5485, obtained from Advent Research Materials) were pressed into printed surface grooves and sealed with two-part epoxy resin (Araldite[®], Rapid, obtained from Huntsman Advanced Materials).

6.4.2.3 Fluidic control

Microfluidic flows were effected by Mitos P-Pump Basic pressure-driven pumps (Dolomite) and inputted into the chip by microfluidic tubing (PEEK, 250 μm internal diameter, obtained from Dolomite) and standard Supelco[®] HPLC fittings and end ferrules (obtained from Sigma-Aldrich).

6.4.2.4 Flow rate measurements

Flow rate measurements of device outlets were carried out by collection of outlet fluids over a measured time (60s) into separate Eppendorfs, and weighing of the fluid to estimate volume. This gave the flow rate as volume min⁻¹.

6.4.2.5 Non-magnetic particle runs

O-rings (nitrile, 6 mm diameter, obtained from Rhondama) were added to each fitting cavity and PTFE tape applied to prevent leakage. Devices were first flushed with PBS before use. Particle suspensions were sonicated (1 min) immediately before use to ensure dispersion. To measure particle loss, 1 µm non-magnetic beads (2.75x10⁸ particles mL⁻¹, PBS, 600 µL) were ran through at 50 mbar and both lines fed into the same Eppendorf. Following this, PBS (1000 µL) was rinsed through the chip and also collected into the same pot. Finally, it was made up to 1.5 mL with PBS before TRPS analysis. Taking into account the liquid held inside the separator channels (~85 µL), dilution was 7.5x.

6.4.2.6 Magnetic particle runs

O-rings (nitrile, 6 mm diameter, obtained from Rhondama) were added to each fitting cavity and PTFE tape applied to prevent leakage. Devices were first flushed with PBS before use. Particle suspensions were sonicated (1 min) immediately before use to ensure dispersion. Magnetic separation testing with 1 µm magnetic beads (1.1x10⁸ particles mL⁻¹, PBS, 1000 µL) was carried out at 50 mbar with a small rod magnet placed at intervals of 1 mm from 0–15 mm in its compartment. Magnetic testing of the combined magnetic separation/RPS chip was carried out via suspensions of 30 µm magnetic particles (1.0x10⁴ particles mL⁻¹) and 20 µm non-magnetic particles (1.0x10⁴ particles mL⁻¹) in KCl (0.25 mM), TWEEN (0.5%) and MB (1 mM) in water.

6.4.2.7 Particle quantification by TRPS

Volumes of particle suspensions (non-magnetic CPC1000 beads or magnetic 1 µm, Dyna[®] MyOne[™] beads, in PBS) after flowing through separator devices were measured by weighing of the gained solutions, using the assumption that solution density=1 gcm⁻³. Concentrations of these particle suspensions were measured by a QNano TRPS instrument (obtained from Izon Sciences) using NP1000 nanopores and a calibration suspension (CPC1000 beads in PBS buffer, 5.0x10⁷ particles ml⁻¹)

controlled by Izon Control Suite software (Version 3.1), both also Izon Sciences. Mean pore stretch was 45.5 mm and applied voltage +0.08V. Subsequently, separation efficiencies were calculated from these gained concentration values, as a percentage of the total number of particles outputted by the device, over the total number inputted, using measured volumes.

6.4.2.8 Investigation of spiral separator mixing

Methylene blue and solochrome red B solutions (1 mM) were each ran under applied pressure (200 mbar) through two spiral separator devices (5 mm pitch and 12 mm inner channel distance from magnet, and 10 mm pitch and 20 mm inner channel distance from magnet) in the inner and outer fluidic channels respectively.

6.4.2.9 Fluorescent particle visualisation

Fluorescence of adsorbed particles inside spiral magnetic separator device was observed inside a UV lightbox (Spectroline® CM-10 UV-viewing cabinet, obtained from Sigma-Aldrich).

6.4.2.10 Microscopy, photography and video filming

Photos of chips and experiments were taken via an Optiphot-2 optical microscope with DS-5M Camera Head controlled by a DS-L1 Digital Sight Camera Control Unit (all obtained from Nikon). Video was recorded on a Meros High Speed Digital Microscope (obtained from Dolomite) using a 35 fps frame rate. Macroscale device photographs were taken using a Sony Cybershot DSC-HX9V digital camera.

6.5 Results and Discussion

The magnetic separation chips in this chapter utilise the same principle: actuation of flowing magnetic particles from a main flow path into a secondary channel, by an applied magnetic field. The main flow path terminates in a non-magnetic species output, whilst the secondary channel terminates in magnetic species output. Chip efficiency was defined as the percentage of total actuated magnetic particles compared to the total number of magnetic particles entering the channel.

6.5.1 Magnetic field measurements through air and Accura® 60

The B-field at increasing distances from a 5 mmx10 mm rod magnet end and side in air, and in five different thicknesses of Accura® 60 cylinders in which the magnet snugly fit into, was measured. The magnetic field strength was found to decrease rapidly with distance in air, as expected²¹ (Figure 6.1). Accura® 60 appeared to disrupt the magnetic field, causing lowered magnetic field strengths and a more linear strength decrease with distance. The magnetic field measured at the side of the magnet through Accura® 60 is relatively weak. So, a stronger magnet was used in the spiral separator modules.

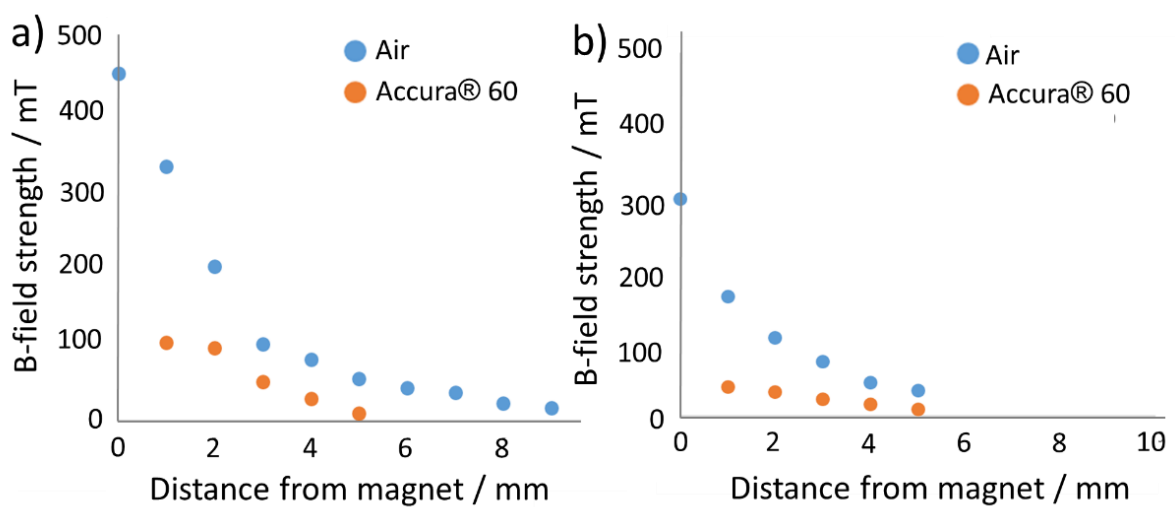


Figure 6.1 B-field measurements taken by a Hall Probe at increasing distances from a) the end and b) the side of a Neodymium rod magnet, in through air and through Accura® 60 polymer.

6.5.2 Y-junction magnetic separator device prototype

An initial Y-junction separator chip prototype was fabricated in Accura® 60 with internal, 1000 μm diameter circular channels (Figure 6.2). A compartment for a 5 mmx10 mm rod magnet was produced by an M6 tap. This cavity allowed the magnet distance to be easily adjusted by hand, allowing simple magnetic strength tuning. Magnetic strength tuning is important when using a range of flow rates: higher flow rates require stronger magnetic field strength in order to quickly actuate particles, and lower flow rates require weaker magnetic field strength to prevent particles fouling onto the channel wall adjacent to the magnet.

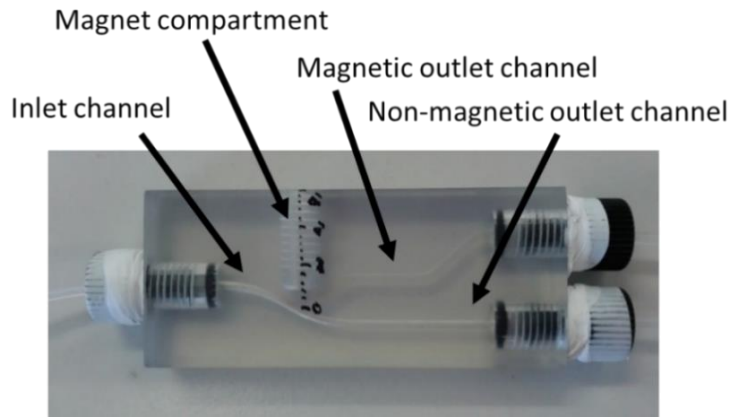


Figure 6.2 Linear magnetic separator device prototype, with Y-junction and magnet compartment. Writing denotes magnet distance from junction.

6.5.2.1 Fluid flow measurement

Flow rate measurements were taken of each separator line using water at a range of applied pressures. It was found that they were almost equal (Figure 6.3). This was a concern as non-magnetic particles/cells could have an affinity to traverse both outlet lines equally—it is preferable for the non-magnetic line to have a slightly higher flow rate, just sufficient enough to cause all particles to traverse it, but with a small enough difference such that a magnet would be able to actuate magnetic particles away and into the magnetic line.

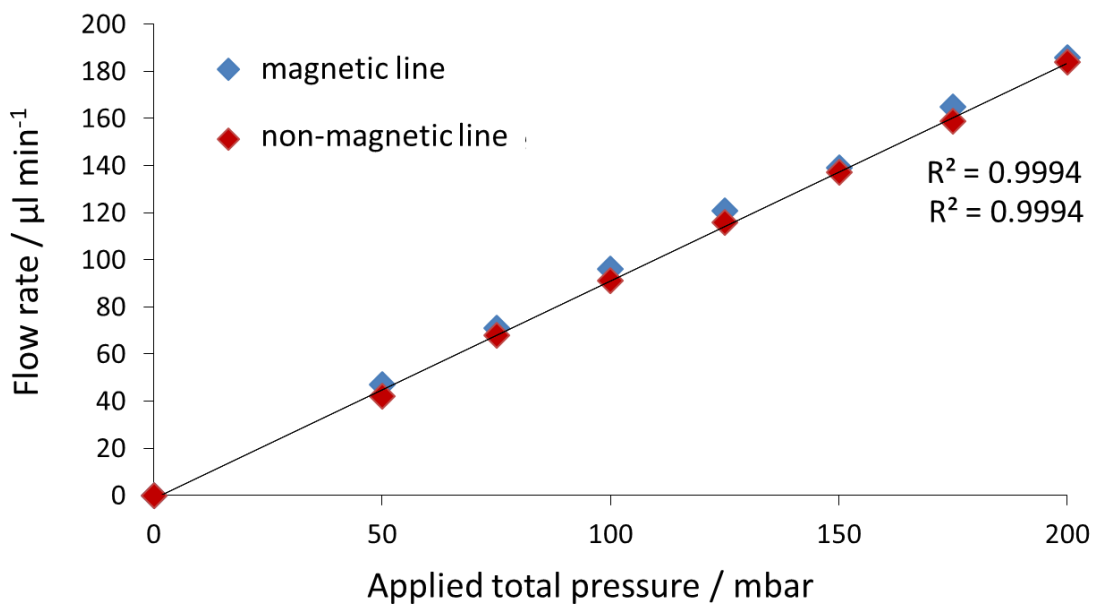


Figure 6.3 Measured flow rates of each line of the Y-junction magnetic separator prototype at a range of applied pressures. Plots and R^2 values include a (0,0) point.

6.5.2.2 Magnetic particle testing

Magnetic separation testing using a $1\ \mu\text{m}$ diameter magnetic bead suspension (1.1×10^8 particles mL^{-1} , in PBS) at 50 mbar with a small rod magnet placed at intervals of 1 mm from 0–15 mm in its compartment found that a distance of 2 mm gave the most efficient separation at this flow rate. A photograph of the collected suspensions at this distance is shown in Figure 6.4. This method of determining the magnet distance for highest separation was only approximate: separation was deduced by eye, by observing the darkness of the fluidic output from the magnetic line relative to that of the non-magnetic line, and to a 5.0×10^7 particles mL^{-1} PBS control suspension. It was noted that the volume of the non-magnetic flow was significantly lower than that of the magnetic line—it was thought that the surrounding liquid around the magnetic particles was also actuated along with the magnetic particles.

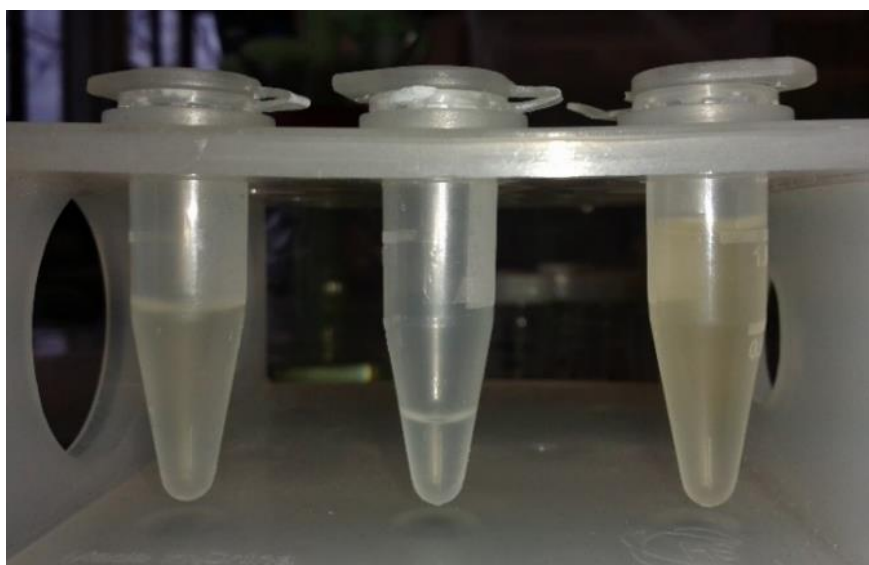


Figure 6.4 Collected fluid outputs from the Y-junction linear magnetic chip prototype at 2 mm magnet distance, after a $1\ \mu\text{m}$ particle suspension (1.1×10^8 particles mL^{-1} in PBS) was run through at 50 mbar. Left-to-right: collected magnetic line output, collected magnetic line output, collected non-magnetic line output, and a control suspension (5.0×10^7 particles mL^{-1} in PBS) for comparison.

The suspension collected from the magnetic output line under a 2 mm magnet distance was quantified by TRPS and a separation efficiency of 90% calculated (as covered in Chapter 6.4.2.7). It was also observed that a number of magnetic particles had become trapped in the chip on the channel wall adjacent to the magnet compartment (Figure 6.5). A fraction of the unaccounted 10% will be these fouled particles; it is believed that a significant amount of the rest will be found in the device inlets/outlets (after the findings in Chapter 3.5.6.3).

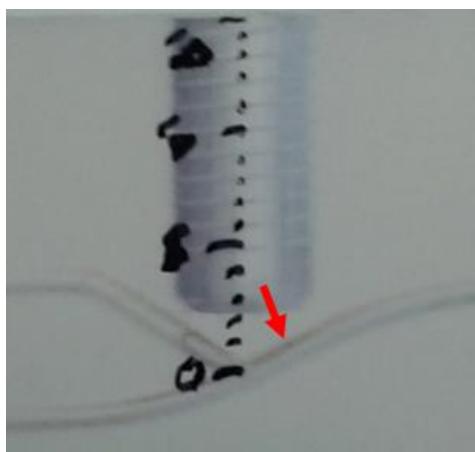


Figure 6.5 Magnetic particle fouling (indicated by the red arrow) onto the microchannel wall adjacent to the magnet housing, observed after magnetic particle testing.

6.5.2.3 Non-magnetic particle testing

In order to deduce non-magnetic particle loss into the device, a suspension of 1 μm non-magnetic beads (2.75×10^8 particles mL^{-1} , PBS, 600 μL) was run through the device at 50 mbar followed by a PBS (1000 μL) rinse. After taking into account dilution, efficiency (in terms of regained beads out of both outlet lines) was $\sim 82\%$. This loss was assumed to be mostly due to loss into outlets/inlets, and adsorption onto the circular, rough channel surfaces.

6.5.3 Integrated magnetic separator/resistive pulse sensing device: 1st prototype

A magnetic separator chip was designed that incorporated both in-line magnetic separation, and subsequent RPS sensing. The hydrodynamic focusing junction from the optical chip in Chapter 4 was added to allow more precise separation, by enabling the particles to be manipulated as a thin stream³⁸, and RPS pore channels from the device outlined in Chapter 5 were added to each output line. Figure 6.6 shows an initial prototype. The design included two magnet compartments to allow choice of magnetic position along the channel as well as use of a second small rod magnet for further actuation (for higher flow rates) if desired, in addition to being able to tune the magnet distance from the channel. The separation point was a simple Y-junction. The RPS pore channels had a 500 μm length and 80 $\mu\text{m} \times 80 \mu\text{m}$ cross-section, to allow differentiation of 20 and 30 μm beads (non-magnetic and magnetic, respectively). It was found that despite the magnetic compartments being given an extra 2.0 mm nominal diameter, laser overcure was such that widening via a file was required in order to house the magnets. There were also issues with pore reproducibility due to difficulty in quickly and

uniformly clearing uncured resin out of a relatively large device. For example, Figure 6.7 shows photographs of the two pores in one device copy, with one of the pores being considerably narrower. In other device copies, certain pores did not clear at all. Pore reproducibility is a concern in these chips as pores would have to be the same volume in order to produce comparable pulses.

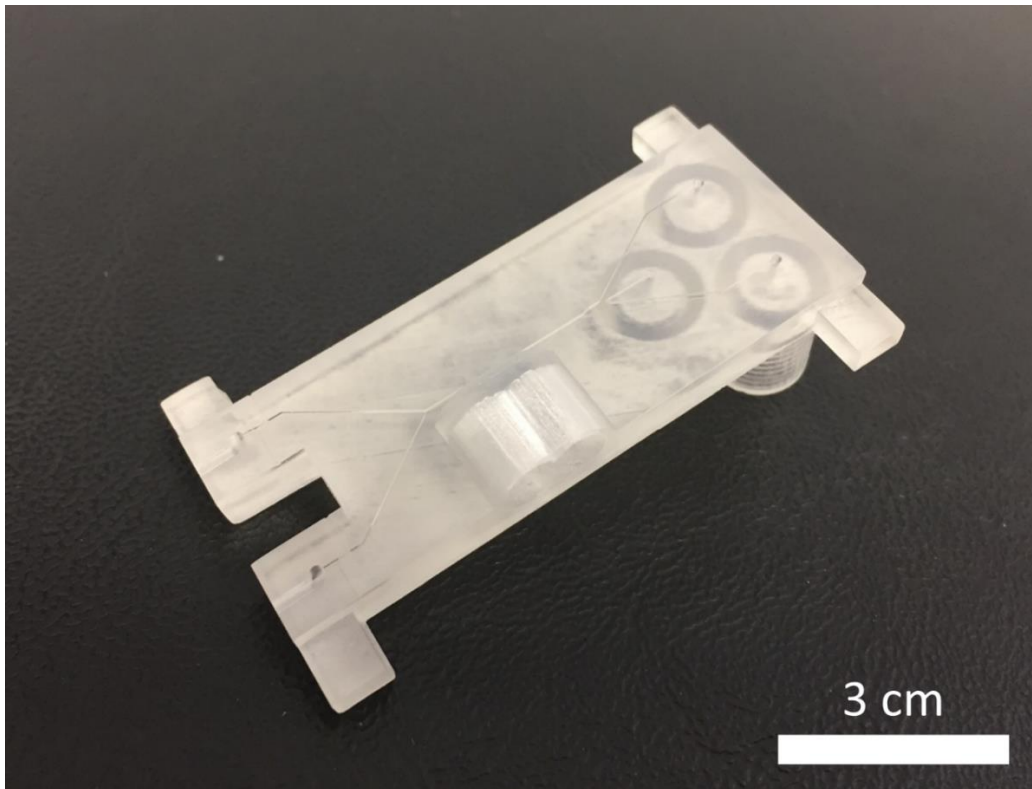


Figure 6.6 Initial prototype of combined magnetic separation/RPS measurement chip. The gap between the RPS channels is to allow sealing of the inner electrode grooves with glue to ensure water tightness.

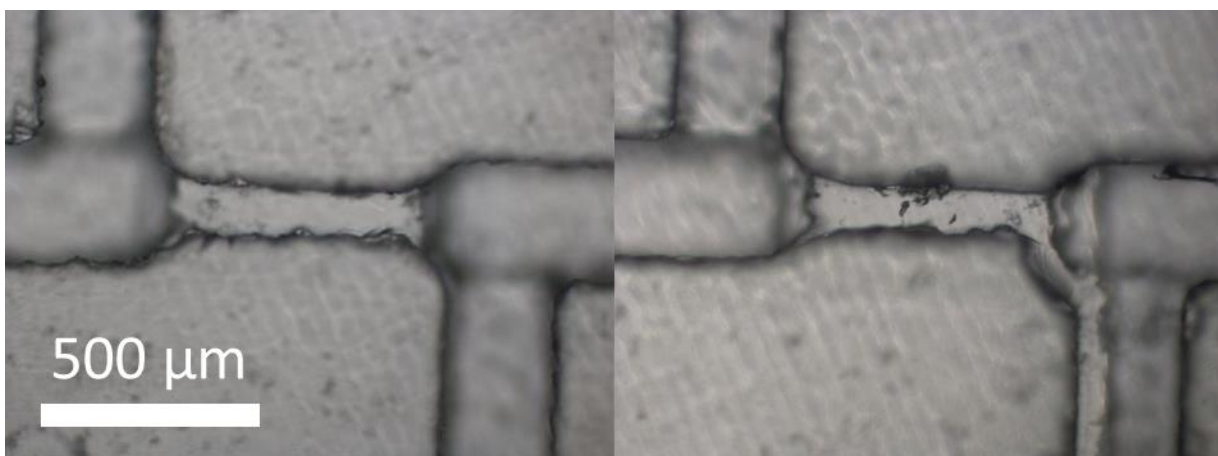


Figure 6.7 Photographs of RPS pore channel pairs in a combined particle magnetic separation/RPS analysis chip, made by SLA in Accura® 60.

6.5.3.1 Flow testing

For optimum magnetic separation, the central sample stream should naturally travel down the non-magnetic line, and the applied magnetic field should actuate particles away from this flow into the magnetic line. Methylene blue dye was used to visualise sample stream flow. Figure 6.8 shows the effects on flow of different combinations of flow rates.

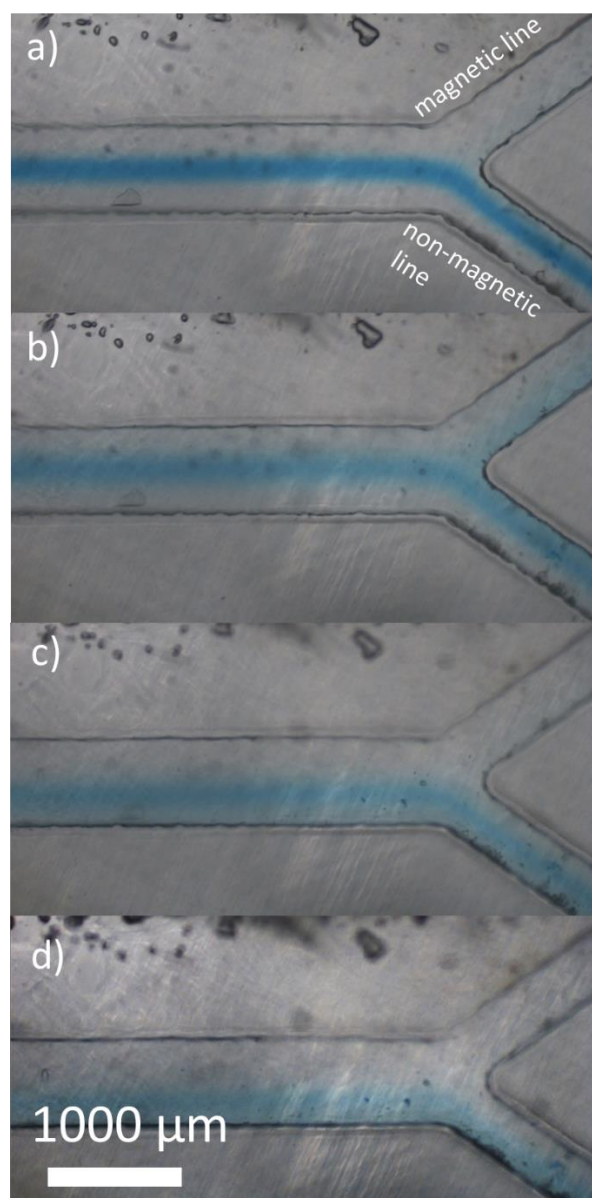


Figure 6.8 Tuning of focused MB (1 mM, aq) streams in the Y-junction of the combined magnetic separation/RPS chip. *a) 100 mbar applied across all 3 inlets, b) 30 mbar applied across all 3 inlets c) topmost sheath flow=35 mbar, other flows 30 mbar d) topmost flow=40 mbar, other flows 30 mbar.*

At higher equal flow rates (Figure 6.8a), the sample stream naturally traverses the non-magnetic line. At lower flow rates (Figure 6.8b), a small portion of the sample stream travels down the magnetic line, but this is easily remedied by increasing the pressure of the opposite stream (Figure 6.8c-d).

6.5.3.2 Particle separation testing

A mixture of 30 μm magnetic particles and 20 μm non-magnetic particles was used to test the combined magnetic separation/RPS chip: in an ideal separation, all 30 μm magnetic particles will be actuated into the magnetic line whilst all 20 μm non-magnetic particles will remain in the main path, and far larger pulses should be detected in the magnetic line RPS junction. TWEEN was also added to the mixture to prevent magnetic particle aggregation, and MB dye was added in order to visualise the sample flow. Due to difficulties in pore clearance post-printing (as covered in Chapter 6.5.3), RPS analysis could not be carried out. Figure 6.9 shows stills taken from recorded videos of attempted particle separation in the combined magnetic separation/RPS chips. At 30 mbar applied pressure at all outlets and the magnet placed at 0 distance, the magnetic particles became lodged at the wall adjacent to the magnet chamber, whilst non-magnetic particles (outlined by red circle) travel down the non-magnetic line (Figure 6.9a). Between roughly 2 and 4 mm distance, varying amounts of larger magnetic particles foul onto the wall whilst smaller magnetic particles travel down the magnetic line (Figure 6.9 b; magnetic particles outlined by yellow circles), and small magnetic particles are not sufficiently actuated and continue down the main path. It was noted that the magnetic particles had a particle size distribution of 20 μm –50 μm , and if a more homogeneous sample had been used, separation efficiency should be far higher at these intermediate magnet distances. At magnet distances >4 mm, no magnetic particles were trapped or migrated across into the magnetic line (Figure 6.9 c): the yellow outlines show a large magnetic particle cluster travelling down the non-magnetic line. Figure 6.9 d shows a magnet distance of 2 mm and MB dye in the sample stream, and again illustrates a smaller magnetic particle not being actuated far enough to escape the main path, whilst a larger magnetic particle is separated into the magnetic output line.

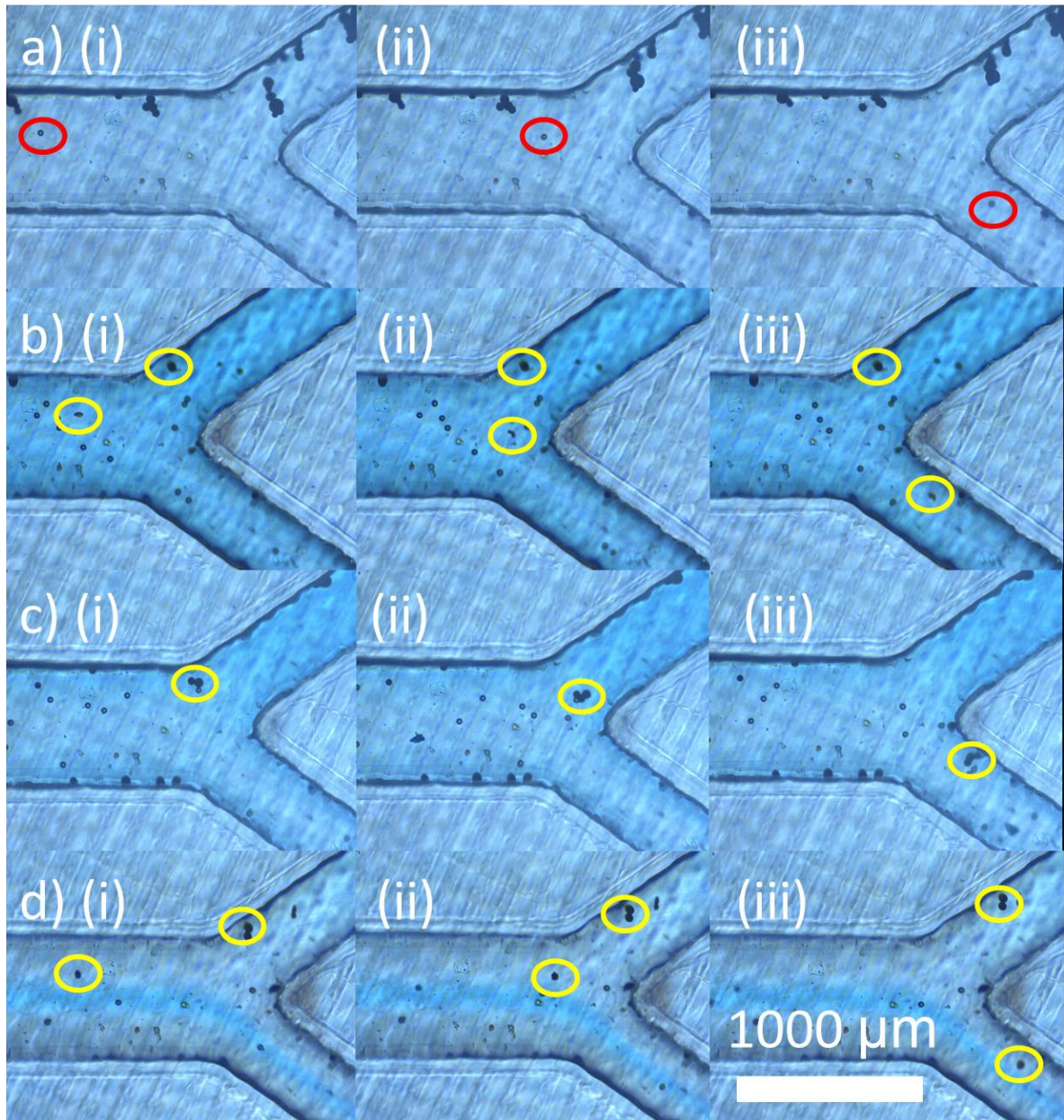


Figure 6.9 Stills from videos recorded of attempted magnetic particle separation in the combined magnetic separation RPS chip using a 6.9 kg pull magnet, at 30 mbar applied pressure to all three lines. a) Magnet distance=0 mm, b) Magnet distance=2 mm, c) Magnet distance=7 mm, d) Magnet distance=2 mm and dye (MB, 1 mM) used in the particle suspension. Particle suspension=30 μm magnetic particles (1.0×10^4 particles mL^{-1}), 20 μm non-magnetic particles (1.0×10^4 particles mL^{-1}) in KCl (0.25 mM), TWEEN (0.5%) and MB (1 mM), aq. Under all conditions, the non-magnetic particles did not travel down the magnetic line. Time: (i)=1 s, (ii)=2 s, (iii)=3 s.

6.5.4 Integrated magnetic separator/resistive pulse sensing device: 2nd prototype

A second magnetic separation/RPS measurement chip prototype was designed (Figure 6.10) that incorporated a single magnet compartment, this time in a long trough shape, to allow easier distance adjustment of the long magnet. Also, instead of a Y-junction, a staggered junction split was used (Figure 6.10 a) to prevent non-magnetic particles from traversing the magnetic output line. Figure 6.11 a shows a photograph of the printed chip. The magnetic housing was given diameters with 5.0mm extra, which fit the magnet, however, support structures were present inside them (Figure 6.11 b) that had to be snapped off and the stumps filed down. The RPS pore channels had the same 500 μm length and 80 μm x 80 μm cross-section. However, due to time constraints in this project, this device was not tested.

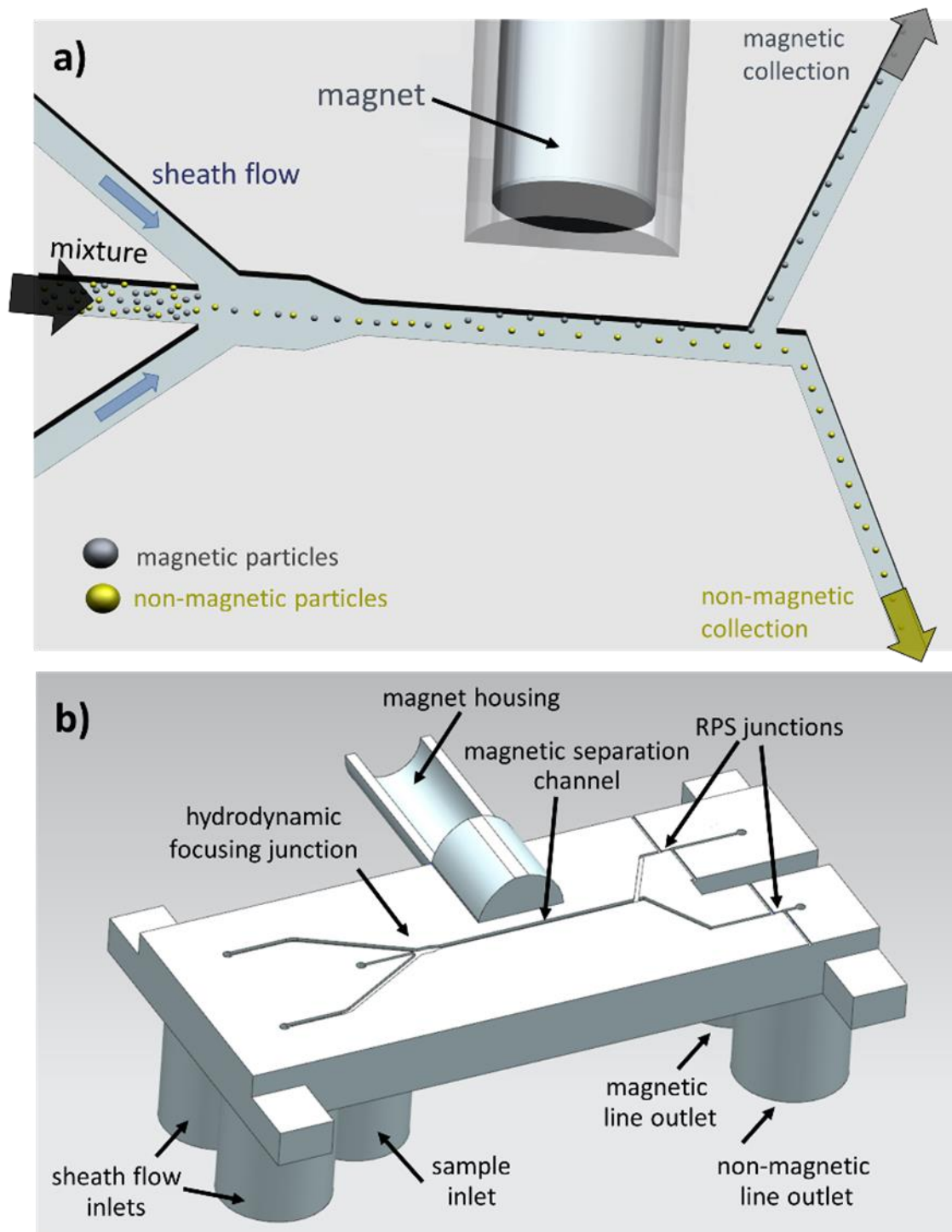


Figure 6.10 Combined magnetic separation/RPS measurement chip concept: a) illustration of separation process (initial hydrodynamic focusing followed by magnetic actuation of magnetic particles into a separate output line) and b) chip CAD file, outlining various sections including single magnetic housing in a trough configuration.

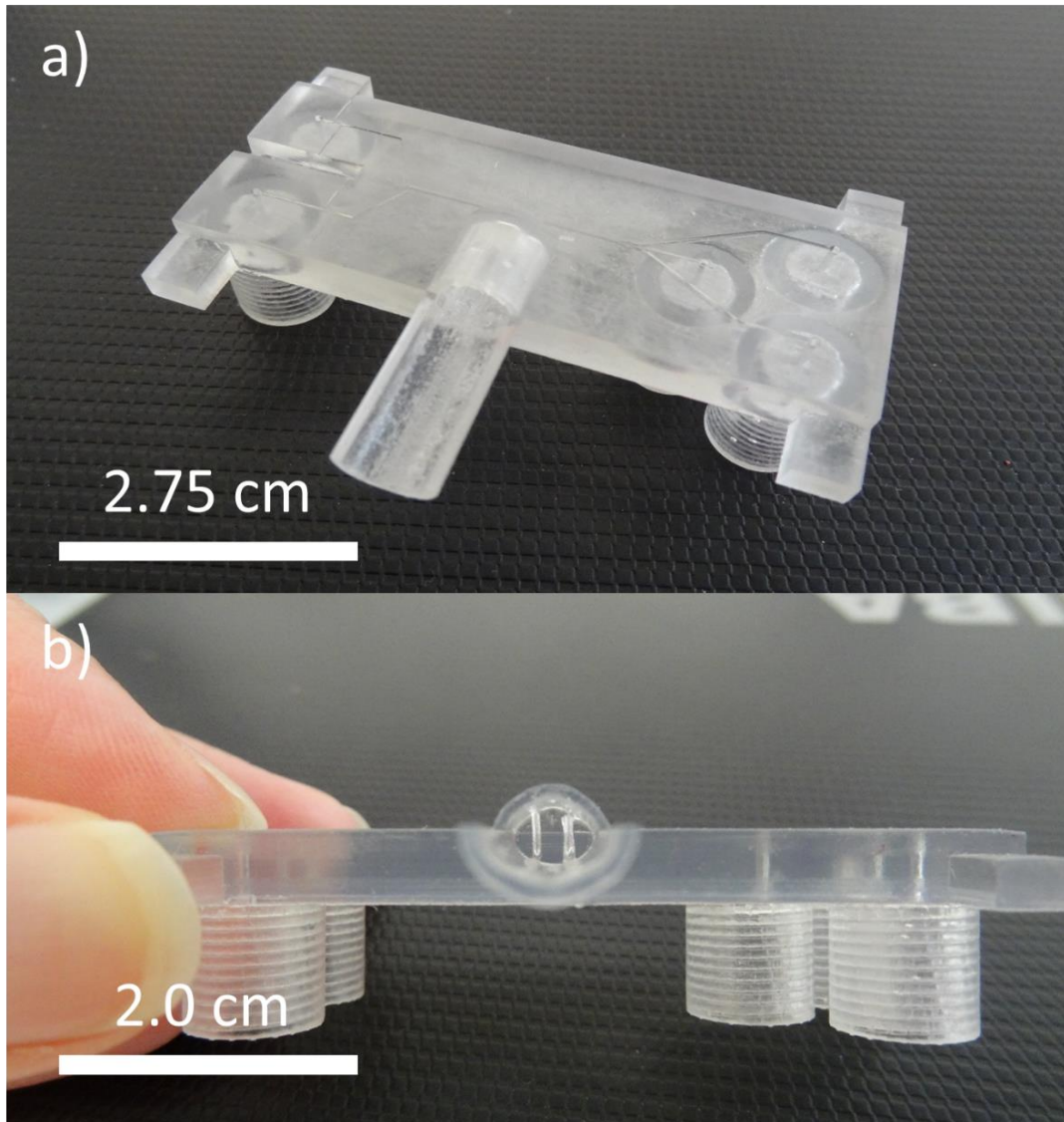


Figure 6.11 *Second prototype of combined magnetic separation/RPS measurement chip. a) View of top of chip. b) View from side of chip, showing support structures present inside the chip magnet compartment.*

6.5.5 Spiral magnetic separator devices

An alternative separator design was fabricated consisting of a central magnet chamber surrounded by two adjacent spiral channels running in parallel, with a number of channel bridges connecting them (Figure 6.12). Particle suspensions are fed into the outer line. Non-magnetic particles should remain in this line, whilst magnetic particles should migrate across the bridges towards the magnet, into the inner, magnetic line. Similar to Y-junction cascade systems^{36,41,42}, the use of these bridges allow >1 separation opportunity: magnetic particles still in the outer line leftover from the previous bridge have another chance to migrate inwards to the magnetic collection at the next bridge, and so on, thus

increasing the magnetic separation efficiency of the system. Such a three-dimensional device is impossible with conventional photolithographical microfluidic methods. The devices incorporated 1000 μm diameter circular microfluidic channels.



Figure 6.12 Photographs of three printed spiral magnetic separators printed via SLA in Accura® 60 polymer, each comprising of a central magnet cavity surrounded by two parallel, bridged microfluidic channels. Left to right: a) bridges: 6, pitch: 10.0 mm, shielding polymer thickness: 3.0 mm, and air gap: 1.0 mm, turns: 4, b) bridges: 12, pitch: 7.0 mm, shielding polymer thickness: 3.0 mm, turns: 7, c) bridges: 12, pitch: 5.0 mm, shielding polymer thickness: 2.0 mm, turns: 7.

Figure 6.13 shows a top-down view of the spiral separator device in Figure 6.12 c, with the bridges denoted. The outer spiral is the non-magnetic line whilst the inner spiral is the magnetic line.

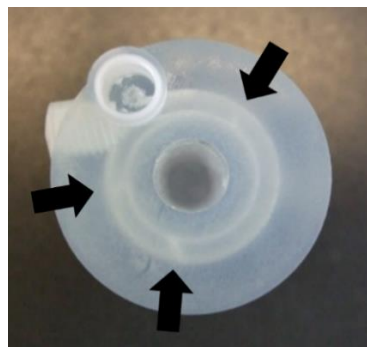


Figure 6.13 Top-down view of 4.5 mm pitch spiral separator, showing three channel bridges at different heights.

6.5.5.1 Fluid flow measurement

Channel flow rate measurement through both channels in the 10.0 mm pitch spiral device found that flow in the inner, magnetic line channel was faster than that of the outer, non-magnetic channel (Figure

6.14) at a range of applied pressures. This is unwanted as all particles, both magnetic and non-magnetic, could be swept into the magnetic line by the latent fluid flow, regardless of magnet presence or not.

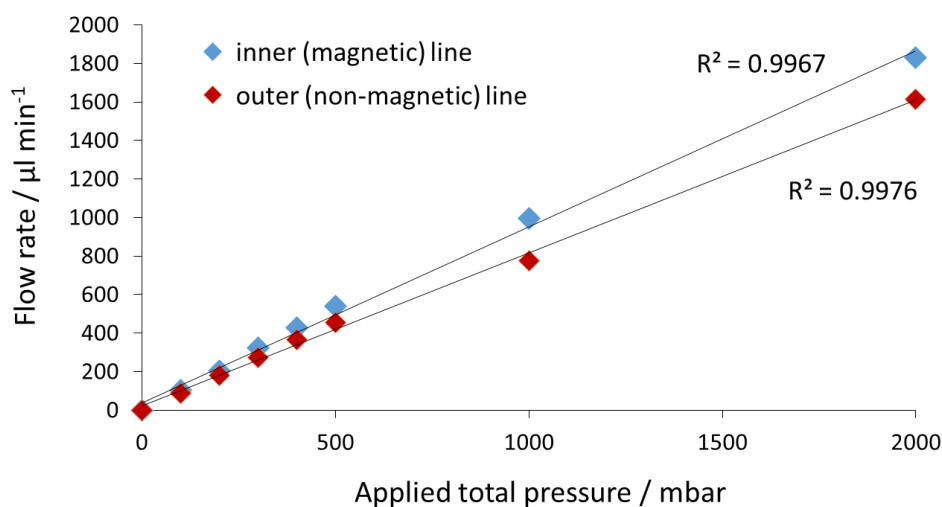


Figure 6.14 Unequal flow rates observed in 10.0 mm pitch helical separator device at a range of applied pressure. Plots and R^2 values include an (0,0) point.

6.5.5.2 Investigation of fluid mixing across channel bridges

Running of different-coloured dye solutions (methylene blue and solochrome red B, 1 mM) through the two channels of two spiral devices (one 5 mm pitch, 12 mm inner channel distance from magnet, one 10 mm pitch, 20 mm inner channel distance from magnet) at 200 mbar applied pressure for both lines showed that fluid mixing across bridges became visible approximately halfway down. This indicated that the bridges were fully formed (as opposed to being blocked by resin) and fluid flow across them was possible. However, this could also be a problem in terms of particle separation: if the outer channel fluid flows into the inner channel flow with no magnet present then non-magnetic particles/cells could be pulled into the inner line. This corroborates the concern about the faster magnetic line flow in Chapter 6.5.5.1.

6.5.5.3 Fluorescent particle testing

The circular channel cross-section, and spiralled channel curvature in the fabricated spiral magnetic separation devices entails that the channel walls are entirely covered in stair-stepping from the 3D printing process. Thus, it was thought that particle sedimentation into crevices might be observed ubiquitously over the channel wall surfaces. However, this was found to not be the case: visualisation

in a UV lightbox after running of a fluorescent bead suspension through both channels showed that particles had deposited onto the channel floors (Figure 6.15), indicating that gravitational forces were more to blame for particle loss in these devices than trapping into wall crevices.

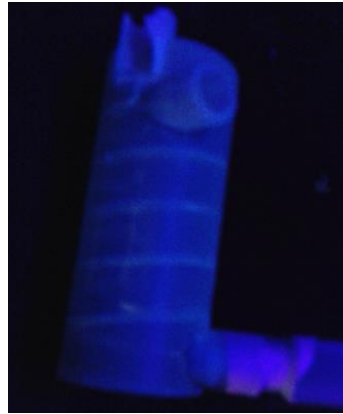


Figure 6.15 Photograph of helical device (6 bridge, 10.0 mm pitch separator) under visualisation box after flush with fluorescent beads, showing deposited beads on the channel floors.

6.5.5.4 Single-turn bridged magnetic separator device

Figure 6.16 shows an alternative, compact spiral magnetic separator chip design comprising only a single turn, and bridges spaced more closely. There were 4 blockages in the inner, magnetic line (3 outlined via red arrows, 1 obscured behind threading) due to incomplete flushing of uncured resin after printing.

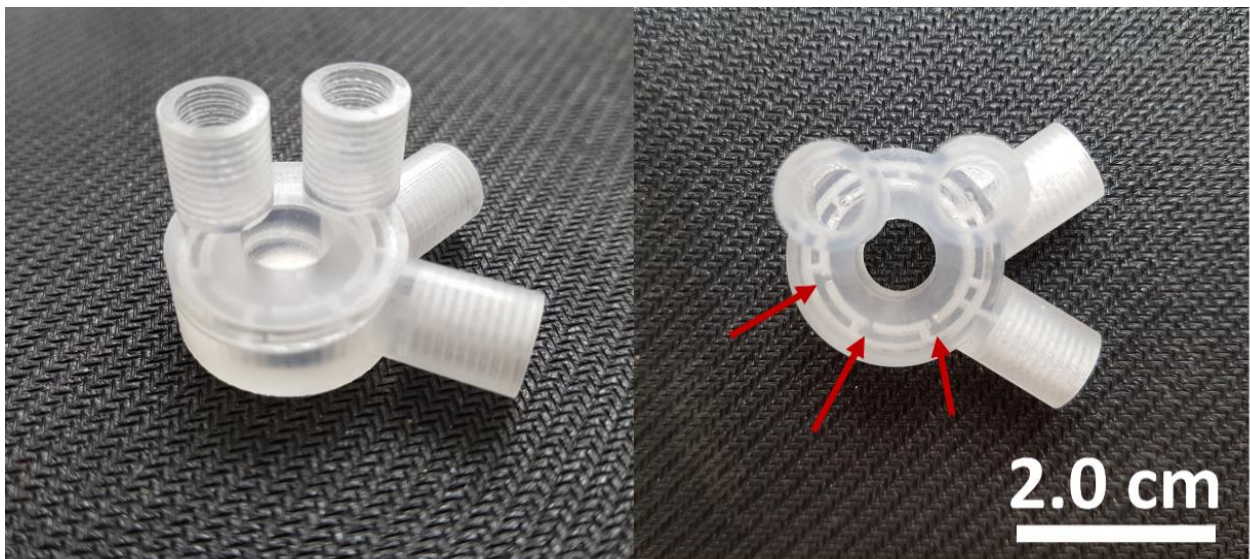


Figure 6.16 Photographs of a single-turn, bridged magnetic separation device, printed via SLA in Accura® 60 polymer, bridges: 7, pitch: 4.5 mm, shielding polymer thickness: 3.0 mm, turns: 1. Three channel blockages are denoted by red arrows.

6.5.6 Advanced spiral magnetic separator device

A further iteration of the spiral magnetic separator devices was envisioned: Figure 6.17 illustrates a concept, bridged, double-spiralled magnetic separator device, where the non-magnetic line (pink) is a spiral with a gentle slope, encircled by the magnetic line (blue), a much tighter spiral. The two lines are connected by a number of bridges (bright blue) that radiate outwards from each innermost maxima of the magnetic line spiral. Thus, magnetic fouling of particles in the magnetic line onto the channel wall is prevented as the spiral brings them away from the magnet for the majority of the time, unlike the previous spiral devices. Also, the device is extremely compact, yet magnetic particles would still have many chances to be actuated into the magnetic line.

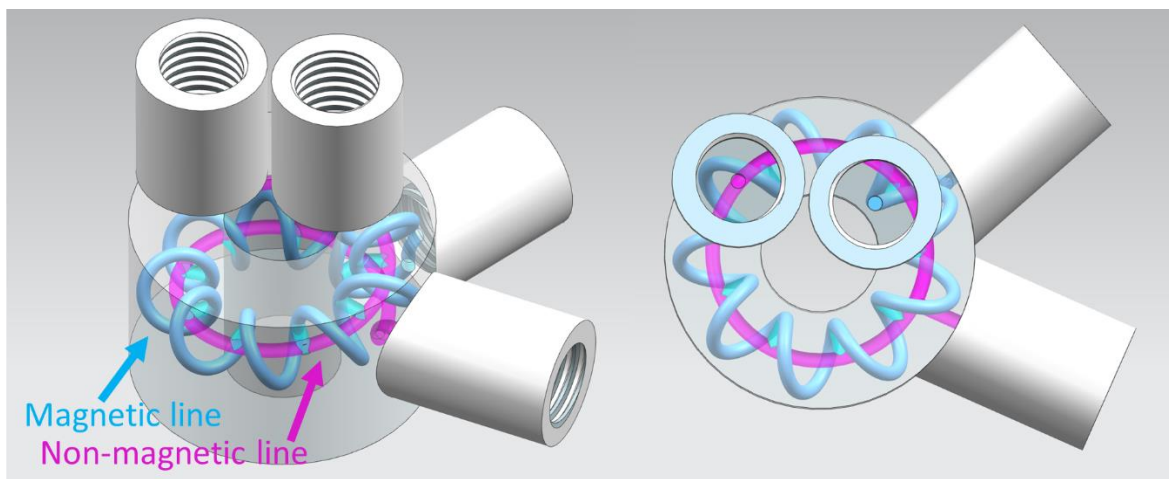


Figure 6.17 Concept, bridged, double-spiralled magnetic separator device. The non-magnetic line (pink) consists of a gentle spiral that encircles the central magnet cavity, and is itself encircled by the magnetic line (blue), a much tighter spiral. The two are connected by a series of bridges (bright blue) that radiate outwards from the points of the magnetic line spiral closest to the magnet.

6.6 Conclusions

Initial proof-of-concept studies for 3D printed microfluidic modules for continuous magnetic particle separation were carried out. This encompassed simple, planar chips as well as a number of multi-bridged, three-dimensional, spiralled chips. These latter designs would be extremely hard to fabricate by conventional photolithographic microfluidic fabrication methods.

During this work we identified numerous challenges, one of the most critical being achieving a suitable ratio between non-magnetic and magnetic lines, where the non-magnetic flow is slightly faster.

However, incorporating a hydrodynamic focusing junction enabled fine-tuning of the sample stream to traverse the non-magnetic line, greatly improving separation control. We also had issues with blockages in internal spiral channel at diameters of 1000 μm —we believe that achieving spiral channel diameters smaller than this will be difficult. We also observed significant particle fouling onto the floor of a spiral chip, possibly due to low flow rates. Other challenges included poor pore reproducibility in combined RPS/ magnetic separation chips, and poor separation due to magnetic particle heterogeneity.

The ending of this project cut short the work in this chapter and so recorded data is limited, especially on the spiralled separator chips. A ~90% magnetic separation efficiency was measured in a simple linear chip, but this requires repeats and a great deal of device configuration optimisation is needed. However, device prototyping and the involved iterations would be greatly accelerated by AM. After optimisation, magnetic separation would be a useful preparation step before particle/cell analysis, enabling assays and sample separation out of matrices.

6.7 References

- 1 N. Pamme, J. C. T. Eijkel and A. Manz, *J. Magn. Magn. Mater.*, 2006, **307**, 237–244.
- 2 S. Bhuvanendran, N. Gourikutty, C. Chia-Pin and D. P. Poenar, *J. Chromatogr. B*, 2016, **1011**, 77–88.
- 3 A. Myklatun, M. Cappetta, M. Winklhofer, V. Ntziachristos and G. G. Westmeyer, *Sci. Rep.*, 2017, **7**, 1–8.
- 4 J. Wu, Q. Yan, S. Xuan and X. Gong, *Microfluid. Nanofluidics*, 2017, **21**, 1–12.
- 5 N. Pamme and C. Wilhelm, *Lab Chip*, 2006, **6**, 974–980.
- 6 S. Martela, C. C. Tremblay, S. Ngakeng and G. Langlois, *Appl. Phys. Lett.*, 2006, **89**, 233904.
- 7 E. P. Furlani, *J. Phys. D*, 2007, **40**, 1–28.
- 8 B. D. Plouffe, S. K. Murthy and L. H. Lewis, *Rep. Prog. Phys.*, 2015, **78**, 016601.
- 9 I. Šafarík and M. Šafaríková, in *Scientific and Clinical Applications of Magnetic Carriers*, eds. U. Häfeli, W. Schütt, J. Teller and M. Zborowski, Springer, Boston, MA, USA, 1997, pp. 323–340.
- 10 M. Meza, in *Scientific and Clinical Applications of Magnetic Carriers*, eds. U. Häfeli, W. Schütt, J. Teller and M. Zborowski, Springer, Boston, MA, USA, 1997, pp. 303–309.
- 11 M.-C. Lim, J. Y. Park, K. Park, G. Ok, H.-J. Jang and S.-W. Choi, *Food Control*, 2017, **73**, 1541–1547.
- 12 Q. Xiong, X. Cui, J. K. Saini, D. Liu, S. Shan, Y. Jin and W. Lai, *Food Control*, 2014, **37**, 41–45.

- 13 L. Chen, T. Wang and J. Tong, *TrAC Trends Anal. Chem.*, 2011, **30**, 1095–1108.
- 14 J. Porter and R. Pickup, in *Environmental Monitoring of Bacteria (Methods in Biotechnology)*, ed. C. Edwards, Humana Press Inc, Totowa, NJ, USA, 1999, pp. 75–96.
- 15 M. Iranmanesh and J. Hulliger, *Chem. Soc. Rev.*, 2017, **46**, 5925–5934.
- 16 A. Van Reenen, A. M. De Jong, J. M. J. Den Toonder and M. W. J. Prins, *Lab Chip*, 2014, **14**, 1966–1986.
- 17 M. Husakova, R. Dziejzinska and I. Slana, *BioMed Res. Int.*, 2017, **2017**, 5869854.
- 18 M. A. M. Gijs, F. Lacharme and U. Lehmann, *Chem. Rev.*, 2010, **110**, 1518–1563.
- 19 M. A. M. Gijs, *Microfluid. Nanofluidics*, 2004, **1**, 22–40.
- 20 R. Ganguly, A. Sinha and I. K. Puri, in *Microfluidics and Nanofluidics Handbook: Fabrication, Implementation, and Applications*, eds. S. K. Mitra and S. Chakraborty, CRC Press, Boca Raton, FL, USA, 2012, pp. 433–484.
- 21 N. Pamme, *Lab Chip*, 2006, **6**, 24–38.
- 22 N. Pamme and A. Manz, *Anal. Chem.*, 2004, **76**, 7250–7256.
- 23 F. Huaxue, H. Yong-Qing and J. Feng, *Chinese J. Anal. Chem.*, 2017, **45**, 1238–1247.
- 24 J. Zeng, Y. Deng, P. Vedantam, T. R. Tzeng and X. Xuan, *J. Magn. Magn. Mater.*, 2013, **346**, 118–123.
- 25 F. Wittbracht, A. Weddemann, B. Eickenberg, M. Zahn and A. Hütten, *Appl. Phys. Lett.*, 2012, **100**, 123507.
- 26 A. Lenshof and T. Laurell, *Chem. Soc. Rev.*, 2010, **39**, 1203–1217.
- 27 N. Huang, Y. Hwong and R. Lai, *Microfluid. Nanofluidics*, 2018, **22**.
- 28 D. Jaiswal, A. T. Rad, M.-P. Nieh, K. P. Claffey and K. Hoshino, *J. Magn. Magn. Mater.*, 2017, **427**, 7–13.
- 29 M. Hejazian, W. Li and N.-T. Nguyen, *Lab Chip*, 2014, **15**, 959–970.
- 30 B.-Y. Qu, Z.-Y. Wu, F. Fang, Z.-M. Bai, D.-Z. Yang and S.-K. Xu, *Anal. Bioanal. Chem.*, 2008, **392**, 1317–1324.
- 31 N. M. Karabacak, P. S. Spuhler, F. Fachin, E. J. Lim, V. Pai, E. Ozkumur, J. M. Martel, N. Kojic, K. Smith, P. Chen and E. Al., *Nat. Protoc.*, 2014, **9**, 694–710.
- 32 C. Ruffert, *Micromachines*, 2016, **7**, 1–17.
- 33 H. Tekin, G. Cumhur and A. Martin, *Lab Chip*, 2013, **13**, 4711–4739.
- 34 K. Hoshino, Y.-Y. Huang, N. Lane, M. Huebschman, J. W. Uhr, E. P. Frenkel and X. Zhang, *Lab Chip*, 2011, **11**, 3449–3457.
- 35 K. S. Kim and J.-K. Park, *Lab Chip*, 2005, **5**, 657–664.
- 36 N. Modak, A. Datta and R. Ganguly, *Microfluid. Nanofluidics*, 2009, **6**, 647–660.

- 37 F. Del Giudice, H. Madadi, M. Villone, G. D'Avino, A. Cusano, R. Vecchione, M. Ventre, P. Maffettone and P. Netti, *Lab Chip*, 2015, **15**, 1912–1922.
- 38 S. A. Khashan, S. Dagher, A. Alazzam, B. Mathew and A. Hilal-Alnaqbi, *J. Micromech. Microeng.*, 2017, **27**, 1–10.
- 39 S. Dutz, M. E. Hayden, A. Schaap, B. Stoeber and U. O. Häfeli, *J. Magn. Magn. Mater.*, 2012, **324**, 3791–3798.
- 40 S. Dutz, M. E. Hayden and U. O. Häfeli, *PLoS One*, 2017, **12**, 1–24.
- 41 Y. Jung, Y. Choi, K. Han and A. Frazier, *Biomed. Microdevices*, 2010, **12**, 637–645.
- 42 J.-J. Lee, K. J. Jeong, M. Hashimoto, A. H. Kwon, A. Rwei, S. A. Shankarappa, J. H. Tsui and D. S. Kohane, *Nano Lett.*, 2013, **14**, 1–5.
- 43 C. A. Grande, J.-L. Dubois, J. C. P. Cambor, Ø. Vistad, T. Didriksen, R. Blom, A. I. Spjelkavik and D. Akporiaye, Additive Manufacturing: Haute Couture for Chemical Industries [online], 2015 [Accessed 17/12/2017]. Available from <https://doi.org/10.13140/rg.2.1.1356.5520>.
- 44 A. J. Capel, S. Edmondson, S. D. R. Christie, R. D. Goodridge, R. J. Bibb and M. Thurstans, *Lab Chip*, 2013, **13**, 4583–4590.
- 45 W. Lee, D. Kwon, W. Choi, G. Y. Jung and S. Jeon, *Sci. Rep.*, 2015, **5**, 1–6.
- 46 K. G. Lee, K. J. Park, S. Seok, S. Shin, D. H. Kim, J. Y. Park, Y. S. Heo, S. J. Lee and T. J. Lee, *RSC Adv.*, 2014, **4**, 32876–32880.
- 47 L. Krejcova, L. Nejdil, M. A. M. Rodrigo, M. Zurek, M. Matousek, D. Hynek, O. Zitka, P. Kopel, V. Adam and R. Kizek, *Biosens. Bioelectron.*, 2014, **54**, 421–427.
- 48 W. Lee, D. Kwon, B. Chung, G. Y. Jung, A. Au, A. Folch and S. Jeon, *Anal. Chem.*, 2014, **86**, 6683–6688.
- 49 C. Park, J. Lee, Y. Kim, J. Kim, J. Lee and S. Park, *J. Microbiol. Methods*, 2017, **132**, 128–133.
- 50 D. Kirby, M. Glynn, G. Kijanka and J. Ducree, *Cytom. Part A*, 2015, **87**, 74–80.
- 51 D. Kirby, J. Siegrist, G. Kijanka, L. Zavattoni, O. Sheils, J. O'Leary, R. Burger and J. Ducree, *Microfluid. Nanofluidics*, 2012, **13**, 899–908.

Chapter 7 Conclusions and Further work

7.1 Conclusions

The current demand for LOC technologies in low-cost POC, environmental and QC applications is not being efficiently met by conventional photolithographic microfluidic fabrication techniques, which are relatively slow and expensive¹. In the last 7 years, the various types of 3D printing have been explored as an alternative. However, printed microfluidic sensors so far have neglected to investigate particle/cell analysis, which is critical in the aforementioned areas. This thesis aims to fill this gap, by developing additively manufactured chips for particle/cell analysis, and trialling two different detection systems: optical and electrochemical. We also briefly explored continuous magnetic particle separation modules, to add further functionality and greater utilise the 3D freedom enabled by AM. Lastly, we investigated particle adsorption, a significant issue in conventional microfluidics, but as yet uncovered in 3D printed microfluidic systems.

The optical and electrochemical particle/cell analysis chips both utilised label-free detection and carried out particle characterisation by way of pulses (either light or electrical current). The pulses allowed both particle counting and quantification of particle size. The design of the optical chip was based on flow cytometry, incorporating a hydrodynamic focusing junction for the focusing of particles/cells by flanking sheath liquid flows into single-file for individual analysis, followed by an optical interrogation zone involving low-cost, multimode optical fibres. Assembly of the detection system was very simple: cutting of commercial fibres with scissors followed by polishing and dropping into printed grooves included in the part design, and sealing. In contrast, the electrochemical chip design was based on resistive pulse sensing (RPS), and detected particles by way of drops in ionic current brought about by translocation through a printed pore channel.

Chapter 3 explored device feature fabrication and particle adsorption. A microfluidic printing style popular in recent years was used, where channels are printed open on the device surface and post-sealed with a cover layer, in order to maximise printing resolution. The effect of build direction on microchannels was investigated by printing of an optical chip prototype, and it was found that the Y-direction (device built flat) gave the highest channel quality: the X-direction (device built on end) produced a residual support structure that blocked the mouth of the central inlet channel, and the Z-direction (device built on side) gave channels with far lower reproducibility between part copies along with far higher channel variability along their lengths. In addition, both the X- and Z-direction

builds had very rough channel walls due to the staircase effect and laser-curing of overhanging structures. It was also found that the Y-direction allowed the narrowest stable focused core stream. Due to these findings, all subsequent microfluidic chips were built in the Y-direction. Following this, the reproducibility of pore channels was investigated and their printing resolution limit under the surface printing style was found ($\sim 54 \mu\text{m}$). Additionally, it was found that straight and diagonally printed sensor grooves produced printed widths that were wider and narrower than nominal, respectively, and that a straight printed groove with a nominal width of $235 \mu\text{m}$ gave the best fit for our $250 \mu\text{m}$ diameter sensors. Finally, particle fouling into channels and in the form of adsorption onto Accura[®] 60 SLA polymer was investigated, and found to be mostly due to trapping into device inlets and outlets, as opposed to adherence onto printed step structures.

Chapter 4 covered an optical particle analysis chip. The device laminar hydrodynamic focusing and optical detection sensitivity were first tested by the sizing of liquid dye core streams of a range of widths. It was found that core stream stability was slightly better at higher overall flow rates, and that the device could produce stable core streams down to $\sim 5 \mu\text{m}$ width, as well as accurately size them ($R^2=0.9986$). Following this, the device was used to analyse $30 \mu\text{m}$ diameter beads. Due to sample pulse spectra being greatly affected by device flow and optics variables as well as sample concentration, this analysis was optimised by application of a GA. The GA screened five experimental conditions: optical fibre core diameter, particle concentration, core flow rate/sheath flow rate ratio, overall flow rate, and the presence of a dye in the sample core stream (this latter variable was added as it was postulated, incorrectly, that device sensitivity might increase if samples were detected as a drop in dye absorbance). The GA generated a set of particle runs and ranked the subsequent pulse spectra according to three objectives: pulse magnitude, pulse magnitude variance, and pulse periodicity, moving forward favourable experimental conditions whilst adding new combinations in order to explore the reaction space. The GA was run for a total of 3 generations, after which a set of conditions was deemed to be 'optimal'. This optimum set of conditions was used to demonstrate device counting power, where it was found that $30 \mu\text{m}$ beads could be counted to a high degree of accuracy ($R^2=0.9983$). Finally, the optimised condition set was also used in a study to demonstrate device sizing power, where a mixture of 10 and $30 \mu\text{m}$ beads was analysed and the two bead sizes differentiated by pulse magnitude. However, it was thought that pulse uniformity was too poor to allow characterisation of a cell population.

In contrast, Chapter 5 covered an electrochemical chip based on RPS. The effects of pore aspect ratio on I-V curves, counting throughput and pulse morphology were investigated. I-V curves were found to

be linear in all but the lowest flow rates and KCl concentrations in the Hp,Wp,Lp=100 μm pore, as to be expected for microscale pores. Particle throughput was very similar for the Hp,Wp,Lp=100 μm and Hp,Wp=100 μm , Lp=500 μm pores, with the cover layer application having a more significant effect. An unusual, double-peaked pulse shape was observed in the Hp,Wp=100 μm , Lp=500 μm pore. This was identified as likely being due to the cover layer adhesive. Following this, the narrowest pore channel was found to have the highest sensitivity but severe problems with blocking and lower throughput. The RPS chip had superior resolving power to the optical chip, being able to resolve 20 and 30 μm beads, as well as characterise a population of skeletal muscle cells. Its linear dynamic range was slightly lower ($0\text{--}3.25 \times 10^4$ beads mL^{-1} versus $0\text{--}5.00 \times 10^4$ particles mL^{-1}) and correlation ($R^2=0.9981$) similar to that of the optical chip, but its throughput was higher, being able to count up to ~ 1380 particles min^{-1} versus ~ 270 min^{-1} , respectively. However, having a constrictive pore channel, these chips suffered badly from particle aggregation and blocking. Also, the RPS devices were highly susceptible to electrical noise and so required protection in the form of a Faraday cage, thus hindering their potential application in portable applications. For use in POC and in-field situations, a shielded benchtop readout device in conjunction with microfluidic disposable cartridges may have to be used, whilst the optical chip by comparison has greater potential for these applications due to the greater opportunity for optical element integration. Lastly, with its far greater pulse detail, the RPS chip has the potential to elucidate further particle information such as transport mode, whilst the optical chip does not.

Finally, Chapter 6 covered initial groundwork in printed continuous magnetic separator modules, intended to act as sample preparation steps within the printed analysis systems. Linear and spiral designs were produced, with the following better-utilising the three-dimensional freedom enabled by 3D printing. A $\sim 90\%$ magnetic separation efficiency was measured in a linear configuration chip, but this requires repeats and significant device configuration optimisation. An integrated magnetic separator and RPS detection chip was produced, but testing of this, as well as the spiralled designs, was hindered by the finishing of this project.

7.2 Further work

7.2.1 Additively manufactured microfluidic fabrication

Variance across separate prints has not been thoroughly investigated in this project, and all parts in Chapter 3 were printed in the same build (or, in the case of the sensor grooves and pore channels, the

same part). Furthermore, with the exception of the $H_p, W_p=100 \mu\text{m}$, $L_p=500 \mu\text{m}$ pore device, only channel/groove widths have been investigated, with the three-dimensional shape of channels and grooves not examined. Examination of cross-sections would be beneficial, especially in the RPS pore wafer in Chapter 3, but a very fine blade such as that of a dicing saw would be required to prevent device damage and give an accurate representation. FIB cutting is also possible, but parts would have to be reprinted with a very small thickness, and pre-coated in a conductive metal. Another alternative method for three-dimensional profiling is by carrying out SEM at an angle, which is described in Chapter 5 for pore channel analysis. Additionally, channel roughness would be better analysed using a profilometer as opposed to carrying out image analysis, which is subjective.

In addition, a study of particle adsorption onto the cover layer TESA[®] tape adhesive under controlled conditions has not been carried out. Fouling onto the cover layer was commonly observed during use of the devices in this project. Also, the Accura[®] 60 wafer particle adsorption study is only a crude way of inferring polymer charge; other methods that could corroborate surface heterogeneities include AFM², XPS, and the 'forced spreading' method³. Solution displacement in microfluidic channels is another alternative method that measures microchannel surface charges in solution⁴, as opposed to flat polymer wafers, which may have different surface properties. To prevent particle fouling, optically transparent AM polymers with weaker particle attraction could be explored⁵, or surface coatings/chemical modifications could be carried out on the channel surfaces⁶. However, these do not solve the problem of tape adhesive fouling. There exist various complicated set-ups to prevent microfluidic fouling, such as ultrasonics⁵, but these are inappropriate for the small, low-cost chip systems in this project.

7.2.2 Optical particle analysis device

To improve the optical device resolution in order to detect smaller particles, a higher intensity light source such as a laser could be used in conjunction with a small optical fibre core and/or a printed lens^{7,8} integrated into the chip for beam focusing and light loss reduction. This could also be coupled with three-dimensional focusing in the vertical plane, by inclusion of printed elements such as chevrons in the device design⁹. Further work could also be done towards complete, on-chip component integration, including use of on-chip light-emitting diodes (LEDs)¹⁰ or laser diode sources⁷. Lastly, fluorescence spectroscopy could be used to analyse further particle/cell characteristics than merely diameter.

7.2.3 Resistive pulse sensing particle analysis device

The skeletal muscle cell population size data recorded by the RPS device should be compared with size measurements taken from microscope images, in order to confirm accurate characterisation. In terms of device performance, better electrical noise shielding would increase sensitivity and allow detection of beads $<10\ \mu\text{m}$. Furthermore, non-spherical pore channel shapes, which would be relatively easily produced by AM, allow additional probing of particle morphology¹¹.

It should be noted that during the final stages of the writing of this thesis, a collaborator (Marcus Pollard) made further investigation into the hypothesis that the double-peaked pulse shape witnessed in the $H_p, W_p=100\ \mu\text{m}$, $L_p=500\ \mu\text{m}$ pore device was due to tape adhesive aggregating at the pore mouth: studies were carried out where particle suspensions were ran through the pore in each direction. The resulting pulse morphologies were mirror images of each other, indicating that the morphology producing the pulse shape is stationary. Furthermore, replacing the cover layer on the same printed device body produced a slightly different double-peaked pulse shape that was still repeatable by reversing sample flow.

7.2.4 Magnetic separator devices

Device optimisation in terms of configuration, dimensions and fluid and particle modelling of the spiral devices is required before particle separation trials can be carried out, including channel dimensions and cross-section, number and placement of bridges, magnet strength and distance, and spiral pitch and diameter. In addition, modelling of magnetic particle trajectories under the influence of a magnetic field whilst also being subject to lift forces inside spiral microfluidic channels needs to be carried out. This work is beyond what was possible in the project timeframe. After device optimisation has been carried out, a GA could be implemented to optimise particle concentration and flow rates for various different analytes, as in Chapter 4. Even further work would involve investigating the possibility for further sample discrimination by size or density in addition to magnetic property, by utilisation of centrifugal forces generated inside spiral channels¹²⁻¹⁵.

7.2.5 Concluding remarks

The work covered by this thesis are initial, proof-of-concept studies that demonstrate the possibility to 3D print microfluidic devices for particle sensing and analysis. Further work could be done to explore

device reproducibility, especially across different 3D printers. In addition, much more could be done towards making the chips stand-alone, true integrated LOC devices (as opposed to chips-in-a-lab), as in their current form they still require bulky external hardware: fluidic pumps and a gas line, and a tungsten light source and spectrometer, and Faraday cage and current amplifier, for the optical and electrochemical chips respectively. The waveguides and electrodes could be printed on-chip, as well as the means of fluidic control (in the form of 3D printed pumps and valves). Additionally, some components could be swapped out for integratable commercially available elements, such as replacing the light source for an LED, and spectrometer for a photodiode. However, the related electronics and shielding of the RPS device would be difficult to refashion on-chip, and so it would be more suitable as disposable cartridges to use in a dedicated benchtop device containing these features.

3D printing is currently developing rapidly, with regular advancements in resolution¹⁶. Printed component functionality is also continually advancing due to better multiprocess printing¹⁷, and a host of recent new methods have made microfluidic printing more accessible¹⁸. During this project, a host of new milestones were reached in AM, including the release of mass production systems by major 3D printing players in 2017, and the introduction by Dolomite of the first commercial 3D printer for microfluidic systems. It is predicted that AM will continue to act as an enabling, revolutionising force in the field of microfluidics for the foreseeable future.

7.3 References

- 1 L. R. Volpatti and A. K. Yetisen, *Trends Biotechnol.*, 2014, **32**, 347–350.
- 2 Y. Kim, S. Lee, J. Kuk and S. Hong, *Desalination*, 2015, **367**, 154–160.
- 3 R. K. Lade, E. J. Hippchen, C. W. Macosko and L. F. Francis, *Langmuir*, 2017, **33**, 2949–2964.
- 4 D. Mampallil, D. Van Den Ende and F. Mugele, *Electrophoresis*, 2010, **31**, 563–569.
- 5 F. Scheiff and D. Agar, in *Micro-Segmented Flow: Applications in Chemistry and Biology*, eds. Köhler, J. Michael and B. P. Cahill, Springer-Verlag, Berlin, Germany, 2013, pp. 123–127.
- 6 K. Wu and S. Kuhn, *Chim. Oggi.*, 2014, **32**, 62–66.
- 7 X. Liang, A. Liu, C. Lim, T. Ayi and P. Yap, *Sensors Actuators A. Phys.*, 2007, **133**, 349–354.
- 8 T. Ngermsutivorakul, C. M. Cipolla, C. E. Dugan, S. Jin, M. D. Morris, R. T. Kennedy and F. W. L. Esmonde-White, *Anal. Bioanal. Chem.*, 2017, **409**, 275–285.
- 9 J. P. Golden, J. S. Kim, J. S. Erickson, L. R. Hilliard, P. B. Howell, G. P. Anderson, M. Nasir and F. S. Ligler, *Lab Chip*, 2009, **9**, 1942–1950.
- 10 F. Cecil, M. Zhang, R. Guijt, A. Henderson, P. Nesterenko, B. Paull, M. Breadmore and M.

- Macka, *Anal. Chim. Acta*, 2017, **965**, 131–136.
- 11 P. Hinkle, T. M. Westerhof, Y. Qiu, D. J. Mallin, M. L. Wallace, E. L. Nelson, P. Taborek and Z. S. Siwy, *Sci. Rep.*, 2017, **7**, 1–14.
 - 12 S. Dutz, M. E. Hayden and U. O. Häfeli, *PLoS One*, 2017, **12**, 1–24.
 - 13 D. Kirby, M. Glynn, G. Kijanka and J. Ducree, *Cytom. Part A*, 2015, **87**, 74–80.
 - 14 S. Dutz, M. E. Hayden, A. Schaap, B. Stoeber and U. O. Häfeli, *J. Magn. Magn. Mater.*, 2012, **324**, 3791–3798.
 - 15 D. Kirby, J. Siegrist, G. Kijanka, L. Zavattoni, O. Sheils, J. O’Leary, R. Burger and J. Ducree, *Microfluid. Nanofluidics*, 2012, **13**, 899–908.
 - 16 J. R. Tumbleston, D. Shirvanyants, N. Ermoshkin, R. Januszewicz, A. R. Johnson, D. Kelly, K. Chen, R. Pinschmidt, A. Rolland, Jason P. Ermoshkin and J. M. Samulski, Edward T DeSimone, *Science*, 2015, **347**.
 - 17 E. MacDonald and R. Wicker, *Science*, 2016, **353**, 1512–1522.
 - 18 P. G. Shankles, L. M. Millet, J. A. Aufrecht and S. T. Retterer, *PLoS One*, 2018, **March**, 1–16.

Chapter 8 Attended Conferences

Conference Name	Location	Presentation	Dates attended
MNE2017 (43 rd International Conference on Micro and Nanoengineering)	INL (International Iberian Nanotechnology Laboratory), Braga, Portugal	Poster	17/09/17–22/09/17
Bright Sparks Symposium (BSS) 2017	Bath University, Bath, UK	Poster	11/09/2017
East Midlands 3 Minute Thesis™ Final 2017	Nottingham University, Nottingham, UK	Oral	13/09/17
RSC Analytical Research Forum 2017	Burlington House, London, UK	Oral	07/07/17
RSC Chemistry World Science Communication Competition	Burlington House, London, UK	Oral <i>Prize awarded: Winner</i>	27/06/17
EMUA (East Midlands University Association) Student Conference 2017	Loughborough University, Loughborough, UK	Oral <i>Prize awarded: Best Talk in Science & Technology section</i>	1/09/2017
Loughborough University 3 Minute Thesis™ Final	Loughborough University, Loughborough, UK	Oral <i>Prize awarded: Runner-up</i>	22/06/2017
RSC Twitter Poster Competition 2017	Loughborough University, Loughborough, UK	Poster <i>Prize awarded: 3rd Prize in Analytical Division</i>	20/03/2017
Research Conference: Influence and Impact	Loughborough University, Loughborough, UK	Poster <i>Prize awarded: Runner-up</i>	31/10/2016
4 th RSC Early Careers Symposium	Strathclyde University, Glasgow, UK	Oral	23–24/06/16
Loughborough University Summer Showcase,	Loughborough University, Loughborough, UK	Poster <i>Runner-up, Best Poster in category Enabling Technologies</i>	22/06/16
5 th Annual Science Matters Conference	Loughborough University, Loughborough, UK	Poster <i>Prize awarded: Runner-up, Best 2nd Year PhD Poster,</i>	20/06/16
4 th Annual Science Matters Conference	Loughborough University, Loughborough, UK	Oral <i>Prize awarded: Best Talk</i>	20/06/15

Chapter 9 Publications

3D printed microfluidic device with integrated optical sensing for particle analysis

S.M. Hampson, W. Rowe, S.D.R. Christie and M. Platt, *Sens. Actuators B Chem.*, 2018, **256**, 1030–1037.

Additively manufactured flow-resistive pulse sensors

S.M. Hampson, M. Pollard, P. Hauer, H. Salway, S.D.R. Christie and M. Platt, *Anal. Chem.*, 2019, **91**, 2947–2954.